Identification of kinematic boundary conditions triggering removal of material in tectonically erosive margins

Insight from scaled physical experiments

DISSERTATION
zur Erlangung des akademischen Doktorgrades doctor rerum naturalium (Dr. rer. nat.) im Fachbereich Geowissenschaften der Freien Universität Berlin
vorgelegt von

Francisca Albert

Potsdam, December 2012

Tag der Disputation: 11. Feb 2013

Prof. Dr. Onno Oncken (1. Gutachter) Freie Universität Berlin, GeoForschungsZentrum Potsdam

Prof. Dr. Nina Kukowski (2. Gutachter) Friedrich-Schiller-Universität Jena

“Failure doesn't mean anything, it just means changing paths.”
― Alejandro Jodorowsky

To my beloved parents, sister and cat.

TABLE OF CONTENTS

DEFINITION OF TERMS

Since some terms to describe erosion is unclear or changing in different publications, the following list of terms and definitions used in this study is presented below:

Basal erosion: Removal of material from the base of the wedge and entrained with the subducting plate and subducted arcwards (Scholl et al, 1980; von Huene and Lallemand, 1990). It is described as a result from abrasion and hydrofracturing above the subduction channel (von Huene et al., 2004).

Basal accretion: addition of material at the base of the wedge, thickening and uplifting the wedge. Also referred in this study as underplating.

Distributed deformation: (often termed distributed strain) Deformation spread over a broad region.

Frontal erosion: Removal of material from the frontal segment of the wedge. It results from a combination of erosion and structural collapse of the forearc wedge into the trench. Common when no sediment is offscraped, oversteepening the front by mass wasting (slumps and slides). Subducting asperities are often cited to cause it (von Huene and Lallemand, 1990).

Localized deformation: (often termed localized strain) also referred in this study as localized shear zone or localized shear slip lines.

Material input: the amount of sediment added to the wedge. With no external material supply (no incoming sand-layer), the only source of input material came from the frontal erosion. Thus, the average thickness of sediment supply at the wedge toe was estimated as the bulk rate of the previously frontally eroded sediment by cm of convergence.

Material output: the amount of wedge material transported on the subducting plate exiting the system. It is the layer above the basal detachment transported through the subduction gap.

Out-of-sequence-thrust: a thrust fault initiated at the subduction gap (at an oblique angle), cross cutting rear to middle of the wedge (at an oblique angle and rotating to base-parallel beneath the middle slope in some cases).

Subduction Channel (SC): material transported between the descending plate and overriding block, transported further arcwards towards the subduction gap.

Subduction erosion: the tectonic removal of strata from near the leading edge of the upper lithospheric plate in a subduction zone.

Subduction gap (SG): the size of the basal open gate, which allows subducted material to be transported further arcwards. In nature it represents the global capacity, governing amount of material deeply subducted (Cloos and Shreve, 1988a).

Taper: sum of the surface slope and plate dip angle (Davis et al., 1983)

Tectonic erosion: material removal from the base of an overriding plate, derived from the subduction of the oceanic plate. It causes consumption and thinning of the upper plate.

Underplating: addition of material at the base of the wedge, usually as duplexes (Platt, 1986). Referred in this study as accretion of material beneath the wedge.

Wedge: In nature, it is the region between the subduction zone and the volcanic arc. Also referred as backstop, prism or forearc.

Abstract

High rates of tectonic activity and the presence of abundant ore deposits have made convergent plate margins places of intense research. Of the two end-member types (accretionary and erosional), tectonically erosive margins make up at least 60% of all convergent margins. Their study is more complicated than for accretionary ones because of the lack of a geological record, which is consumed at the margin. This is probably the reason for the much larger amount of research performed on accretionary systems. This study is focused on erosive margins, which are less known despite comprising the majority between both end-member margin types.

Several common features among natural erosional margins were derived in the first conceptual models attempting to explain the consumption of the forearc. Compared to accretionary foreacs, erosional convergent margins have larger tapers and the geometry of the slope is typically segmented into a lower, middle and upper slope. The slope shows extensional features, including normal faulting, landward tilted blocks and seaward tilted forearcs, active mass wasting and related irregular surfaces. The incoming oceanic plate is rougher, moves faster and is covered by a thinner blanket of sediments. Subduction channel (SC) thickness in the erosive case is usually thinner than 2 km, the frontal prism is usually smaller. The subsidence with simultaneous tilting and normal faults deforms either the middle or upper slope, or both. Some erosional margins feature steep scarps in the middle slope. The location of enhanced subsidence occurs mostly at the upper-middle slope, which is commonly related to basal erosion.

We attempt to identify potentially relevant parameters involved in or controlling mass-transfer modes in brittle, tectonically erosive forearcs. This challenge is addressed by four series of sandbox experiments, which were built with granular materials, deforming similarly to brittle crustal rocks. Each series was aimed at one parameter potentially triggering subduction erosion: the amount of sediment that can be transported downdip through the SC; the normal load of the overburden as a consequence of the change of the surface taper of the wedge; the internal properties of the wedges (strength); the basal interface topography interacting with the wedges. Together with the scaled physical models, we were able to identify particular patterns of mass transfer by using PIV, a method to visualize material flow.

We analyzed our experiments regarding the evolution of internal and basal material transfer (vertical and horizontal components of the velocity field), mass transfer mode patterns, wedge geometry, SC evolution and frictional properties of the analogue granular material. For each experimental series, these parameters were discussed and connected to the respective characteristics of the different erosional margins worldwide, evaluating their relevance in the erosional process.

The deformational behavior of Mohr Coulomb materials (as rocks or granular material, which was used here) is characterized by variable frictional strength values (peak, stable static or stable dynamic strengths). This implies that for a critical taper analysis, mechanical interpretations are subjected to the spatio-temporal frictional strength variations.

First, a hypothetical erosional forearc (the reference experiment) was designed to create the scenario most favorably driving basal erosion. To achieve this, we built a wedge without incoming sand layer, featuring a high-friction basal detachment, and composed of “strong”

granular material. The wedge initially had a critical taper and was subject to rear material loss. The first obtained observations pointed to a strong interaction between SC segmentation and wedge deformation. The spatial distribution of the frictional strength within the wedge mainly controlled the loci and/or volumes of modes of mass transfer. Peak strength controlled the frontal segment of the wedge. Beneath the middle and upper slope, deformation was governed by the frictional strengths that shifted between stable, static and peak and defined the SC (whose upper boundary is a shear zone) back segment. The behavior of the latter controlled the mechanics of the wedge, defining the Middle and Rear segment of the wedge. Basal erosion was mainly concentrated beneath the middle-upper slope. Phases in the evolution of the components of the velocity field were observed, implying that subduction erosion may be an irregular process.

The variable behavior of the frictional strength also determined the flow inside the SC. The first experiment series, in which the amount of material loss at the wedge's rear was systematically varied, confirmed the strong influence of the SC on the wedge evolution. Wedges with a small amount of rear material loss developed a SC with uniform velocities along the base of the wedge, resulting in an "accretionary margin". A larger amount of material loss led to the development of a SC with an inhomogeneous distribution of velocities along the base of the wedge, segmenting the SC and the slope geometry. The latter was comparable to observations in natural forearcs, which are segmented into a lower, middle and upper slope. The second experimental series was designed to analyze the influence of different surface taper angles. This series showed that the temporal variability of the different frictional strength values controlled the geometry of the SC and the stability of the wedges. Stable wedges (defined by a large taper) showed a larger erosion ratio (basal-/frontal-erosion) than critical ones (with a smaller taper), where the first is comparable to estimates of erosional ratios in nature. Additionally, wedges with tapers greater than the critical taper showed an important trend (~40%) to form thick SC structures, similar to what is observed off the North of Chile or off Japan. The third series, which evaluates the effect of internal friction properties of the granular material of the wedges, indicated that basal erosion was more favorable for strong wedges, which may be the case for wedges composed of crystalline basement (usually the case for erosional margins). The fourth series tested the response of the wedge to topographic highs and lows on the incoming plate. These bathymetric anomalies favored frontal erosion and basal erosion at the frontal segment of the wedge and inhibited basal erosion at the rear part of the wedge.

This study represents the first investigating potential kinematic boundary conditions for subduction erosion in a systematic manner. For the subduction erosional process, the aperture at the box's rear, which allowed rearward material loss, was shown to have the largest influence on obtained results. If the amount of material leaving the system was larger than the amount of material subducted at the wedge's toe, the margin evolved as erosional. We found the surface slope to be the second important parameter, which strongly controls the amount of basally eroded material.

Acknowledgements

It was a hard path, which sometimes I really thought it was not going to be possible to finish, although it was at the end!

First of all, I want to thank my supervisor Professor Nina Kukowski. Her help during my work, the provided assistance, support and advice made this possible.

Likewise, I would like to express my gratitude to Onno Oncken, Andres Tassara, Karen Leever and Marcos who provided me valuable information, comments and support in an important part of this work. In the same line, to Professor Christoph Heubeck and family, who helped me during my first period in Germany.

Thomas and Frank, thank you also for your efficiency and good disposition to help in the lab.

My mom, my dad and sister: I love you. Your hope that I would be successful was one of the pillars of my perseverance.

At the end, but not less important, all my friends; you were the other pillar without which I would have definitely failed: Amerika y Lisandro, Christian Sippl, Alejandro, Julia, Karsten, Moppel, Jose Ramón, Isabel, Jorge, Aliressa, you will always occupy an important part of my heart, since you gave me your sincere friendship and many times support when I needed it in particular and fundamental periods of my life in Germany. I miss you every day, but I hope we will see each other again in our lives. Kira and Matze, same for you: my last weeks were wonderful living next to you, you are great guys! Potsdam is a nice city and you made it better.

It is a pleasure to thank all those who made this thesis possible.

Sincerely,

Francisca

1. INTRODUCTION

Oceanic-continental subduction zones are one of the most dynamic features on Earth, responsible for crustal deformation and subsequent mountain building that causes shallow, frequent and strong seismic activity. Their active magmatism and the development of metallic mineral deposits enhance the importance of their study. Therefore, numerous investigations attempting to understand their internal dynamic defined by their mass balance and deformation have been carried out in the last decades.

This study focuses on the shallow brittle part of subduction zones (i.e. <30 km depth). Based on material supply at the tip of the forearc, they can be classified into accretionary (Silver, 1969) and erosional (Coats, 1962; Gilluly, 1963; von Huene and Scholl, 1991) types (Fig 1.1). The former partially scrape off and accumulate the blanket of sediment deposited on top of the oceanic crust growing a submarine accretionary wedge. The latter are defined by their consumption of forearc material and structures, where an accretionary prism is rather small or absent (cf. Section 2.1).

Actually, roughly 60% of the global convergent margins are classified as erosional (von Huene and Scholl, 1991; Clift and Vannucchi, 2004; Fig. 1.1). The greater amount of erosional convergent margins compared to accretionary ones implies that subduction erosion might be a dominant process at active margins, and that convergence likely favors consumption relative to construction of margins. As the resolution of seismic data decreases with depth (> 15 km) and as drilling is only possible to a few kilometers depth, the visualization of forearc structures at great depth is largely impossible. Fortunately, the geological record left at frontal prisms at accretionary margins can be studied *in situ*. In contrast, the lack of geological record caused by the process of consumption in tectonically erosional forearcs makes investigating them particularly difficult (von Huene and Scholl, 1991; Lallemand et al., 1992; Clift et al., 2003; Heki 2004; Ranero et al., 2008). This could explain that significantly more research has been carried out in accretionary forearcs. Within such a frame, this study focuses on the less well understood tectonically erosional convergent margin type.

The phenomenon of tectonic erosion of the forearc was first recognized at the Chilean margin four decades ago, where the truncation of off-shore forearc structures and a lack of trench sediments were documented, suggesting subduction erosion as a significant process (Miller 1970a and 1970b; Rutland, 1971; Scholl et al., 1980).

In addition to erosion, material transfer at erosional margins may occur through underthrusting and basal accretion (Cloos and Shreve, 1988b; von Huene and Scholl, 1991; Lallemand et al., 1994). Sediment and rock ablation by subduction erosion can be expressed in two forms. Frontal erosion is the removal of material from the tip of the frontal slope, and basal erosion from the underside of the forearc. The first process is directly inferred by the absence of accretionary complexes and also explains trench retreat and inland migration of the volcanic front (Miller, 1970a; Rutland, 1971). Basal erosion, which is more difficult to image, has been inferred by forearc subsidence, thinning, truncation and extensional structures across the sediment apron, as well as

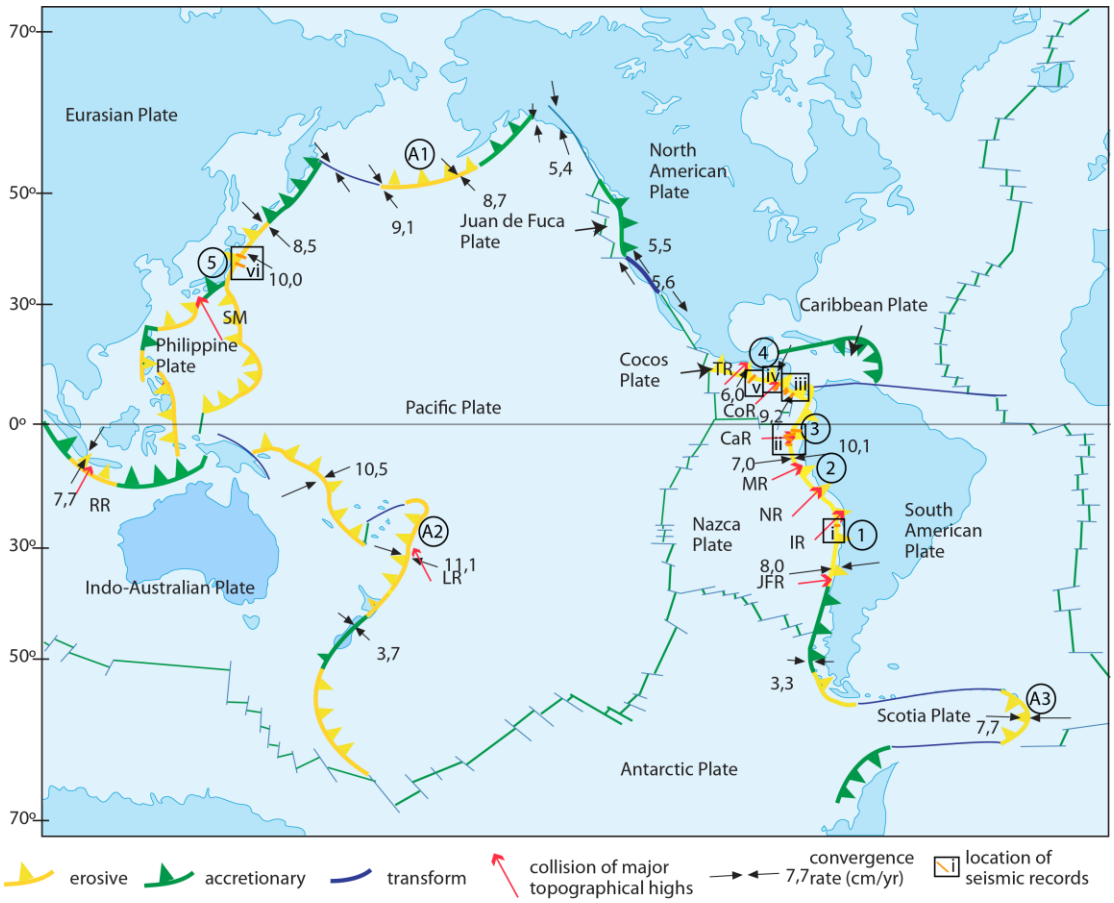

Figure 1.1. *a) Map of the circum Pacific illustrating the distribution of accretionary and erosional subduction zones. Numbers inside circles show margins: 1) Nortern Chile, 2) Peru, 3) Ecuador, 4) Costa Rica, Nicaragua and Guatemala, 5) Japan. Red arrows show zones of collision of major topographic features along some convergent margins. JFR-Juan Fernandez Ridge, IR – Iquique Ridge, NR – Nazca Ridge, MR – Mendaña Ridge, CaR - Carnegie Ridge, CoR – Cocos Ridge, TR – Tehuantapec Ridge, RR - Roos Rise, SM – Seamount and LR – Louisville Ridge (After Scholl, 2002, Kopp et al., 2006, Tilling et al., 1987). A1) Aleutians, A2) Tonga and A3) South Sandwich are described in Appendix A1. i - vi are seismic reflection lines shown in Figures 2.2.1 – 2.2.5 and A1.2 – A1.5. i) CINCA SO104-13; ii) South to North: SIS-72, SIS-18, SIS-12, SIS-64; iii) South to North: SO 81-Line 4, BGR 99-15, BGR 99-17 (in Fig. A1.2); iv) South to North: BGR 99 Line 41 (in Fig. A1.3), Nic1; v) GUA 15 (in Fig. A1.4); vi) South to North: SR 101 (in Fig. A1.5); ORI 78-4.*

seaward tilting of the surface slope (Fig. 1.2; Scholl et al., 1980; von Huene and Lallemand, 1990).

Early investigations of the structural evolution of convergent erosional margins have defined specific parameters governing material transfer. For example, the role of basal friction has been discussed in a considerable number of publications (e.g. Hilde, 1983; Jarrard, 1986; von Huene and Ranero, 2003; Ranero et al., 2008). Nevertheless, the impossibility to directly investigate structures at such depths makes it difficult to validate or falsify proposed hypotheses. Typical features of erosional margins, such as a considerable roughness of the incoming lower plate (i.e. high-relief tops and lows, subduction of seamounts and ridges; Fig. 1.1) or a low supply of sediment at the trench (<1 km thick; Section 2.1) led to the first conceptual models with a high basal friction triggering basal

subduction erosion (cf. Section 3.3.3), by abrasion of the underside of forearcs (Hilde, 1983; Jarrard, 1986). In contrast, a later study proposed that low basal friction would be involved in the basal erosion process due to overpressure of fluids released from basally transported material (Murauchi and Ludwig, 1980). This idea was subsequently developed, where hydrofracturing and erosion as lense-shape bodies play a primary role (von Huene et al., 2004; Ranero et al., 2008, Vannucchi et al., 2012). Hence, the mechanisms removing substrate from the forearc at erosional margins are discussed controversially, and so the internal dynamics of erosional margins remains largely enigmatic. This brought us to our first question to address: what would be the role of basal interface topography interacting with the continental plate?

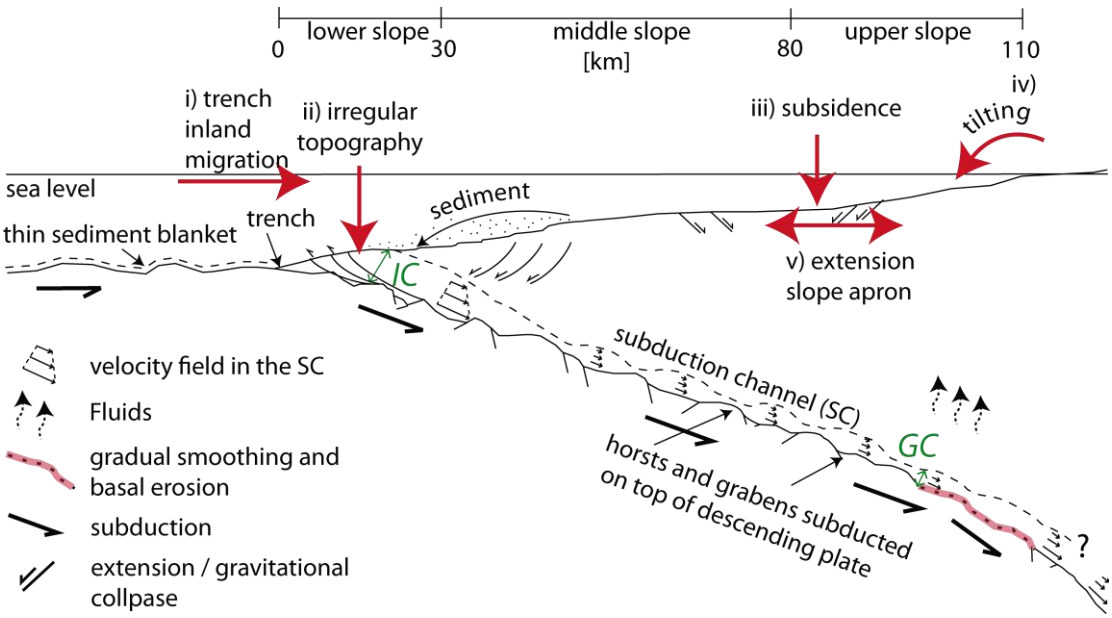

Figure 1.2. *Sketch illustrating the characteristics of an erosional convergent margin, based on conceptual models and seismic data (Cloos and Shreve, 1988a and b; von Huene and Ranero, 2003; Sage et al, 2006). Typical features include a steeper slope than in accretionary systems, subsidence on the middle and upper slopes, gravitational collapsing on the lower slope and a thin layer of sediment on the subducted plate. In general, the steepest segment corresponds to the lower slope, decreasing updip, where the shallowest segment corresponds to the upper slope. Widths of the segments of the slope based on a Chilean profile example; small variations of these values are found along different margins. The vertical and horizontal variation in the strain rate of the basal flow corresponds to that observed in our experiments. IC and GC are the inlet and global capacities, as defined by Cloos and Shreve (1988a) in their SC model. i-v are related to frontal and basal erosional processes (further details in the text). In the vicinity of the stick-slip zone, the horsts structures, which are cut by faults seems to be very deformed and begin to disintegrate landward, smoothing the surface of the lower plate (Tsuru et al., 2000). Basal erosion occurs below the middle-upper slope (Ranero and von Huene, 2000; von Huene and Ranero, 2003; cf. Section 2.2 and Appendix A1)*

Originally developed for accretionary systems, the critical taper theory (Davis et al., 1983; Dahlen, 1984; Dahlen et al., 1984) provides hints to the mechanics of forearcs using the basal- / internal- friction relationship (i.e. the frictional ratio; Adam and Reuter, 2000). Theoretically, either increasing basal friction or decreasing internal friction increases the critical taper of a continental wedge (Dahlen, 1984). Accretionary analogue experiments have been used to simulate such settings by introducing materials in the experiments with different and contrasting internal frictions, achieving good approximations to natural examples (Gutscher et al., 1996; 1998b; Kukowski et al., 2002; Lickorish et al., 2002; Bonini, 2007; Bose et al., 2009).

The behavior of material transported between the descending plate and overriding block (i.e. subduction channel (SC)) seems to be governed by several factors. As expressed by Cloos and Shreve (1988a), those would explain mass balance at a given subduction margin (Fig. 1.2). This concept described the material inside the subducting mélange deforming like a viscous fluid with several small shear border-parallel zones inside. However, variations in density and viscosity by increased vertical load arcwards could lead to changes of shear stresses on the upper border of the SC and its interaction with the overriding plate. They also concluded that where the SC is thicker, shear stress would be greater. The current geometry/stability of the forearc in this way defines SC evolution, varying overriding plate configuration and mass balance (Cloos and Shreve, 1988b). Analysis of seismic profiles and physical experiments has indicated that conditions defining the SC evolution would have implications for the tectonic configuration of forearcs (e.g. Lohrmann et al., 2006; von Huene et al., 2009; Calahorrano et al. 2008; Contreras-Reyes et al., 2010). For example, the relation between the amount of sediment "into" and "out" of the SC defines the efficiency of erosional vs accretive processes at a given subduction margin (Cloos and Shreve, 1988a and b; Kukowski et al., 1994; Gutscher et al., 1998b). The increasing normal load of the upper plate arcwardly must be a significant parameter controlling changes along the SC (Cloos and Shreve, 1988b). The "erodibility" and rate of alteration may differ from one type of rock to another, varying the fashion in which the material is added to the SC (e.g. large rocks or piecemeal; Cloos and Shreve, 1988a). Since the visualization of the SC in seismic images is hardly possible at depths greater than 15 km beneath the seafloor, the results from previous studies can just be compared with information from surface slope or volumetric estimate of material loss. On the other hand, the very different interpretations of the same seismic line in Northern Chile (von Huene and Ranero, 2003; Sick et al., 2006) have opened new inquires about how the dynamics of one erosional margin may differ from that of others. Hence, physical conditions along the SC at depth and the control on the volume of material eroded from the base of the overriding plate are scarcely understood and thus constitute important open issues to be studied.

This brought us to our second task: what would be the likely physical conditions at depths on the SC such as a) the geometric configuration of forearcs, b) differences in rock type or c) control on amount of rear material loss, for the current tectonic configuration of erosional convergent margins?

Numerical and experimental simulations are able to explicitly show how and where deep processes develop in nature (e.g. Gutscher et al., 1998a; Lohrmann et al., 2006; Keppie et al., 2009). Parameters controlling deformation can be systematically studied, permitting to estimate/quantify the effect of each isolated parameter involved in the process. In particular, analogue experiments have shown good agreement with margin configurations (e.g. Davis et al., 1983; Kukowski et al., 1994; Gutscher et al., 1998a; Gutscher et al., 1998b; Kukowski et al., 2002; Glodny et al., 2005; Bonini, 2007; Hoth et al., 2007; Nilforoushan et al., 2008). However, literature focusing on non-accretive margins is very rare (Gutscher et al., 1998b; Kukowski et al., 1994; Hampel et al., 2004; Lohrmann et al., 2006). Although those few have given important contributions to the understanding of potential parameters controlling tectonic processes, mass balance or what triggers and maintains basal erosion at depth remains unclear.
Therefore, this study focuses on the identification and evaluation of first-order erosional mechanisms controlling mass transfer and deformation in erosional margins. In doing so, the aim is to explore the interaction of the upper and lower plates along their interface, and the variables governing the internal and basal transport of sediments. For this task, we analyze 2D scaled physical analogue experiments. The present study represents the first one addressing those parameters potentially controlling subduction erosion in a systematic manner.

Before these challenges are addressed, an account on erosional vs accretionary margins is given (Chapter 2). This is followed by a summary of concepts, introducing the Critical taper theory, Subduction Channel and proposed erosional mechanisms (Chapter 3). Based on this information and concepts, constraints were identified to (i) generate a basic hypothetical tectonically erosional wedge and (ii) incorporate this preliminary model into the sandbox setup.
The deformational behavior of the granular materials used to build the wedges (e.g. sand) is a reliable representation of brittle rocks (Chapter 4), as long as boundary conditions are properly chosen and scaling is correct (Hubbert, 1937; Lallemand et al., 1992b; Calassou et al., 1993; McClay, 1996; Schellart, 2000; Lohrmann et al., 2003). Chapter 5 presents a detailed description of what we obtained from our experiment series. The experiments were analyzed with a technique for flow visualization, the *Particle Image Velocimetry* (PIV). This optical monitoring system provides time-series of the displacement field (and derivatives) within the wedge and the SC. We put special emphasis on tracking particles inside the wedge.
To reach our goals, four series of experiments representing a brittle forearc aimed at investigating the role of:

a) The interaction between the amount of sediment that can be transported downdip, the SC behavior and wedge mechanics (chapter 5.2);
b) The impact of the normal load of the overburden as a consequence of the change of the surface taper of the wedge (chapter 5.3);
c) The internal properties of the wedges (strength) and related dynamic and kinematic wedge evolution (chapter 5.4);
d) The basal interface topography interacting with the wedges and

related dynamic and kinematic wedge evolution (Chapter 5.5)

Experimental results suggest that the spatio-temporal distribution of deformation follows a distinct pattern, from where we identified three evolutionary phases (or stages). The similarity of duration and wedge response of the individual erosional phases supports the robustness of the stages. A reference experiment is described in terms of these three phases (or stages), in addition to a description of the SC evolution and quantitative analysis and discussion of the mass transfer modes. This forms the base for the subsequent characterization of the different series. Finally, we discuss and analyze the consequences of imposed conditions in our experiments. Our results are compared with data compiled from geological and geophysical studies of different offshore forearcs worldwide (Chapter 5).

We conclude that SC evolution is strongly influenced by the conditions imposed in deeper parts of forearcs and roughness of the incoming basal plate. All those changes create conditions favorable or unfavorable for subduction erosion. The ratio between ingoing and outgoing sediment volume defines whether significant basal erosion occurs (for ratios larger than 1). The amount of sediment "out" from the system strongly controls the amount of basal erosion and the deformation of the analogue wedges. Forearc geometry has an important impact on the tectonic evolution of the SC, which can develop in a very different way under similar initial conditions. For substantial basal erosion to occur, the wedge taper must be in a critical state. The amount of eroded material is influenced by the strength of the wedge, where strong wedges showed a higher total amount of basally eroded material than weak ones. Incoming surface topography has an important impact on frontal erosion, contributing to the consumption of the frontal prism. That provides hints about which parameters may be involved in the structural evolution in an erosive environment.

2. GEOLOGICAL SETTING OF EROSIONAL CONVERGENT MARGINS

In this review chapter we first introduce the main characteristics which define/distinguish an accretionary margin from a non-accretionary one (Section 2.1; Fig. 2.1). Afterwards, a summary table (Section 2.2) compiles characteristics of those convergent erosional margins, which have been investigated in detail, points out those features which will be later a base for comparison with our experimental results. Erosional margin reconstructions, drilling expeditions and seismic data are mainly available for Northern Japan, Northern Chile, Peru, Ecuador and Middle America. As we will see further, there are several common features among them but also differences from which conceptual generic models for subduction erosion have been derived.

2.1 Main features of accretionary margins vs erosional margins (Fig. 2.1)

Accretionary margins have a large frontal accretionary prism. From previous analogue experimental studies, we know that the growth of the prism proceeds in cycles throughout time (Gutscher at al., 1996, 1998a; Hoth et al., 2007). They also show narrow tapers, a smooth surface of the slope and the subducting plate, low convergence rates (<6 cm/yr; Clift and Vannucchi, 2004) and a thick sediment layer (>1 km) feeding the trench. Subduction channel thickness may be as thin as a few hundred meters (e.g. between Sumatra and Java; Kopp and Kukowski, 2003) and as wide as 8 km (Eberhart-Phillips and Martin, 1999; Tsuru et al., 2002; Oncken et al., 2003; Abers, 2005).

On the other hand, because of the consumption of the margin, erosional margins have smaller frontal prisms (5-20 km wide and ~1-2 km high). From seismic data, subduction erosion is thought to be more an episodic process during interplate thrust events rather than continuous (Wang et al., 2010). At shallow depths, it is unclear whether it is continuous or episodic (Heki, 2004). Geometrically, erosional convergent margins have larger tapers, extensional features, including normal faulting, landward tilted blocks and seaward tilted forearcs (e.g. Aleutians, Scholl (2002); midslope Tonga, Clift and McLeod (1999); Guatemala, Aubouin et al. (1984); Peru, Bourgois et al. (1988); Chile, von Huene et al. (1999); Mariana Islands, Wessel et al. (1994)), active mass wasting and related irregular surface slopes (e.g. Japan, Cadet et al., 1987), a rougher oceanic plate, faster convergence (>6±0.1 cm/yr; Clift and Vannucchi, 2004) and a thinner blanket of sediments (<1 km) covering the subducting plate (von Huene and Scholl, 1991; Lallemand et al., 1994; Clift and Vannucchi, 2004; Cloos, 2006; Oncken et al., 2006). Subduction channel thickness is usually thinner than 2 km (Section 2.2).

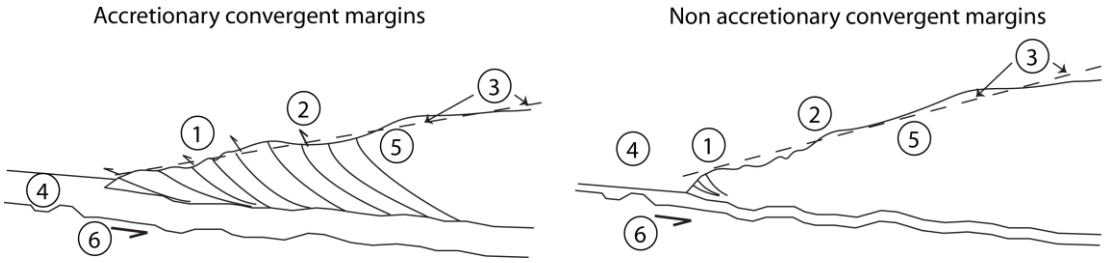

Figure 2.1 *Sketch with main features of Accretionary vs Erosional margins:*

1) frontal accretionary prism ~22 km wide, formed by a frontal and middle prism (von Huene et al., 2009). It consists of imbricated thrust sheets and it can contain upper and/or lower plate materials (Contreras et al., 2010; von Huene et al., 2009). 2) forearc basin on the inner flank of the subduction accretionary complex (Clift and Vannucchi, 2004). 3) Mean of slope angle is 3° (Clift and Vannucchi, 2004). 4) Incoming sedimentary pile >1km, from which 83% is subducted. Thickness is inversely proportional to taper. Transfer of material from the subducting plate either by off scraping at the toe or underplating at depths (Clift and Vannucchi, 2004). 5) rock framework (structurally the inner prism) backs accreted material (middle prism). It consists of igneous or metamorphic basement and /or lithified sedimentary rock (von Huene et al., 2009; Contreras Reyes et al., 2010). 6) Convergence rate <7.6 cm/yr (Clift and Vannucchi, 2004).

1) small frontal accretionary complex (von Huene et al., 1999; Laursen et al., 2002). Basement strong, plutonic, volcanic and mantle rock, ~15 km wide and ~1-2 km high (Clift and Vannucchi, 2004; von Huene et al., 2009). Frontal prism strength is similar to accreting margins (von Huene et al., 2009). 2) gravitational collapse of the lower and middle slopes and extensional structures. Contractional structures are associated to the start of subduction (von Huene, Aubouin et al., 1985). 3) variable slope angle: steepest dip at the lower slope, intermediate at the middle slope and shallowest slope at the upper slope. Average slope angle ranging 7-15° (Clift and Vannucchi, 2004 and references therein). Middle and upper slopes have basins. The upper slope shows an extensional regime. 4) a thin or absent blanket of sediment covering the incoming oceanic plate. A median of 22% of the total material subducted is derived from sediments in the oceanic plate (Clift and Vannucchi, 2004). 5) The middle prism consists of decomposed and fractured framework. The coherent framework is igneous or metamorphic basement and/or lithified sedimentary rock (von Huene et al., 2009).6) convergence rate >6 cm/yr (Clift and Vannucchi, 2004).

2.2 Structural characteristics of erosional margins

Geometrically, the slope is typically segmented into a lower, middle and upper slope. The small frontal prism (Ranero et al., 2000) reduces friction where the lower slope has a disrupted topography (von Huene and Lallemand, 1990; von Huene et al., 2000; Vannucchi et al., 2001). The frontal prism shows an irregular surface due to continuous gravitational collapse. The forearc block is subject to long-term (>10 My; Section 3.3.1) subsidence with simultaneous tilting and normal faults deforming either the middle or upper slope, or both (Fig. 2.2.1a). There are numerous faults, which mostly have a relatively small vertical displacement (<300 m; Peru and Japan margins) compared to subsidence (4-6 km at the Peru and Japan margins; von Huene and Lallemand, 1990). Some margins show steep scarps in the middle slope. The location of enhanced subsidence varies from margin to margin, which is commonly related to basal erosion. Subsidence is not static, but migrates upslope, downslope or intensifies at some locations or in certain periods of time and thus is not evenly distributed (e.g. Japan, Lallemand et al., 1992a, von Huene et al., 1994; Tonga, Clift and McLeod, 1999; Guatemala, Weinrebe and Ranero, 2003; Vannucchi et al., 2004). Different studies indentified basal erosion to take place either below the trench-near area (e.g. Chile, Japan), below the middle and upper slopes or above the updip limit where interplate seismicity occurs (e.g. Guatemala, von Huene, Aubouin et al., 1985; Costa Rica, Ranero and von Huene, 2000; Chile, Laursen et al., 2002; Wang et al., 2010) or further downdip (Kukowski and Oncken, 2006).

The flexure of the oceanic crust as it descends into the trench is imaged in seismic profiles, thus accentuating its normal faults (von Huene, Aubouin et al., 1985). The variety of roughness of the lower plate goes from very smooth to very rough at different margins. Additional roughness comes from subducting topographic highs like seamounts and ridges. The nature of the SC adapts to the roughness of the top of the lower plate, with thickness of 0.15-0.5 km over a smooth surface (von Huene and Scholl, 1991; von Huene and Ranero, 2003; von Huene et al., 2004; Sage et al., 2006; Vannucchi et al., 2008; Fig. 2.2.2a and e), becoming locally thicker over grabens (e.g. Ecuador and Chile; von Huene and Ranero, 2003; Sage et al., 2006) and thinner over high structures (i.e. seamounts or horsts in Ecuador and Chile, respectively; Sage et al., 2006; Collot et al., 2011; Fig. 2.2.2d).

The following summary table contains data related to characteristics we could later compare with our experimental results (for further details see Appendix A1). Seismic lines from northern Chile, Costa Rica, Nicaragua and Japan are shown below.
Numbers between brackets [] refer to references. Abbreviations are the same as in Fig. 1.1 and positions of the seismic reflection lines in Figs. 2.2.1 - 2.2.5 are also shown in Fig. 1.1.

Ecuador (Fig. 1.1 and 2.2.2) [13; 14; 15]	Peru (Fig. 1.1) [3; 8; 9; 10; 11; 12]	Central Chile [6]	Northern Chile (Fig. 2.2.1) [1; 2; 3; 4; 5; 6; 7; 34]	Margin [References]
60	100	80	100	**Forearc Size [km]**
7 – 3.5 – 2	9.5 –4.4 – 2.4	22 – Terrace –25	7 – 7 - 3.5	**Lower - Middle – Upper slope [°]**
Basaltic rock	Crystalline Rock of high densities (2600–2800 kg/m^3) covered by thin veneer of sediments	Magmatic rocks intruded and superimposed upon, intrusive rocks and metamorphosed remnants of an accretionary prism	Andesites (associated with granitic intrusions) overlies metamorphosed sedimentary rock and is overlain by sedimentary rock. Resting on basement rocks are marine and non-marine sedimentary sequences.	**Type of rock basement**
1; over smooth surface: 0.15-0.5; over grabens: 0.6 thick x 10 length – Riedel shear zones and basal thrust faulting; lens-shaped structures	>0.3		>0.3 [3] / 1-2 [1; 34] / 5 [4] - over horst: 0.1's; over grabens: 1 [2]	**Subd. Channel width [km] – structures**
Smooth to the south of Grijalva Fracture Zone (GFZ) and rough to the north of GFZ	Almost depleted of a sedimentary cover. Prominent roughness, which decreases to the south. Northern NR: several ridge-shaped bodies. Southern NR: important roughness of the oceanic plate.	Affected by the JFR, accelerating subsidense at the middle slope. Northern JFR: lower and middle slopes cut by seaward dipping normal faults, implying basally removed material.	Horsts and grabens between 22-24ºS have a relief up to 500 - 800 m. IR between ~22-23ºS.	**Ocean plate topography**
3 - 10	<20		<5	**Frontal prism width [km]**
Middle and upper slope	Midslope	Inner edge middle slope basin, close to upper slope	Lower [5; 7] / middle slope [6]	**Subsidence loci**
Several normal faults cross the thick sediment apron at the middle slope	Canyons and high-angle normal faults	Normal faults within the sediments in Valparaiso Basin are scarce and they do not reach the basement	Extension and mass wasting	**Main extensional structures**

NW Japan (Figs. 1.1 and 2.2.5) [29; 30; 31; 32; 33]	Guatemala (Fig. 1.1) [14; 20; 25; 26; 27; 28]	Nicaragua (Figs. 1.1 and 2.2.4) [14; 20; 22; 23; 24]	Costa Rica (Figs. 1.1 and 2.2.3) [14; 15; 16; 17; 18; 19; 20]
40	70	70	35 - 60
Scarp ~20. Beneath scarp: 1; Above scarp: 9 - Terrace – 12	6 -3 – almost horizontal	6 – 17 –2.5	8 – ? – 3.5
Siliceous claystone unconformably overlain by a 48 m thick breccia-conglomerate which contains hypabyssal dacitic to rhyolitic boulders	Basic and ultrabasic basement overlain by 300 m sedimentary sequence	Igneous rock	Fractured, altered or eroded and accreted oceanic plateau terrane
1 - 1.5		<1	0-0.4; – lens-shaped bodies
Horsts structures are cut by faults. They are very deformed and begin to disintegrate landward, smoothing the surface of the lower plate in the vicinity of the stick-slip zone	Horst and graben structures below a thin sediment layer. Not large seamounts are pre-sent in the area	Pervasively fractured	Three segments with different degrees of roughness: the CoR in the south, a seamount segment in the center and a smooth surface segment to the NW
3 - 15	<10	<10	4
Upper slope (24-2 My) / Lower slope (15 My)	Middle slope	Upper slope	Middle and upper slope: Megalenses and tunneling
Small normal faults and fractures increase in number from lower to middle slope. Steep normal faults along strike at the middle slope-terrace	Failure and several scarps in the lower slope. In the common. From the middle slope, up across the shelf edge and also in the upper slope basin, some few contractional structures are seen.	Echelon ridges, slumps and canyons interrupt the sur-face of the lower slope, and massive normal faults cut the middle slope	Thrusts at the lower slope and normal faults at the middle and upper slope. NW flank of the CoR shows compressional structures at the middle slope (some of the thrust faults have been reactivated as normal faults)

[1] Sallarès and Ranero, 2005; [2] von Huene and Ranero, 2003; [3] Contreras and Carrizo, 2011; [4] Sick et al., 2006; [5] Adam and Reuter, 2000; [6] Laursen et a., 2002; [7] Hampel et al., 2004; [8] Kukowski et al., 2008; [9] Clift and Hartley, 2007; [10] Krabbenhöft et al., 2004; [11] Scholl et al., 1970; [12] Calahorrano et al., 2008; [13] Ranero and von Huene, 2000; [14] von Huene et al., 2000; [15] Christeson et al., 1999; [16] Zhu, 2010; [17] von Huene and Ranero, 1998; [18] Vannucchi et al., 2001; [19] Weinrebe and Ranero, 2003; [20] Exp. 334, 2011; [21] Ranero et al., 2000; [22] von Huene et al., 2004; [23] Ranero et al., 2008; [24] Harders et al., 2011; [25] von Huene, Aubouin et al., 1985; [26] Aubouin et al., 1984; [27] Vannucchi et al., 2004; [28] von Huene et al., 1994; [29] von Huene and Lallemand, 1990; [30] Tsuru et al., 2000; [31] von Huene and Culotta, 1989; [32] Cadet et al., 1985; [33] Lallemand et al., 1992; [34] Patzig, 2000.

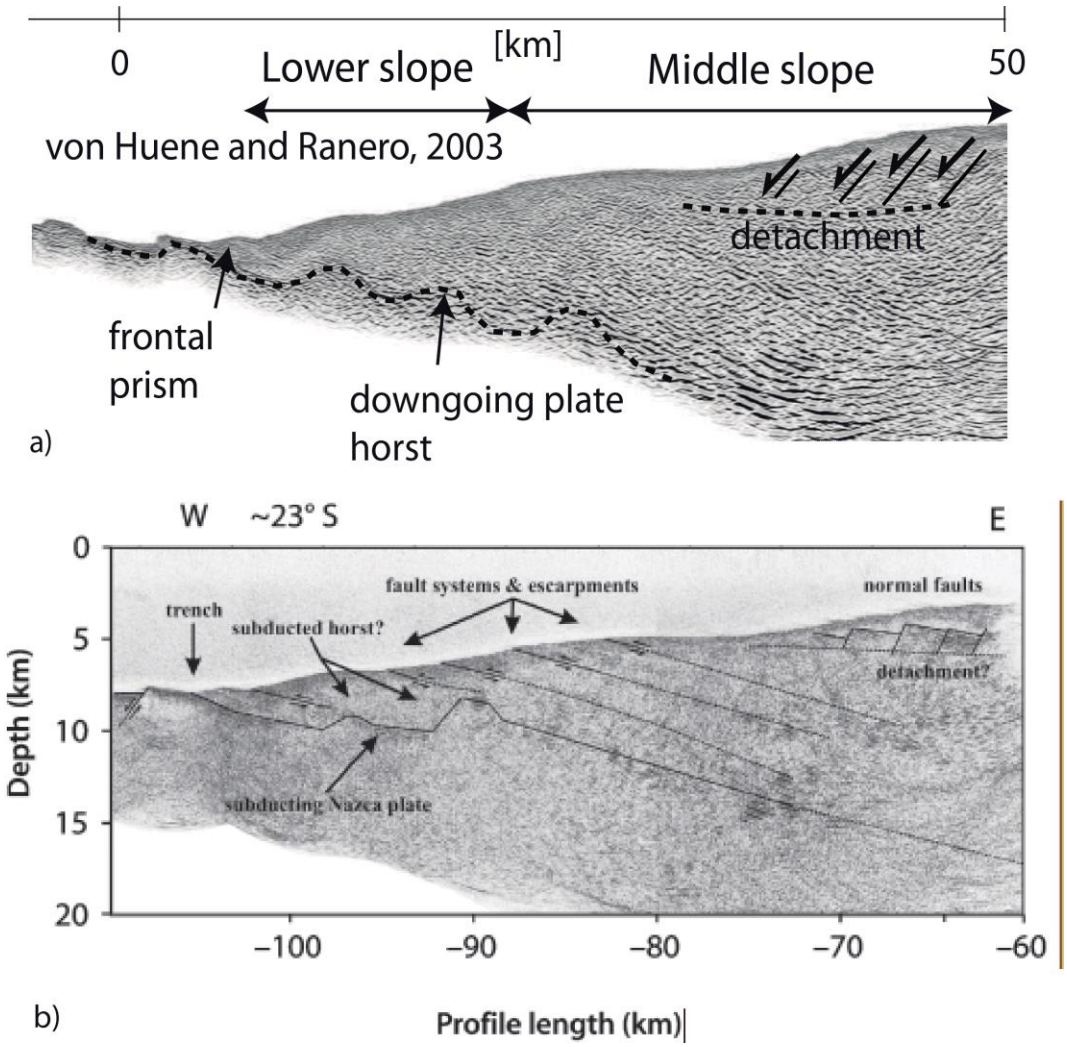

Figure 2.2.1. *Seismic lines and their tectonic interpretation from Northern Chile (CINCA SO104-13). a) Prestack, after von Huene and Ranero, 2003; b) Reprocesed data and tectonic interpretation by Sick et al., 2006.*

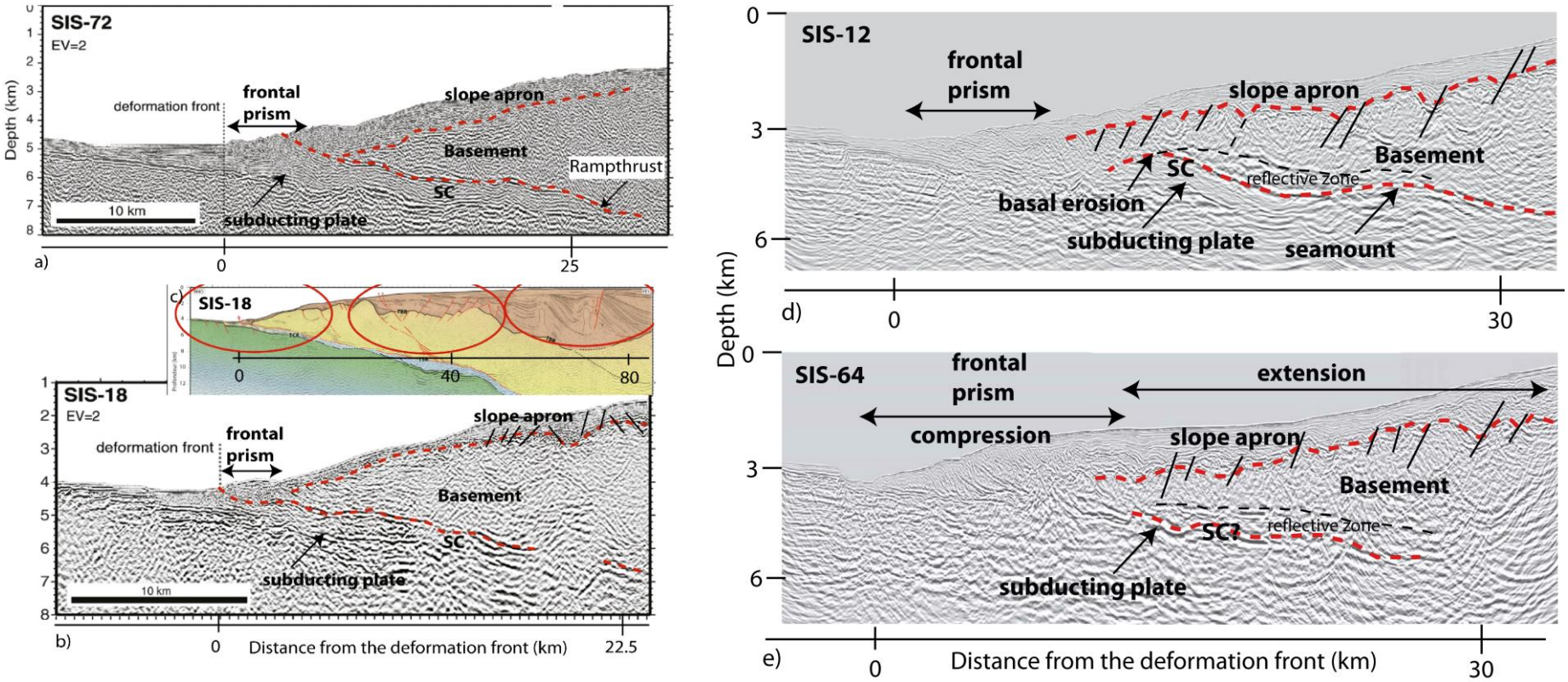

Figure 2.2.2. *Seismic lines across the Ecuadorian margin. The upper red-dashed line shows the bottom of the sediment covering the slope, lower dashed red line indicates the top of the subduction channel. The bold black lines highlight some of the normal faults cutting the slope apron and/or basement (After Calahorrano et al., 2008 and Collot et al., 2011 (a and b), Calahorrano, 2005 and Sage et al., 2006 (d and e)). a) seismic line SIS-72, at the south of the Grijalva Fracture Zone. The morphology of the ancient 32 Ma Farallon plate is smooth here. b) seismic line SIS-18, to the north of the Grijalva Fracture Zone. The Nazca plate is younger (0-24 Ma) and rougher lithosphere than to the North of GFZ. An extended tectonic interpretation is shown in c (Calahorrano, 2005), d) seismic line SIS-12 showing the segment of the margin where the seafloor is rough, spotted by seamounts. The intrabasement reflector thinning seaward indicates basal erosion. The reflective zones are here interpreted as penetrative, fluid-driven rock damaging processes. e) seismic line SIS-64, at the southern end of the smooth segment, where the top of the incoming plate is smooth. The seafloor is cut by small-offset normal fault scarps. SC is too thin, thus not resolved in the seismic data (<150 m).*

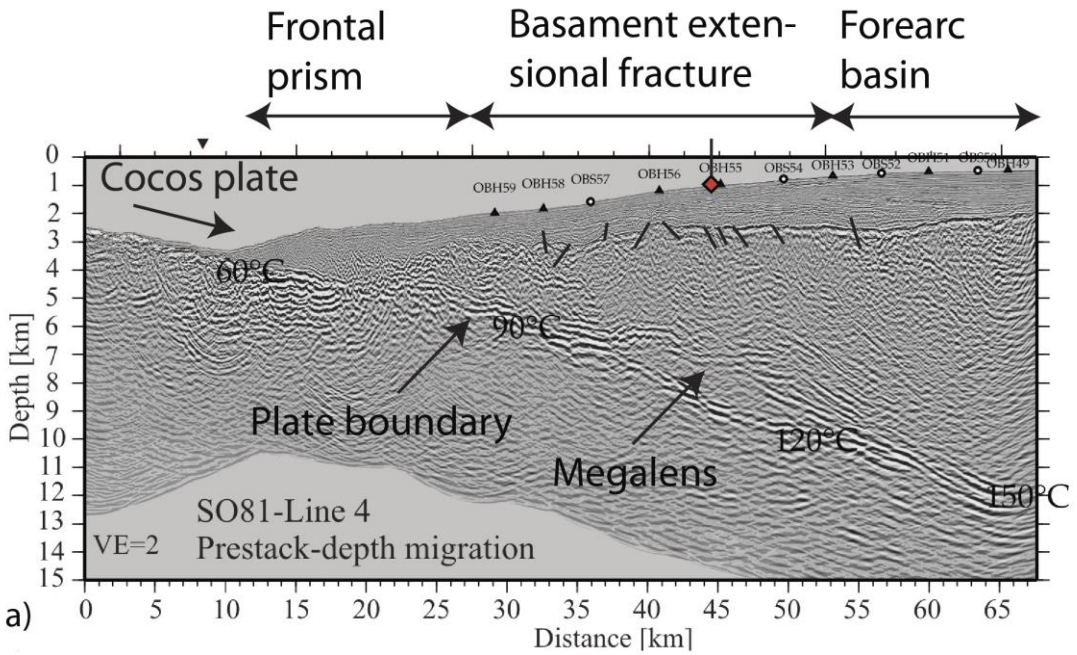

Figure 2.2.3. *Multichannel seismic profiles across the Costa Rica convergent margin (after Ranero et al., 2008 and Zhu, 2010). The frontal sediment prism is a distinct morphological unit, tectonically active composed of reworked slope sediment. Thrust faulting occurs only here. Beneath the slope apron, the upper slope is smooth, cut by small throw normal faults. Downslope, the roof of the forearc becomes rougher. The canyons in the upper and middle slope indicate a relatively stable environment where no seamount has recently underthrusted. Plate boundary bifurcation identifies a rock megalense*

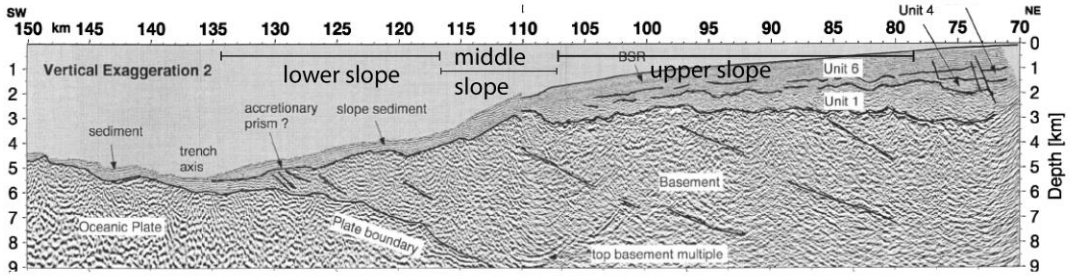

Figure 2.2.4. *Interpretation of seismic units and tectonic boundaries from a prestack depth migration of a line across Central Nicaragua (after Ranero et al., 2000)*

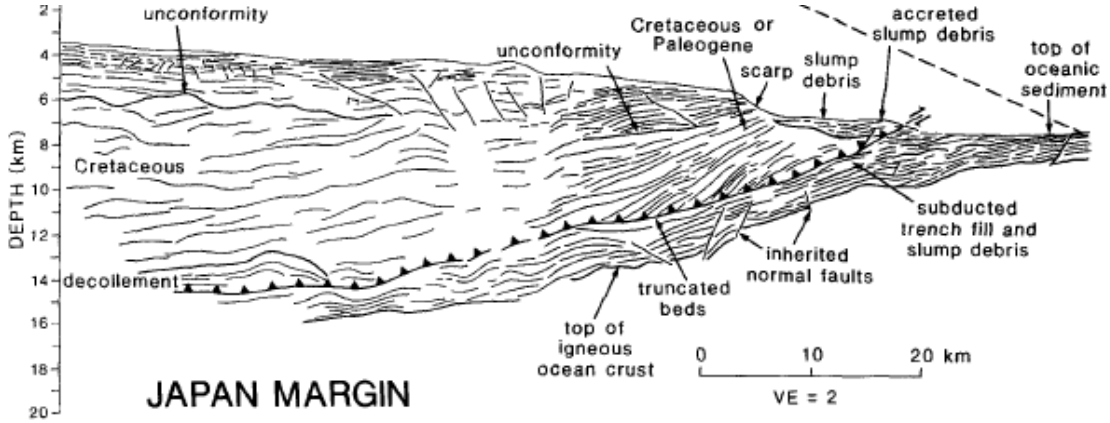

Figure 2.2.5*. Line drawing of seismic section ORI 78-4 across the Japan convergent margin (after von Huene and Lallemand, 1990).*

3. CONCEPTS TO EXPLAIN WEDGE MECHANICS

After erosional convergent margins were identified, the first conceptual models began to appear. Some of those features distinguishing them from accretionary margins (e.g. seafloor topography, convergence rate, etc.; see Section 2.1) have been recognized to explain subduction erosion. With better seismic images and a larger amount of surveys, new discussions arrived, where further parameters (e.g. role of fluids, mechanisms controlling basal erosion at depth, etc; see Section 3.3) controlling mechanical deformation, seismic behavior or characterization of Subduction Channel (SC) were also discussed. Additionally these parameters have been also studied with analogue experiments and numerical simulations.

Here, we introduce the results from some of the more popular discussions, intending to explain subduction erosion, and also later observations, which were in conflict with them. This overview will help to have a better understanding about the process of subduction erosion itself and theories related to it.

The following summary first introduces the Critical Taper theory, which relates the geometry of the overriding plate with its basal and internal strengths. Secondly, the Subduction Channel (SC) concept is presented, where the fluid content in the material transfer would play a significant role in the erosion of the margin. Lastly, previous models based mainly on interpretations from the seismic lines and also attributed to characteristics of the SC are discussed.

3.1. Critical Taper theory and Mohr Coulomb diagrams

Geological and seismic data reveal a variety of structural patterns at convergent margins worldwide. Common features have been observed in cross section among crustal wedges which undergo compression (Chapple, 1978): (i) a basal detachment or décollement, which dips towards the interior of the mountain belt; (ii) significant horizontal compression in the material above the décollement and little deformation within the material below it and (iii) a characteristic wedge shape of the deformed material, tapering towards the foreland of the mountain belt.

These basic observations formed the basis for the critical taper theory (Davis et al., 1983), which follows the fundamental premise that any wedge with a plastic frictional behavior is governed by the Mohr-Coulomb failure criterion. Thus, the overall mechanics of crustal wedges are also exhibited in small-scale soil or sand wedges formed in front of a bulldozer or snow plow pushing the wedge (Davis et al., 1983; Fig. 3.1a)

The critical taper concept relates some parameters with the geometry of an orogenic wedge, i.e. cohesion, effective internal and basal friction, as well as internal and basal pore pressure. Thus, deformation of a wedge is driven by the relative magnitude of the frictional resistance along the base and the compressive strength of the material of the wedge (Dahlen, 1990, Fig. 3.1a).

Such soil or snow plow wedges deform internally until they achieve a “critical” shape, whereupon the wedge slides stably on its base. If new material is added at the toe, the wedge will grow self-similarly by promoting internal

deformation to incorporate the new material. If no material is accreted, the wedge will become the thinnest body that can be thrust over its detachment without internal deformation.
The above description indicates that basal properties, strength of the wedge material and shape of the wedge must be related.

The Coulomb failure law criterion on which the critical taper approach is based, can be expressed as

$$| \tau | = C + \mu_i (\sigma_n - p_f) \text{ or}$$
$$| \tau | = C + \mu_i \sigma_n^*$$

where shear stress τ is a function of cohesion C, the coefficient of internal friction μ_i, normal traction σ_n and pore fluid pressure p_f. The angle of internal friction of the material relates as $\mu_i = \tan\phi_i$. The form $\sigma_n^* = \sigma_n - p_f$ represents the effective normal stress (Hubbert and Rubey, 1959).
For dry and subaerial wedges (as those generated in this study), the pore fluid pressure is $p_f = 0$.

In nature, fluid pressure plays a fundamental role in the mechanics of orogens. Fluids cannot support shear stresses, thus their respective pressure has the same magnitude in all directions. Therefore, fluid pressure reduces the magnitude of the principal stresses, but the differential stress remains constant. As a result, the corresponding angle between the highest normal stress and the failure plane is reduced with respect to the case where no fluid pressure is present.

In the case of subaerial wedges, where the water table is at the rock surface (Davis et al., 1983 and literature therein), the pore pressure equals the hydrostatic pressure for shallow depths (i.e. the pore pressure is the same as that exerted per unit area by a column of water from sea level to a given depth). Below some position stratigraphically controlled, the pore fluid pressure exceeds the hydrostatic pressure, reaching a constant gradient in some point in the range between the hydrostatic and lithostatic gradient. This constant gradient was defined by Hubbert and Rubey (1959) as $\lambda = p_f / \sigma_z$, where σ_z is the vertical normal traction exerted by the lithostatic overburden.

In the case of submarine wedges, the rock surface is submerged below the sea level, where the rock is generally weaker than for subaerial wedges. This special case was considered by introducing a generalization of the Hubbert and Rubey's ratio (Davis et al. (1983):

$$\lambda = (p_f - \rho_w g D) / (|\sigma_z| - \rho_w g D)$$

where the weight of the overburden (σ_z) at any point in the wedge is assumed to be due to the lithostatic and hydrostatic overburden (Fig. 3.1a). ρ_w is the constant density of the overlying water. The parameter g is the constant acceleration of gravity and D is the local thickness of the water overburden, measured along the direction of gravity. Thus, the term $\rho_w g D$ corresponds to the hydrostatic pressure at the seafloor.

Shear stress is affected by cohesion mostly at the frontal segment of the wedge. At depths of a few kilometers, the effect of cohesion (in the order of 1 to 150 MPa; Dahlen and Suppe, 1988) is negligible relative to the pressure-dependent term in the failure equation. Hence where the wedge is thicker, the pressure dependent term will dominate, then

$$| \tau | = \mu_i \sigma_n^* \qquad (1)$$

It follows from equation (1) that the Coulomb failure criterion is depth-dependent and independent of temperature or strain.
In the critical taper concept (Fig. 3.1a), the internal and basal friction values will define the stability of a wedge as:

$$\alpha+\beta= \psi_b - \psi_0 \qquad (2)$$

where α represents the slope angle and β is the dip of the downgoing oceanic plate. $\alpha+\beta$ is the wedge taper. ψ_b is the angle between the maximum compressive stress σ_1 and the base, while ψ_0 is the angle between the maximum compressive stress σ_1 and the surface.
These angles can be expressed as,

$$\psi_b = ½ \arcsin (\sin \alpha^* / \sin\phi_i) - ½ \alpha^*$$
$$\psi_0 = ½ \arcsin (\sin \phi_b^* / \sin\phi_i) - ½ \phi_b^*$$

Here, $\alpha^* = \arctan [([1-(\rho_w / \rho)] / [1-\lambda]) \tan \alpha]$ is the effective α. ρ is the density of rock. ϕ_b^* represents the effective angle of basal friction and the effective coefficient of basal friction is defined by $\mu_b^* = \tan \phi_b^* = \mu_b [(1- \lambda_b) / (1- \lambda)]$. The parameter λ_b corresponds to the basal pore fluid pressure ratio, defined by Dahlen (1984) as:

$$\lambda_b = (p_f^{\,b} - \rho_w g D) / (|\sigma_z| - \rho_w g D)$$

where $p_f^{\,b}$ is the basal pore fluid pressure.

While introducing the different parameters λ and λ_b one allows for the fact that the pore fluid pressure may experience a sudden change across the basal décollement. Basal detachments are usually zones of weakness either because of a lower strength with respect to the internal strength of the overriding plate, or because of the elevated fluid pressures.

For dry wedges, variables λ_b, ρ_w and $\lambda = 0$; thus $\phi_b^* = \arctan \mu_b = \phi_b$ and $\alpha^* = \alpha$.

Then (2) becomes:

$$\alpha+\beta = ½ [\arcsin (\sin \alpha / \sin \phi_i) - \alpha] - ½ [\arcsin (\sin \phi_b / \sin \phi_i) - \phi_b] \qquad (3)$$

Equation (3) defines a taper stability field with three dynamic states (Fig. 3.1b): stable, critical and non-stable (sub- or super-critical).
(i) The state of a wedge is called stable if it slides over its basal décollement without internal deformation or deforming dominantly at its base. It will remain stable as long as its boundary conditions do not change (i.e. mechanical properties, material eroded, material supply, etc.). (ii) The wedge is called “critical” at the limits of the stable field. Basal and internal strengths are in equilibrium, thus the wedge is on the verge of shear failure everywhere. The critical wedge is failing both internally and along its base, while sliding stably at a constant taper, growing self-similarly and reaching a dynamic equilibrium.
(iii) In the under-critical (below the lower limit - shortening field) or super-critical (over the upper limit - extensional field) state, the shape of the wedge will adjust by internal deformation (failing or thrusting) towards the critical state and thus, the wedge deforms mostly internally and by changing its taper.

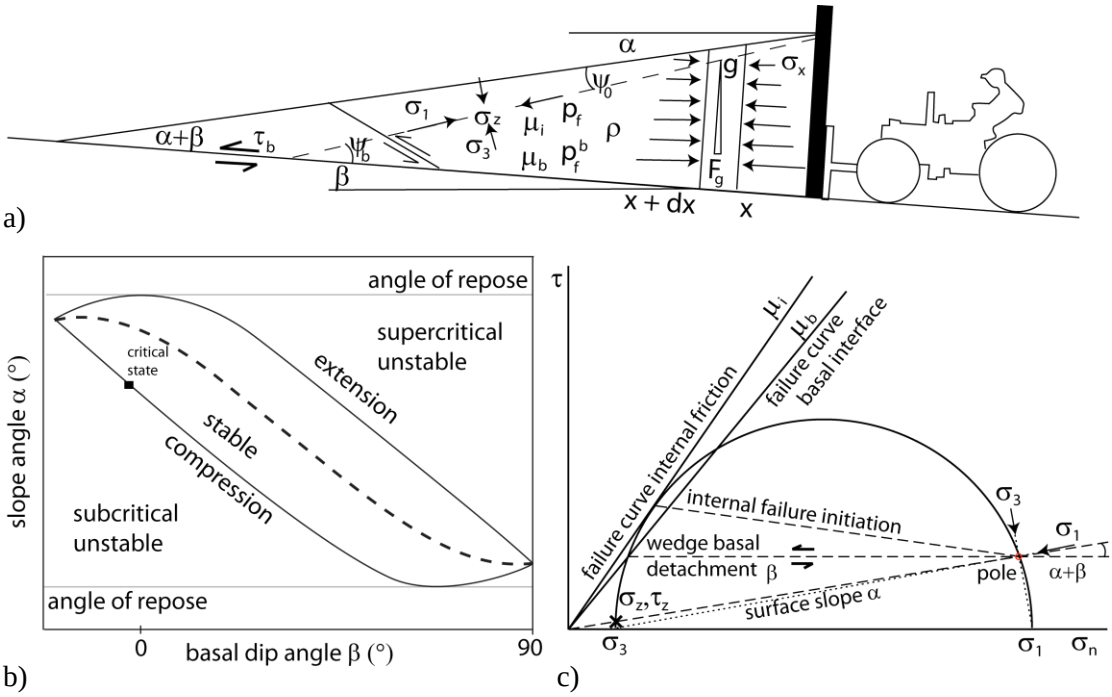

Figure 3.1. *a) Cross-section through a wedge with a taper α+β. ψ_b is the angle between the maximum compressive stress σ_1 and the base of the wedge, ψ_0 the angle between σ_1 and the surface, ρ wedge density, p_f pore fluid pressure, p_f^b basal fluid pressure. Forces acting upon an arbitrary wedge-column of width dx are: (1) push from rear, (2) gravitational body force and (3) basal traction resisting wedge slide up the hill (after Davis et al., 1983, Dahlen and Suppe, 1988; Lohrmann et al., 2003). b) Wedge stability field (after Dahlen, 1984). During basal erosion the stability field is minimised to a line (dashed line). c) Mohr diagram of a critical wedge, illustrating the general states of stress at depth z (σ_z, τ_z) and related internal fault kinematic of the wedge (after Lehner, 1986).*

The critical taper theory predicts that basal erosion would occur if the wedge is at its stability limit, i.e. when basal strength is nearly equal to internal strength (i.e. $\mu_b \approx \mu_i$; Dahlen, 1984). If the contrast between basal and internal friction disappears, the former region of the stability diagram for a stable wedge shrinks to a narrow line (Fig. 3.1b).

Alternatively to the mathematical expression of the critical taper concept of Dahlen (1984), a graphical method was developed by Lehner (1986). The Mohr stress circle (Fig. 3.1c) provides a rapid understanding of the exact geometry and mechanics of the wedge. It illustrates the actual range and sense of movement for the sets of slip lines of brittle wedges.

The limiting states of stress (effective normal stress and shear stress) can be obtained for any point (σ_z, τ_z) at depth z. A line, inclined by the slope angle α, passes through the (σ_z, τ_z) point, bringing to a second interception with the Mohr circle, called the "pole" (Fig. 3.1c). Using the pole construction method (Terzaghi, 1943), the stresses determined by the second intersection with the Mohr circle of any line passing through the pole, acting on a plane oriented parallel to that line in physical space.

3.2 The Subduction Channel SC

3.2.1 The Subduction Channel at active convergent margins as imaged in seismic images

A detailed analysis of the seismic data has allowed us to have a better understanding about the nature of the

Subduction Channel in the two main end-members – erosive and accretionary – of convergents margins. The erosional margins best-documented by seismic images are Chile, Costa Rica and Ecuador.

At erosional margins, the thin sediment layer on top of the oceanic convergent plate is almost completely subducted and a very small portion or no material at all is offscraped at the toe of the forearc. The subducted material gets entrained in the Subduction Channel (SC), which appears as a low velocity reflector in reflection seismic profiles and is interpreted to represent a fluid rich corridor between the upper and lower plate (Sick et al., 2006; Calahorrano et al., 2008; Fig. 2.2.2). Seismic reflection profiles across the Ecuadorian subduction zone show three segments of the SC (Collot et al., 2002; Calahorrano et al., 2008; Collot et al., 2011; Fig. 2.2.2). These three zones have contrasting physical properties (derived from their different Vp) and roughly match the segments or areas of the overriding prism. Variations in their pore fluid pressure, content of fluids, degree of lithification and arrangement of shear zones characterizes the different segments (Vannucchi et al., 2012).

Reconstructions from an improved seismic image of the SC across the Ecuador convergent margin (Fig. 2.2.2a) show Riedel shears and basal thrust faulting, suggesting the promotion of basal erosion (Collot et al., 2011; Section 2.2). The detailed structural interpretation also reveals lens-shaped structures (Section 2.2) and a low-Vp velocity zone. The latter was interpreted as either underplated sediment that was not as well imaged as the lens-shaped body or to fluid-rock interaction in a damage zone.

The seimic images also reveal that the shape and width of the SC varies along the plate boundary: in the toe area, the SC width is ~0.02 – 0.04 km, widening up to 0.2 – 1 km arcwards, at least until the seismogenic zone (Collot et al., 2002; Collot et al., 2011; Vannucchi et al., 2012). Where the surface of the subducting plate is considerably rough, important width variations define the SC geometry (Section 2.2 and bibliography therein).

3.2.2 Fossil subduction channels

There are some fossil SCs now exposed on land whose features have added new information relevant to the former SC concepts (e.g. New Zealand, Fagereng and Sibson, 2007; Northern Apennines, Vannucchi et al., 2008; Central Alps, Bachmann et al., 2009). A fossil example of a SC from the northern Apennines (Vannucchi et al., 2008) was identified as an erosive type. It represents the shallowest 5 km of depth and it has a thickness of 0.5 km. It shows an upper and lower detachment and exhibits deep basal erosion as well as shallow frontal erosion. Changes in the stress regime from extension (~first 4 km depth) to compression (~4-7 km depth) can also be deduced from this example.

3.2.3 The role of the Subduction Channel at erosional forearcs

The pattern of flow and the thickness of the SC depend upon sediment supply and rock density, the subduction speed, and the pressure gradient along the channel. A control point is located where the channel capacity changes as a result of a sharp variation in the density of the overriding wedge (e.g. where the accretionary prism abuts crystalline rock), in the slope of the wedge surface or in the dip of the descending plate (Cloos and Shreve, 1988a).

The control points and SC capacities defined by Cloos and Shreve (1988a) predict under which conditions a forearc will evolve into an accretionary or an erosional system, and also whether it will switch from one type to the other (Fig. 1.2).

- Local subduction channel capacities control variations of the flow pattern and subduction channel thickness along the channel. It is the maximum amount of sediment that can pass arcwards. It is controlled by the speed of the subducted sediment or by the pressure gradient along the SC.
- Local control points define the locus of minimum local capacities. At the leading edge of the SC, the inlet capacity restricts the total amount of sediment going into the subduction channel (IC; Fig. 1.2).
- The global control point will determine the maximum of material in the SC that will be deeply subducted. It is localized where SC capacity decreases because of a sharp increase in the density of the overlying rocks, the wedge slope or the dip of the oceanic plate. The capacity at the global control point (global capacity = GC; Fig. 1.2) defines how much sediment will be subducted deeply.

The SC concept introduced by Cloos and Shreve (1988a) establishes the IC/GC ratio as a critical parameter that defines channel behavior and thus the wedge evolution. The GC must play a key role in convergent margin tectonics, since it seems that subducted material is not entirely underplated (as indicated by thinning of the forearc; see Section 2.2). Hence, the GC would partially govern the SC and also material flow within it. Later contributions (e.g. Clift and Vannucchi, 2004) have analyzed how much material is probably recycled to the crust and how much is subducted to depths (e.g. Table 1).

3.3 Previous studies and proposed erosional mechanisms

Several concepts to explain the significant subsidence, extensional structures and related basal erosion observed along some convergent margins have been developed since the truncation of the Chilean margin was identified (Miller 1970a and 1970b). However these concepts apply mostly to geometry, convergence rate or topography of the lower plate. The most recent theories involve a more active role of fluids and mechanical interaction with the SC.

In this section, we present the most popular hypotheses explaining the subduction erosion process and related features left by the process of erosion (e.g Section 2.2 and 2.1). Further in the text, these hypotheses represent the base for the discussion after the experimental results are described.

3.3.1 Steady state subduction erosion

There seem to be two mechanisms of subduction erosion occurring on very different time scales. The first is during relatively short geological periods, caused by the collision of large topographic highs, like subducting aseismic ridges, mid-ocean ridges, or major seamounts. It is associated with pulses of forearc uplift and subsequent subsidence (e.g. Costa Rica, Peru). The second occurs in a “steady-state” on long time scales (i.e. >10 My.).

Large topographic relief has a profound influence on the rates of material transfer in short geological

periods, especially on subduction erosion (Table 1; Mendaña Rigde and Central Peru since Middle Miocene, Clift et al., 2003; Clift and Hartley, 2007; Central Chile, Laursen et al., 2002; Cocos Ridge in Costa Rica, Vannucchi et al., 2003; Weinrebe and Ranero, 2003). Seamounts produce reentrants at the deformation front (Ranero and von Huene, 2000; von Huene et al., 2000), however no important trench retreat is associated because they only affect local parts of the continental margin. In "steady-sate" erosional margins, long-term subduction erosion removes large volumes of basal and frontal material from the margin (Vannucchi et al., 2003; Ballance et al., 1989; von Huene et al., 1999; Clift et al., 2003). We will refer to those margins belonging to the last group simply as erosional margins.

From systematic investigations of erosional margins, several hypotheses have been put forward to explain the observed subsidence and/or the consumption of material. A compilation of mechanisms suggested to drive forearc subsidence is presented below:

i. Basal subduction erosion or crustal thinning (e.g. Scholl et al., 1980; von Huene and Lallemand, 1990). At the near trench area enhanced subsidence seems to be controlled by the passage of major subducting bodies as ridges (Laursen et al., 2002; Fig. 3.2b).

ii. Extension of the forearc because of gravitational collapse. As erosional wedges have usually steep slopes, gravitational collapses are commonly observed (Platt, 1986), especially on the middle slope (e.g. Northern Chile, Adam and Reuter 2000; Japan, von Huene and Culotta, 1989).

iii. Extension by rollback (Uyeda and Kanamori, 1979) or the backward motion of the subduction zone relative to the motion of the plate, which is being subducted.

iv. Increase of the dip of the subducting ocean plate (e.g., Karig et al., 1976; Cloos, 1993; Williams, 1997). Variations of the dip of the subducting slab can occur because of the load of the accretionary prism is increasing towards the orogen (Karig et al., 1976) or crustal loading from arc magmatism (Ranero et al., 2000). It also can be a consequence of the higher bulk density of an old subducting plate compared with that from a younger one (Langseth et al, 1980; Hilde and Uyeda, 1982).

v. Onset of subduction. Subduction initiation leads to compression and uplift in the near-trench region (~1 km uplift) and to rapid subsidence more landward (> 3 km in < 10 My) driven by the slab sinking into the mantle (Gurnis, 1992; Toth and Gurnis, 1998; Ranero et al., 2000).

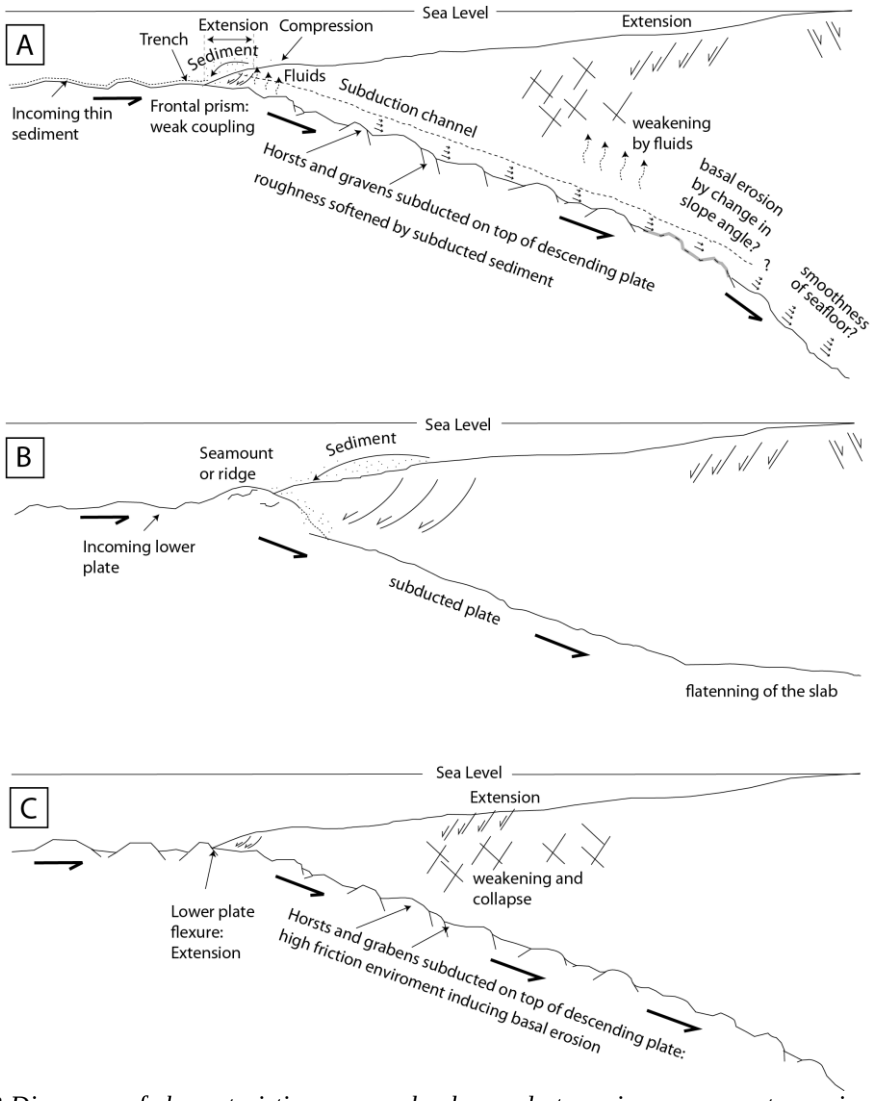

Figure 3.2 *Diagrams of characteristics commonly observed at erosive convergent margins, according to literature. Typical features include a steeper slope than in accretionary systems, subsidence on the middle slope and a thin layer of sediment on the subducting plate.*
A) low basal friction caused by high pore fluid pressure: Integrated model whose grabens are enlarged by continued plate flexure, centering crustal thinning in the middle slope. Pore fluid pressure reduces decollement friction. Fluids released from lower plate hydrofractures the upper plate base, weakening it (Murauchi and Ludwig, 1980; Lallemand et al., 1994; Kanamori and Brodsky, 2001; von Huene et al., 2004).
B) ridge or seamount as effective frontal erosive agents. After the seamount passes by beneath the tip, collapse of material causes enhancing of frontal erosion. (Ballance et al., 1989; von Huene and Sholl, 1991; Lallemand et al., 1994; Clift and MacLeod, 1999; Ranero and von Huene, 2000; Hampel et al., 2004; Bangs et al., 2006; Cloos, 2006)
C) Horst and graben structures, a basal high friction environment: Considered as an abrasive scraping and high basal coupling (Hilde, 1983; Jarrard, 1986; Adam and Reuter (2000).

Further, several mechanisms potentially driving frontal and basal removal of material from forearcs have been proposed:

i. Strong coupling, maybe due to contact with a horst and graben or "washboard" topography of the oceanic crust, affecting the underside of the overriding plate through abrasive scraping (Hilde, 1983; Jarrard, 1986; Fig. 3.2c). This is more a frontal erosion mechanism than a basal one (Ranero and von Huene, 2000). Frontal erosion and tunneling by the passage of

ridges and seamounts are linked to an initially considerable uplift followed by fast subsidence. (Lallemand et al., 1992b; Clift and MacLeod, 1999; Ranero and von Huene, 2000; Clift et al., 2003; Clift and Vannucchi, 2004; Hampel et al., 2004; Bangs et al., 2006, Kukowski and Oncken, 2006).

ii. Weak coupling between upper and lower plate, or basal friction reduced by high pore fluid pressure, which promotes gravitational collapse of the steep frontal forearc slope (Davis et al., 1983; Aubouin et al., 1984; Bourgois et al., 1988; von Huene and Ranero, 2003; Fig. 3.2a).

iii. Lenses of rock can be removed beneath the middle and upper slopes (further details in sections 2.2 and 3.2). As they occur at depths where the plate interface is entering the zone of stick slip behavior, they are thought to be associated to an environment of increasing friction (Ranero and von Huene, 2000)

iv. By "perturbative equilibrium" events (Lallemand et al., 1992a) such as thermal effects: shallowing of the angle of the subducting slab and associated fast convergence, initiating a period of subduction erosion along the plate boundary (e.g. after the kinematic plate reorganization in late Oligocene – early Miocene along the Middle American Trench; Nicaragua, Ranero et al., 2000; Guatemala, Vannucchi et al., 2004; Aleutians, Scholl et al., 2002).

v. Indirectly by typically rough oceanic crust which induces vertical movement, weakening, and collapse of the overriding forearc material (von Huene and Scholl, 1991)

vi. By reactivation of faults and fractures in the oceanic plate, to accommodate the flexure as it descends into the trench (Fig. 3.2c; Armijo and Thiele, 1990; Kirby et al., 1996; Laursen et al., 2002; von Huene and Ranero, 2003)

vii. Hydrofracturing by fluids in subducting grabens, which are filled with sediment, material from the frontal wedge, or material offscraped from the underside of the overriding plate, is inferred to fragment rock along the base of the upper plate that is then transferred into lower plate graben (von Huene and Ranero, 2003; Ranero et al., 2008)

viii. Elevation of pore fluid pressure in the frontal prism reduces décollement friction, allowing complete subduction of trench sediment (Fig. 3.2a). Fluid from the subducted plate flows into the upper plate, penetrating extensional fractures (Fig. 3.3). The resulting hydrofracturing separates fracture bound pieces from the plate-interface hanging wall. These are dragged into the subduction channel and transported toward the seismogenic zone. Fracturing along the base of the upper plate may begin within the seismogenic zone and increase updip as the plate interface shallows (von Huene et al., 2004).

ix. The extensional regime observed in the middle slope of erosional margins (Section 2.2) reflects a weak basal fault, inconsistent with a strong fault

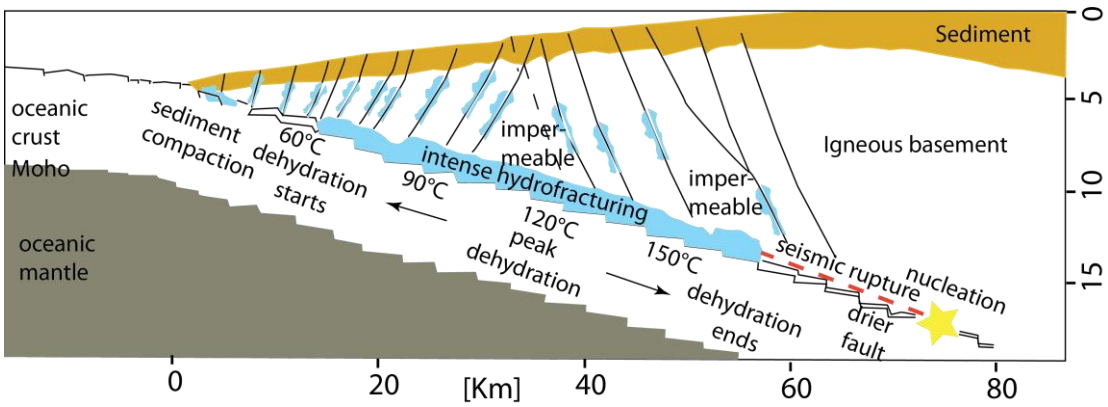

Figure 3.3. *Interpretation of processes at erosive convergent margins. Fluid plays a key role in forearc processes. The wet megathrust is weakly coupled, partially accommodating upper plate subsidence with normal faults. Beyond where temperature is >150°, the fault becomes drier and high pore fluid pressure vanishes, increasing the effective stress on the plate-boundary fault. Slip is localized on a narrower fault zone and the upper plate, being less faulted, stores elastic energy. Nucleation of interplate earthquakes takes place here, and rupture may occur in the shallower parts of the overriding plate (modified from Ranero et al., 2008).*

as previously proposed (Adam and Reuter, 2000). In a steady-state erosion scenario, however, fluid overpressure would also weaken the basal fault, making it incapable of eroding material. To settle this inconsistency, variations in the strength of the fault and middle prism during inter- and co-seismic cycles are invoked. Strengthening of the basal fault beneath the middle prism and weakening of the wedge should occur during coseismic and immediately after seismic periods. Hence, erosion is not a continuous process, but occurs in brief episodes (Wang et al., 2010).

3.3.2 Quantification of material transfer at natural erosional margins

The most recent hypotheses suggest that pore fluids play a fundamental role governing basal erosion (Section 3.3.1; Fig. 3.3). However, features among individual forearcs show that too many parameters change in nature to unequivocally state that a single one could control the processes of subduction erosion themselves. A transient SC behavior (lenses, content of fluids, shape, thickness, etc) indicates that additional or alternative parameters may control forearc deformation, like rock type or degree of alteration, topography of the incoming subducting plate, stability of the surface slope or the relative amount of material that can be deeply subducted.

The different volumes of material involved in each mass-transfer mode may hint at the relative importance of possible parameters controlling the tectonic growth of the brittle crust. Reconstructions of steady-state erosive margins have led to the estimate that basal erosion could be as much as two to four times more effective than frontal erosion (i.e. erosional ratio = basal erosion / frontal erosion > 1; von Huene and Lallemand, 1990; Vanneste and Larter, 2002; IODP Prel. Rept. 334, 2011). The previous statement indicates that mechanisms driving basal erosion play a fundamental role in the dynamic evolution of erosional margins.

The following table summarizes volume estimates for the different mass transfer modes along erosive convergent margins.

***Table 1**. Estimations of rates of subduction erosion at erosive convergent margins. The values of rates correspond to specific periods of time, in general controlled by the pre- or post- approach and passing of major topographic structures beneath the margin, indicated by * and **. For nomenclature of the topographic structures see Fig. 1.1.*

	Frontal Erosion [km2/my]	Basal Erosion [km2/my]	Trench Retreat [km/my]	Frontal Erosion + Basal Erosion [km2/my]	Long term subsidence of the slope [km/my]	Timing
Tonga, before*/after LR [1; 2; 3]**		40-50	<1.5* / 3.9**	75*		
Peru, before*/after NR [4]**			<1.1* / 10**	35.2*		Since Eocene i.e. 47 My* / since 11 My Lima Basin**
Peru [3, 5, 6]		25 / (31-46)*	3.1 / (2.5-3.5)*	60	5*	Since 16 My*
Northern Chile [3; 8]		35	(1.25 – 1.75)*	(45-50)*	0.2*	Since ca. 20 My*
Northern Chile, before*/after IR [9; 10; 11; 12]**			(3-4)**	(37-56)* / (96-128)**	(0.3-0.5)**	Since ca. 4 My* / since 10 My**
Chile, before JFR [3; 11; 22; 23]			3	25-70	0,2	
Central Andes [12; 14]			1,5-2	40		
Aleutian [13]		40*			0,1	*at least since Cenozoic
Ecuador / Colombia [23; 24]			3	42		Since 8 My
Costa Rica before*/after CoR [15]**		(34-36)* / (107-123)**	(3-3.5)* / 8**		(0.1-0.15)* / (0.55-0.6)**	Since 17 My* / last 5-6.5 my**
Costa Rica [16; 17]			4-10		3	
South Sandwich Islands [19]	12.4-18.8	18.6-28.2		31-47	3.1-4.7	
Guatemala [18]		11.3-13.1	0.8-0.9		0,1	Since ca. 25 My
Japan [3; 5; 6; 7; 20]	20*/12**	60*/55**	3**	80*-95	0.1-0.4	Since ca. 24 My / 26 My* / since 20 My** /
Nature min ~	13	11	1	25	0,1	
Nature max ~	19	55	10	128	5	

[1] Balance et al., 1989; [2] Clift and MacLeod, 1999; [3] von Huene and Scholl, 1991; [4] Clift et al., 2003; [5] Lallemand et al., 1992a; [6] von Huene and Lallemand, 1990; [7] Heki, 2004; [8] von Huene and Ranero, 2003; [9] Scheuber, 1994; [10] von Huene et al., 1999; [11] Kukowski and Onken, 2006 and references therein; [12] Scheuber and Reuter, 1992; [13] Scholl et al., 2002; [14] Scholl and von Huene, 2009; [15] Vannucchi et al., 2003; [16] Vannucchi et al., 2001; [17] Lallemand et al., 1998; [18] Vannucchi et al., 2004; [19] Vanneste and Larter, 2002; [20] von Huene et al., 1994; [21] Clift and Vannucchi, 2004; [22] Stern, 1991; [23] Clift and Vannucchi, 2004; [24] Mercier de Lepinay et al., 1997.

4. METHODS

Simplifying natural processes with simple analogue experiments allows us to identify and evaluate the key parameters controlling such processes. The mechanical similarity between sand and the brittle portion of forearcs makes sandbox experiments applicable to the study of brittle rocks behavior (Section 4.1.3). As sandbox simulations enable investigations of single parameters, they have contributed significantly to our understanding of deformation processes in the brittle uppermost 30 km of convergent margins. The identification of their main governing parameters yields constraints on the tectonic growth or steady-state tectonic erosion mechanisms.

In this study, we used analogue tectonic modeling (2D sandbox wedges) combined with digital image analysis (PIV; Section 4.2). With the use of both techniques –sandbox experiments and PIV– we were able to obtain quantitative and qualitative results. Our results were compared with concepts, hypotheses and estimates derived from surface studies and geophysical data of several erosional margins as well as with other studies using sandbox and numerical simulations. We also analyzed geometrical similarities between modeled and natural wedges. By observing in our experiments at equivalent depths where otherwise seismic images resolution is not longer sharp (>15 km), implications from deep processes for the surface could be identified.

There is a multitude of likely parameters associated with the shallow brittle part of the continental plate, which may be controlling subduction erosion. In particular, the kinematic boundary conditions on the basal transport of mass should define whether a convergent margin develops as accretionary or erosional. Under this standpoint, Subduction Channel (SC) evolution is a key for understanding the mechanical conditions for deformation in erosional margins. Sandbox experiments here played a key role, as they were capable of showing the internal spatio-temporal evolution of experiment and the patterns of basal and internal material transfer. In contrast, the visualization of forearc structures at great depth (>15 km) with geological and geophysical data is mostly impossible. The choice of variable parameters in our experiment series derived from previous discussions and concepts (Sections 3.2.3 and 3.3.1), chosen in accordance to their expected importance for erosion to occur. The variable parameters were: the role of "an aperture" governing the maximum amount of material that can be deeply subducted, the basal interface topography, the geometric configuration of forearcs, and the differences in rock strength.

In order to study the modes of mass transfer, we quantified frontal and basal erosion, tip retreat, subsidence, and accretion of sediment from our experiments. Then, through upscaling our experimental results to nature, we also evaluated our results by comparison with rates of subduction erosion derived from natural forearcs. By using the Particle Image Velocimetry (PIV), we were able to track particles inside the wedge, which is particularly useful for describing modes of mass transfer and SC kinematics.

A set of ~70 preliminary small test

experiments (Appendix A2) were performed to investigate a wide range of parameters. The models were organized into groups depending on the parameter to be analyzed: i) Initial surface slope, ii) Position, composition and size of bodies embedded in the wedge, iii) Basal dip, iv) Height of the opening at the lower edge of the back wall (referred to as well as subduction gap), v) Basal topographic/material properties and vi) Strength of the wedge. Bodies embedded in the wedge act as heterogeneities, with glass beads being used for a weak material, and corn flour for a strong material. The results of the test experiments allowed us to tune the final configuration of the experimental series, which then were performed in a considerably bigger experimental apparatus.

In order to initially build a wedge with a critical geometry, an undeformed sand-layer of 100 cm length was accreted. This was followed by a short erosional phase where the conveyor belt had no material on it, to ensure criticality. The critical slope value obtained with this test experiment was considered the initial geometry for the experiments in the bigger box (i.e. ~13º). Also, different basal dips were tested in the preliminary small tests. The results showed that the amount of basally accreted material was distributed differently for $\beta \neq 0$ than for $\beta = 0$, but the overall geometry (i.e. taper) and structures were virtually the same. The latter observation confirmed that by increasing the basal inclination, the surface slope of the wedge decreased (Critical Taper theory, Davis et al., 1983; further details in Section 3.1).

4.1 Model setup and materials

Results from previous experimental studies (in literature and preliminary test realized for this study; Appendix A2) form the foundation for our idealized subduction erosion setup. This "ideal" setup simulates a purely erosional environment without frontal or basal accretion. In doing so, the effects of subduction erosion on the wedge are isolated from other processes which may influence its tectonic evolution. Additionally, we imposed an open setup to ensure a net negative mass balance of the system and high basal friction to induce underthrusting of the material arcwards (Kukowski et al., 1994; Gutscher et al., 1996, Gutscher et al., 1998b). Thus, in order to "recreate" those features commonly seen in convergent erosional margins, we considered three basic aspects: (i) material leaving the system, (ii) material input < material output and, (iii) high basal friction (Section 2.3).

Table 2 outlines the systematic series of analogue experiments which were performed, with the following parameters varied in each series: (I) size of the global capacity, (II) geometry of the wedge, (III) strength of the wedges, (IV) topography of the conveyor belt surface. With these experiment series we intend to elucidate factors potentially controlling modes, loci and rates of frontal and basal erosion as well as the kinematic evolution of an erosional wedge.

4.1.1 Experimental setup

All our experiments were carried out in a sandbox of 3 m length and 20 cm width, with sidewalls made of glass (Fig. 4.1.1). A belt emplaced on the rigid basal plate of the box was pulled by a motor representing the motion of the subducting oceanic plate. The basal angle β was set to zero for all experiments. A wedge-shaped body overlying the belt represented a forearc and the back of the wedge leaned

against the vertical rigid backwall of the box. The material composing the wedge was sifted in different layers separated by thin black sand layers and triangular-shaped markers (not influencing mechanical behavior; Lohrmann et al., 2003) so that we could visibly identify the internal wedge deformation. For the setup of "erosional" experiments, an incoming sediment layer on the surface of the conveyor belt was not included. At the rear, the backwall can be raised to create an aperture at its base, allowing a controlled amount of material to leave the system through this aperture (Subduction Gap, SG in Fig. 4.1.1; Gutscher et al., 1998a; Bangs and Cande, 1997; Clift and Vannucchi, 2004). The SG represents the global capacity (Cloos and Shreve, 1988a), which governs how much material will be deeply subducted (see Section 2.2.3).

***Table 2**. Model setup conditions of the five experimental series performed in this study*

Varied Parameters	Experiment nomenclature	Initial length (cm)	Sand:Sugar	Topography conveyor belt	Conver-gence (cm)	Height Wedge (cm)	initial slope angle α (°)	Gap backwall (mm)
Subduction gap SG	G1	125	2:3	Rough	500	30	α = 13.5	2
	G2	125	2:3	Rough	500	30	α = 13.5	4
	R0	125	2:3	Rough	500	30	α = 13.5	6
Surface taper ST	T1	125	2:3	Rough	500	15	α = 7	6
	T2	125	2:3	Rough	500	22	α = 10	6
	R0	125	2:3	Rough	500	30	α = 13.5	6
	T4	125	2:3	Rough	500	35.8	α = 16	6
	T5	125	2:3	Rough	500	45.6	α = 20	6
Internal friction IF	R0	125	2:3	Rough	500	30	α = 13.5	6
	F3	125	3:2	Rough	500	30	α = 13.5	6
	F2	125	4:1	Rough	500	30	α = 13.5	6
	F1	125	1:0	Rough	500	30	α = 13.5	6
Highs and lows HL	HL.1	125	9:1	Rough	480	30	α = 13.5	6
	HL.2	102	9:1	Highs and Lows	600	30	α = 38	6

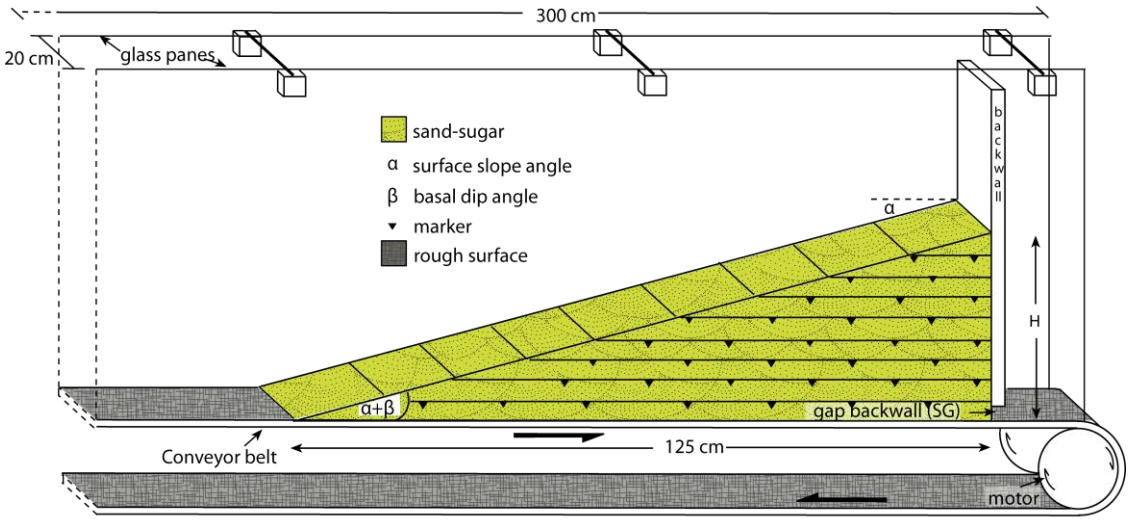

Figure 4.1.1. *Model configuration. The height of the rear part of the wedge H varies with the initial slope angle. Basal angle β is set to zero in all the experiments*

4.1.2 Physical properties of the analogue materials

We chose sand and similar granular materials for the experiments, as it has been previously demonstrated that these materials can adequatly represent forearc wedges (Section 4.1.3; Hubbert, 1937; Lallemand et al., 1992b; Calassou et al., 1993; McClay, 1996; Lohrmann et al., 2003). Sand is the more common granular material used in analogue simulations to represent forearcs. However, as mentioned before, most analogue simulations are focused on (and designed for) accretionary systems. Since we aim to emulate the crystalline upper plate of a subduction erosional forearc, we added sugar, as it creates mechanically stronger material than sand. The influence of sugar in the internal mechanical properties of the mixture was studied in a systematic manner. We analyzed mixtures between sand and sugar with different relative proportions of both materials, i.e. 1:0, 9:1, 4:1; 3:2 and 2:3 of sand and sugar, respectively (Table 3).

SEM data

The characterization of the grains was made with a Scanning Electron Microscope (SEM), with a magnification ranging from 20X to approximately 60X (sand and sugar spectra). The quartz sand used for the experiments shows characteristics (shape, rounding, etc.) similar to the ones obtained by Lohrmann et al. (2003), thus its mechanical properties are similar to brittle upper-crustal rocks. This condition was fulfilled by sieved sand, well sorted, round to very round and mostly consisting of spherical grains with sizes ranging from 0.20 to 0.63 mm. The sugar consisted of well defined crystals, sizes <0.7 mm, well sorted, mostly equidimensional and sub-angular to angular. The differences in shape are manifested in the frictional properties of the different materials.

RST measurements: internal and basal friction

(i) internal friction

The internal and basal mechanical properties of the granular materials used for the experiments were measured using a ring shear tester (RST-01, Schulze, 1994).

The material to be tested was sieved into a shear box, which was

subsequently loaded with six different loads ranging from 500 to 16000 Pa. The loads, which were doubled with each step, were similar to those utilized in the experiments. From equation (1), the coefficient of internal friction μ_i is obtained by linear regression, varying the normal load σ_N. The evolution of the shear stress through time (Fig. 4.1.2) was obtained with the range of normal loads. To minimise measuring errors, each test was performed three times (Lohrmann et al., 2003; Panien et al., 2006).

Studies of Coulomb-type material (i.e. pressure-dependent and time-independent failure criterion, as rock or materials used here) have shown that their internal mechanical properties change during deformation (Brace and Byerlee, 1978; Paterson, 1978). The Coulomb-type materials are defined to be non-cohesive and follow a linear elastic stress-strain relationship, until pressure-dependent failure occurs (Eq. 1). Hence, distinctions must be made between the properties of a deformed and undeformed material. A fractured material will show a smaller strength than an undeformed material.
This was confirmed by our RST results by means of two shear-load cycles with the same normal load: Shear stress increases as the granular material deforms (Fig. 4.1.2). Prior to faulting, an initial (linear) elastic stress-strain relationship is followed by a plastic one. After the frictional strength is exceeded (i.e. the *peak strength;* Fig. 4.1.2; μ_P in Table 3), the now deformed material requires a lower and nearly-constant frictional strength to keep sliding along the shear plane (i.e. the *stable dynamic strength;* Fig. 4.1.2; μ_{SD} in Table 3). If faults are reactivated (i.e. the *stable static strength;* Fig. 4.1.2; μ_{SS} in Table 3), the frictional strength is then higher than neccessary to cause sliding but smaller than neccesary to fracture undeformed material.

The values of internal friction obtained for our granular materials (i.e. mixtures of sand and sugar) agreed with the characterization of a strain-dependent deformation behaviour. They showed pre-failure strain hardening and post-failure strain softening (Fig. 4.1.2), such as the non-linear deformation behaviour of brittle crustal rocks.

(ii) basal friction and friction ratio
To measure the basal properties of the granular material used in our experiments with respect to the conveyor belt, the same procedure explained for internal measurements was followed. The base of the shear box was covered with the conveyor belt and a thin layer of the granular material (~2 mm) was sifted. The conveyor belt had a rough surface, and a coefficient of basal friction similar to the different materials used in this study ($\mu_{BSD} \approx 0.54$; Table 3). The difference between the internal friction of the material and the basal friction along its contact with the conveyor belt was thus not larger than ~0.06 – 0.02, maintaining an erosive regime (Gutscher et al., 1998b). Since the base of the SC is equivalent to a continuously active internal shear zone at the base of the wedge, basal friction corresponded to the internal stable dynamic friction of the granular material. For all mixtures, the basal friction (μ = 0.54 - 0.56) was in accordance with those of natural erosional margins μ = 0.6 - 0.7 (Davis et al., 1983; Kukowski et al., 1994; Adam et al., 2003).

Lohrmann et al. (2003) demonstrated the strong influence of the preparation technique (sifted, poured or sprinkled) of the granular material and grain-size distribution in determining its internal

properties. A larger similarity between brittle upper-crustal rocks and the granular material is found if the sifted (i.e. well compacted) granular material has a grain-size distribution ranging between 20-630 mm.

Therefore the filling technique was by sifting, thus obtaining well compacted granular materials. Differences in compaction were related to the internal properties, where a strong granular material was associated with lower compaction (Fig. 4.1.2).

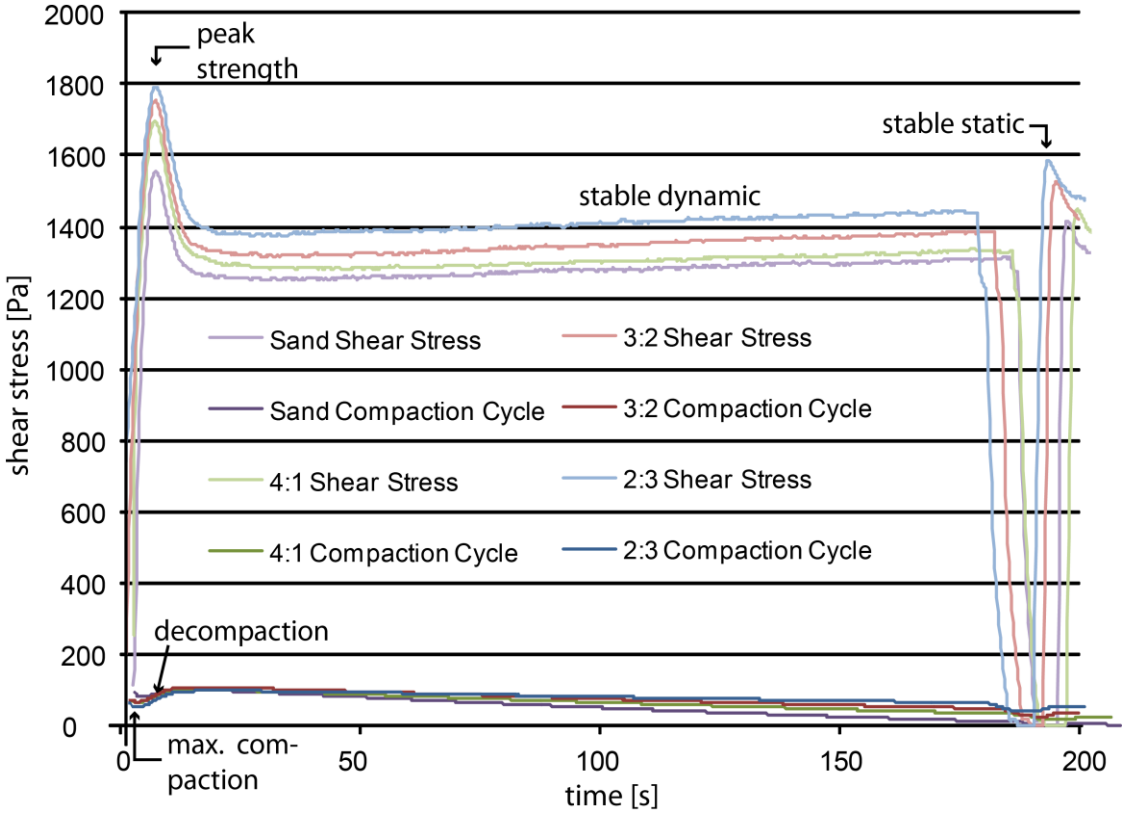

Figure 4.1.2. *Shear stress and thickness variation of the sample plotted as a function of time (sec) for dry sand and mixtures 4:1, 3:2 and 2:3 Sand:Sugar. Normal load corresponds to 1600 Pa. Onset of failure occurs at peak strength value, preceded by strain hardening. Once the maximum strength has been achieved, strain softening occurs and strength drops gradually toward a dynamically stable value. At this nearly constant stress, faults slides. Compaction-dilation relates to the material strength. Major compaction and also the major dilatancy correspond to the strongest granular material (2:3 mixture), whereas minor compaction and dilatancy correspond to the weakest material (sand). Maximum compaction occurred shortly before the failure of the material*

4.1.3 Scaling

Results from experiments are only representative of nature if both systems are dynamically similar. For the system to develop dynamics similar to those in nature, the mechanical properties of the materials have to be properly scaled. This condition is fulfilled if both, experiments and nature (Hubbert, 1937):

1. are geometrically similar, i.e. all corresponding lengths are proportional and angles between corresponding lengths are equal;

2. are kinematically similar, i.e. if both geometrically similar bodies deform similarly;
3. if the ratio between the forces acting on corresponding particles in both geometrically and kinematcally similar bodies is constant,

Considering the values of cohesion C and density ρ for crustal rocks (C= 0.7-105 MPa; ρ= 2000-3000 kg / m^3, Byerlee, 1978; Landolt-Börnstein, vol. I "Physical properties of rocks" available at www.springerlink.com) and for the analog materials (Table 3), a scaling factor can be calculated as (Ramberg, 1981):

$$K = [C\ \rho_{experiment}] / [C_{experiment}\ \rho]$$

Given that the densities of analogue materials are in the order of 1400 – 1800 kg/m^3 and cohesion is in the order of <40 – 70 Pa, the scaling factor is roughly $1x10^5$ (Horsfield, 1977; Kukowski et al., 1994; Koyi, 1997; Schellart, 2000). This means that 1 cm of the model corresponds approximately to 1 km in nature.

Table 3. *The mechanical properties were measured using the Ring Shear tester, with a standard error smaller than 0.007 (RST-01, Schulze, 1994).*

Properties	Sugar	Mixture 40% Sand 60% Sugar	Mixture 60% Sand 40% Sugar	Mixture 80% Sand 20% Sugar	Mixture 90% Sand 10% Sugar	Sand
Grain size spectra [mm]	<0.7	<0.7	<0.7	<0.7	<0.7	<0.63
Filling method	sifted	sifted	sifted	sifted	sifted	Sifted
Bulk density [gr/cm^3]	0.97 (±0.01)	1.40 (±0.02)	1.59 (±0.11)	1.67 (±0.03)	1.72 (±0.01)	1.71 (±0.02)
C [Pa]	47(±16)	<40	59(±8)	59(±9)	67(±13)	<40
μ_P	0.87 (±0.006)	0.797 (±0.004)	0.762 (±0.005)	0.734 (±0.008)	0.703 (±0.011)	0.681 (±0.004)
μ_{SS}	0.75 (±0.002)	0.69 (±0.001)	0.664 (±0.001)	0.63 (±0.001)	0.606 (±0.003)	0.615 (±0.002)
μ_{SD}	0.608 (±0.003)	0.598 (±0.001)	0.573 (±0.001)	0.556 (±0.001)	0.54 (±0.001)	0.541 (±0.001)
μ_{BSD} (conv. belt/material)		0.54 (±0,001)	0.561(±0,001)	0.54 (±0,001)	0.538 (±0,004)	0.55 (±0,002)
μ_{BSD} / μ_{SD}		0.9	0.98	0.97	1	1.02
Wood/material					0.423 (±0,002)	

4.1.4 Limitations of the experimental approach

As said before, the use of granular material offers an excellent opportunity to study continental-scale phenomena by reproducing them on smaller scales. However, the experimental approach bears some limitations, which must be kept in mind when interpreting experimental results.

A difficultly in applying experimental results to natural forearcs is that analogue materials (as those applied in this study) are homogeneous. Thus, the

granular materials represent an approximation of natural rocks. One should keep in mind that the interpretation of seismic reflections shows variations in seismic velocities arcwards, reporting variations in material properties. This observation is especially important when interpreting results from the critical taper approach, which is based on homogeneous materials.

Another difficulty is that the imposed boundary conditions depict necessary simplifications of natural systems. In experiments, those boundary conditions may represent unrealistic assumptions, as some of them are based on conceptual models (e.g. global capacity; Section 3.2.3). With the current depth of penetration and difficulties in resolving complex structures from seismic data, such boundary conditions cannot be checked. Thus, we are aware of the fact that we should consider our experimental results as "models". However, in order to validate our results, they are compared and discussed with a variety of similar observations from nature stemming from shallow depths (e.g. Section 5.3.5).

In nature, the layer of sediments entering the trench (with an important fluid content) reduces the friction in the contact between layer surface and the underside of the frontal prism. In our idealized erosional setup, the absence of pore pressure in the dry granular material affected mostly the frontal segment of the wedge. This resulted in larger taper angles and angles of repose than in submarine wedges. Arcwards, the presence of fluids is considered to weaken the rock by hydrofracturing. The present-day setup is not able to model the latter in a realistic way; however, we tested the influence of internal strength in wedges, from where some hints can arise. Besides, our experimental setup included a kinematic boundary condition which may be a first order parameter, overimposing its effect and stressing the erosional effect of the pore fluid effect, i.e. the global control point. Finally, former analogue physical studies have supported the validity of using analogue materials, as the critical taper approach is still applicable for dry wedges (Section 3.1).

Another limitation is the apparently inherent form of localized failure in a porous, poorly consolidated material like our granular media, which differs from that in a consolidated, low porosity brittle rock (Du Bernard et al., 2002). Packing and grain-size distribution of sand cannot be accurately scaled to nature, thus faulting does not occur as discrete failure, but as dilatant shear zones. The localized shear planes are characterized by a localized increase in porosity within a tabular band of an average 1–2 mm thickness (ca. 2 - 3 grains of sand). In rocks, shear planes occur as fractures or joints in a planar opening-mode with two discrete surfaces. The implications from this limitation are going to be discussed further in the corresponding chapter (Section 5.1.).

4.2 Monitoring experiments by the PIV system

Particle Imaging Velocimetry (PIV) is an optical non-intrusive method originally developed for flow visualization (Adam et al., 2005; White 2001). It allows to monitor the displacement of groups of particles between several photographs with a sufficiently high camera resolution (1 in Fig. 4.2.1). The evolution of an experiment was entirely recorded with an 11 Mpx digital camera. The

sequence of digital images recorded by PIV was taken with a frequency of ~0.25 Hz, equivalent to 2 mm of convergence (accuracy of the displacement measurement is ~0.5 mm (Adam et al., 2005); velocity of the conveyor belt was ~0.5 mm/s). This represents 0.2 km of convergence in nature. The total convergence of the experimental run was 5000 mm, resulting in a total of ~2500 digital images per experiment. Referring to rates of convergence between the Nazca plate and the South American plate, respectively (DeMets and Dixon, 1999; also representative for erosional margins: Fig. 1.1), which from Miocene to present was about 10 cm yr^{-1}, the total experimental run was equivalent to a period of 5 My in nature.

The digital camera was calibrated prior to image acquisition in order to correct the distortions that occur as a consequence of the view angle of the camera. During acquisition, a mapping function corrects the images and transforms the original scale of the images pixels to millimeters.

The software DaVis (developed by La Vision GmbH, Göttingen) was used to process and analyze the images. Applying an adaptive cross-correlation algorithm, successive images are compared and the incremental displacement field is calculated.

The image processing subdivides each image from the sequential images (image 1 at time t = t1 and image 2 at time t+dt = t2) into corresponding "interrogation windows" IW. Intensity values are assigned to each IW and the correlation function operates on the intensities inside each IW (IW1 and IW2; 2 in Fig. 4.2.1). It follows that IW2 has moved incrementally to dx and dy with respect to IW1, in the xy plane. Local displacement vectors are calculated for each IW, as a result of a spatial average for each entire IW. Further, a correlation between the intensities for IW1 and IW2 is calculated for each position by a Fast Fourier Transformation algorithm. Results are saved in a correlation map. The highest peak in the cross-correlation image is the most likely displacement vector.

Using an adaptive multi-pass correlation, the spatial resolution can be increased by calculating an intermediate vector field. The vector field is first estimated in a large IW. From one iteration to the next, the size of the interrogation window decreases to half of the previous size. The first vector field is used as a reference for the current pass as best estimation for the most probable movement (Fincham and Spedding, 1997; Scarano and Riethmuller, 2000; Wieneke, 2001; Adam et al., 2005). Hence, this method detects large deformation with the small IW sizes, improving the spatial resolution, reaching an accuracy of 0.5 mm in typical sandbox experiments.

The resulting displacement field forms the basis for the further calculation of derivative parameters (e.g. horizontal and vertical velocity components). Derived values have an associated relative error in the range of 0.3-1.25%. The derivative Exy is the strain tensor component and xy denotes the change of the x-component of the velocity vector in the y-direction and thus represents the horizontal shear strain. The rotational shear rot-z = Eyx-Exy determines the two-dimensional vorticity in the xy-plane and thus delineates shear zones. For our analysis, the displacement field and the derivative rotational shear rot-z = Eyx - Exy are especially useful, as they enable us to study basal material transport in the SC.

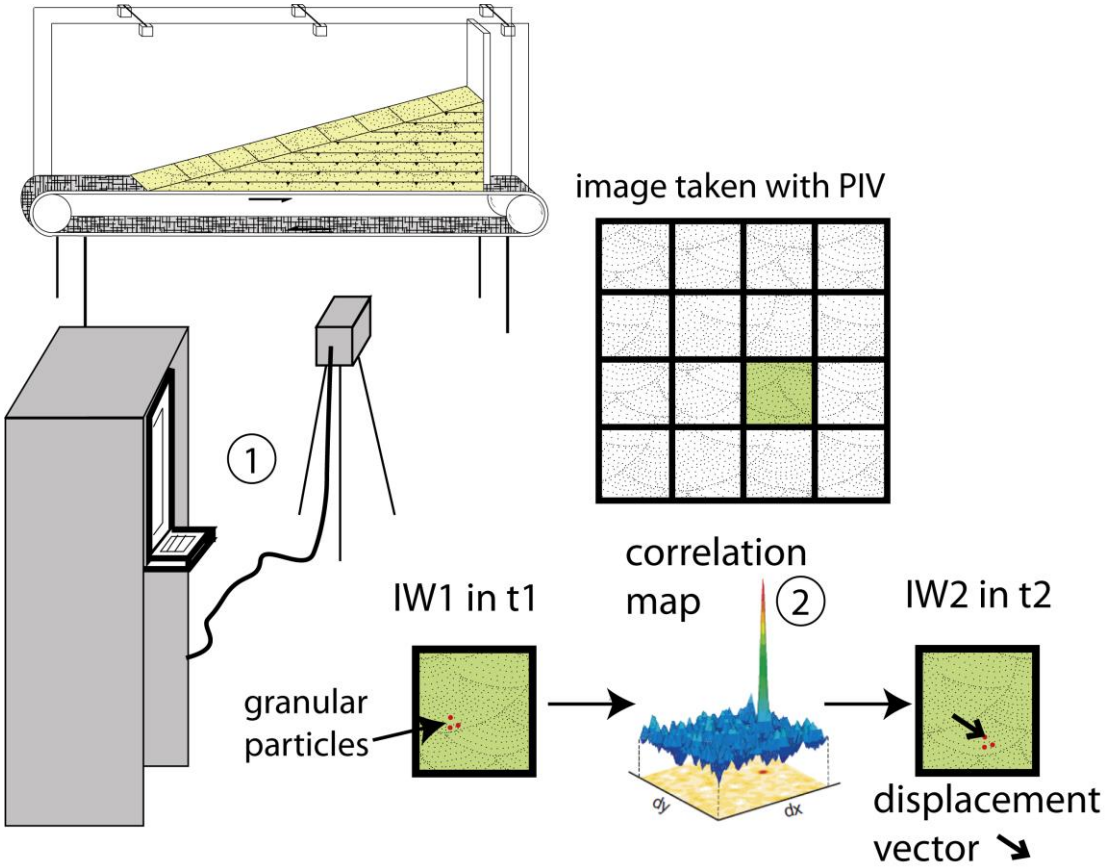

Figure 4.2.1. *Schematic representation of the PIV (particle image velocimetry) technique for the study of a granular flow. The process is recorded with the PIV camera (number 1). The image is subsequently divided in smaller interrogation windows IW. The displacement vector is derived with a method of cross correlation from time frame 1 to time frame 2 (number 2) (after LaVision).*

4.3 Definition of processes and measured quantities

A segmentation of the wedges was observed in all experiment series, whose different zones are later linked to processes within the SC, which also showed a segmentation. Here, we explain how we defined these segmentations and how we estimated values for volumes of material transfer, comparing them later with data from natural foreacs.

4.3.1 Identifying different mass transfer modes

The different mass transfer modes (*Frontal Erosion*, *Basal Accretion*, and *Basal Erosion*) were identified by changes in the position of the marker lines and from the geometry of the wedge (Fig. 4.3.1).

Basal accretion can be visualized by the upward motion of a marker line with respect to its previous horizontal position. Shortening of the wedge is quantified by the tip retreat. The basally eroded material can be visualized by the downward motion of a marker line, with respect to its previous horizontal position. Frontal erosion and subsidence are measured as the areas at the front of the wedge and at the middle slope surface, between the two consecutive pictures (Fig. 4.3.1).

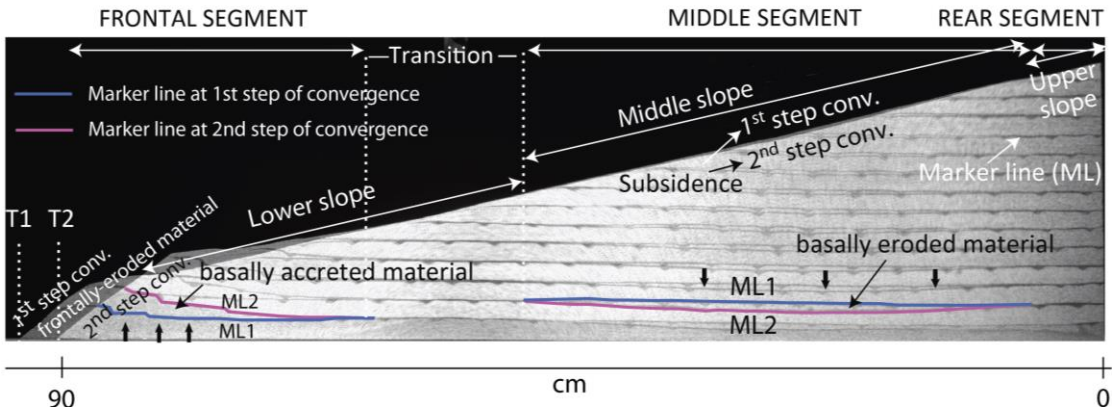

Figure 4.3.1 *The procedure to detect basal and frontal erosion, basal accretion and subsidence. The image shows two pictures superimposed at stage 100 cm and 150 cm of convergence. The wedge segmentation was defined by the loci of the different modes of mass transfer. The size of the gap at the bottom of the back-wall (SG) is 6 mm. T1, ML1 and T2, ML2 represent the position at first and second intervals of convergence respectively of* ***T****ip and* ***M****arker* ***L****ine. Vertical arrows indicate the sense of the marker line movement, showing the basal accretion and erosion positions. The areas between ML1 and ML2 account for rates of basal accretion at front and basal erosion at middle segments, respectively. Basal erosion is observed on the surface as subsidence, defining a middle segment of the wedge and middle slope respectively. At the leading edge of frontal segment and at the middle slope segment, the missed area between the first and the second state (or step) accounts for the frontal eroded material and subsidence, respectively.*

4.3.2 Quantification of the material transfer modes

The different mass transfer rates were determined from PIV images, every 50 cm of convergence. The change in position of the triangular markers and marker lines proved useful for the overall description and quantification of material transfer within the wedges. Thus, the area between two consecutive positions of the same marker line is used to estimate mass transfer rates (Fig. 4.3.1). The rate of Frontal erosion is calculated by the area of the leading edge of the frontal part of the wedge from two consecutive images (Fig. 4.3.1). The rate of subsidence is the area calculated between the surface slope of the wedge from two consecutive images (Fig. 4.3.1).

Estimated bulk rates for every mass transfer are derived from the quantities measured in the serial digital images (Fig. 4.3.1). They correspond to the cumulative value of the mass transfer rates divided by the total convergence. With no external material supply (no incoming sand-layer), the only source for frontal underplating of material comes from the frontal gravitational collapses. Thus, the average thickness of sediment supply at the wedge toe (estimated IC) was estimated as the bulk rate of the previous frontal eroded sediment by cm_{conv}.

The rates were specified as cm^2/cm_{conv}. (i.e. cm^2 of material per cm of convergence) or cm/cm in case of 1 dimensional numbers (tip retreat and subsidence). In order to compare experimental results (in $[cm^2/cm_{conv}]$) with estimates of erosion rates from natural forearcs (in $[km^2/My]$), we referenced the convergence rate in Chile (Section 4.2), establishing 10^2 x $[km^2/My]_{nature} = [cm^2/cm_{conv}]_{model}$ ratio.

Initially, a soil or sand wedge pushed by a bulldozer deforms internally until it achieves a “critical” shape, whereupon the wedge slides stably on its base (Section 3.1). In the

experiments, the wedges were built with an initial geometry close to the critical state to minimize the initial phase of adjustment. During this transitional stage, the strong changes observed in wedge taper and kinematics are not representative, as the wedge is adjusting to the new conditions. Thus, quantitative analysis for comparing the different mass transfer modes was carried out after the first 50 cm of convergence, when the wedge had deviated from the initial conditions and SC showed a more constant behavior.

4.3.3. Data mining

In order to measure areas of the wedges, convergence intervals of 50 cm of the digital images recorded by PIV were drawn with a graphic design software (Adobe Illustrator). All volumetric data derived from this method were normalized with respect to the same scale in order to directly compare experiments. Since data collected by this method was in pixels, it was corrected to the millimeter/centimeter domain. With this method, the size of each pixel in the drawing could be estimated as 0.0095 cm^2

5. INFLUENCE OF KINEMATIC BOUNDARY CONDITIONS ON EROSIONAL WEDGES

Based on previous analogous experiments and theoretical models we set different kinematic boundary conditions on our wedges, where each different boundary condition represents one series (Fig. 5.1).

The most important observation among all experiment series was their three different phases. They were identified by changes in the trends of the rates of the different modes of mass transfer, which were later linked with evolution of the velocity field within the Subduction Channel (SC). Hence, special emphasis shall be laid upon the variations of vertical and horizontal components of the velocity field and the associated geometry of the SC.

A segmentation of the wedge was observed in the reference experiment and in all experiment series. Their different zones and their link with processes within the SC, will be later discussed. Later in the text, we will use the segmentation of the wedge to estimate values for volumes of mass. The evolution of a reference experiment, whose kinematic evolution can account as a reference for all wedges of the experiment series, is described in detail in each state. The information obtained from the SC as velocity field components and relation to flow behaviors account for deformation of the wedges. Finally, we discuss the influence of the backwall boundary condition on the structural evolution of the wedge.

Each series of experiments is examined with respect to the reference and the specific differences among models are pointed out. The results from the experiments are first described and we discuss the results afterwards.

5.1 The reference experiment (R0)

The reference experiment represents a wedge with those "basic" features observed at erosional margins. In doing so, (1) the initial geometry was chosen to be close to the geometry of a wedge in a steady state (for further details see Section 5.3.6) and, (2) we recreated the "global capacity" (Cloos and Shreve, 1988a), which allows the eroded material to move at depths (Section 2.2.3).

5.1.1 The segmentation within the wedge

Different segments of the wedge correspond to the location of various mass transfer modes (Figs. 4.3.1).

At the *Frontal* part of the wedge, frontally eroded material was underthrusted and underplated (Fig. 5.1.1ii). As a result, this area was shortened and uplifted. Accretion of material was mainly by activation of backthrusts.

The *Middle* segment is where basal mass removal took place (Fig. 5.1.1ii). Subsidence occurred at the surface middle slope, triggered by the removal of sediment at the wedge underneath (i.e. basal erosion).

The *Transition* segment was localized between the Frontal and the Middle segments (Figs. 4.3.1 and 5.1.1ii) and was associated with no vertical motion of the marker line.

At the back of the wedge, in the contact zone with the backwall, the *Rear* segment (Fig. 5.1.1ii) showed limited vertical movement.

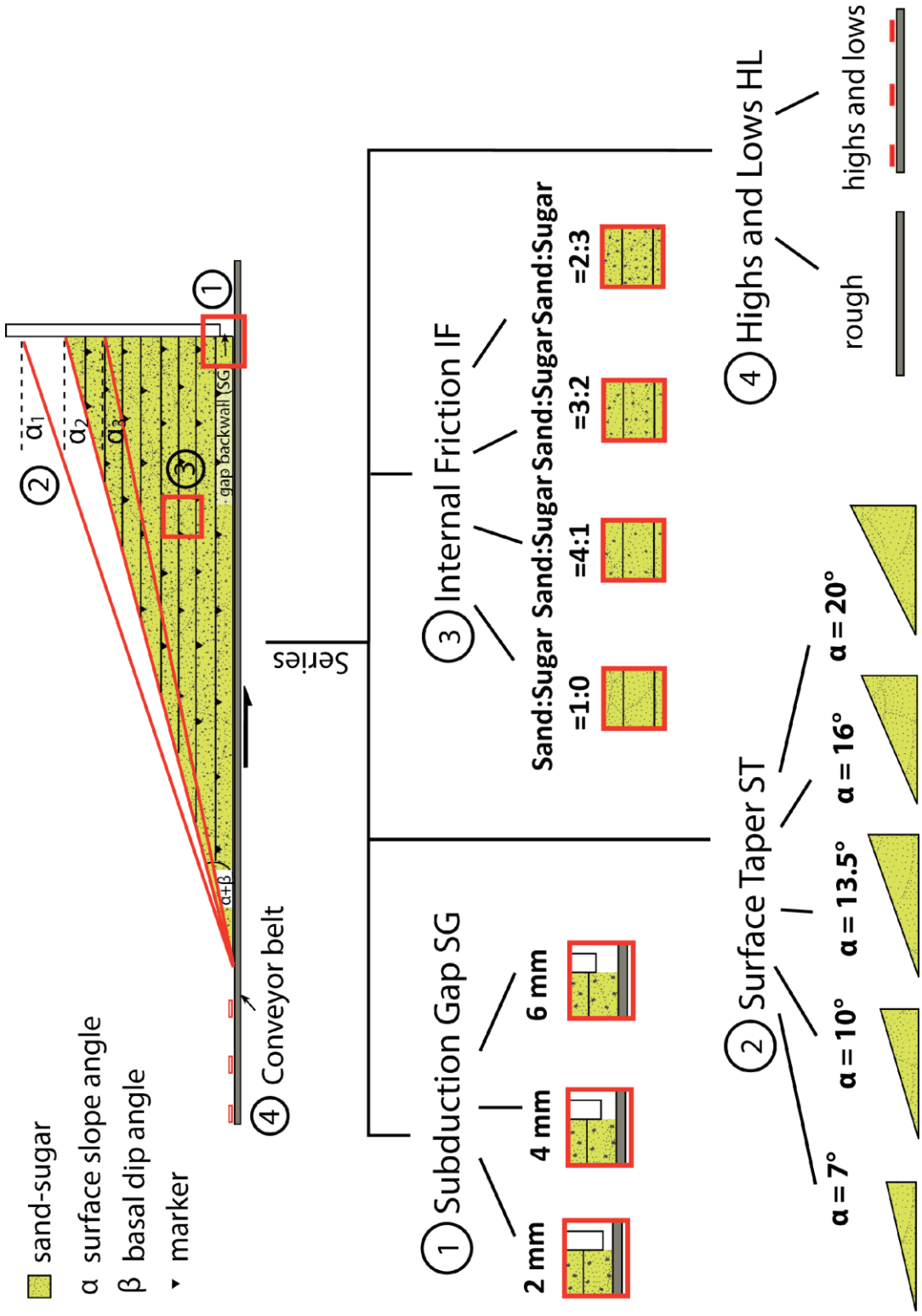

Figure 5.1. *Diagram summary of the four series performed in this study. Every series represents a different kynematic boundary condition: 1) first series varied the size of the aperture at the bottom of the back wall, 2) second series varied the surface taper angle, 3) third series varied the internal friction of the wedges and, 4) fourth series varied the topography of the conveyor belt.*

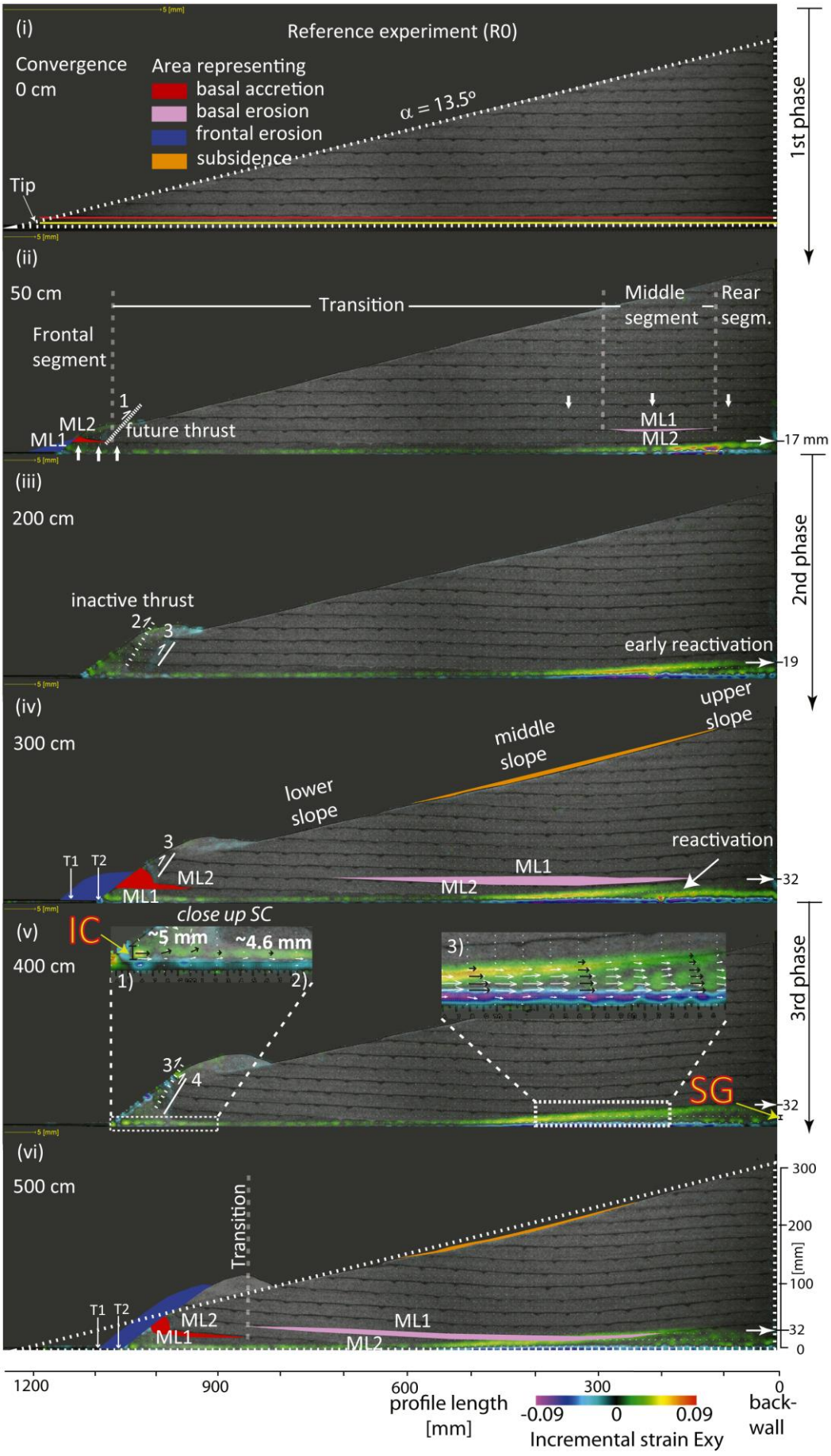
(i)
Reference experiment (R0)
Convergence
0 cm
Area representing
basal accretion
basal erosion
frontal erosion
subsidence
α = 13.5°
Tip
1st phase
(ii)
50 cm
Transition
Middle segment
Rear segm.
Frontal segment
1
ML2
ML1
future thrust
ML1
ML2
17 mm
(iii)
200 cm
inactive thrust
2
3
early reactivation
19
2nd phase
(iv)
300 cm
upper slope
middle slope
lower slope
3
T1
T2
ML2
ML1
ML1
ML2
reactivation
32
(v)
400 cm
close up SC
IC
~5 mm
~4.6 mm
1)
2)
3)
3
4
SG
32
3rd phase
(vi)
500 cm
Transition
T1
T2
ML2
ML1
ML1
ML2
300
200
100
32
0
[mm]
1200
900
600
300
0
profile length
[mm]
back-
wall
-0.09
0
0.09
Incremental strain Exy

Figure 5.1.1. *Evolution of the reference experiment through its different phases. Horizontal arrows show the width (mm) of the SC at each interval. Numbers indicate successive initiation of backthrusts. Symbols same as in figure 4.3.1. i) Initial state. ii) Around 50 cm of convergence the first thrust occurred. iii) Around 200 cm of convergence an early reactivation of thrust was recognized at the top of the basal shear zone. iv) The reactivation of a thrust and the current subdivision of the slope (lower, middle and upper) are shown. v) The white dashed rectangles are enlarged above and show part of the 1) Tip-, 2) Central- and 3) Back segment of the basal shear zone or Subduction Channel SC. A close-up of the SC shows the velocity vectors variations along it, the width at the inlet (IC) and at the rear (SG). Black arrows point out differences of velocity vectors throughout the SC. They illustrate the magnitude and sense of displacement of single particles inside the active shear zone. Numbers show the thickness of the flow in the different segments of the SC. vi) Snapshot at the end of the process. Transition zone became a single line, by the union of the Frontal and Middle segments. Initial geometry of the wedge is compared with the last state geometry (dashed lines). See video of experiments on DVD.*

5.1.2 The segmentation within the subduction channel

An important feature of our models was the evolution of the SC, which was bounded by active upper and lower shear zones (SZUB and SZLB, Fig. 5.1.2). SZLB kinematics was controlled by the stable dynamic internal friction; SZUB kinematics was controlled by the three values of internal friction in different periods over time (Table 3; see Section 4.1.2iii). The vertical position of the SZUB determined the SC segmentation based on the different thicknesses into Tip-, Central- and Back-segments. The base-parallel shear zone Tip begins at the toe, continuing to the point where the shear décollement downsteps. Arcwards, the Central segment ends with the thickening of the SC. This thickening of the SC is characteristic for the Back segment which continues to the backwall. Thickness changes of the SC are related to horizontal velocity variations and roughly coincide with the internal segmentation of the wedge. The velocity gradient field (or flow strain rates) shows measureable particle displacement.

The horizontal and vertical component of the velocity field (v_x and v_y, respectively) were derived from a base-parallel line above the conveyor belt. For v_x the line is 4 mm above the conveyor belt (yellow in Fig. 5.1.1i), showing the velocity of the particles inside the SC. For v_y the line is 10 mm above the conveyor belt (red in Fig. 5.1.1i), showing the vertical displacements of the particles inside the wedge close to the SC's SZUB (upward and downward displacement of particles indicated by positive and negative values, respectively).

(i) Vertical variations of the horizontal velocity components: As the upper and lower SC shear zones are in contact with the static wedge underside and the dynamic conveyor belt, SZUB and SZLB behave according to their boundary conditions (Fig. 5.1.2). At the SZLB, the horizontal velocity component shows the largest velocities $u = u_0$. It decreases upwards and at the SZUB it reaches its lowest value $u \approx 0$ (u_0 < velocity of the conveyor belt). As observed previously, transport velocities in the subduction channel are lower than the convergence velocity (Lohrmann et al., 2006).

(ii) Longitudinal variations of the horizontal velocity components: At the Tip segment, the fast flow rates at the inlet must match these slower rates down the channel. Thus, the horizontal velocity decreases from the tip backwards (Fig. 5.1.2 Tip1 and Tip2): The Central segment is marked by relatively uniform strain (Fig. 5.1.2 Central1 and Central2) and as soon as

the SC becomes wider, the strain rate increases (Fig. 5.1.2 Back1 and Back2). The Back segment is marked by ceaseless fault reactivation. This characterization of the SC was commonly observed in all experiment series, where the specific variations will be specified for each series.

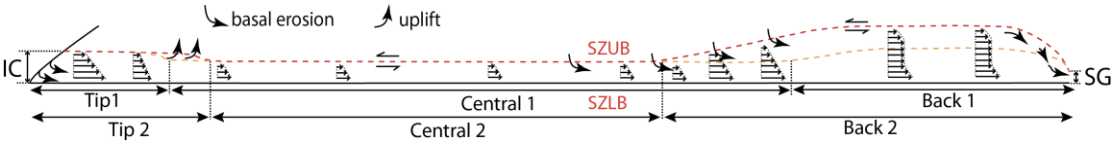

Figure 5.1.2. *Main characteristics of the SC, based on the close up image of the SC in figure 5.1.1v. The SC is confined by upper and lower continuous active shear zones (SZUB and SZLB). Arrows illustrate magnitude and sense of displacement of single particles inside the SC. The lateral differences of the vector velocity field define its Tip, Central and Back segments. The length and width of the SC segments were transient over time, here illustrated with Tip1, Central1 and Back1 during a first step of convergence and Tip2, Central2 and Back2 during a second step of convergence. The upper boundary of the Back segment additionally underwent an upward migration due to the migration of the faster particles (also see Figs. 5.1.4b and c). The transverse velocity gradient behaves as that of a channel flow (the velocity at the bottom is the largest, as adjoins that of the conveyor belt and decreases upward until reaching its lowest value at the top). Basal erosion occurs along the contact with the Central and Back segments but is the strongest where the SC widen, i.e. the frontal part of the Back segment (see also figure 5.1.4b; see Section 5.1.5).*

5.1.3 Kinematic evolution of an erosional wedge during the different phases

Based on the observation of the reference experiment, the kinematic evolution of an erosional wedge is divided into three stages or phases.

(i) The first phase

It covers the initial ~50 cm after convergence is initiated, and is a transient stage before the stable state or steady state is reached. It is characterized by fast compaction of the material within the wedge with frontal diffuse deformation, without any localized shear zone. From the mass transfer rates point of view, this is well displayed by a quick rise and subsequent drop of tip retreat (8.3 cm/cm to 1.5 cm/cm; Fig. 5.1.3a). The frontally eroded material and its subsequent accretion formed a frontal prism. The sediment addition was accommodated by underplating. The amounts of v_y covered a relatively narrow surface and were strong. The formation SC's Tip and Back segments were defined during this phase (Fig. 5.1.4a and c).

(ii) The second phase

The second phase occurs between ~50 and 300 cm of convergence. The overall evolution is observed to be steady-state alike, when compared with the previous first phase. The analysis of processes will be described in details from this phase on.

The Frontal segment underwent basal accretion by activation of new backthrusts (1, 2, 3, Fig. 5.1.1ii and iii). The generation of new thrusts favored uplift and controlled rearward migration of accretion beneath the wedge. Basal Accretion by underplating migrated backwards during further convergence, increasing considerably the basal accretion area (E in Fig. 5.1.4b.v and vi). The largest and lowest rates of frontal erosion and basal accretion occurred during this phase (frontal erosion: 20.6 and 7.6 cm^2/cm; basal accretion: 11.8 and 1.6 cm^2/cm; Fig. 5.1.3a). While the rates

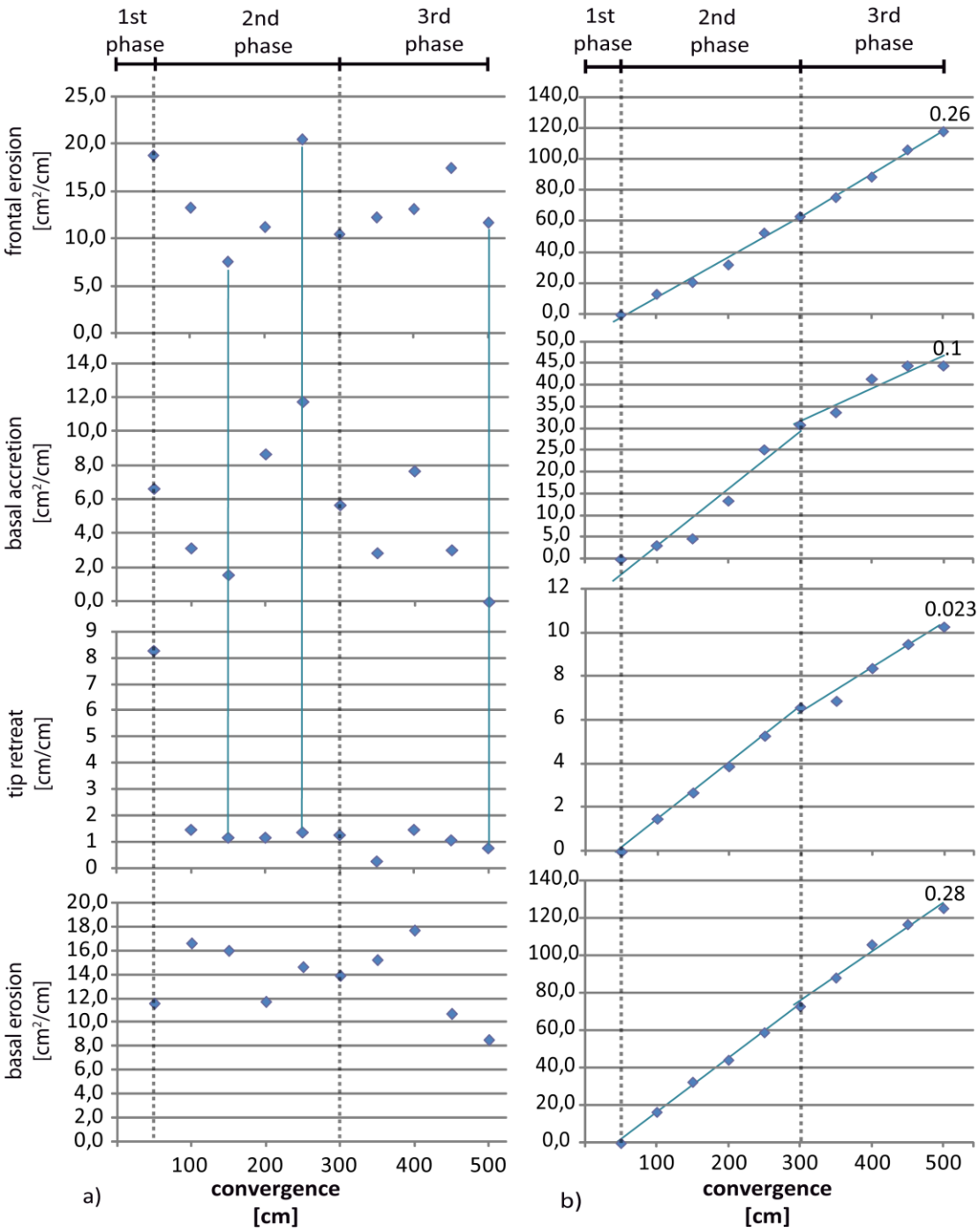

Figure 5.1.3. *a) Different mass transfer rates of the reference experiment R0, after the wedge deviated from the initial conditions. Different phases are specified. A coeval distribution of rates between frontal erosion, basal erosion and tip retreat is visible (light blue vertical lines). b) Different cumulative mass transfer volumes of the reference experiment. The numbers represent the bulk material transfer rates as derived from the final values of the bulk areas (or displacement in the case of tip retreat). Expressed as equivalent values in nature (km² eroded/my or km eroded/my when corresponds), a) frontal erosion: 26, b) basal accretion: 10, c) tip retreat: 2.29, and d) basal erosion: 28. Quantities were normalized for direct comparison (initial values null at 50 cm of convergence). Note the slope variation of the trend line after 300 cm of convergence.*

for frontal erosion and basal accretion were constantly in the ranges of ±18.9 cm^2/cm and ±7.1 cm^2/cm, respectively, the rate of tip retreat showed a decreasing trend during this phase (±8.3 cm/cm until 100 of convergence and ±1 cm/cm later on). The downward displacement of particles (basal erosion), moved forward and additionally extended the horizontal width of the erosion area (cf. Fig. 5.1.1ii with iv; Fig. 5.1.4b.v with vi). Both v_x and v_y components showed a less uniform behavior than the next stage. A faster forward migration of the particles and larger rates for basal erosion than in the subsequent phase were likewise observed (cf. C and F respectively in Fig. 5.1.4a.i and b.v with the corresponding in Fig. 5.1.4a.iii and b.vii).

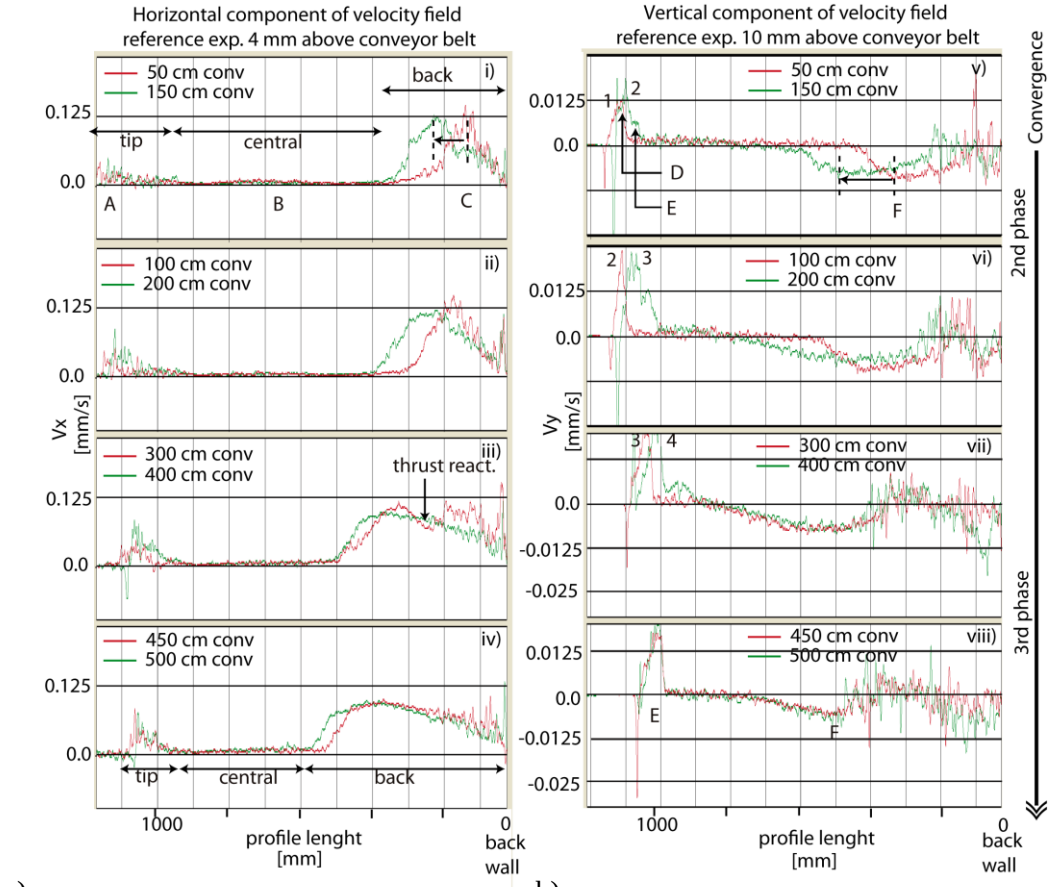

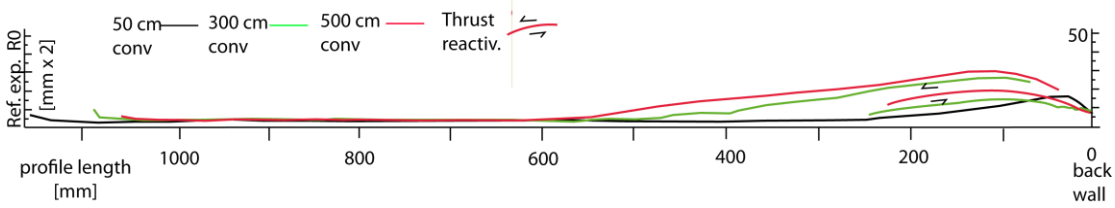

c)

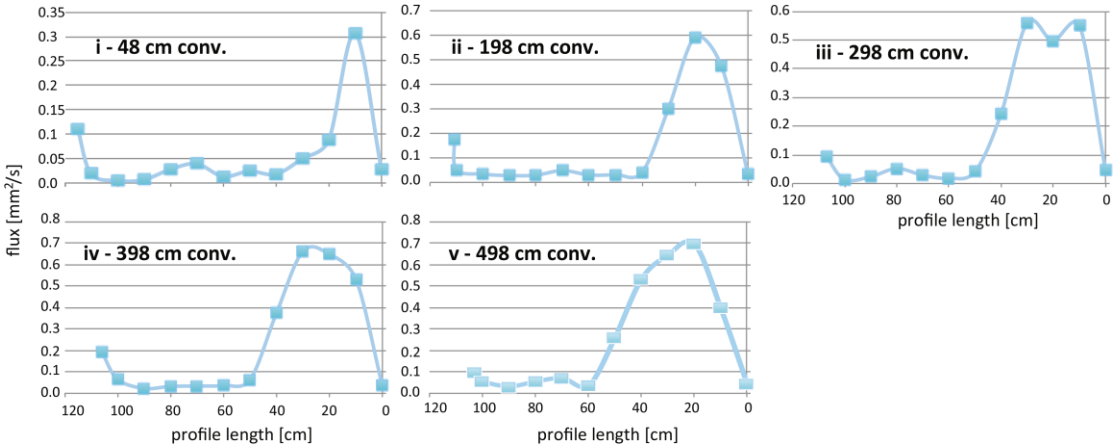

d)

Figure 5.1.4. *Horizontal component of the velocity field and b) Vertical component of the velocity field, as derived from figure 5.1.1 (yellow line at 4 mm and red line and 10 mm above the conveyor belt, respectively), during different convergence intervals. Velocity (horizontal component of the velocity field) distribution defines SC segmentation into Tip, Central and Back (see also Fig. 5.1.2). From slowest to fastest, this order: B, A and C. Notice the migration forward between one stage and the following. Characteristics of vector velocity field correlate with the vertical particle displacement (vertical component of the velocity field), providing a tool to localize specific mass flows, as erosion or underplating. D denotes the upward movement of the particles by activation of thrusts and numbers the active thrusts in figure 5.1.1. E denotes the upward displacement by underplating and F the downward displacement of the particles. The forward migration of F correlates with the migration in C. c) Subduction Channel thickness evolution for the reference experiment. d) i-v) fluxes of the SC at different stages of convergence. A decline of flux matches the thrust at the Back segment at 300 cm of convergence.*

The Middle segment subsided slowly, thus the middle slope basin began to be defined (e.g. Fig. 5.1.1iv). In general, high rates of mass transfer characterized this stage. Upward and downward displacements of the particles were bigger than in the next phase (cf. Fig. 5.1.4b.vi and viii) and flux was larger (cf. Fig. 5.1.4d.ii and iv).

The SC's Back and Tip segments experienced length variations. During this last stage of this phase the initiation of a long reactivation of thrusts at the Back segment is also observed. This process continues during the next phase (covered about from 260 cm of convergence until the first 28 cm of the next phase; 5.1.1iii and iv). The inner edge of the Tip segment moved backwards (Fig. 5.1.1). Tip and Central segments did not show any considerable variability of their width during this stage (Tip: ~5 mm and Central: ~4.6 mm, Fig. 5.1.4c).

(iii) The third phase

During this phase (from 300 cm of convergence on), rates showed more constant values than in the previous phase. For example, the rate range of basal accretion changed from ±7 cm^2/cm in the second phase to ±5 cm^2/cm in the third phase (Figs. 5.1.3). Basal erosion and basal accretion rates reach their lowest value with 8.6 and 0.0 cm^2/cm respectively (Fig. 5.1.3a). Figures 5.1.4b.vii and b.viii show that during this phase, "basal accretion" continued moving rearward and "basal erosion" forward, extending its horizontal width, until 450 cm of convergence. As a consequence, the "*Transition* area" became narrow until

almost the end of the third phase outlined as a vertical line (Fig. 5.1.1vi). After 450 cm of convergence, there was a reduction of the area affected by particles moving downward. This was not evident in the digital images (i.e. Fig. 5.1.1vi), as it was small.

The final SC thickness was established at the rear zone of the Back segment (~32 mm, Figs. 5.1.1iv-vi and 5.1.4c). During the beginning of this phase, the reactivation of thrusts at the back segment is clear (Fig. 5.1.1iv). New short reactivations also occur. An additional long reactivation of a thrust started around 436 cm of convergence, lasting until the end of the experimental run. Tip and Central segments maintained their widths (Fig. 5.1.4c).

The SC analysis of our experiments provides a tool that relates the different mass transfer processes to specific points along the channel. The velocity gradient field (or flow strain rates) shows measureable particle displacement. This provides us a tool to localize specific mass flow patterns along the SC, such as erosion or accretion.

Underplating occurred at the Tip segment because of the small overburden. It is displayed through the velocity field vectors by the decreases in the horizontal velocity component from the tip backwards (Fig. 5.1.2 Tip1 and Tip2). The small overburden required low shear traction to underthrust material (for further information see Section 5.3.4). Along with an increase of normal load, this part of the wedge underwent underplating and thickening. The inner edge of the Tip segment moved backwards by activation of a new thrust (Fig. 5.1.4a.i-iii and b.v-vii).

The Back segment became longer by the migration of the fast particles and the incorporation of material to the flux widened it quickly over time (Figs. 5.1.1iii-iv and 5.1.4c). The high rates of mass transfer during the second phase were mirrored by bigger upward and downward displacements of the particles (cf. Fig. 5.1.4b.vi and viii) and flux increased (cf. Fig. 5.1.4d.ii and iv). The less uniform behavior of v_x and v_y components during the same stage than in the subsequent phase, together with the extension of the horizontal width of the erosion area are connected to the faster forward migration of the particles and the larger rates for basal erosion.

During the third phase, the reduction of the area affected by particles moving downward (after 450 cm of convergence) is mirrored by a drop of the basal erosion rates (Fig. 5.1.3a). Consequently, the lower rates of the forward migration of the fast particles at the Back segment and rearward migration at the Tip were also observed (cf. Fig. 5.1.4b.vii and b.viii).

5.1.4 Quantification of the mass transfer modes

We found a relationship between the different mass transfer rates in the reference experiment (R0). Variations of frontal erosion, basal accretion and tip retreat values showed to be positively co-related, especially during the second phase. That is to say, there was a coeval increase and decrease in their rates (Fig. 5.1.3a). Nevertheless, basal erosion did not show a clear connection with the other mass transfers.

While the average of basal erosion grew three times faster than basal accretion, it was slightly higher than frontal erosion, achieving an equivalent of 53.6% of the total

material eroded (numbers in Fig. 5.1.3b).

5.1.5 Analysis of the horizontal vs the vertical component of the velocity field inside the SC

The base for the segmentation of the SC was the variations observed in v_x and v_y components, clearly defined in the reference experiment. The v_y component showed that velocities at the Tip were faster than along the Central segment while the Back showed faster velocities than the Central segment (i.e. Fig. 5.1.4a). The vertical positive or negative (i.e. upward or downward) displacement of the particles was linked to the largest absolute values of the horizontal velocity gradient (Fig. 5.1.4b). It is observed that the largest downward displacement of particles have two components, one in front of the fastest particles and another occurring at the rear, next to the backwall. Whenever a reactivation of fault occurs, downward displacement of particles is locally activated by block rotation over the reactivated roof thrust (Fig. 5.1.4b.vii).

These previous observations let us indirectly connect the basal erosion process with the kinematics of the SC roof thrust where the emergence of the thrust (where the highest incremental strain occurs, e.g Fig. 5.1.1iv) incentives the mass removal. The rear component of the downward displacement was not observed in the digital images due to its small area.

5.1.6 Flux of the SC through convergence

From Cloos and Shreve's SC concept (1988a), we know the critical factor IC/GC ratio defines SC behavior and thus wedge evolution (Section 2.2.3). At the front and rear of the wedges the values of the SC widths were influenced by the boundary effects. At the leading edge of the SC, both frontal erosion and accretion occur simultaneously with the continuous retreat of the toe, hence a precise location of the IC was problematic. This resulted in poorly constrained data for IC and similarly occurred with the GC values. Thus, we estimated the fluxes at different points not affected by the boundary effects. Fluxes (width of the SC times velocity) at different points along the SC were estimated, as the flow through a line perpendicular to the base of the wedge at specific distances from the backwall (Fig. 5.1.4d).

The results showed that at the Back segment, the flux before starting the second phase is low, increasing afterwards. Then, during the third phase, the flux remained approximately the same (Fig. 5.1.4d.i-iii and d.iii-v). Locally, at 280 cm of convergence the kinematics of the thrust controls the flow: behind the emergence of the reactivated thrust is expressed by a decrease of flux at that convergence (Figs. 5.1.4a.iii and d.iii at 20 cm profile length). At the emergence of the thrust the flux is increased (Fig. 5.1.4a.iii and d.iii at 30 cm profile length). Thus, activation or reactivation of thrust promoted basal mass removal locally.

5.1.7 The effect of the back wall boundary condition

In numerical and analogue simulations, the "extremes" or "boundaries" effects are one of the most problematic issues. In particular, the backwall is one of the most influencing restrictions in sandbox experiments. Previous laboratory experiments have introduced a "backstop" with a considerably stronger material than sand, to isolate the sand wedge from the backwall (Byrne et al., 1993; Kukowski et al., 2002; Gutscher et al., 1998a; Lohrmann et al., 2006). In the

present study, we built long wedges to avoid the effects from proximity to the backwall, thus for the structural analysis we focused on areas no longer affected by this (i.e. the Rear segment, Section 5.1.1). Herein, we discuss the role of the backwall, esspecially the effect from the SG (Fig. 4.1.1).

During the experiments, a forethrust in the rear part of the wedge was occasionally formed in some of the experiments (FT in Fig. 5.1.5). The material removed from the system promoted the formation of the localized shear zone that roots in a velocity singularity (Willet et al., 1993; S in Fig. 5.1.5). The reason is that the velocity of particles just before reaching the backwall was V=0, changing to the conveyor velocity $V=V_0$ ($V_0>0$) behind the wall. The rapid change in the strain rate within the layer is likely accommodated by a localized shear zone. This began at the bottom of the backwall, forming after ca. 100 cm of convergence in the ~50% of the cases (see Appendix A3), which will be discussed further in the corresponding sections (i.e. Sections 5.2.6 and 5.3.5).

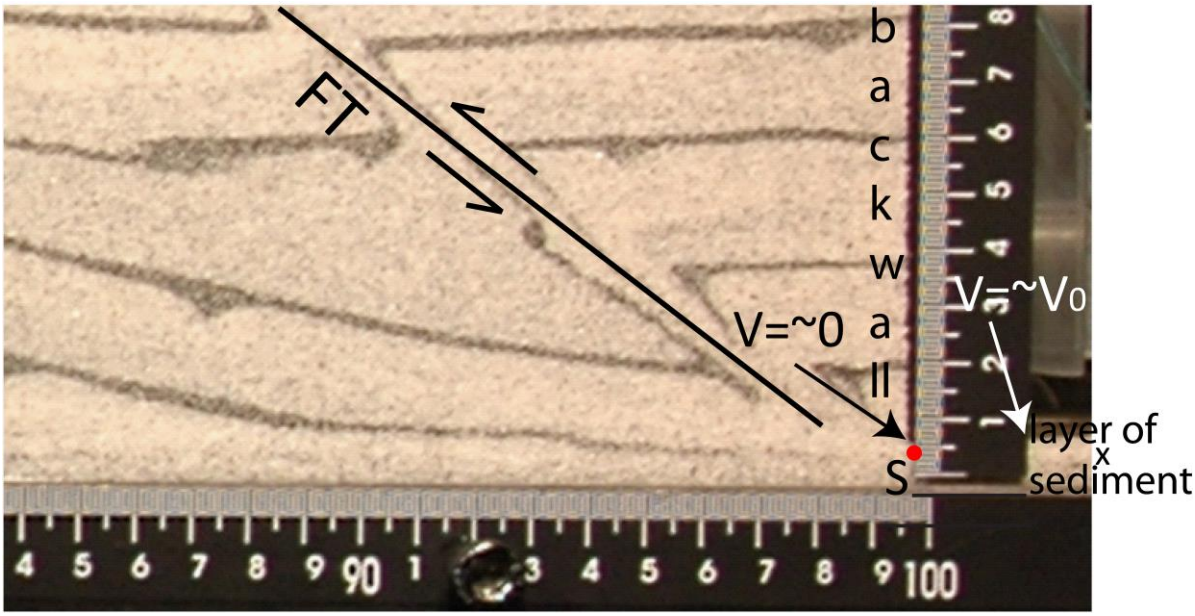

Figure 5.1.5. *The Singularity point indicated in red.*

5.1.8 Analysis and discussion of the role of the subduction channel evolution in erosional margins

How does erosion work and why does it occur in the places where it occurs?

The estimations of the dynamics and tectonic processes involved in subduction erosion to compare with the experimental wedges originate from natural observation and scaled physical as well as numerical models.

The concept of the "subduction channel" introduced by Cloos and Shreve (1988 a and b), might be able to explain tectonic growth or consumption of the cortical plate in forearcs (Beaumont et al., 1999; Ellis et al, 1999; Lohrmann et al., 2006; Cloos, 2006). However, the flux mechanics can only be speculated about theoretically, since no direct observation of the processes is possible. Seismic images and evidence

from the field reveal the shallower portion of the SC into the offshore forearc. A recent study described in detail the complete range of most probable characteristics along the SC as it goes downdip, until 15 km depth (Vannucchi et al., 2012). We discuss our results with those former studies and also analyze, what rests on the geometrical similarities between the laboratory and natural wedges.

Adam and Reuter (2000) and Clift and Hartley (2007) assumed a steady state evolution of the Chilean and Peruvian margins, respectively, ensuring the preferential subduction erosion also close to the trench of the continental wedge. The Peruvian case also shows slow uplift by underplating after 2 Ma below the coast. This, together with the almost stationary coast and the retreat of the deformation front, has probably steepened the wedge taper. Nevertheless, steepening cannot be indefinitely maintained as steady state and they present an intermittent development of the margin. Periods of enhanced basal erosion and no underplating are thus documented in the aforementioned contribution. Periods of slower erosion may alternate with times of faster erosion and trench retreat. Wang et al. (2010) also proposed a cyclical behavior for subduction erosion, being more or less favorable as a consequence of the seismic cycle and its phases (Section 2.2). From our experiments, the velocity field evolution over time and rates of mass transfer show that basal erosion is an irregular process, defined by different phases.

Studies from natural forearc examples with basal erosion indicate that accelerated midslope subsidence happens above the updip limit where interplate seismicity occurs (e.g. Laursen et al., 2002; Section 2.2). It is suggested that erosion would relate to the transition from aseismic to stick-slip behavior along the plate interface (environment of increasing interplate coupling). At the Central Chile margin, below the fastest subsidence zone, is where the transition to interplate stick-slip behavior occurs (or a place of increasing interplate coupling). This would indicate that basal erosional processes are accelerated near the transition (Laursen et al., 2002), similar to what was imaged in seismic data from the Costa Rica margin (Ranero and von Huene, 2000). The latter implies that at shallow depths, subduction erosion is less likely due to greater fluid content and hence, poorly coupled. In our experiments, basal erosion occurred mainly beneath the middle slope, controlled by the SC kinematics.

As Cloos and Shreve stated (1988b), subduction erosion occurs wherever the shear stress along the SZUB is sufficiently great. This is well displayed by the digital images from our experiments, where enhanced basal erosion is closely connected to where the highest shear stress occurs (Figs. 5.1.1 and 5.1.2). Thus, the digital images show evidence that the particle velocity inside the SC is not homogeneously distributed and that their different velocity patterns determine erosion or accretion locus (Fig. 5.1.2). In this case, the edge of the SC's Back segment should correspond to the updip boundary of the seismogenic zone.

At the surface, the transient Back segment behavior defined a segmentation of the slope of the wedge, with a decreasing angle arcwards, as observed in erosional margins (Section 2.2). Nevertheless, the middle and upper slopes in the experiments subsided not by discrete

shear zones (as in nature), but by distributed deformation. This was attributed to the intrinsic features of granular materials (for further details see Section 4.1.4).

The fast forward migration of the quick particles of the Back segment during the second phase, may connect with the proximity of the subduction gap. It may also correlate with larger rates of mass transfer than the next phase, expressed as a larger dip of the trend line (Fig.5.1.3b). The third phase had slower forward migration than the second phase. The variation of fluxes also connected with changes of phase (Fig. 5.1.4d).

Differences of the SC thickness might also be related to the lateral earthquake rupture propagation (Contreras and Carrizo, 2011). Likewise, longitudinal variations of the SC thickness might play a role in the seismicity distribution; however, this idea is beyond the scope of this study and must be developed further.

5.2 Material removal through a Subduction Gap aperture at the rear part of the wedge: the first series Subduction Gap (SG)

We used the same initial geometry for all experiments in the first series (Table 2). The parameter tested here was the width of the gap (termed Subduction Gap SG). We have the reference experiment named as R0, the second experiment named as G2 and the third experiment labeled G1. Lifting the backwall 2 mm in G1, 4 mm in G2 and 6 mm in R0 (scaled to 200, 400 and 600 m to nature) controlled the thickness of material leaving the system through the SG.

5.2.1 Kinematic evolution of three erosional wedges with different subduction gaps during the different phases

(i) The first phase

During the first stage all experiments of the series developed in a similar way as previously described for the reference experiment. There were no localized shear zones at the frontal domain of the wedge during this phase. The rates of tip retreat and frontal erosion were similar between experiments. Basal erosion rates dimished if SG decreased.

Widths of the Tip and Central segments were similar in experiments G1 and G2 (~5.5 mm and ~5 mm). Length and width of the SC's Back segment varied from experiment to experiment. The G1 Back segment reached a width of ~4 mm. The reference experiment R0's Back segment lengthening was slower than G2's but its maximum width reached a higher value (17 mm and 14 mm respectively).

(ii) The second phase

During the second phase, the range of the rates and the upward and downward displacement of particles were the largest of the whole convergence (Fig. 5.2.1a and 5.2.2). While the largest range of the rates accounted for frontal erosion (experiments G1, G2 and R0, respectively): ±14.4 cm2/cm, ±17.3 cm2/cm and ±18.9 cm2/cm, the range of the basal accretion rate were ±12.1 cm2/cm, ±8.7 cm2/cm and ±7.2 cm2/cm and the range of the basal erosion rate were ±1.6 cm2/cm, ±8.8 cm2/cm and ±11.6 cm2/cm. (Fig. 5.2.1a). The largest accretion rate was observed in experiment G2 (for further discussion see Section 5.2.5), closely followed by the experiment G1. The basal erosion rates increased if the SG widened, reaching an almost null value for G1. The highest value of upward displacement by thrusting was for the experiment G2 (Fig. 5.2.2b.iii). The minimum values of upward displacement by thrusting dropped from experiment G1 to R0 along with the SG size (Fig. 5.2.2a.iii-c.iii). Upward displacement by underplating diminished if SG size increased.

The height of the SG partially controlled the SC thickness at its Back segment. The SC's Back segment in experiments exceeding 4 mm SG became wider and longer over time (Fig. 5.2.3). Experiment R0 had a faster forward migration than G2, in accordance with velocity of migration of the fastest particles. Shortly before 3 meters of convergence, the final SC thickness was established at the rear zone of the Back segment (~28 mm in G2, 32 mm in R0 and in G1 remained constant ~4 mm; Fig. 5.2.3). The Tip continued lengthening over time due to thrusting; G2 reached the longest and

R0 the shortest length (Fig. 5.2.2b.iii and c.iii).

As for the experiment R0, we related the large range of the rates with the large upward and downward displacement of particles (Figs. 5.2.1a and 5.2.2).

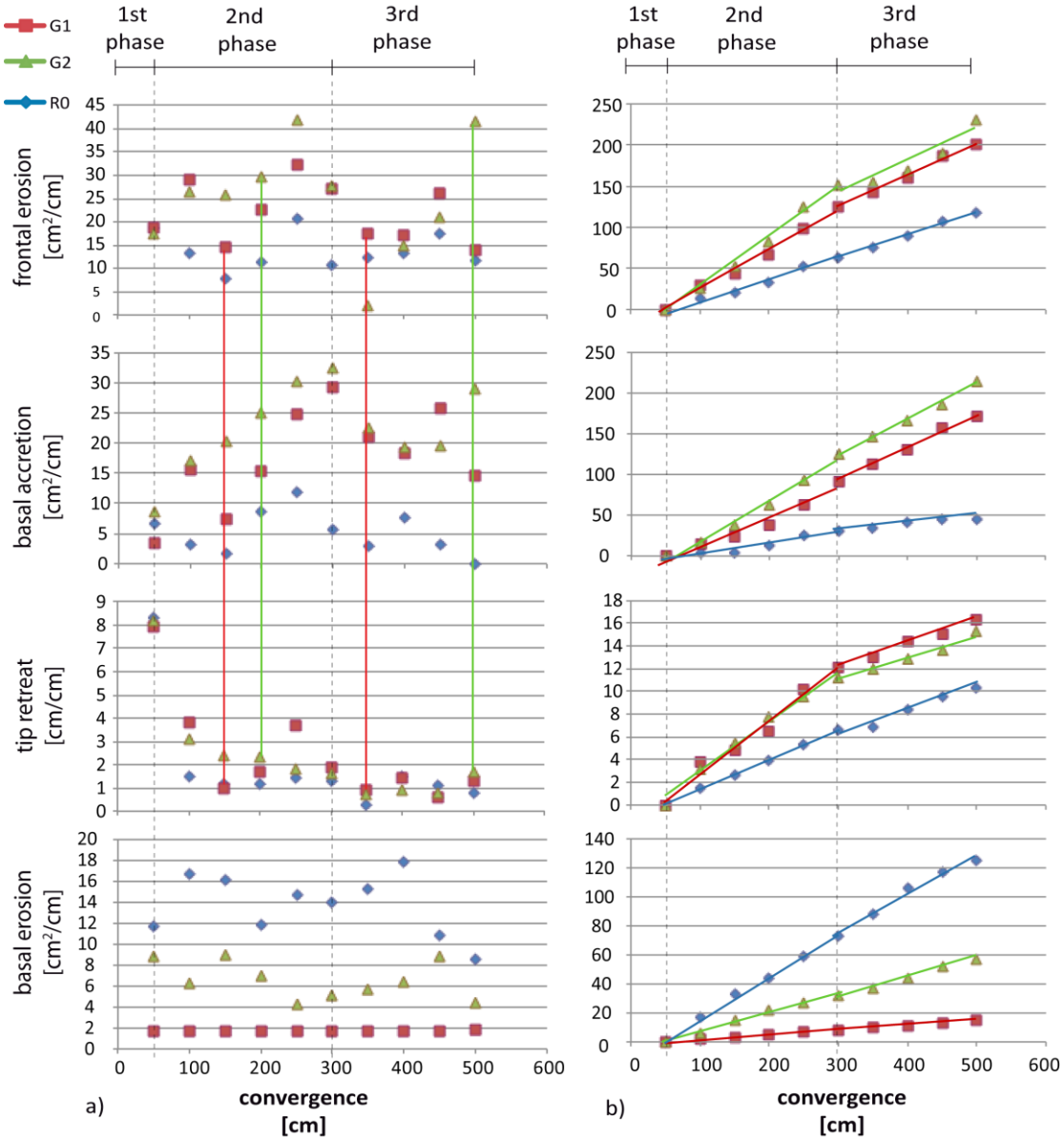

Figure 5.2.1. *a) Comparison of the different mass transfer rates of experiments of the first series SG while testing different subduction gaps, after the wedges deviated from the initial conditions. Different phases marked by variations on the rate patterns are specified. The coeval distribution of rates between frontal erosion, basal erosion and tip retreat is displayed by vertical lines with the same colors than symbols. b) Comparison between the different mass transfer volumes of the series. Quantities were normalized for direct comparison of volumes (initial values null at 50 cm of convergence). Note the slope variation after 300 cm of convergence of the trendline. Further discussion in Section 5.2.5.*

(iii) The third phase

The third phase showed a smaller range of rates than during the second phase, leading to rates with a more regular behavior and values of mass transfer volumes slightly smaller than in the previous phase (Fig. 5.2.1a and b respectively). As in the second phase, the largest range of the rates corresponds to frontal erosion and were more moderate for basal accretion and basal erosion (experiments G1, G2 and R0, respectively: ±12.1 cm^2/cm, ±25.6 cm^2/cm and ±5.8 cm^2/cm for frontal erosion; for basal accretion: ±11 cm^2/cm, ±9.9 cm^2/cm and ±4.8 cm^2/cm; for basal erosion: ±0.2 cm^2/cm, ±4.5 cm^2/cm and ±7 cm^2/cm; Fig. 5.2.1a).

In the experiment G2 a forethrust in the rear part of the wedge was observed after 350 cm of convergence (cf. Section 5.1.7 and 5.3.5), affecting mass balance in particular at the frontal segment of the wedge (namely frontal erosion and basal accretion rates).

Thrusting showed a similar trend in the third as in the second phase, in that the higher maximum value was observed for G2, followed by G1 and the lower maximum was for R0 (Fig. 5.2.2a.iv-c.iv). Their minimums decreased in accordance with the SG size. Upward displacement by underplating diminished if SG size increased and subsidence decreased if the SG width was reduced, reaching almost a null value for G1. Tip and Central segments showed no important variations in width in all experiments of the series (Fig. 5.2.3). The active backthrusts demarcated the onset of basal accretion, establishing in this way the longest Tip for G2 and shortest Tip for R0.

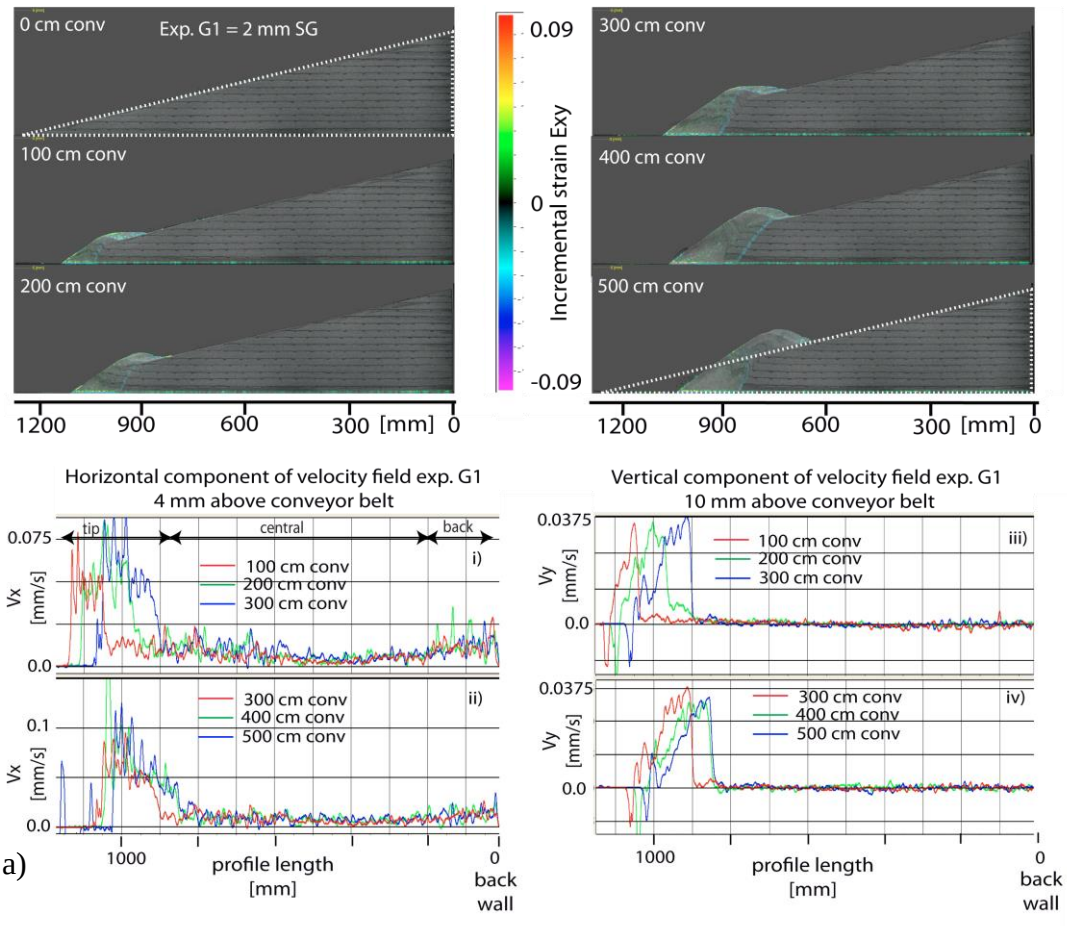

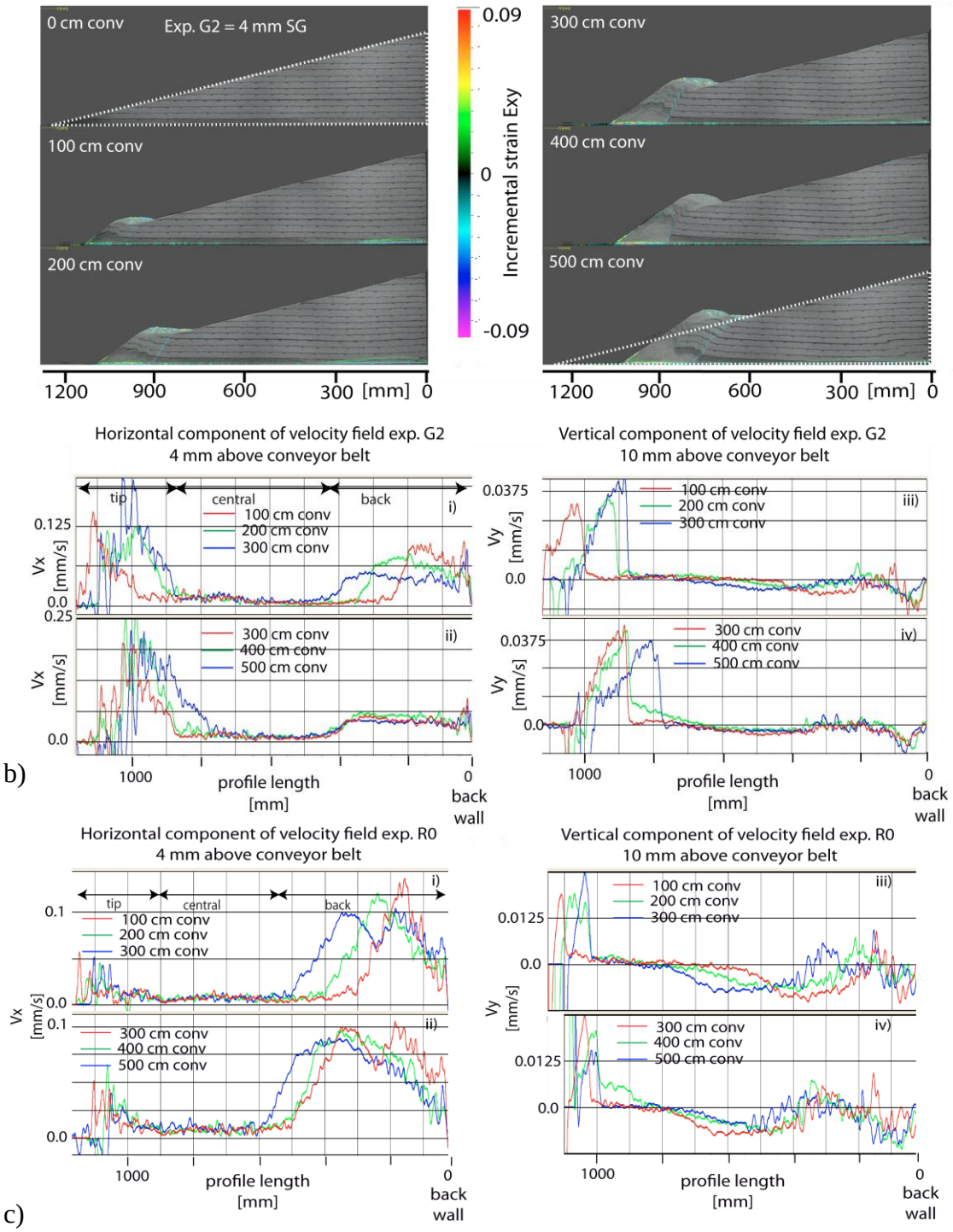

Figure 5.2.2. *Snapshots of experiments every 100 cm of convergence, for subduction gaps a) 2 mm, b) 4 mm, c) 6 mm, respectively. The corresponding particle velocity v_x and vertical displacement v_y of particles are directly compared (at 4 mm and 10 mm above the conveyor belt, respectively) for the second phase (upper plot) and third phase (lower plot). Different stages every 100 cm of convergence are represented by the sequential color order red, green and blue. Initial geometry of the wedge is compared with the last state geometry (dashed lines)*

Basal accretion values for experiments G1 and G2 were uniformly higher than for R0, which was correlated with the values showed by v_y in both experiments (5.2.1b and 5.2.2a.iv-c.iv).

5.2.2 Quantification of the mass transfer modes

Basal accretion, tip retreat and frontal erosion reached large and similar values for the narrowest and intermediate SG (Fig. 5.2.4). In particular, frontal erosion and basal accretion in experiment G2 were larger in comparison to G1, indicating that the SG parameter was not the only control on mass balance (for further details see Section 5.2.5). In addition, basal erosion and subsidence were shown to depend upon SG. As SG increased, erosion became more predominant than underplating. Particularly basal erosion led to noteworthy results. For the widest SG, the primary mode of erosion was basal, which comprised 53% more than the amount of material frontally eroded. The intermediate and narrower SG resulted in respectively ~18% and 4% of the total erosion.

5.2.3 Analysis of the horizontal vs the vertical component of the velocity field inside the SC

Velocities at the Tip were faster than along the Central segment. In comparison the Back segment showed faster velocities than the Central segment (i.e. Fig. 5.2.2b and c) in experiment R0 and G2. The velocities in the experiment G1 (i.e. Fig. 5.2.2a) remained similar for the Central and Back segments. This was linked to a lack of downward displacement of the particles (Fig. 5.2.2a). The components of the vector velocity field also documented the connection size of the SG – mass flux balance (Fig. 5.2.2). That is, small sizes of the SG matched fast velocities at the Tip. At the Back segment, velocities trend upward with the widening of the SG (Fig. 5.2.2a-c). The vertical (positive or negative) displacement of particles was observed to be linked to large values of horizontal velocity gradients (e.g. compare v_x and v_y components in Fig. 5.2.2c). Vector velocities at the SC's Back segment were faster when the SG was wide. Thus, downward displacement was larger in R0.

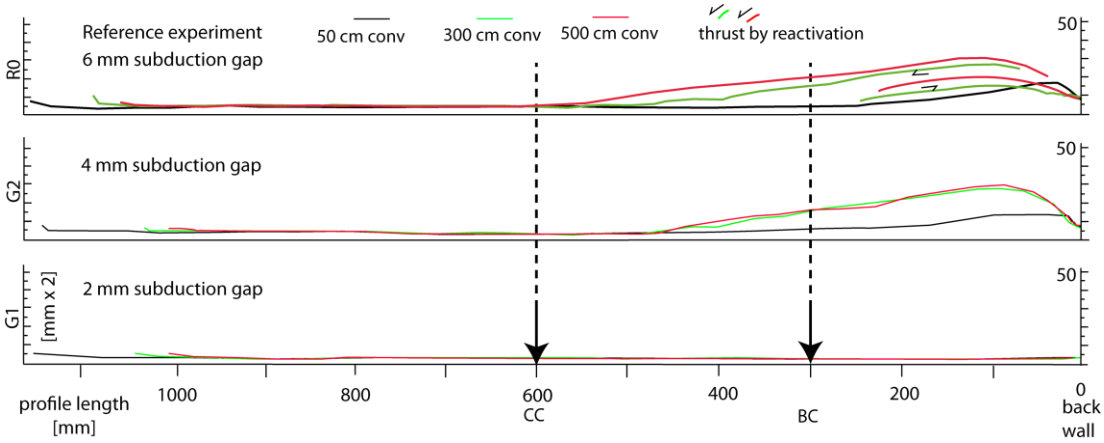

Figure 5.2.3. *Subduction Channel thickness evolution for the different experiments of the first series SG. CC and BC are points at the Central and Back segments of the SC, corresponding to distances at 600 cm and 300 cm from the backwall, respectively.*

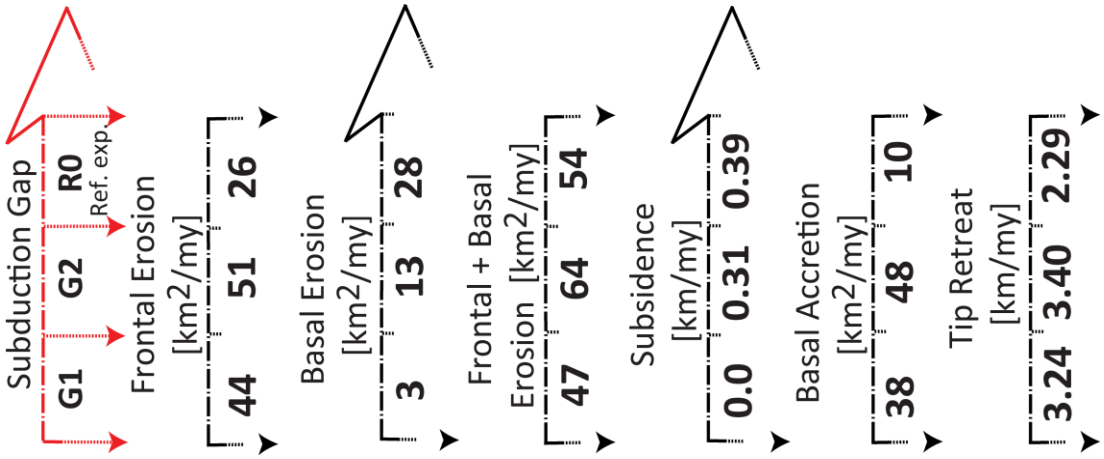

Figure 5.2.4. *Bulk mass transfer rates expressed as equivalent values in nature (km eroded/my) derived from the final values of the bulk areas/displacement during the second and third phases (after 50 cm of convergence). Arrow heads show the trend direction of mass transfer increments, where no clear trend is discernible no arrow heads are displayed.*

5.2.4 Flux of the SC through convergence

As described in section 4.3.2, both accretion and basal erosion added width to the SC, the first by adding material and the other by removing it. In order to compare fluxes among the different experiments of the series, two "strategic" positions along the SC were chosen. One point of the flow (CC = at 600 mm from the backwall; Fig. 5.2.3) was never affected by neither accretion nor basal erosion through convergence. The second point (BC = at 300 mm from the backwall; Fig. 5.2.3) was located where basal erosion occurred in order to see the effect of the size of the SG on the flux.

In experiments G1 and G2, the velocity of the sediment and width of the SC were similar at the point CC, while R0 had the widest SC with the slowest velocity. The resulting flux of the different experiments was similar, with a trend to increase over time (Table 4 and Fig. 5.2.5a). At the position BC, the forward migration of the Back segment started to impact on the SC's flux after 150 cm and 200 cm of convergence for experiments G2 and R0. Here the effect of the widening of the SG was clear, leading to an increase in the flux when the SG increased (Table 4 and Fig. 5.2.5b).

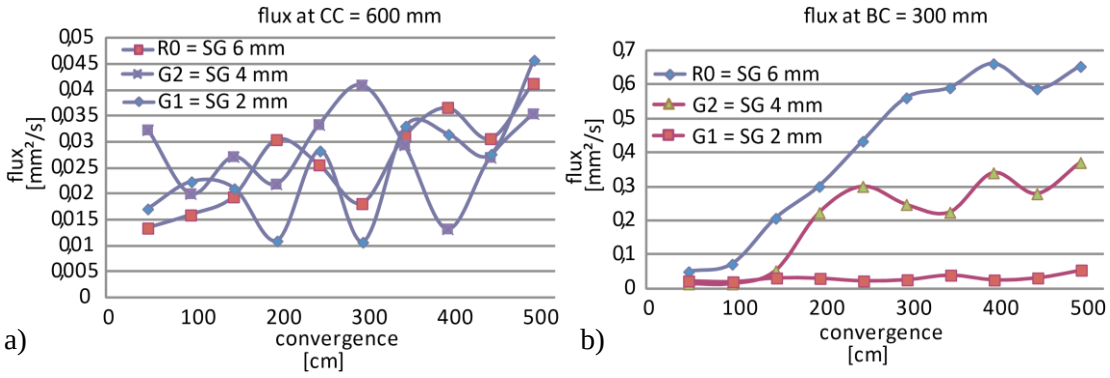

Figure 5.2.5. *Fluxes every 50 cm of convergence at a distance a) CC = 600 cm and b) BC = 300 cm from the back wall in series SG during the convergence (for location see Fig.5.2.3).*

Table 4. *Width and velocities at specific locations along the profile length during convergence, Widths and velocities correspond to the average of the different values every 50 cm of convergence during convergence, Numbers between brackets are the standard deviation, which become large by the seaward migration of the Back segment, that broadens the SC (see further explanation in section 5.1.2).*

	G1 = SG 2 mm	G2 = SG 4 mm	Ref. exp. R0 = SG 6 mm
SC width at Tip segment = TC [mm]	5,00	5,50	5,00
SC width at 600 mm = CC [mm]	2,58 (±0,5)	2,73 (±0,53)	4,60 (±0,77)
SC velocity at 600 mm [mm/s]	0,009 (±0,004)	0,010 (±0,003)	0,006 (±0,002)
SC width at 300 mm = BC [mm]	2,42 (±0,54)	6,55 (±3,3)	11,07 (±4,9)
SC velocity at 300 mm = BC [mm/s]	0,013 (±0,003)	0,03 (±0,013)	0,03 (±0,012)
Erosion ratio (basal erosion/frontal erosion)	0,07	0,25	1,08
TC / SG	2,5	1,38	0,83
flux at 600 cm =CC [mm/s]	0,023 (±0,012)	0,028 (±0,008)	0,026 (±0,009)
flux at 300 cm = BC [mm/s]	0,03 (±0,01)	0,207 (±0,13)	0,4 (±0,24)
Estimated IC [mm/cm conv]	4.4	5.1	2.6

5.2.5 The effect of the back wall boundary condition

The forethrust at the rear that was already mentioned (Section 5.1.7) was here observed as a response to large sizes of the subduction gap. The more material removed from the system, the more likely the formation of the localized shear zone. In experiments where SG ≥4 mm (as experiments R0 and G2), the forethrust was occasionally observed whereas with the thinnest SG in experiment G1, it was never initiated. In the experiment G2, this forethrust developed in a late state of convergence (Section 5.2.1), which led to high rates and final amounts of frontal erosion and basal accretion (Figs. 5.2.1 and 5.2.4). That may explain their counter-intuitively larger volume compared to experiment G1 and also their similar final amount compared with experiment R0.

Additional experiments also showed that with larger gaps (i.e. 10 mm), the forethrust occurred (see Appendix A3.2).

5.2.6 Analysis and discussion about the role of the subduction gap (or the global capacity) in erosional margins

(i) Analysis of the IC/GC role in basal erosion

The critical factor IC/GC ratio defines SC behavior and thus wedge evolution (Cloos and Shreve, 1988a). In the experiments, IC was influenced by the boundary conditions (see Section 5.1.4); consequently we measured and compared the TC/SG between the models. The TC value represents the mean width of the Tip segment and SG the subduction gap size.

Relations of TC/SG in the series (~2.5, 1.4 and 0.8 for G1, G2 and R0 respectively; Table 4) showed a dependence of frontal erosion on the TC/SG ratio. If TC<SG, frontal erosion was controlled by SG (case widest SG, R0 wedge) and if TC>GC, by TC (cases G1 and G2 wedges). This was depicted with high and similar final volumes of frontal erosion when TC/SG>1 and a major difference for TC/SG<1 (Fig. 5.2.4). Besides, a ratio TC/SG>1 was linked to low rates of basal erosion (Table 4). Figure 5.2.4 also showed a direct relation between

frontal erosion and tip retreat, that was additionally, controlled by the amount of basal accretion. Smaller values of basal erosion, controlled by the SG size, reflected lower subsidence at the middle and upper slopes, becoming almost zero for the narrowest G1's SG size.
Those segments of the SC not affected by the proximity to the backwall or the toe of the wedge (i.e. point CC) behaved similar and developed similar fluxes.

In our experimental wedges, the sediment supply at the inlet was smaller than the thickness of the sediment corridor measured in the experiments (Estimated IC and TC in Table 4), hence some material must be eroded from the overriding wedge. Less vertical load acting on the SC Tip requires lower shear traction. When the drag in the hanging wall is less than the critical value necessary to continue erosion, this part of the wedge should undergo underplating and thickness, exhibited by accretion. As it is exhibited in the erosional margin, our models show erosion at the base of the overriding wedge and simultaneously accretion at the frontal segment (von Huene et al., 1994; Heki, 2004).

Horizontal/vertical velocity gradient variations are well expressed in the experiments G2 and R0, which have wider back segments, and not noticeable in the experiment G1. Small variations in the horizontal component of the velocity field between the Central and Back segments in experiment G1 resulted in a nearly uniform velocity. Basal accretion was superiorly described by a thick Tip segment with a fast flux, compared with the neighboring Central segment. We correlated the faster velocities at the Tip segment in G1 and G2 in accordance with larger final amounts of frontal -erosion and -underplating (Fig. 5.2.4), evolving in a large "accretionary margin" type. Frontal material loss was immediately replaced, thus it never underwent neither basal erosion nor subsidence but underplating and uplift.

Comparatively, a larger amount of material loss led to the development of a SC with an inhomogeneous distribution of velocities along the base of the wedge, segmenting the SC and the slope geometry (further details in Section 5.1.8). In the Back segments of the experiments G2 and R0, the areas of active basal erosion were marked by the increment of the SC thickness and velocity of the flow compared with the neighboring Central segment. At the Back, the upward trend of the flux coupled with the SG size (Fig. 5.2.5), correlated with an increase of basally eroded material.

(ii) Comparison with former analogue experiments
Comparison between our experiments and previous physical analogue simulations confirm the significance of the rearward loss of material. Kukowski et al. (1994) results suggest that in a highly frictional environment, the ratio IC/SG must be >>1 for underplating to occur. Our first experiment series demonstrated that this is not necessarily true, as underplating became significant, whenever the relation TC/SG was somewhat larger than 1. Gutscher et al. (1998b) described in a series of high basal friction experiments "accretionary" wedges with steeper surface slope as well as periods with retreat of the deformation front and frontal erosion. Basal erosion from the backstop was only possible when the fraction of input material was smaller than the output. Our experiments with no incoming sediment and a subduction gap forced the removal of

material from the underside of the wedge toe. Unlike our experiments, in Gutscher's series the material was primarily eroded from the front by collapsing, but was very scarce at the base arcwards. Normal faulting and subsidence near the lower slope along with tilting was also observed, all typical features of natural erosional forearcs.

(iii) Comparison with nature

The concept of the "SG" or global capacity (Section 3.2.3) cannot be visualized with the current technology. However, with our experimental wedges, we were able to prove that small variations on its size strongly control a wedge's mass transfer.

The SG modified the thickness of the SC's back segment, which in turn controls the volume of eroded material. The largest SG was the only gap where subsidence rate was 0.4 km/my and the erosion ratio was larger than 1, as expected from nature (Fig. 5.2.4, Table 4 and Table 1, respectively). In nature, a wide SG may reflect an increment in the deflection of the subducting plate downward (von Huene et al., 1999; von Huene and Ranero, 2003), beyond the seismogenic zone. Erosional convergent margins are also associated with starved trenches, where a reduction of the sediment might reduce the deep underplated material. This may result in a larger arcward material transfer beyond the global point by "unblocking" it.

The segment between south of the Juan Fernandez Ridge and north of the Mocha block (~33-38°S) is characterized by little sediment supply, a thin SC (<1 km) and a relative wide frontal accretionary prism (20-40 km) (Contreras-Reyes et al., 2010). Our models were capable to develop considerable accretion at the frontal segment even without sediment input, which was controlled by the width of the SG. Consequently, a large accretionary prism in zones with little incoming sediment may indicate a small SG and the variations of SG size may control the transition from a forearc type G1 to R0.

5.3 Surface taper controlling evolution of forearcs: the second series Surface Taper ST

A variety of tapers can be found in natural convergent margins. An indication about the margin type (erosional or accretionary) can be relatively straightforwardly deduced from these, as larger tapers are usually associated with erosional margins, smaller ones with accretionary margins (Section 2.3). Taper variations should affect the Subduction Channel (SC), since the amount of material overlying the SC beneath a large taper is larger than for a shallow taper. Normal load was identified by Cloos and Shreve (1988b) as an important factor controlling rearward material loss. Later studies attempting to understand the effect of wedge thickness on forearc deformation were focused on accretionary systems (e.g. Gutscher et al., 1998a; Lohrmann et al., 2006). Herein, we systematically investigated the effect of differences in vertical load on mass transfer modes at erosional margins.

This experiment series comprised five wedges with different initial slope angles ($\alpha = 20°$ for experiment T5, $\alpha = 16°$ for experiment T4, $\alpha = 13.5°$ for the reference experiment R0, $\alpha = 10°$ for experiment T2 and $\alpha = 7°$ for experiment T1; Table 2). The wedges had heights of 45.6 cm, 35.8 cm, 30 cm, 22 cm and 15 cm at their rear part with a corresponding decreasing vertical load. Changes in the evolution of the slope and SC were the most significant difference among them. The generation or absence of a localized shear zone, which roots at the base of the backwall, controlled the dynamics of the different wedges composing this experiment series (e.g. FT in Fig. 5.3.1; see also Section 5.1.7).

5.3.1 Kinematic evolution of five erosional wedges with different surface tapers during the different phases

(i) The first phase

During the first phase, wedges T1 and T2 with smaller slope than the reference experiment R0 underwent a quicker and stronger retreat of the tip (23.8, 14 and 8.3 cm/cm, respectively; Figs. 5.3.1 and 5.3.2a). Additionally, large amounts of underplated sediment controlled initial frontal thrusting and deformation.

Experiment T4 has a similar retreat as the reference experiment R0 (8.9 cm/cm; Fig. 5.3.2a). A large amount of underthrusted material was also observed in this experiment.

The SC had a similar evolution in all experiments of the series (except T4), with a Central segment thinner than at the Tip, and a Back segment that extends and broadens over time. T4 did not show a clear basal shear zone, but only at its rear part (next to the subduction gap SG) material flux is notorious. In contrast, a thick SC (18 cm) forms, bounded above by an emerging out-of-sequence thrust and bounded below by the basal décollement (Fig. 5.3.1). We called this distinct entrained unit "SC unit".

(ii) The second phase

The rates of the experiment T1 were the most irregular compared with the rest of the experiments (e.g. basal accretion rates was in the range of ±14 cm^2/cm; Fig. 5.3.2). The rates of the experiment R0 trended similarly to experiment T5, showing a comparatively regular behaviour (rates for R0 were in the range of ±10 cm^2/cm and for T5 in the range of ±10.9 cm^2/cm; Fig. 5.3.2).

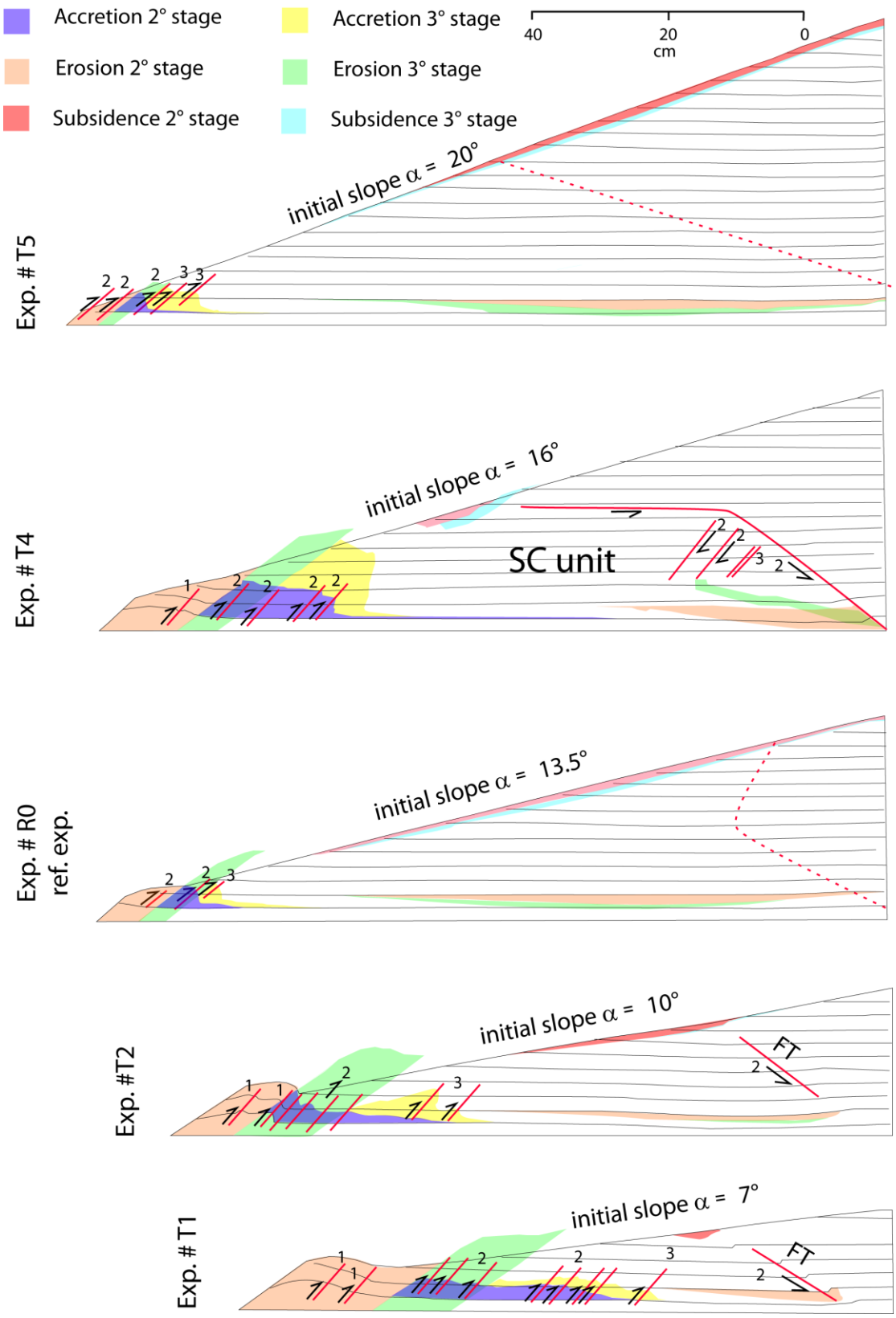

Figure 5.3.1. *Diagram comparing the amounts of material accretion and erosion and the loci of, subsidence and thrusting after 50, 300 and 500 cm of convergence. Numbers indicate phase of thrust occurrence. Red dashed lines separate domains where the marker lines deformed (lower domain) and where horizontal marker lines remained non-deformed (upper domain).*

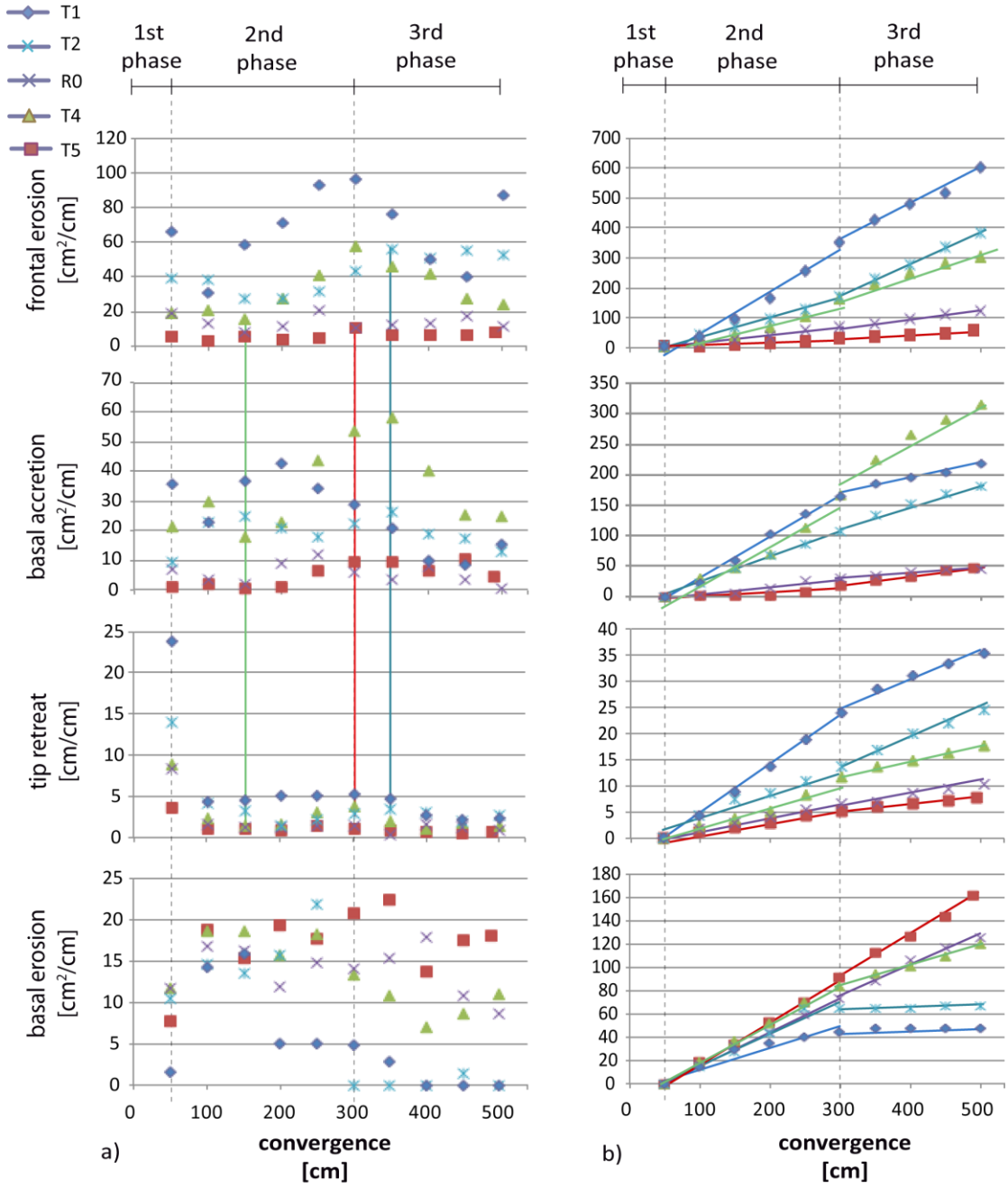

Figure 5.3.2. *a) Comparison of the different mass transfer rates of experiments of the second series ST while testing different surface slopes, after the wedges deviated from the initial conditions. Different phases marked by variations on the rate patterns are specified. The coeval distribution of rates between frontal erosion, basal erosion and tip retreat is displayed as vertical lines, whose color identifies experiments specified in the legend. b) Comparison between the different mass transfer volumes of the series. Quantities were normalized for direct comparison of volumes (initial values null at 50 cm of convergence). Note the slope variation after 300 cm of convergence of the trend lines, whose color identifies experiments specified in the legend.*

The downward vertical displacement of the particles in experiments T1 and T2 was controlled by the initiation of the forethrust FT. This means that shearing was not limited to the SZUB, but was partly accommodated by a forethrust of incidence angle ~38º for T2 and 26º for T1 (Fig. 5.3.1). A

considerable amount of displacement along the FT in experiment T1 manifested as a localized subsidence of the slope where the FT emerges at the surface. The greatest basal erosion rates consistently occurred during this phase for all experiments (Figs. 5.3.2). The highest basal accretion rate was reached in experiment T4 (43.5 cm^2/cm; Fig. 5.3.2), where accretion of material mostly occurred by thrusting (Fig. 5.3.3). The Central segment of experiment T4 shows values of v_x greater than in the rest of the experiments (where they were significantly smaller, close to 0 mm/s). In this experiment, the surface of the Middle-Rear segment maintains a nearly constant slope of 16°. Even though the slope does not show distributed subsidence, the v_y plots make evident downward displacement of particles at the Rear segment, close to the SG, by the activity of the localized shear zone. The largest downward displacement of particles occurs during this stage (e.g. 200 cm of convergence).

Upward and downward displacement of particles was significant in experiments during this stage (Figs. 5.3.3): the downward particle displacement values were large for all experiments (except T4), decreasing through convergence. In experiment T4, the maximum upward displacement of particles was constant over time, slightly smaller than for the rest of the experiments of the series, but covering a broader area.

While the largest maximum upward displacement of the particles occurred in the shallowest wedge T1, values for the experiments R0, T2 and T5 were slightly lower.
In experiments T1 and T2, the upward displacement covered a broader area than for the reference experiment R0 (Figs. 5.3.1 and 5.3.3a - c). Experiment T5 showed a similar amount of upward mass transport confined to the same areal extent as in the reference experiment R0 (Fig. 5.3.3c and e).
In experiments T1 and T2, larger amounts of underplated material and larger areas affected by thrusts were observed than for the reference experiment R0 (Figs. 5.3.1 and 5.3.3a - c).

The evolution of the SC showed important differences between the two thinner wedges T1 and T2 (which were similar), R0 and T5 (which were similar) and wedge T4. When the FT was active (until 250/270 cm of convergence for experiments T2/T1), the Back segment of the SC maintained a constant width of 7 and 10 mm at the back segment (Fig. 5.3.4). From the second phase on, experiments R0 had a wider thickness of the Back segment than T1 and T2. The widest Back segment of the series was formed by the experiment T5 (40 mm; Fig. 5.3.4), the longest one corresponded to the R0 experiment (Fig. 5.3.4).

In contrast, in experiment T4, a SC was not obvious, as the basal shear zone only developed at the rear, while the SZUB corresponded to the emerging out-of-sequence thrust (Fig. 5.3.3). The Back, Central and Frontal segments were only visible by the two components of the velocity field (Fig. 5.3.3d), which showed that the Back segment maintained a similar length over time. Consequently, "segmentation of the SC" in T4 did not evolve over time as for the rest of the experiments. In experiments with a taper angle larger than wedge R0 , this segmentation of the localized shear zone was observed in about every second experimental run (44% of all experiments, including those not

considered in this study;see appendix A3.2; see further analysis in section 5.3.5). Hence, the localized shear zone had a different geometry than for experiments with a taper angle lower than for wedge R0 (cf. Fig. 5.3.1 experiments T4 and T1 and T2). The "SC unit" (as defined in Section 5.3.1i) was subject to intense shearing and stretching as it approaches the subduction gap. The out-of-sequence thrust continued to be active, forming a scarp and a forearc basin at the middle-lower slope as this SC unit moved arcwards. The rearward displacement of the SC unit generated a strong shortening and frontal erosion, forming a prominent frontal prism (Figs. 5.3.1 and 5.3.3d). At the base of the Rear segment, the wedge was crosscut by backthrusts which accommodated the excess material where the SC width began to decrease (Fig. 5.3.1 and 5.3.3d).

Recurrence of thrust reactivation at the Back segment in experiments T1 and T2 was frequent. The Tip and frontal part of the Central segment (where underplating took place) underwent episodic thrust reactivation, widening the channel temporarily for both T1 and T2. Reactivated faults of the Tip and Central SC segments had a curved geometry. For the reference experiment (R0), repeated, short reactivation of small thrusts was observed. At the Back segment, a stably active and long thrust initiated during the last centimeters of convergence of this phase and continued into the next (Section 5.1.3; see Fig. 5.1.1iii and iv). Continuous sliding activity characterized the SZUB in experiment T4 (no thrust reactivation). For the experiment T5, active displacement along reactivated thrusts at the Back segment only lasted very shortly (~16 cm), occurring after about 100 cm of convergence.

The upper plot in figure 5.3.3d shows that in experiment T4, a Back segment does not migrate forward but rather rearwards, which explains its constant length.

Two groups of experiments can be discriminated fromthe observed distribution of frontal erosion and basal accretion rates, which correlates with localized or distributed deformation. The first group, composed by experiments T1 and T2, featured localized shear zones, which promoted localized subsidence and frontal erosion. The second group, composed by experiments R0 and T5, showed distributed deformation that promoted basal erosion and distributed subsidence along the middle slope. Basal accretion rates of experiments T5 and R0 were shown to be roughly similar, with rates of R0 sligthly larger. Experiment T4 also showed to be controlled by the distinctive deformation through the SC unit, behaving differently from the first and second group.

The above described differences were accompanied by remarkable contrasts in the rates of mass transfer modes, which appear to be strongly controlled by the initial geometry (Fig. 5.3.2a).
The large basal erosion rates during this phase (20.7, 18.5, 16.7, 21.7, 15.7 cm^2/cm maximum rates for T5, T4, R0, T2 and T1 respectively; Figs. 5.3.2), are consistent with the large downward particle displacement values (Figs. 5.3.3). In experiments T1 and T2, the larger amounts of underplated material and larger area affected by thrusts than for the reference experiment R0 were mirrored by broad areas covered by the upward displacement of particles (Figs. 5.3.1 and 5.3.3a - c).

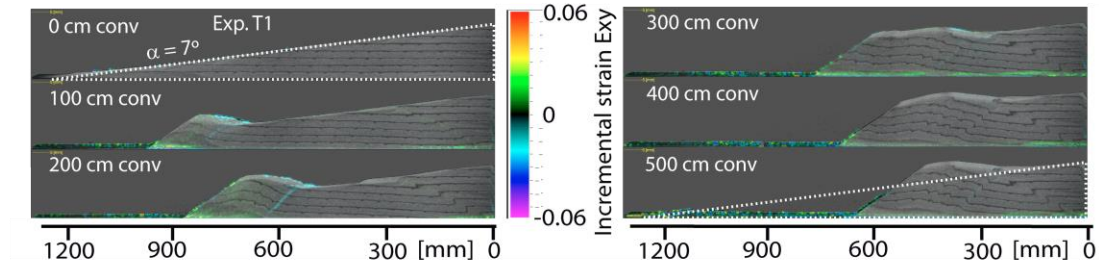
0 cm conv
Exp. T1
α = 7°
100 cm conv
200 cm conv
0.06
0
-0.06
Incremental strain Exy
300 cm conv
400 cm conv
500 cm conv
1200
900
600
300 [mm] 0

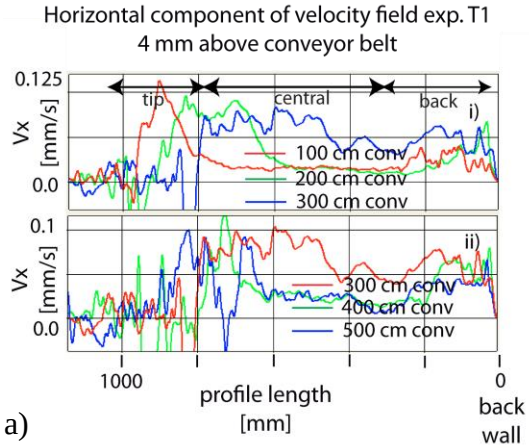
Horizontal component of velocity field exp. T1
4 mm above conveyor belt
0.125
Vx [mm/s]
0.0
tip
central
back
i)
100 cm conv
200 cm conv
300 cm conv
0.1
ii)
300 cm conv
400 cm conv
500 cm conv
1000
profile length
[mm]
0
back
wall

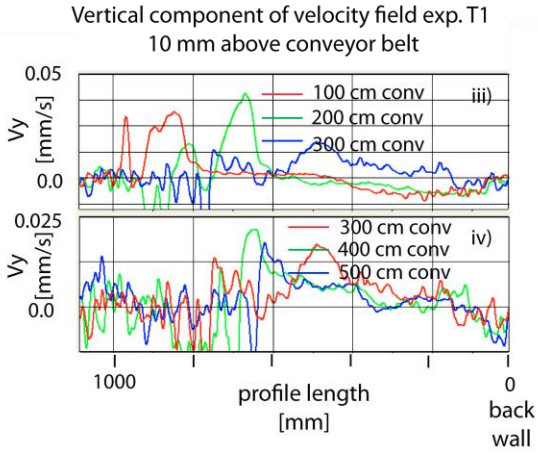
Vertical component of velocity field exp. T1
10 mm above conveyor belt
0.05
Vy [mm/s]
0.0
100 cm conv
200 cm conv
300 cm conv
iii)
0.025
300 cm conv
400 cm conv
500 cm conv
iv)
1000
profile length
[mm]
0
back
wall

a)

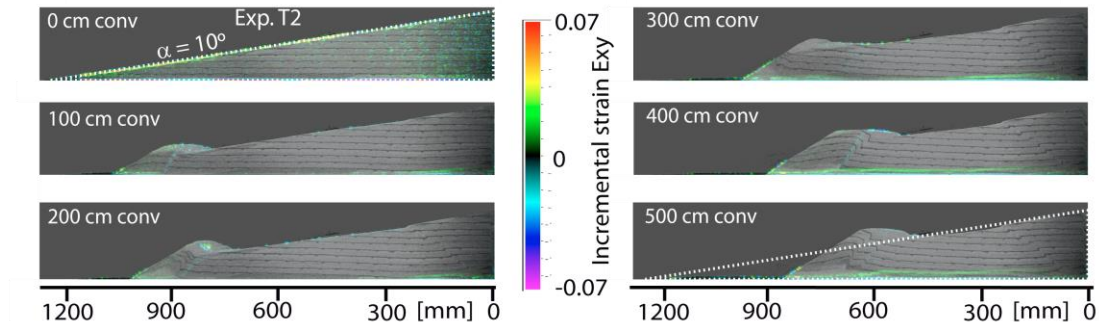
0 cm conv
Exp. T2
α = 10°
100 cm conv
200 cm conv
0.07
0
-0.07
Incremental strain Exy
300 cm conv
400 cm conv
500 cm conv
1200
900
600
300 [mm] 0

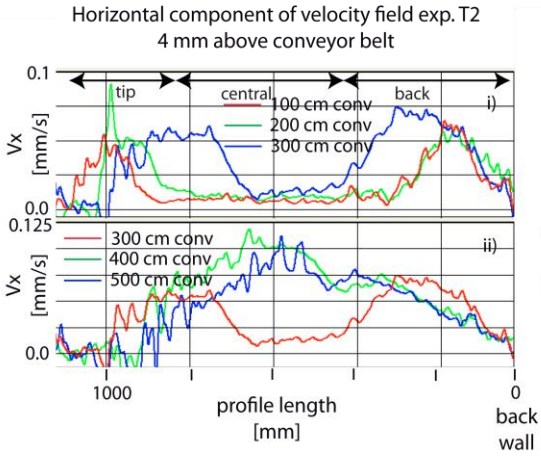
Horizontal component of velocity field exp. T2
4 mm above conveyor belt
0.1
Vx [mm/s]
0.0
tip
central
back
i)
100 cm conv
200 cm conv
300 cm conv
0.125
ii)
300 cm conv
400 cm conv
500 cm conv
1000
profile length
[mm]
0
back
wall

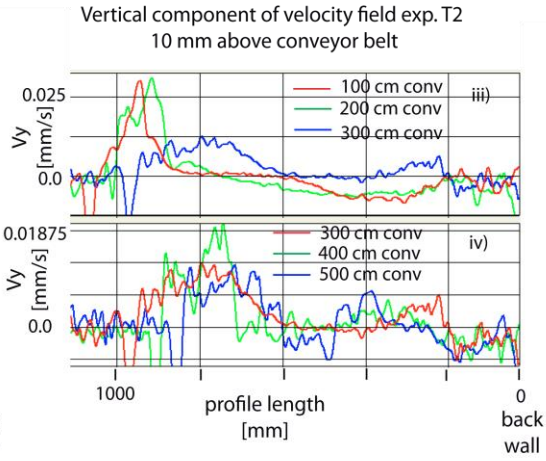
Vertical component of velocity field exp. T2
10 mm above conveyor belt
0.025
Vy [mm/s]
0.0
100 cm conv
200 cm conv
300 cm conv
iii)
0.01875
300 cm conv
400 cm conv
500 cm conv
iv)
1000
profile length
[mm]
0
back
wall

b)

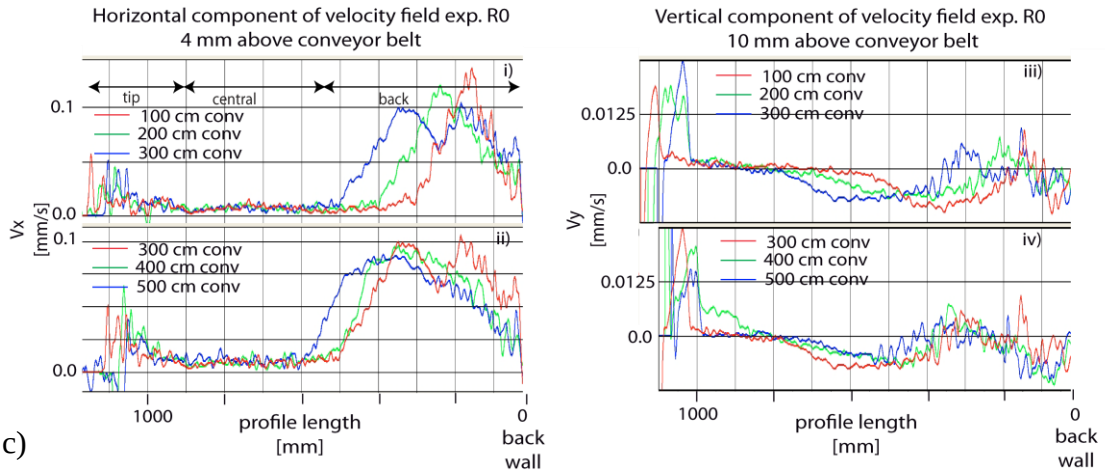
Horizontal component of velocity field exp. R0
4 mm above conveyor belt
i)
tip
central
back
100 cm conv
200 cm conv
300 cm conv
ii)
300 cm conv
400 cm conv
500 cm conv
Vx [mm/s]
0.1
0.0
1000
profile length [mm]
0
back wall
Vertical component of velocity field exp. R0
10 mm above conveyor belt
iii)
iv)
Vy [mm/s]
0.0125
0.0

c)

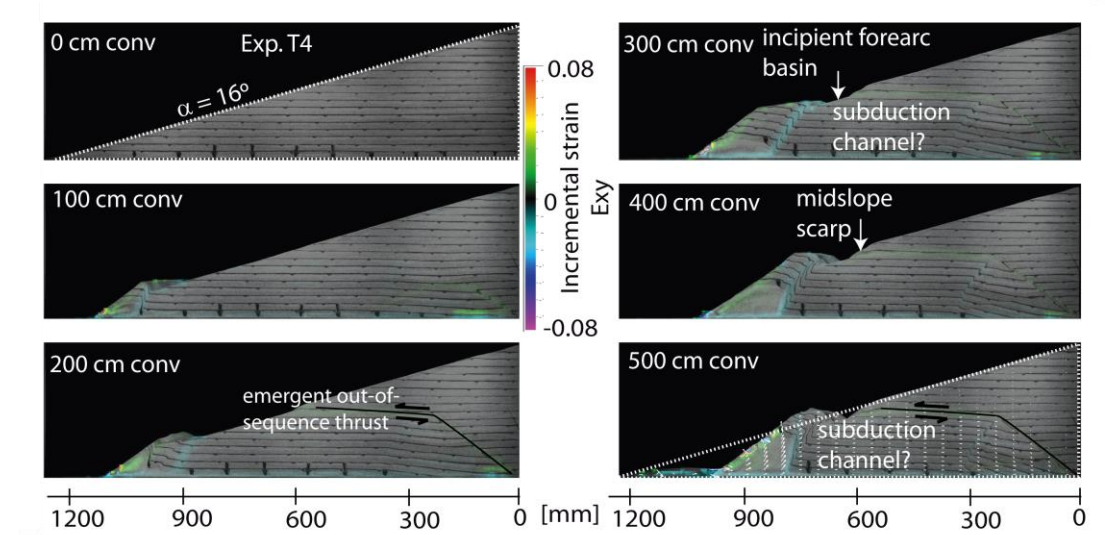
0 cm conv
Exp. T4
α = 16°
100 cm conv
200 cm conv
emergent out-of-sequence thrust
300 cm conv
incipient forearc basin
subduction channel?
400 cm conv
midslope scarp
500 cm conv
subduction channel?
0.08
0
-0.08
Incremental strain
Exy
1200
900
600
300
0
[mm]

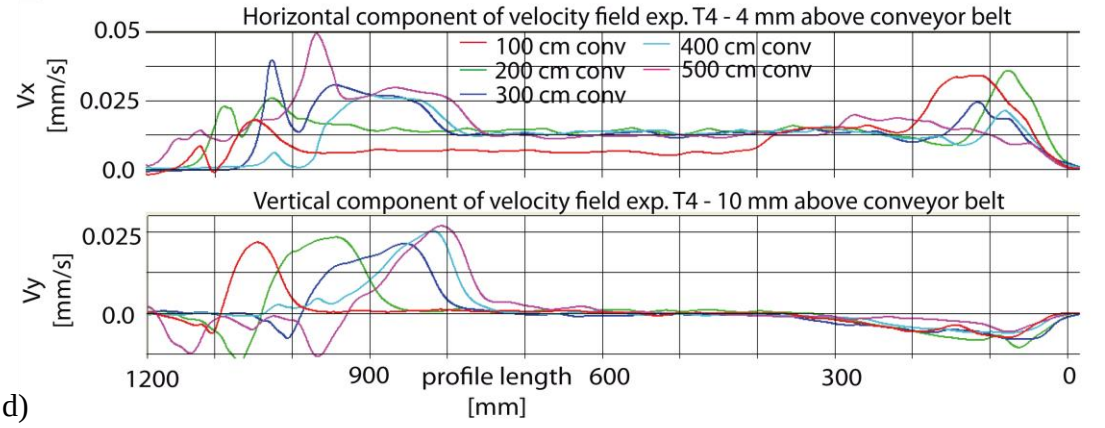
Horizontal component of velocity field exp. T4 - 4 mm above conveyor belt
100 cm conv
200 cm conv
300 cm conv
400 cm conv
500 cm conv
Vx [mm/s]
0.05
0.025
0.0
Vertical component of velocity field exp. T4 - 10 mm above conveyor belt
Vy [mm/s]
1200
900
profile length [mm]
600
300
0

d)

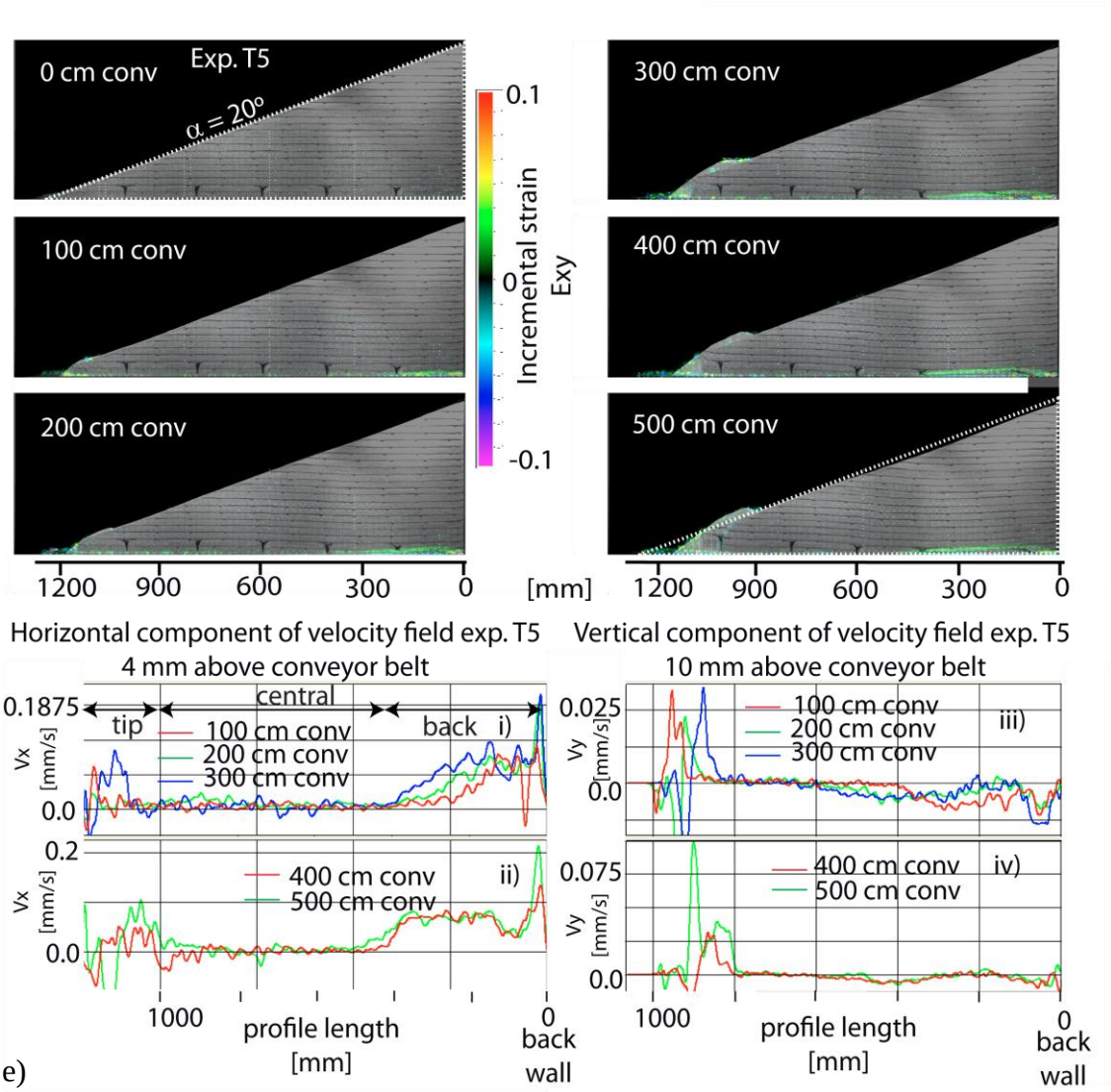

Figure 5.3.3. *Snapshots of experiments every 100 cm of convergence for initial slope angles a) α = 7º, b) α = 10º, c) α = 13.5º, d) α = 16º and, e) α = 20º respectively. The corresponding horizontal and vertical component of the velocity field (v_x, v_y) of particles are directly compared (4 mm and 10 mm above the conveyor belt, respectively) for the 2nd phase (upper plot) and 3rd phase (lower plot). Different stages every 100 cm of convergence are represented by the sequential color order red, green, blue, cyan and magenta. Initial geometry of the wedge is compared with the last state geometry (dashed lines). The vector velocity field is also displayed (Exaggeration: 80-fold) at the last stage of experiment T4. Inside the "SC unit" the velocity is constant, beneath a stable slope. The corresponding horizontal and vertical components of the velocity field of particles (v_x and v_y) are in the lower plot (at 4 mm above the conveyor belt).*

(iii) The third phase

During the third phase, the experiment T5 showed higher material accretion rates when compared with experiment R0 (Figs. 5.3.2). The highest rate of basal accretion occurred at the beginning (experiment T4, 58.8 cm^2/cm; Fig. 5.3.2a), after which it decreased together with the frontal erosion rates.

T1 rates were more uniform than in the previous phase (e.g. the range of basal accretion rate decreases to ±11 cm^2/cm). Observed frontal erosion rates for experiment T2 were somewhat more constant than for T1,

i.e. while the rate in T2 was in the range of ±12 cm^2/cm, for T1 it was in the range of ±47 cm^2/cm. Rates of mass transfer modes for R0 and T5 experiments exhibited lower values than the previous stage of convergence.

Similar to the previous phase, the rates of the experiment R0 and T5 were comparable (but smaller) in the range of ±7cm^2/cm and ±8.5cm^2/cm, respectively. Rates of experiment T4 were not regular, trending more similar to the T1-T2 group than to the R0-T5 group, especially considering frontal erosion and basal accretion rates. Experiment T4 continued in a deformation style similar to what was observed during the second stage, with a continuous gravitational collapse of the scarp and the formation of a forearc basin (Fig. 5.3.3). The surface of the Middle-Rear segment maintained the same geometry and slope, with a slight uplift above the scarp. The highest downward displacement of particles was observed in experiment T5, closely followed by R0, whereas experiments T2 and T1 showed almost none (Fig. 5.3.3). The upward displacement of particles reached its maximum during this phase, where their backward migration was slower compared to the second stage. Similar to the second phase, the upward displacement of the particles in T1 and T2 was small within a broad area.

The SZUB of the SC showed a similar geometry in experiments T5 and R0, with a wide Back segment and similar widths for the Tip segment, whereas the Central segment was thinner (~5 and ~3 mm respectively; Fig. 5.3.4). An important difference between both was the lateral growth of the Back segment. R0 showed a slow but uninterrupted forward migration of the frontmost and quickest particles of the Back segment. However, T5 maintained about the same length throughout the third phase. T1 and T2 showed a completely different behavior at the point where the Back segment "merged" with the Central segment, becoming "one unit". In contrast, the components of the velocity field (Fig. 5.3.3d) showed that the SC unit in experiment T4 reduces the Back segment width and length over time. The Central segment length was affected by the slow backward migration of the Tip segment.

The continuity of the SZUB was interrupted by reactivation of thrusts along the channel in some of the experiments. Continuous sliding activity was observed at the Back segment for the experiment T5, without any reactivation of thrusts. For the experiment R0, the thrust reactivated during the second phase continued its activity for the first 28 cm of convergence. New short reactivations were later observed (for further details see Section 5.1.3). As during the second phase, the recurrence of thrust reactivation at the Back segment in experiments T1 and T2 was frequent. The broad area showing frontal accretion controlled the SC geometry, especially its width at the Tip and Central segments. Thus, the geometry and widths of the SC varied, which explains the wider Tip in experiments T1 and T2 compared to experiments R0 and T5.

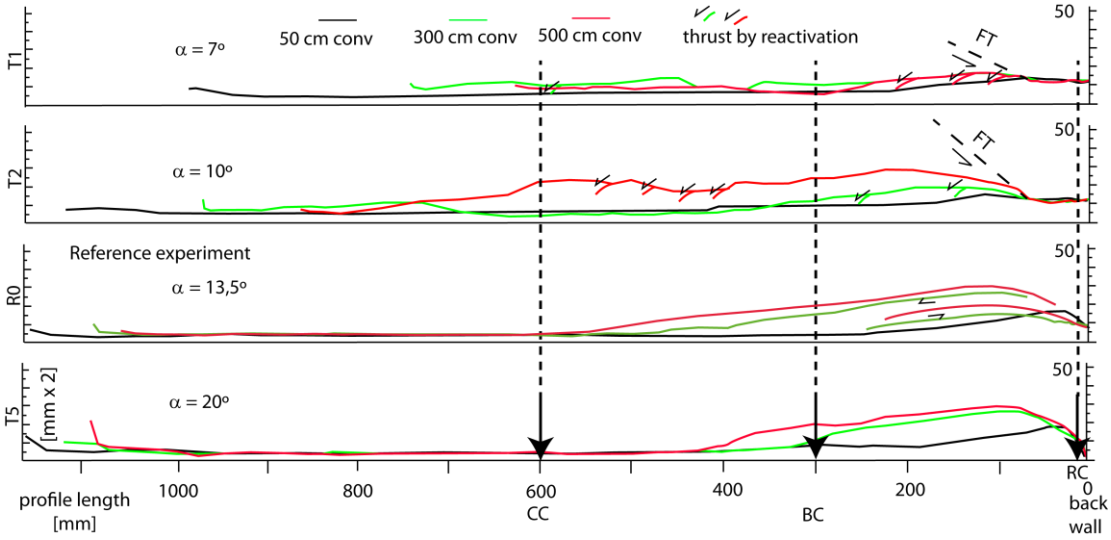

Figure 5.3.4. *Subduction Channel thickness evolution for the different experiments of the second series ST. CC, BC and RC are points at the Central segment, Back segment and at the rear of the SC, corresponding to distances of 600 mm, 300 mm and 11 mm from the backwall.*

5.3.2 Quantification of the mass transfer modes

The two groups of experiments discriminated based on the observed distribution of erosion rates (T1, T2 and R0, T5; see Section 5.3.1) are also represented by the behavior of the bulk rates.

Figure 5.3.5 shows that uniformly large values of basal erosion were retrieved if the initial slope angle was larger than 13.5º (i.e. the reference experiment taper). Basal erosion dominated frontal erosion by a factor of about three in the T5 wedge (see also Table 5). On the other hand, experiments T1 and T2, with an initial slope angle smaller than 13.5°, resulted in uniformly large values for the tip retreat and basal accretion. However, frontal erosion clearly grows with decreasing surface taper. Notice that in experiment T5 almost all frontally eroded material was underplated at the frontal segment, hence material basally eroded came mainly from the rear part of the wedge. This is also confirmed by the small flux at point CC in this wedge (Table 5).

The bulk values of frontal erosion, tip retreat, basal accretion and subsidence for experiment T4 were considerably higher than those for the wedges with slightly steeper and shallower slopes (R0 and T5). The amount of basal erosion was less than half of the frontal erosion, and basal accretion is larger relative to frontal erosion.

We noticed that for the thinnest wedges T1 and T2, the value of accretion is too large and thus is not representative of natural examples, because of their strong shortening component. Thus, ths results in an overestimation of frontal erosion, tip retreat and accretion, which will not be considered for comparison with data from nature (further discussion in Section 5.3.6).

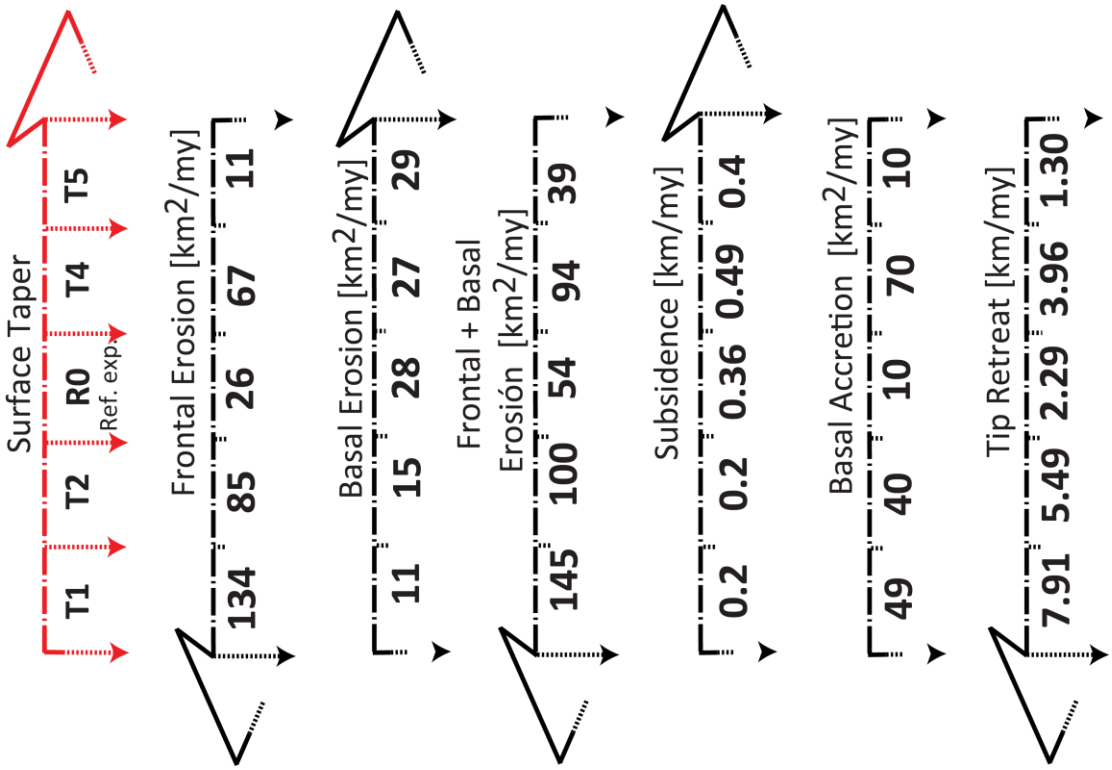

Figure 5.3.5. *Bulk mass transfer rates expressed as equivalent values in nature (km eroded / my) derived from the final values of the bulk areas/displacement during the second and third phases (after 50 cm of convergence). Arrows heads show the trend direction of mass transfer increments, where no clear trend isdiscernible, no arrow heads are displayed.. Notice that experiment T4 is represented by values which deviate from the general trend, due to its different structural evolution (for further details see Section 5.3.1 and 5.3.5)*

5.3.3 Analysis of the horizontal vs the vertical component of the velocity field inside the SC

Experiment T1 had a segmentation of the SC not clearly defined during the third stage (cf. Figs. 5.3.3a.iii and a.iv and 5.3.4). The segmentation was somehow clearer in T2 and even more so in experiments R0 and T5 (cf. Figs. 5.3.3b.iii-iv, c.iii-iv and e.iii-iv, respectively). Upward migration of particles confirmed the much narrower area along the frontal segment covered by R0 and T5 when compared with T1 and T2 (cf. Fig. 5.3.3c.i-ii and e.i-ii with a.i-ii and b.i-ii). During the third phase, in experiments with the FT, the activity of the forethrust was displayed by the downward displacement of the particles close to the backwall. In experiments not showing the FT, the downward displacement of the particles occurred in the Central segment (cf. Fig. 5.3.3a.iv and b.iv with c.iv and e.iv). The horizontal component of the velocity field in figure 5.3.3e.i shows the reactivation of a thrust at 100 cm of convergence at the Back segment in experiment T5 (cf. figure 5.3.3c.i). Additionally, the plots in figure 5.3.3 show a positive correlation between velocities at the Back segment with the normal load.

Deformation of experiment T4 localized the downward displacement of particles at the rear segment during the whole convergence (i.e. no forward migration). The fastest velocities were observed at the frontal segment, reaching the fastest values of the series. It was observed that a fast (or slow) displacement of particles at the

Table 5. *Width and velocities at specific locations along the profile length during convergence. Widths and velocities correspond to the average of the different values every 50 cm of convergence during convergence. Numbers between brackets are the standard deviation, which become large by the seaward migration of the Back segment (BC in experiment R0) or backward migration of the Tip segment (CC in experiments T1 and T2) that broadens the SC (see further explanation in section 5.1.2). Notice that for experiments T1 and T2 the point CC is affected by accretion of material (not occurring in R0 and T4), which increases the width of the channel and the values between brackets.*

	T1 = α 7º	T2 = α 10º	Ref. exp. R0 = α 13.5º	T5 = α 20º
SC width at 600 mm = CC [mm]	3,83 (±2,26)	6,52 (±4,2)	4,60 (±0,77)	2,26 (±1,24)
SC velocity at 600 mm = CC [mm/s]	0,03 (±0,04)	0,04 (±0,03)	0,006 (±0,002)	0,008 (±0,01)
SC width at 300 mm = BC [mm]	5,47 (±2,32)	7,34 (±4,25)	11,07 (±4,9)	10,51 (±5,97)
SC velocity at 300 mm = BC [mm/s]	0,02 (±0,01)	0,03 (±0,02)	0,03 (±0,012)	0,006 (±0,01)
SC width at 11 mm = RC [mm]	11,71 (±3,19)	20,58 (±1,15)	21,16 (±5,59)	18,42 (±3,34)
SC velocity at 11 mm = RC [mm/s]	0,024 (±0,005)	0,024 (±0,005)	0,027 (±0,006)	0,038 (±0,008)
Erosion ratio (basal erosion/frontal erosion)	0,08	0,18	1,08	2,63
flux at 600 mm = CC [mm/s]	0,19 (±0,2)	0,36 (±0,37)	0,026 (±0,009)	0,020 (±0,02)
flux at 300 mm = BC [mm/s]	0,07 (±0,04)	0,03 (±0,029)	0,41 (±0,24)	0,066 (±0,06)
flux at 11 mm = RC [mm/s]	0,28 (±0,10)	0,5 (±0,12)	0,54 (±0,12)	0,71 (±0,24)

Back segment was compensated with a slow (or fast) one at the Tip, i.e. as vx at the Tip increases, it decreases at the Back segment over time. The horizontal component of the velocity field from SZLB to SZUB at the central segment was spatially constant and showed higher velocities than the rest of the experimental wedges of the series (i.e. 0.0125 mm/s vs ~0.002 mm/s; cf. Fig. 5.1.2 and 5.3.3 at 500 cm of conv.). At the Tip and Back segments, v_x reached similar values and almost twice as high as for the Central segment, where they were significantly smaller than for the rest of the experiment series (~0.025 mm/s vs >0.05 mm/s).

The previous paragraphs show that the vertical load controlled the behavior of the SC, modifying their velocities and geometry between the experiments.

5.3.4 Flux of the SC through convergence

Estimates of the average flux through the SC near the rearward end of the box (point RC, Fig. 5.3.4) showed an increase of the flux with increasing normal load. This resulted in a cumulative flux in experiment T5 that was about twice as fast as T1, while R0 and T2 showed a similar final value (Fig. 5.3.6 and Table 5). The bigger average flux closer to the frontal segment in experiments T1 and T2 compared with R0 and T5 (points CC in Table 5; Fig. 5.3.4) is a result from the widening of the Tip segment. At this point in T5 the flux is the lowest of the series, as expected from its similar values for frontal erosion and basal accretion (Table 5).

We interprete that these SC kinematics are intimately linked to the gravitational force acting upon the SC. Depending on the overburden, the required work to underthrust the layer of sediment (SC) would control the frictional resistance along the SZUB.

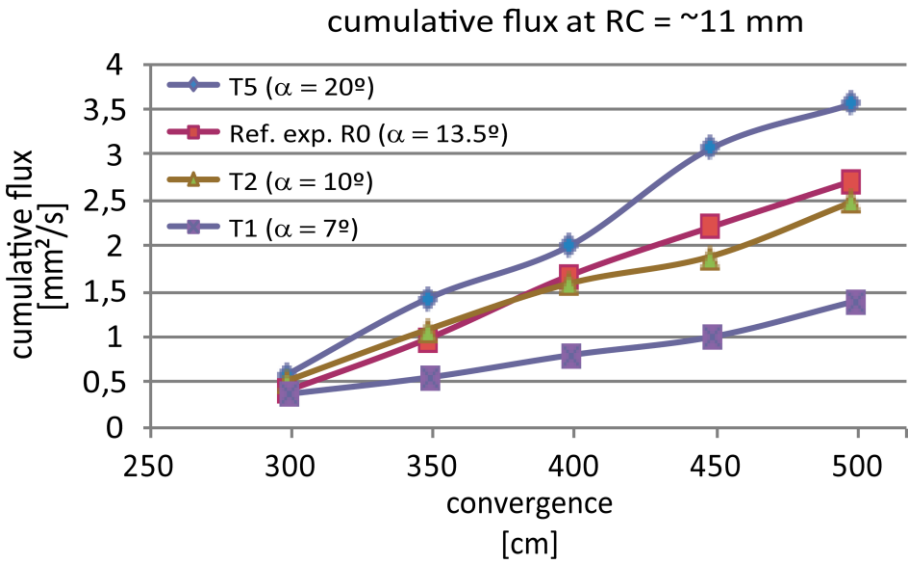

Figure 5.3.6. *Fluxes every 50 cm of convergence at point RC (11 mm from the backwall; for location see Fig.5.3.4) in the second series, after300 cm of convergence.*

The frictional force directly increases along with the normal load (frictional force = μ_{SD} Force). We estimated the normal load along the base of the wedge with the different initial geometries of the wedges. We can calculate the work W required to underthrust an amount of sediment defined by the force F acting along a distance d as:

$$W = F\ d$$

Thus, the work required to underthrust material for a fix distance is proportional to the normal force.
Figure 5.3.7 shows that the work required to underthrust material for a distance of about 35 cm in the experiment with the shallowest wedge T1 is the same as what is necessary to underthrust about 20 cm for the steepest wedge (Fig. 5.3.7b). This allows us to associate the differences of forces acting upon the SC with the strong differences of mass transfers and SC behavior for both end-member experiments T1 and T5: the large amount of underthrusted material, larger horizontal component of the velocity field and larger tip retreat in T1 compared with that occurring in the T5.

The segmentation of the slope in our wedges made clear which of the spatial variations of the mechanical properties controlled deformation. In turn, for experiments such as T1 and T2, the material supply exceeded the capacity of the channel. As a result, a broad frontal prism formed (compared to the small frontal prism in experiments R0 and T5).

5.3.5 The effect of the back wall boundary condition

As discussed earlier (Section 5.2.5), a first condition for the occurrence of the forethrust was connected with the size of the aperture at the bottom of the back wall (subduction gap > 4 mm). In this series, the occurrence of the

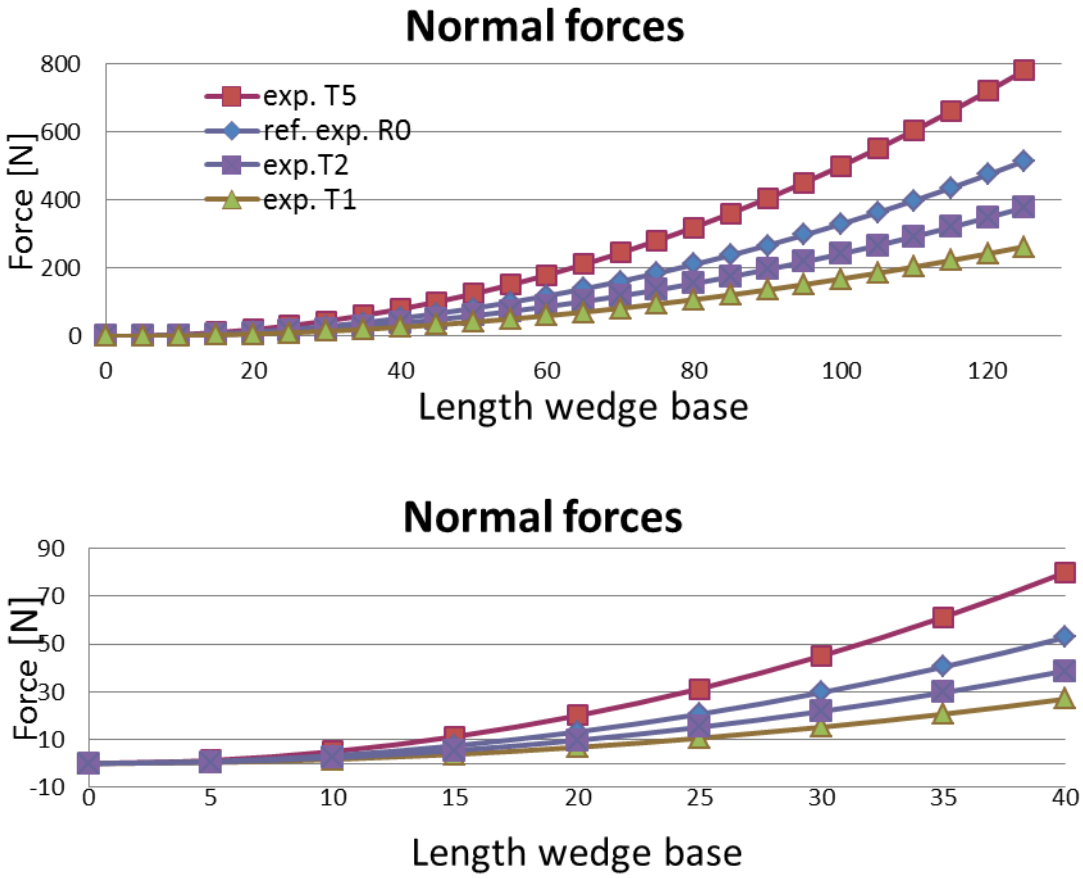

Figure 5.3.7. *Forces acting upon different points along the wedge base as a function of the length wedge base. They are proportional to the required work to underthrust a layer of sediment. Left side shows the first 40 cm from the tip arcwards.*

forethrust FT varied from experiment to experiment. In experiments with shallow wedges, as T1 or T2, the forethrust was always observed, whereas its appearance was less probable when the initial slope angle was larger than 13.5° (in the latter case, the FT occurred in~44% of the experiments; Appendix A3.2). The presence of this fault facilitated frontal erosion but diminished erosion from the underside of the wedge, as observed in experiments T1, T2 and T4 (Figs. 5.3.2b and 5.3.5).

When the FT occurred, the distance from the backwall to the point of thrust emergence varied substantially with the initial slope angle. Smaller slopes than 13.5º showed a straight line (FT), whereas for larger slopes, the initially straight line curves after reaching a certain height, developing as an out-of-sequence thrust. The relative height between the base of the wedge to the point of emergence of the thrust remained roughly constant (cf. experiments T1, T2 and T4 in Fig. 5.3.1).

5.3.6 Analysis and discussion of the role of the surface taper in erosional margins

The initial geometry of the wedges is indicated in figure 5.3.8a, which shows the initial state of stress of the wedges (see Fig. 3.1b), with regard to the frictional strength values. The states of stress over time were controlled by the variable behavior of the SC, whose kinematics defined the temporal

frictional strength of its different segments (Tip, Central or Back).

Theoretically, the initial geometry of experiment T5 is in a stable state. The experiment T4 has a geometry which classifies it as stable for the stable static frictional value and subcritical for the stable dynamic value. The reference experiment R0 is situated very close to the critical state for the stable static frictional value, whereasit is subcritical with regard to the stable dynamic value. . The experiment T2 is shown to be stable for the peak frictional value and subcritical with regard to the stable dynamic and static values. The experiment T1 is subcritical. As experiment T4 showed a different SC geometry during its evolution compared to the other experiments of the series, it will be described separately.

(i) Stability of the experiments and role in basal erosion

During ongoing deformation, the different fault kinematics in the different domains of the wedges illustrate their corresponding values of frictional strength (peak, stable static or stable static; see Section 4.1.2).

The Frontal segment of the wedges oscillated between two states of stress (Section 3.1). The continuous formation of backthrusts indicated that this segment was dominated by the peak strength, thus its states of stress were defined by the widest stability diagram (Fig. 5.3.8a). Additionally, the geometry of the slope varied over time to accommodate the underplated material, defining its subcritical state. At its leading edge, the surface slope reached the angle of repose (~39º). Therefore, this steep frontal slope underwent frontal erosion by episodic slumps, and an extensional or supercritical taper better defines this domain of the Frontal segment. In the reference experiment (R0) during the last 70 cm of convergence the creation of new shear zones and hence the accretion of material stopped. Thus, the geometry of the frontal slope remained constant, indicating a steady state.

In contrast to the frontal segment of the wedge, the Middle domain showed more complex and transitional states of stress. They were inferred from the sub parallel shear zones defining the SC Central and Back segments, both affecting the Middle segment deformation (Section 5.3.1). When the activity along the SZUB was continuous, the more appropriate internal friction corresponds to the stable dynamic ($\mu_i = \mu_{SD}$; Table 3; Section 4.1.2i). In this case, the stability field is defined by the thinnest diagram (Fig. 5.3.8a). When sliding along the SC alternated with reactivation of faults during the experimental run (e.g. Fig. 5.1.1iii and iv), the frictional strength is described by the stable static friction of the sand ($\mu_i = \mu_{SS;}$ Section 4.1.2i). In this case, the stable field widens, decreasing the critical taper (Fig. 5.3.8a). When the SC migrated upward by new thrusting or seaward by widening of the back segment, the frictional strength is better described by the peak friction (Section 4.1.2i).

In the experiments, the reactivation frequency of faults declined with increasing α. Therefore, more frequent switching between continuously - active faults and the reactivation of faults in the SC Central and Back segments was observed for experiments T1 and T2. The Central segment in T1 and T2 migrated upward by new thrusting (especially during the third phase) and later by reactivation of faults (Section 5.3.1; Fig. 5.3.4). The strength of the material

in case of new thrusting is controlled by the peak friction (or widest stability diagram) and in the case of fault reactivation by the stable static friction (or stable static curve). Analogously, the seaward migration and widening of the Back segment were controlled by the peak friction (or widest stability diagram).

On the other hand, reactivation of faults was more recurrent and covered a longer period of activity in the reference experiment (R0) than for experiment T5. There was only one reactivation during the second phase and none in the third in experiment T5, but in the reference (R0) they occurred during the second and third phases (see Section 5.3.1). Hence, the Middle domain of the wedges of this experiment series was described by the alternation of the three stability states defined by the peak, dynamic and static frictions (Fig. 5.3.8a).

The removal of material from the wedge's base in the experiment series evoked two distinct patterns of deformation, eithe distributed or localized deformation. Where this occurred, at the Middle and Rear segments, the appareance of the FT or out-of-sequence thrust governed the structural evolution of the wedges. The position of emergence of this thrust along the slope varied with the angle of the slope. Thus, the change in emergence at the slope appears to be controlled by the surface taper of the wedge and the value of internal friction defined by the SC. A second condition is related with the SC behavior. The middle slope wedge stability will depend on the temporal internal friction value for the SC, the only localized shear zone in the Middle segment. For experiments under the same initial conditions, we did not observe systematic patterns of the thrusts of the SZUB in order to predict the occurrence of the forethrust. However, we did observe that the observation of the out-of-sequence thrust is connected with SZUB behavior. Hence, depending on the fault kinematics and geometry of the slope, one of the three different values for frictional strength defining the stability diagram has been considered for the analysis.

In experiments R0 and T5 the removal of material from the base led to a slow subsidence and slight reduction in the slope angle (Fig. 5.3.1), thus to the retention of a relatively stable geometry. Internally, the resultant deformation of the middle segment of the wedge featured two domains. The upper part of the Middle segment stably subsided, which was also observed at the rear segment of the wedge. In contrast to that, the lower part of the Middle segment showed internally distributed deformation by the basal mass removal as slides (cf. Section 5.1.1; Fig. 5.3.1) for wedges R0 and T5, and localized deformation for T1 and T2 (FT in Fig. 5.3.1). This led to a decreased upper domain area from phase 1 to phase 2 in the experiment R0 (Fig. 5.3.1).

The stability diagram for the experiment T5 was mostly defined by the narrowest plot, as the wedge was almost continuously sliding at its base.

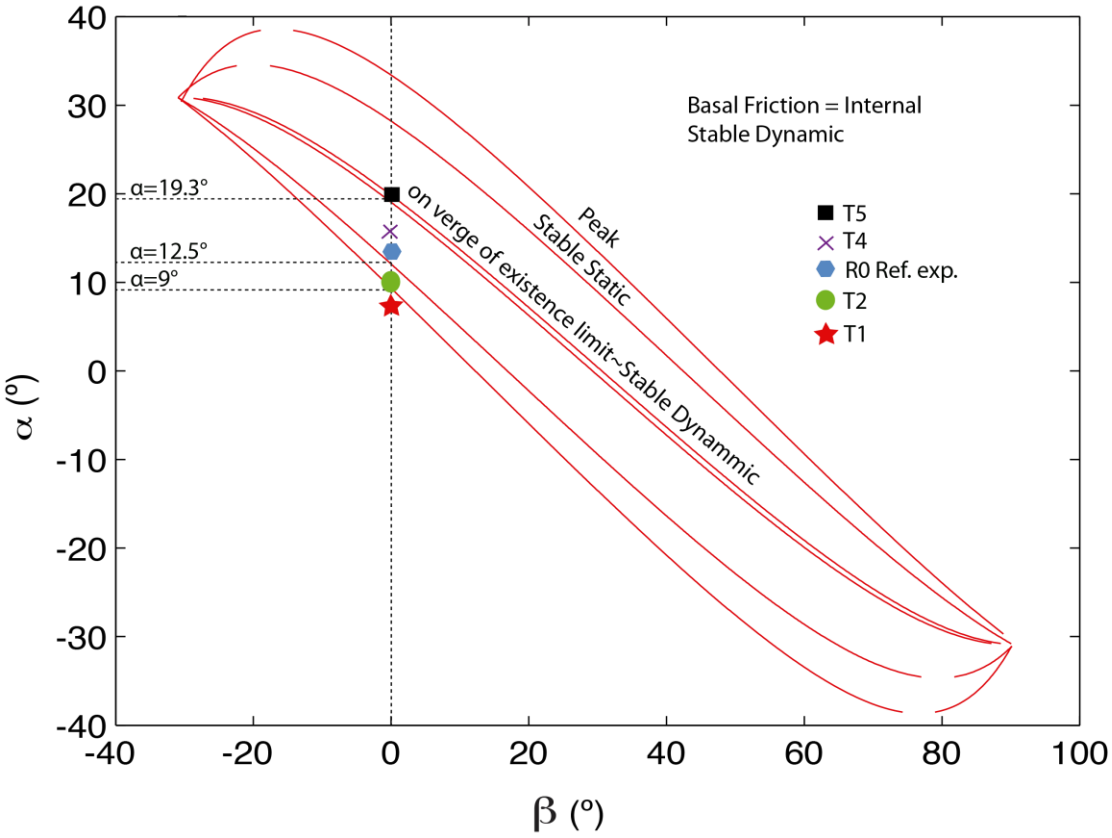
Basal Friction = Internal
Stable Dynamic
Peak
Stable Static
on verge of existence limit~Stable Dynammic
α=19.3°
α=12.5°
α=9°
T5
T4
R0 Ref. exp.
T2
T1
α (°)
β (°)
40
30
20
10
0
-10
-20
-30
-40
-40
-20
0
20
40
60
80
100

a)

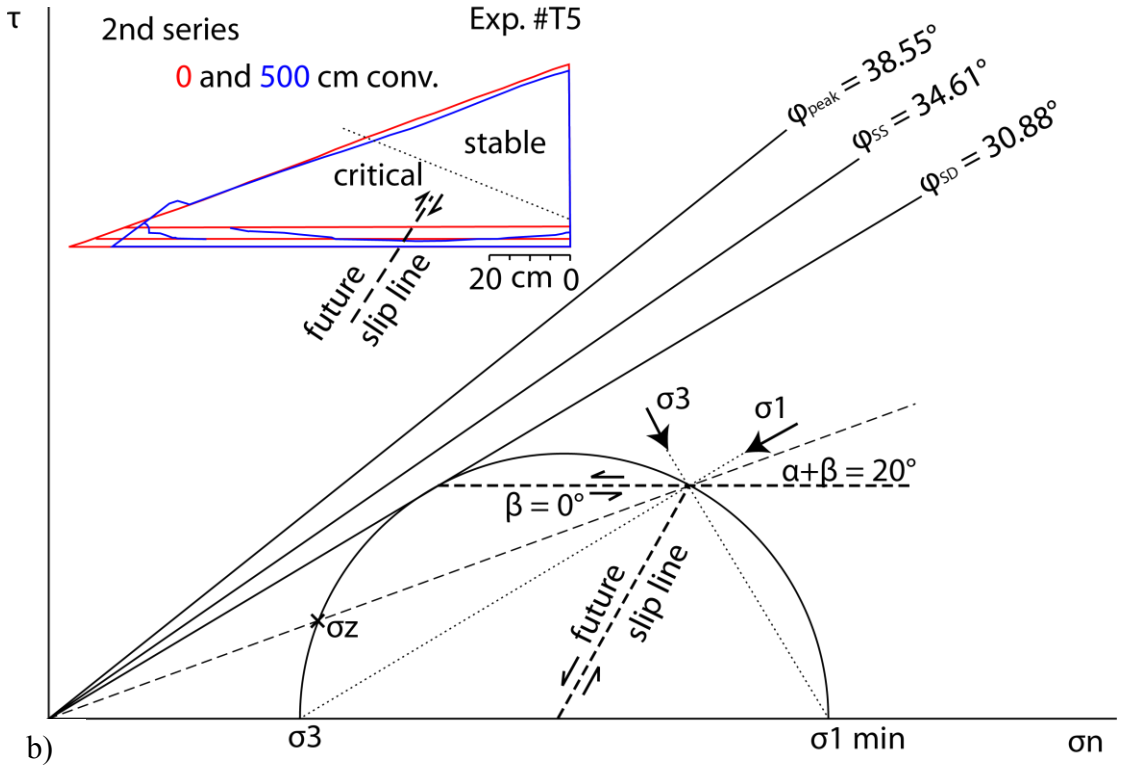
τ
2nd series
Exp. #T5
0 and 500 cm conv.
stable
critical
20 cm 0
future
slip line
φpeak = 38.55°
φSS = 34.61°
φSD = 30.88°
σ3
σ1
α+β = 20°
β = 0°
σz
future
slip line
σ3
σ1 min
σn

b)

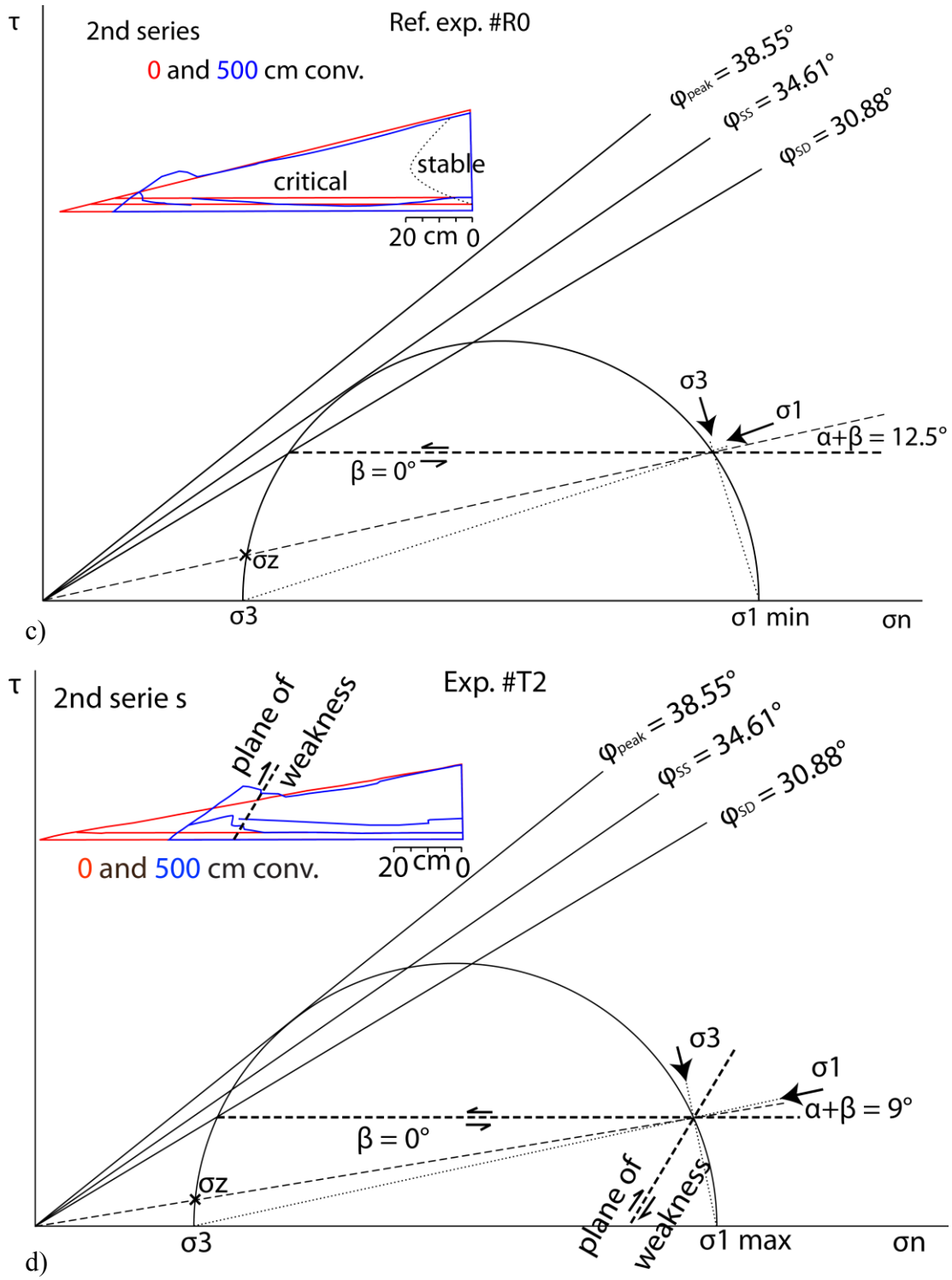

Figure 5.3.8. *a) Taper stability fields for the second experimental series. Symbols show their initial state of stress and numbers the angles for a critical taper to occur. The constraints used are peak, stable dynamic and stable static internal frictions, and stable dynamic internal friction as the basal friction. Mohr Diagrams show the state of stress required for b) basal erosion and initiation of a new slip line, c) basal erosion and d) initiation of new planes of weakness into a critical taper.*

Only a short period of thrust reactivation was observed at the beginning of the second phase and the forward growing of the Back segment stopped during the second phase (Section 5.3.1). This plot sets the wedge T5 into "long term basal subduction erosion" (Section 2.1; Dahlen 1983). In this particular case, any minor variation of the boundary conditions shifts the wedge geometry into an unstable extensional or compressional state of stress. At its existence limit, the minimum differential stress was attained; a basal décollement and formation of slip line were the most probable events (Fig. 5.3.8b). From all experiments of this experiment series, this one had the strongest subsidence, affecting both middle and upper slopes. During the third phase, after the slope wedge had diminished by ~1°-2º, the lower Middle segment domain attained a subcritical state and started to fail (future slip line in fig. 5.3.8b). We attributed the flux differences close to the SG in the tallest wedge T5 to the greater load at the rear. The better-compacted material is able to move faster than a more porous one, basally eroding more sediment (Fig. 5.3.6).

Experiment R0 was, on the contrary, mostly affected by the reactivation of thrusts and the forward displacement of the Back segment. It likely also "jumped" temporarily into the stability diagram defined by the stable dynamic strength during periods dominated by stable sliding. During the last phase, both the lower and upper domains of the Middle segment subsided critically for a final amount of ~1° (Fig. 5.3.8c). When controlled by the static strength, the geometry of the wedge was near the lower boundary of the stable state field. Any small variation during the process of building the wedge (i.e. manual handling) makes it a likely candidate for failure. As the Middle segment was deforming continuously during the last phase, it must be controlled by the static strength, however the wedge did not fail (Fig. 5.3.8c). This would explain the tendency to form an out–of-sequence thrust (see Section 5.3.5). On the other hand, the upper domain of the Middle segment was stable during the second phase and the lower part was critical. During this stage, the upper domain should have been controlled by the peak strength, to remain in the stable state field.

The continuous reactivation of faults along the Back and Central segments and the upward migration of the SZUB in experiments T1 and T2 defined both curves for them, the peak and stable static. In T1 the Back segment was mostly dominated by reactivation of thrusts and in T2, the upward migration of the SC was the preferred mode of thrust formation. When controlled by the peak strength, experiment T2 was stable but T1 was unstable. When controlled by the static strength, both wedge tapers are in the subcritical state. We observed that the Middle segment of the experiment T2 is defined by continuous upward migration and reactivation of thrusts of the SC. This segment of T2 subsided stably (no deformation of the marker lines) until the middle slope reached the lower boundary of the peak curve ($\alpha \approx 9°$; Fig. 5.3.8a and d), staying at the critical state afterwards. New backthrusting at the leading edge of the Middle segment contributed to strong underplating at the wedge front. On the other hand, the subcritical Middle segment of the experiment T1 had a transient slope and deformed internally towards the critical state over time (Fig. 5.3.1). The permanently unstable state of the T1 and frontal thrusting in T2 wedges resulted in significant

shortening and consequently high frontal erosion rates, compared with results from R0 and T5.

The deformation pattern for the SC unit and consequently for the wedge for experiment T4 showed to be different from the other experiments of the series. Once the out-of-sequence thrust was activated, the basal transfer of mass occurred bounded from above and below by continuously active shear zones. A difference from the reference prototype R0 was that in this experiment T4 the Central segment reached a width of 18 cm (18 km in nature). This experiment had larger velocities at the Tip and Central segments compared with the rest of the experiments of the series, but notoriously smaller at the Back segment (up to 4 times smaller). A strong deceleration over time was also noticed in the latter. The uniform and thick flux cannot be maintained towards the narrow SG, which effects failure of the SC unit (Fig. 5.3.8). The peak value defined the stability of the wedge and became stable. No subsidence was observed (basal erosion occurred through the forethrust close to the backwall), contributing to a strong frontal accretion, same as in T1 and T2 (Fig. 5.3.8).

(ii) Comparison with former analogue experiments

The mechanical analysis made by Gutscher (1988a), shows that an initially thick wedge (slope 25º) deters subducted sediment from going too far. The material is primarily accreted below the front of the wedge. Frontal erosion was restricted to gravitational collapses from the lower slope (not including the middle), underplating the material into the trench. In a similar way, the wedges R0 and T5 also restrict underplating at the front. However, basal erosion extended from the middle to the upper slope.

(iii) Comparison with nature

Stability

There is no agreement how to unequivocally identify a forearc in a critical state in nature. A critically-tapered wedge cannot be observed easily and simple models assume a steady state forearc geometry (Clift and Hartley, 2007), as actively shortening orogens should try to reach it. A forearc with distributed and frequent seismicity could indicate such a state, as it is at the failure throughout (Davis et al., 1983).

Adam and Reuter (2000) assumed that the Northern Chile segment is a critically-tapered wedge, whose lower slope with the largest taper represents the perfect candidate for basal erosion to occur. At the front of the margin, they describe a basal friction / internal friction ratio ≥ 1, where the rough and sediment-bare incoming oceanic plate would explain very high basal friction. Thus, they excluded active subduction erosion landward for the lower slope. Instead, they concluded a distribution of stress regimes with predominating compression near the trench, thrust faulting at depths of 20-30 km beneath the coastal area (Delouis et al., 1996), and extension at the middle and upper slopes. Eroded material is underplated beneath the upper slope, causing uplift. In a similar way, Clift and Hartley (2007) proclaimed the preferential subduction erosion close to the Southern Peruvian trench, and slow uplift by underplating after 2 Ma below the coast.

In nature, a more compacted and "dry" basal corridor of sediments may be expected as the forearc moves deeper (Vannucchi et al., 2012). By collecting data along ancient and modern subduction zones, Vannucchi et al. (2012) differentiated three segments along the SC shallow <15 km deep.

They differed from each other by pore pressure, content of fluids, degree of lithification and arrangement of shear zones. This segmentation is controlled by the vertical load of the overburden. The arcward boundary is where the seismogenic zone begins.

Thus, the results from experiments T1 and T2 are not comparable with those obtained from previous studies in natural examples (Table 1 and Fig. 5.3.5). Whereas the experiments T1 and T2 showed a subcritical state of stress, forearcs in nature are assumed to have a "stable" geometry.

In our experiments, the geometry of the wedges together with the SC behavior defined different states of stress, which controlled rates of basal erosion. In nature, the release of fluids from the SC and variations of state of stress during the seismic cycle would act as agents of active erosion, controlling the kinematics of the SC (for further details see Section 3.3).

The estimated rates of steady-state tectonic erosion in natural examples (Table 1) are in the same range as the bulk frontal and basal erosion rates of the experiments that featured criticality at the lower segment and stability at the middle slope's upper segment (Fig. 5.3.5 and Table 5). This may indicate that a critical or stable wedge better represents steady-state tectonic erosion.

Different interpretations for the same seismic line

In Northern Chile, 5 km thick base-parallel structures, visible in seismic images, were interpreted by von Huene and Ranero (2003; Fig. 2.2.1a) as the andesitic La Negra Formation; the same set of structures was later interpreted by Sick et al. (2006) as thrust faults (Fig. 2.2.1b). They show low strain rates, confirmed by outcrops at the surface slope. As a subsequent conclusion, the compressional structures would correspond to the upper part of the subduction channel.

As a consequence of the imposed subduction gap boundary condition in our experiments, an out-of-sequence thrust emerged from the top of the gap, cutting through the wedge (see Section 5.3; Fig. 5.3.1, exp. T4). This "SC unit" slided beneath the stable overriding wedge under low strain rates, defining a scarp at the middle slope as it moves backwards. From these results and from those we found in the SO104 -13 line, we support the proposition that these structures represent detachments of the La Negra Formation, which have been activated as detachments by the basal erosion process.

As planes of weakness, the structures mentioned above promote, for example, the unstability of blocks in subsiding parts of the forearc with respect to the lower slope. For the same reason, they will develop as thrust faults under the compression from subduction, as was analyzed by Sick et al., (2006). The rotation of the leading edge of this detachment (where the out-of-sequence thrust emerges) formed the scarp, similar to the one observed at margins like Chile (detachment in Fig. 2.2.1), Japan (Fig. 2.2.5), Nicaragua (Fig. 2.2.4) or Tonga. In the example of Nicaragua, at 25 km from the trench, the tectonic interpretation shows that this scarp is bounded at the base by continuous base-parallel strata.

The velocities in the Central segment of the T4 experiment represent about 2.5% of the velocity of the subducting plate compared with the nearly 1% for experiments R0 or T5. Thus, this

portion moves as a “coherent” channel, faster than those thinner SCs in the experiments R0 or T5. There was no thrust reactivation along the roof of the SC unit, as observed in the thinner SCs for the rest of the experiment series.

Finally, the only SZUB in the experiment T4 was the out-of-sequence thrust; we did not visualize a basal shear zone as those in the other experiments of the series. This unusual 18 cm thick SC unit (cf. Sections 2.1 and 2.2) also may explain the absence of “a basal SC” in some seismic images (as that in Northern Chile), which has been interpreted as “too thin for seismic resolution” (<200 m; Vannucchi et al., 2012).

5.4 Internal Friction influence on the structural evolution: the third series Internal Friction IF

Earlier models have already described a rheological control on the Andean segmentation (Sobiesiak et al., 2007; Gerbault et al., 2009) controlling evolution of accretionary or erosional systems. This group of experiments was used to evaluate the effect of different values of internal friction on their dynamics, systematically increasing the strength of the initially "weak" granular material sand in a total of four wedges (Table 2). Sugar, which has a higher internal friction than sand, was added in different proportions to increase wedge strength. Ratios of sand and sugar of 2:3, 3:2, 4:1, and 1:0 constitute the composition of wedges R0, F3, F2 and F1, respectively. Thus, the reference experiment (R0) corresponds to the strongest wedge of the series (μ_{SD} = 0.598, Table 3 and Fig. 4.1.2). We maintain the same initial geometry and same subduction gap size as for the reference experiment R0 for all experiments in this series.

The SEM images of sugar revealed well-defined crystals, with sharp corners that would make it more difficult to accommodate stresses by grain rotation than for the more spherical and rounded sand grains. The same low sphericity, even with sifted (i.e. compacted) material, leads to different bulk densities for both granular materials. A larger size and angular shape of sugar increased its porosity, compared to the same volume of a sand sample (Table 3).

5.4.1 Kinematic evolution of four erosional wedges of different strengths during the different phases

(i) The first phase

During the first stage, all experiments of this series developed frontal backthrusts, except for the reference experiment (R0) (e.g. Fig. 5.4.1 and Fig. 5.4.2). Their positions were related to the strength of the wedge. The initiation and position of backthrusts showed a trend towards later stages and larger distance from the backwall with increasing material strength (Fig 5.4.2).

Obtained widths of the Tip segment showed systematic differences as a consequence of the internal friction variation. The weakest wedge (F1) had a ~10 mm width, the experiment with the next higher friction value F2 was ~11 mm wide (Table 6). The next higher friction value experiment F3, showed a 6 mm width Tip segment, and the strongest experiment had the thinnest Tip of 5 mm. Following the same order as for the Tip, the Central segment in F1 was ~9 mm, in F2 was ~12.5 mm, in F3 was ~7 mm and in the R0 was ~ 4.5 mm. Length and width of the SC's Back segment varied from experiment to experiment. The F1 Back segment reached a width of ~1.8 cm. For F2, the width was ~1.5 cm, and in both F3 and R0 it was similar with ~2 cm. Back segment lengthening was slower in experiments R0 and F3 than for the experiments F2 and F1 (~250 cm and ~260cm respectively).

(ii) The second phase

During the second phase, observed rates showed significant variability and a trend of decreasing frontal erosion, basal accretion and tip retreat could be identified (Figs. 5.4.3a). The duration of activity of frontal backthrusts changed over time, with earlier developing faults having shorter times

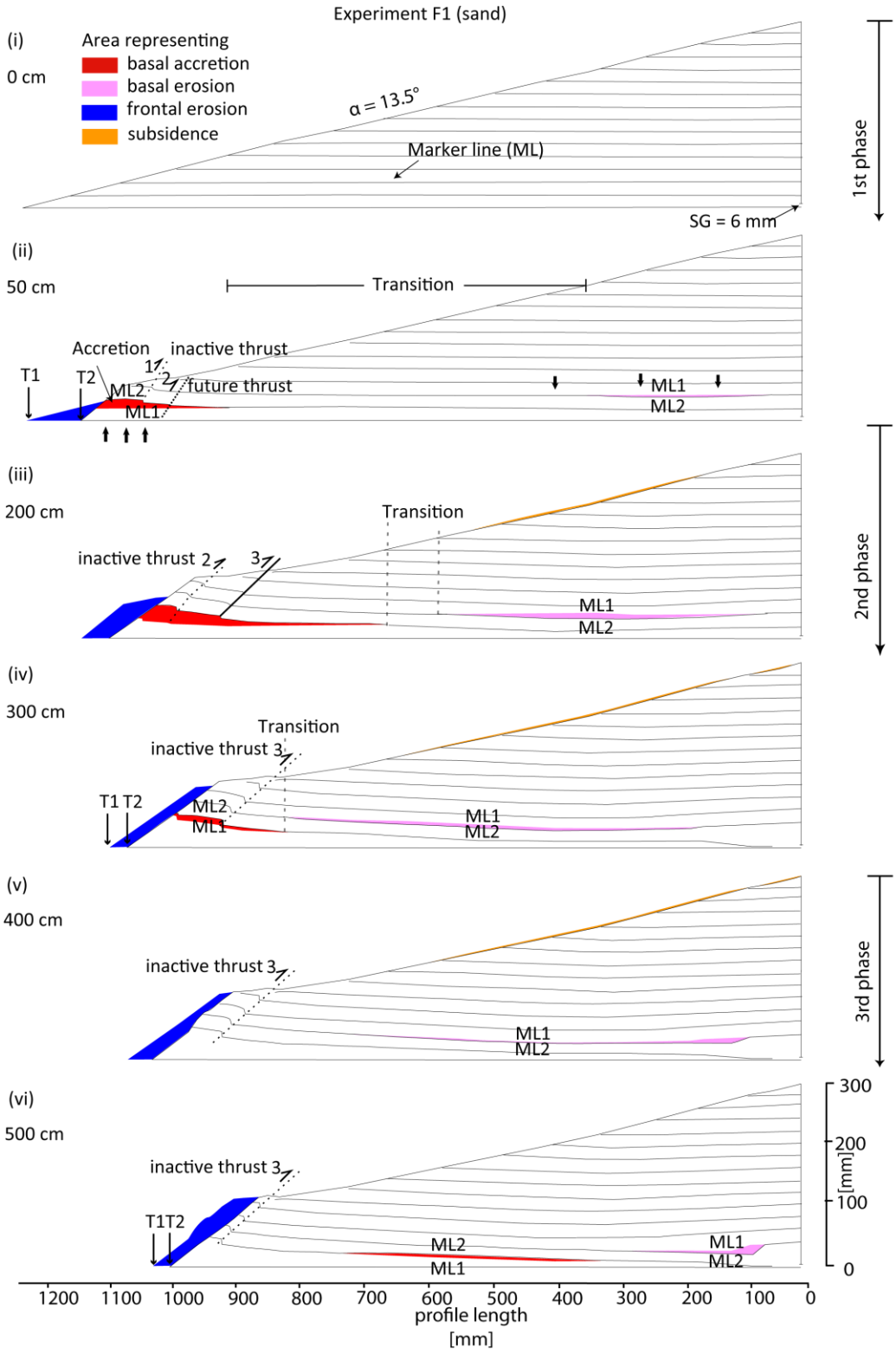

Figure 5.4.1. *Evolution of the weakest wedge of the series (experiment F1) through its different phases. Numbers indicate successive initiation of backthrusts. Nomenclature same as in figure 4.3.1. A continuous subsidence of the middle slope and uplift of the frontal segment slope until 300 cm of convergence are the most notorious changes, together with the variations of the marker lines. During the third phase, the Transition zone became a single line, by the union of the Frontal and Middle segments. See video of experiments on DVD.*

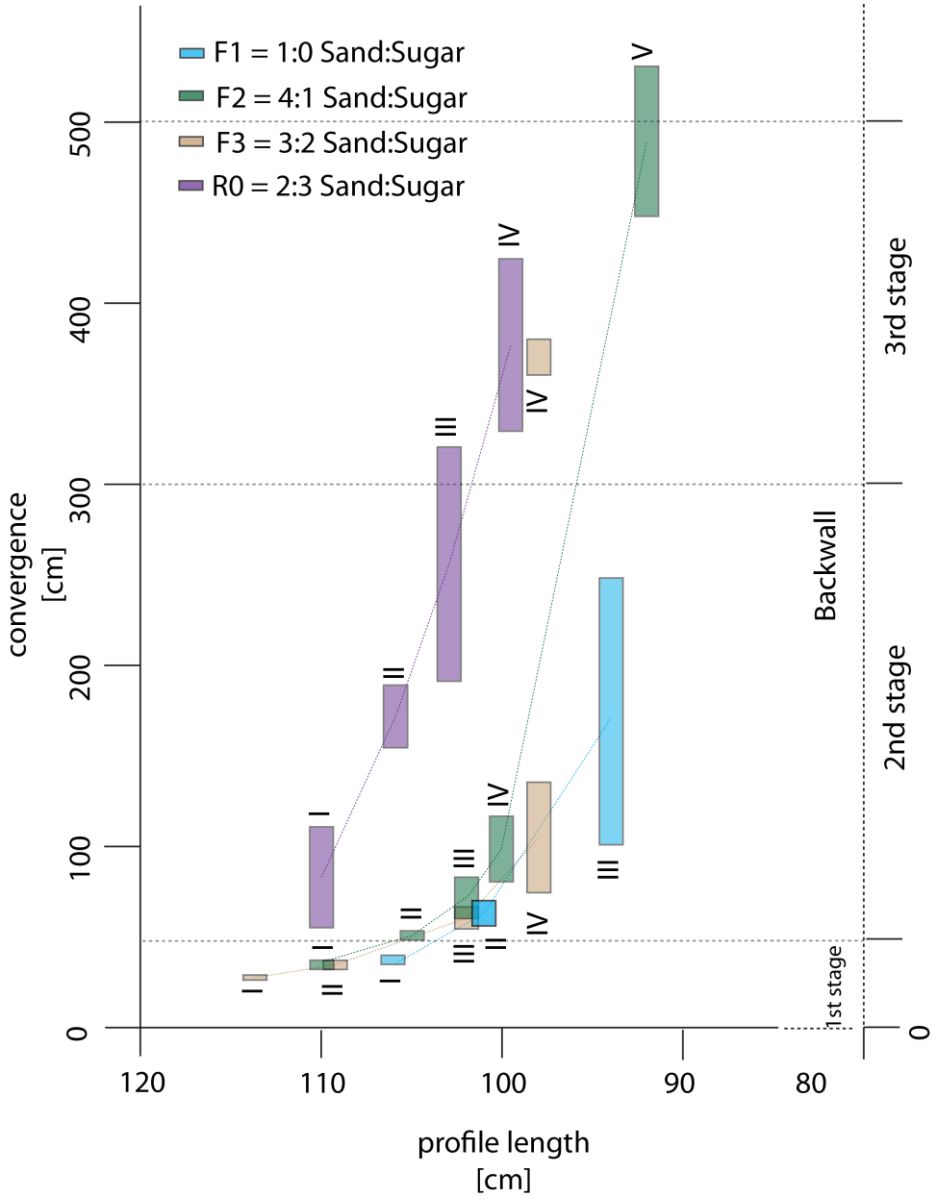

Figure 5.4.2. *Diagram representing activity of frontal thrusts in the third series IF.*

of existence than the later developing ones. In general, activity of old faults was terminated when new ones were formed. The strongest wedge of the series formed narrowly spaced frontal thrusts and it was the only wedge where the thrust phase was initiated after the first stage. The latter is also described by the value of upward displacement by thrusting, where the smallest value was observed in F1, followed by F2 and F3 (Fig. 5.4.4). Of all experiments, the R0 underwent accretion almost exclusively by thrusting, with a long-term activity of the faults (5.4.2). The lowest rates of basal accretion were observed in this experiment (Fig. 5.4.3). The values of downward displacement dropped from experiment R0 to F1 along with the wedge strength.

Evolution of the SC showed some similarity between the wedges F1, F2 and F3, where it reached similar lengths and thicknesses. As in the previous phase, similar widths of the Tip and Central segments characterized this stage during its first centimeters of convergence. However,

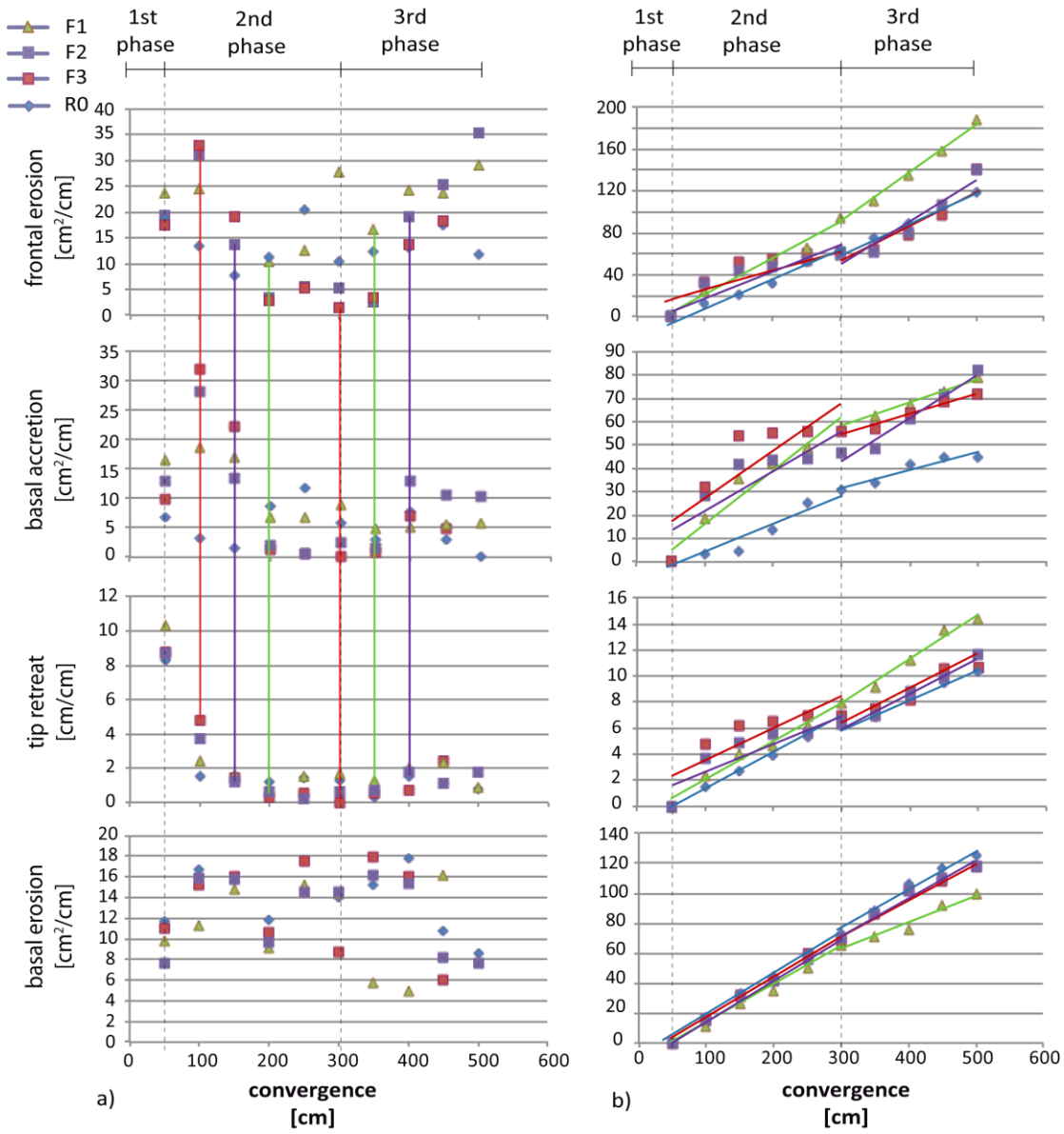

Figure 5.4.3. *a) Comparison of the different mass transfer rates of experiments of the third series IF while testing different wedge strengths (internal frictions), after the wedges deviated from the initial conditions. Different phases marked by variations on the rate patterns are specified. The coeval distribution of rates between frontal erosion, basal erosion and tip retreat is displayed as vertical lines, whose color identifies experiments specified in the legend. b) Comparison between the different mass transfer volumes of the series. Quantities were normalized for direct comparison of volumes (initial values null at 50 cm of convergence). Note the slope variation after 300 cm of convergence of the trend lines, whose color identifies experiments specified in the legend.*

once the generation of backthrusts stopped, the Tip length was controlled by the accretion of material close to the wedge tip (e.g. experiments F2 and F3). Thus, the uniformly shorter and similar Tip lengths were ~10±1 cm for R0, F2 and F3, whereas experiment F1 reached ~20 cm. After approximately 2 meters of convergence, their Back segment reached a final and regular width (~4 cm in F1 and ~3.2 cm in F2 and F3 experiments; Fig. 5.4.5). This point in their evolution coincided with the lowest basal and frontal erosion

rate (Fig. 5.4.3). Activity of thrust reactivation at the Back segment was constant and almost uninterrupted in the weakest experiment F1, while the frequency of thrust reactivation in F2 and F3 was slightly lower. On the other hand, the Back segment of the reference experiment's (R0) recurrence of reactivated thrusts was less frequent (Section 5.1.3). The lengths of the Back segment decrease with the strengths of the wedges, therefore the strongest wedge had the shortest Back segment, and the weakest wedge featured the longest Back segment.

(iii) The third phase

A smaller range of observed rates for basal erosion and tip retreat were retrieved for this phase compared to the second phase, yielding similar values for frontal and basal erosion. This leads to smaller values of mass transfer volumes than in the previous phase (Fig. 5.4.3a and b, respectively). Results of the third phase indicate that there was a tendency for frontal erosion rates to increase, while after ~400 cm of convergence, the rates of the remaining mass transfer modes decreased (Fig. 5.4.3a). In this stage, the IV fault in F3 was the only one to be reactivated and the strongest wedge of the series (R0) was the only experiment where faults III and IV were active. Experiments R0 and F2 showed generation of new thrusts during the present phase, with the last fault (V) of experiment F2 beginning to develop at a late stage of convergence and continuing further (Fig. 5.4.2). Thrusting showed a similar trend in the third as in the second phase (Fig. 5.4.4). However, the two end-member experiments R0 and F1 varied their frontal mass transfer fashion during this phase. F1's Frontal segment reached a stable geometry after 300 cm of convergence, with a final slope angle of 7°. The locus of accreted material migrated from beneath the Frontal segment to behind the Transition line (Fig. 5.4.1vi), restricting material removal closer to the backwall (Fig. 5.4.1vi). On the other hand, the frontally eroded material in R0 was completely underthrusted after 430 cm of convergence (for further details see Section 5.3.6ii-A). Accretion by underplating showed smaller amounts for the experiment R0.

The downward displacement of particles was localized almost entirely next to the SG in the weakest F1 experiment (also see Fig. 5.4.1). The rest of the experiments had a downward displacement of particles similar to that described for the reference experiment R0 (two components of downward displacement, one in front of the fastest particles and another occurring at the rear, next to the backwall; cf. Section 5.1.5). F3 and F2 showed similar values in both components while the largest displacement values occurred in R0.

The Central segment of the experiment F1 was "consumed" by the forward displacement of the Back segment. The length for the Tip segments of the rest of the experiments was similar to that during the second phase, with values of 11±3 cm. The widths of the Tip and Central segments showed no important variations in all series of experiments.

The experiment R0 obtained its final SC thickness at the rear zone of the Back segment during this stage (~32 mm, Figs. 5.1.1iv-vi and 5.1.4c). Reactivation of thrusts at the Back segment continued similarly to the second phase, showing important activity in experiments F1, F2 and F3, while appearing more moderate in R0.

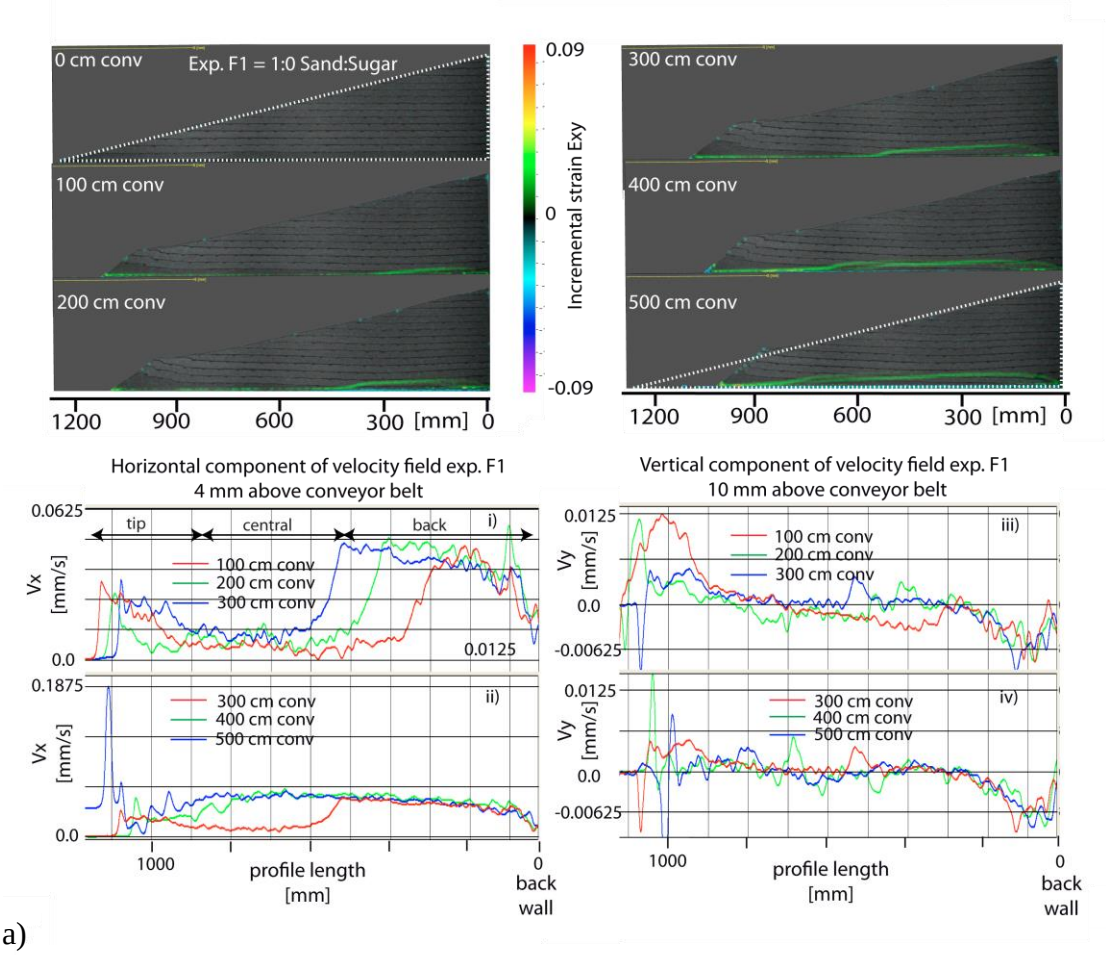
0 cm conv
Exp. F1 = 1:0 Sand:Sugar
100 cm conv
200 cm conv
0.09
0
-0.09
Incremental strain Exy
300 cm conv
400 cm conv
500 cm conv
1200 900 600 300 [mm] 0
Horizontal component of velocity field exp. F1
4 mm above conveyor belt
Vertical component of velocity field exp. F1
10 mm above conveyor belt
tip
central
back
i)
ii)
iii)
iv)
Vx [mm/s]
Vy [mm/s]
0.0625
0.0125
0.1875
0.0
-0.00625
1000
profile length [mm]
back wall

a)

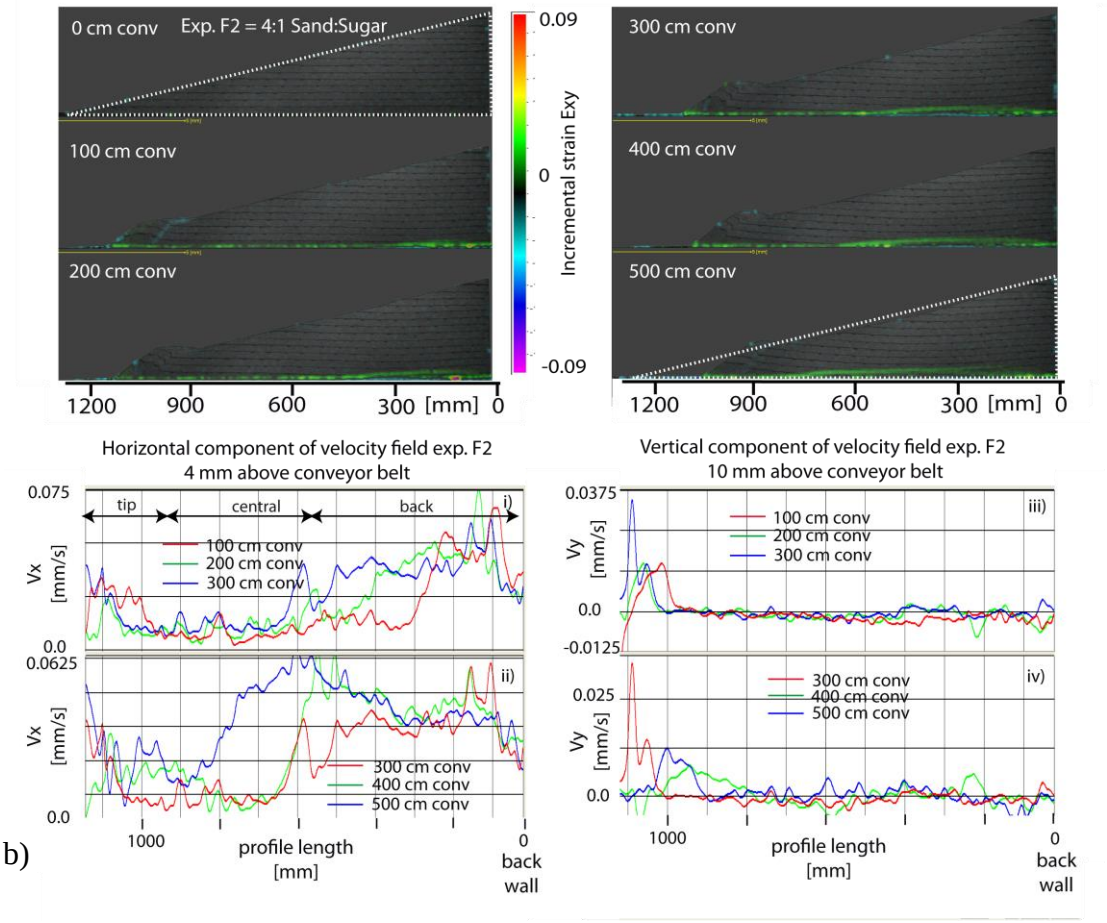
0 cm conv
Exp. F2 = 4:1 Sand:Sugar
100 cm conv
200 cm conv
0.09
0
-0.09
Incremental strain Exy
300 cm conv
400 cm conv
500 cm conv
1200 900 600 300 [mm] 0
Horizontal component of velocity field exp. F2
4 mm above conveyor belt
Vertical component of velocity field exp. F2
10 mm above conveyor belt
tip
central
back
i)
ii)
iii)
iv)
Vx [mm/s]
Vy [mm/s]
0.075
0.0625
0.0375
0.025
0.0
-0.0125
1000
profile length [mm]
back wall

b)

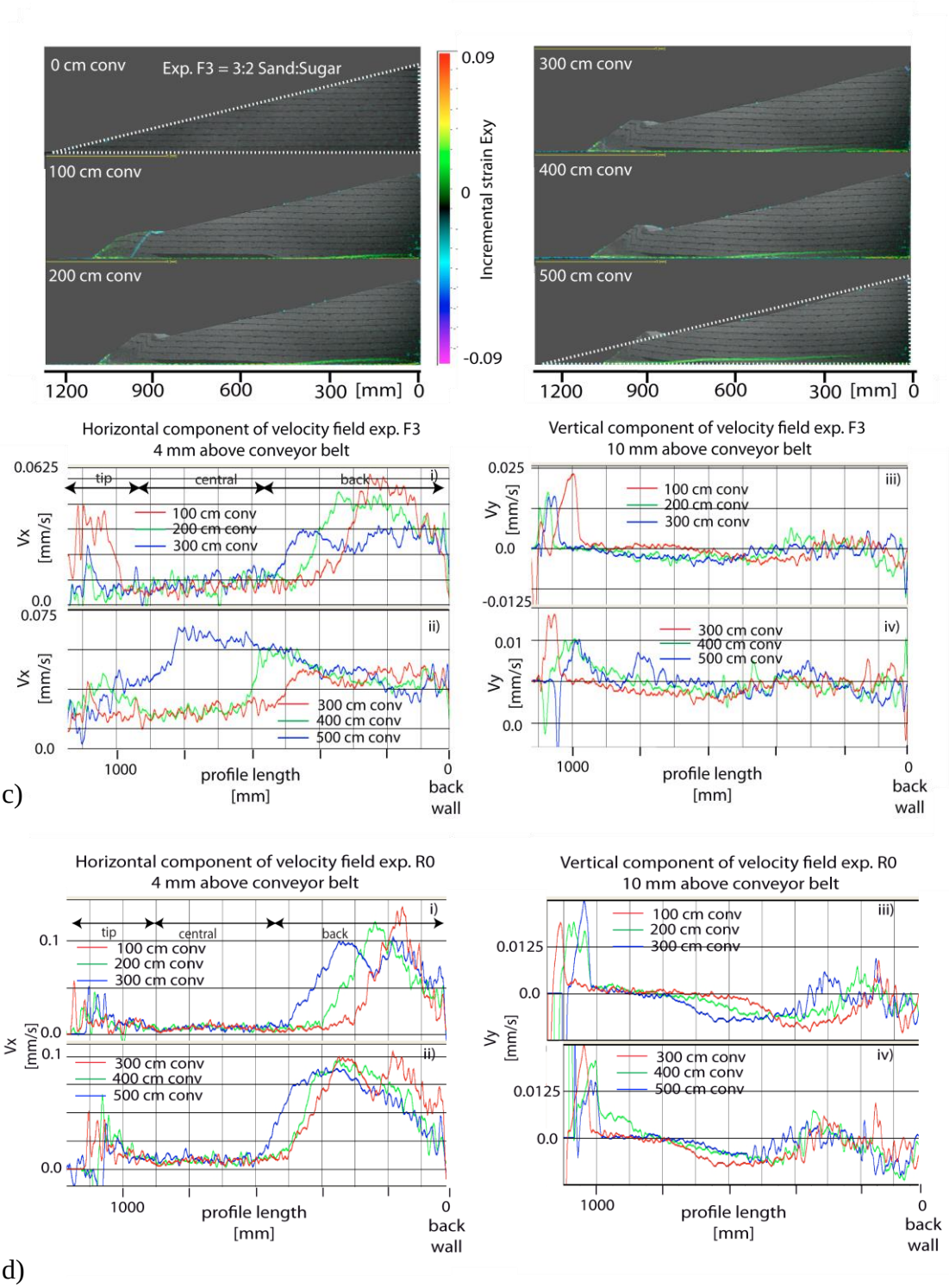

Figure 5.4.4. *Snapshots of experiments every 100 cm of convergence for different proportions of sand and sugar as a) 1:0, b) 4:1, c) 3:2 and d) 2:3 sand: sugar, respectively. The corresponding horizontal and vertical component of the velocity field (v_x, v_y) of particles are directly compared (4 mm and 10 mm above the conveyor belt, respectively) for the 2nd phase (upper plot) and 3rd phase (lower plot). Different stages every 100 cm of convergence are represented by the sequential color order red, green and blue. Initial geometry of the wedge is compared with the last state geometry (dashed lines)*

5.4.2 Quantification of the mass transfer modes

Observed differences in basal accretion between the different experiments showed that the wedge that contained 60% sugar (i.e exp. R0) behaved distinctly from the rest of the series. Similar behavior was observed for frontal erosion in the experiment in which the wedge was made of pure sand (F1) compared to rest of the experiments. However, the graphic representation of bulk rates shows that the general trend is, with growing wedge strength, frontal erosion, basal accretion and wedge tip retreat diminish (Fig. 5.4.6). It is illustrated that smaller friction values resulted in decreased basal erosion and total erosion, favoring basal accretion. By comparing basal erosion with frontal erosion, the material with the lower strength affected the amount of frontal erosion twice as much as basal erosion. This proportion declined with increasing internal friction, i.e. the volume of basal erosion for the strongest wedge exceeded the volume of frontal erosion by 2 km^2/my.

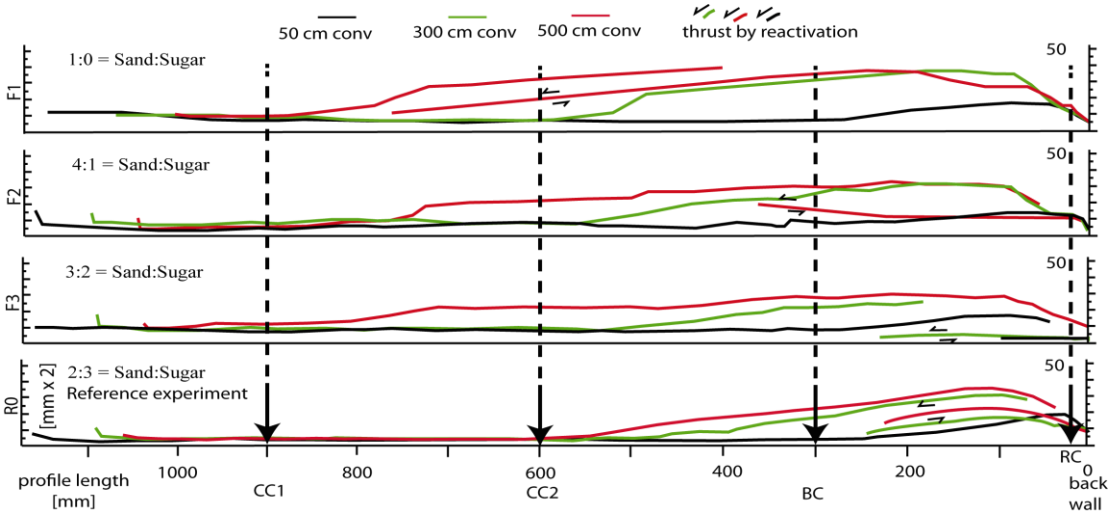

Figure 5.4.5 *Subduction Channel thickness evolution for the different experiments of the third series IF. CC and BC are points at the Central and Back segments of the SC, corresponding to distances at 600 cm and 300 cm from the backwall, respectively.*

5.4.3 Analysis of the horizontal vs the vertical component of the velocity field inside the SC

The wedge strength controlled the behavior of the SC, modifying its internal velocity and its geometry from experiment to experiment. All wedges exhibited Tip, Central and Back segments, only varying in their lengths and/or widths except for the experiment F1 during the last phase. Upward migration of particles showed a broader area covered by accreted material in F1 compared with R0, F3 and F2 (cf. Fig. 5.4.4a.iii - iv with b.iii - iv, c.iii - iv and d.iii - iv). The last 200 cm of convergence of F1 had a constant value of the horizontal component of the velocity field along the SC, indicating no basal mass removal beneath the Middle segment, confirmed by the null downward displacement of particles there (Fig. 5.4.4a.ii and iv), but beneath the Rear segment (i.e. close to the backwall). The values for the horizontal

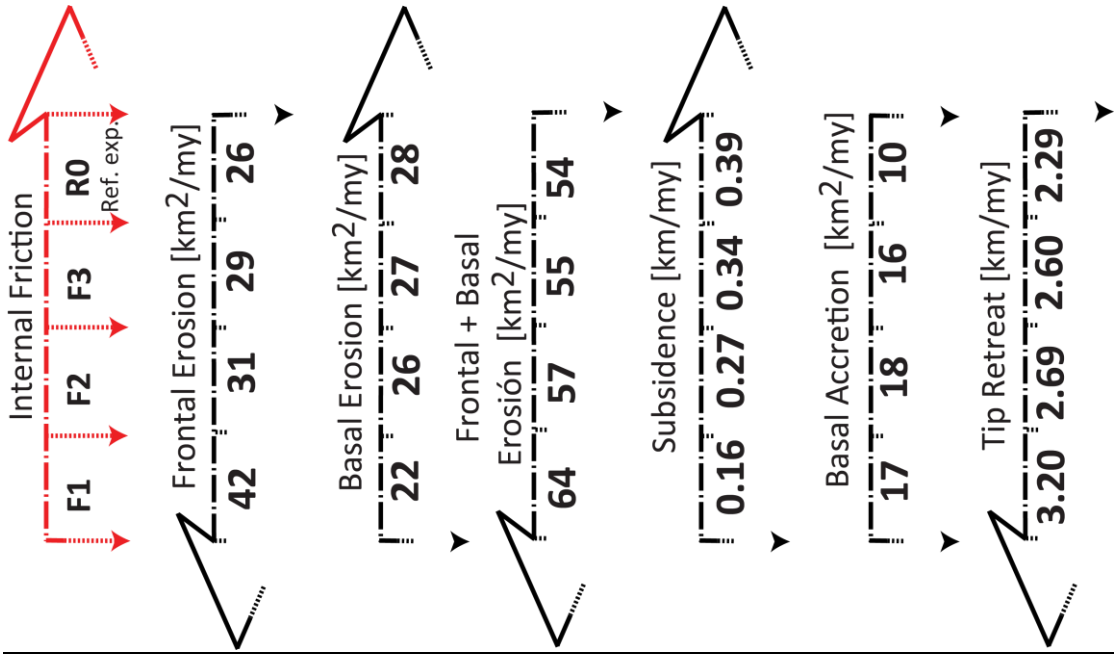

Figure 5.4.6. *Bulk mass transfer rates expressed as equivalent values in nature (km eroded to my) derived from the final values of the bulk areas/displacement during the second and third phases (after 50 cm of convergence). Arrows heads show the trend direction of mass transfer increments, where no clear trend is discernible no arrow heads are displayed.*

component of the velocity field at the Back segment in figure 5.4.4a, b, c and d, show an increase along with the strength of the wedge. The lowest values were observed for experiment F1, F2 and F3 featured uniform values and the greatest values corresponded to the experiment R0.

5.4.4 Flux of the SC through convergence

Four positions along the SC were chosen to compare flow rates: at 900 mm, 600 mm, 300 mm and around 5-10 mm from the backwall (CC1, CC2, BC and RC respectively; Fig. 5.4.5; see more details in Section 5.1.6). Flux at point CC1 in experiment F1 started being affected by the proximity of the fast particles in the Back segment after 300 cm of convergence, depicted by the fast flux increment (Fig. 5.4.7a). Of all experiments, F1 had the fastest flux with the resulting largest amount of frontal erosion. The fluxes for experiments F2 and F3 showed this influence after 400 cm of convergence, while experiment R0 was never affected.

At the second point (CC2 = at 600 mm from the backwall; Fig. 5.4.7b), the effect of the Back segment began about after 300 cm of convergence. In experiment F1, the flux declines at 400 and 500 cm of convergence, as a result of thrust reactivation. The thrust reactivation along a well-developed shear zone defined two domains of the horizontal displacement of particles inside the SC. Those particles between the boundaries of the reactivated thrust show a horizontal component of the velocity field decreasing from top downwards to its base (Fig. 5.4.8). The particles inside the areas below and above the shear zone had a uniform and faster horizontal displacement. As a result, the total flux decreased by the effect of this localized deceleration.

This may explain the flux differences between experiments, expressed by the

final volume of basal erosion. The Back segment affected by the most reactivated faults (i.e. exp. F1) had the more limited final amount of transported material, though it was the longest and widest of the entire series.

Moving closer to the backwall, at point BC the flux was observed to be similar in experiments F2 and F3 (Fig. 5.4.7c), larger in R0 and the greatest value was observed for F1. Paradoxically, the wedge with the smallest amount of basally eroded material (F1) showed the highest flux. This apparent paradox is resolved when considering the mean width of the SC at this point, which was largest from 200 cm of convergence on (Fig. 5.4.5 and Table 6). In the point closest to the backwall (RC in Fig. 5.4.5), the flux appeared to be controlled by the wedge strength, with the largest flux obtained for the strongest wedge R0 and values decreasing along with the strength. Thus, the smallest value corresponded to the weakest wedge F1 (Fig. 5.4.7d). The excess material between 300 mm from the backwall and the backwall was probably accreted, as evident from the observed uplift (see figure 5.4.4d.iii and iv) between 200 mm and 100 mm from the backwall in the profile length (this uplift was not observed in the digital images).

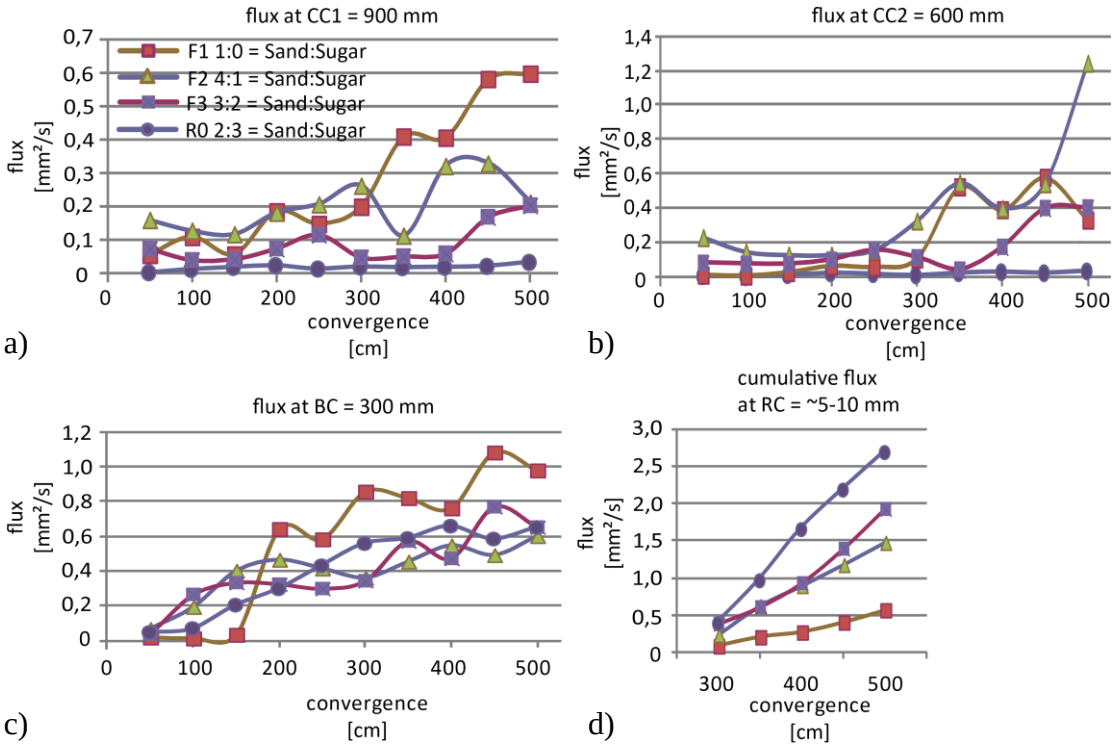

Figure 5.4.7. *Fluxes every 50 cm of convergence at a distance a) CC1 = 900 mm, b) CC2 = 600 mm, c) BC = 300 mm and RC = ~10-5 mm from the back wall in series IF during the convergence* (*for location see Fig.5.4.5).*

Table 6. *Width and velocities at specific locations along the profile length during convergence, Widths and velocities correspond to the average of the different values every 50 cm of convergence during convergence. Numbers between brackets are the standard deviation, which become large by the seaward migration of the Back segment that broadens the SC (see further explanation in section 5.1.2).*

	F1 1:0=Sand:Sugar	F2 4:1=Sand:Sugar	F3 3:2=Sand:Sugar	Ref. exp. R0 2:3=Sand:Sugar
SC width at Tip segment = TC [mm]	10	11	6	5
SC width at 900 mm = CC1 [mm]	9,23 (±1,81)	12,58 (±1,34)	6,70 (±2,13)	4,5 (±0,83)
SC velocity at 900 mm = CC1 [mm/s]	0,028 (±0,017)	0,016 (±0,005)	0,01 (±0,004)	0,01 (±0,003)
SC width at 600 mm = CC2 [mm]	15,41 (±11,93)	16,17 (±6,3)	7,21 (±1,96)	4,6 (±0,77)
SC velocity at 600 mm = CC2 [mm/s]	0,022 (±0,017)	0,023 (±0,014)	0,03 (±0,002)	0,006 (±0,002)
SC width at 300 mm = BC [mm]	21,72 (±8,6)	18,28 (±5,45)	16,82 (±7,2)	11,0 (±4,8)
SC velocity at 300 mm = BC [mm/s]	0,029 (±0,01)	0,021 (±0,005)	0,023 (±0,01)	0,03 (±0,01)
SC width at 50-110 mm = RC [mm]	10,73 (±1,72)	12,14 (±1,5)	10 (±5,59)	21,16 (±5,58)
SC velocity at 50-110 mm = RC [mm/s]	0,010 (±0,002)	0,025 (±0,005)	0,039 (±0,006)	0,03 (±0,01)
Erosion ratio (basal erosion/frontal erosion)	0,52	0,84	0,93	1,08
TC / SG	1,6	1,8	1	0,83
flux at 900 mm = CC1 [mm/s]	0,28 (±0,21)	0,21 (±0,08)	0,09 (±0,06)	0,05 (±0,02)
flux at 600 mm = CC2 [mm/s]	0,22 (±0,22)	0,39 (±0,34)	0,16 (±0,13)	0,026 (±0,009)
flux at 300 mm = BC [mm/s]	0,57 (±0, 41)	0,4 (±0,16)	0,2 (±0,21)	0,41 (±0,24)
flux at 50-110 mm = RC [mm/s]	0,12 (±0,04)	0,30 (±0,07)	0,38 (±0,12)	0,54 (±0,11)

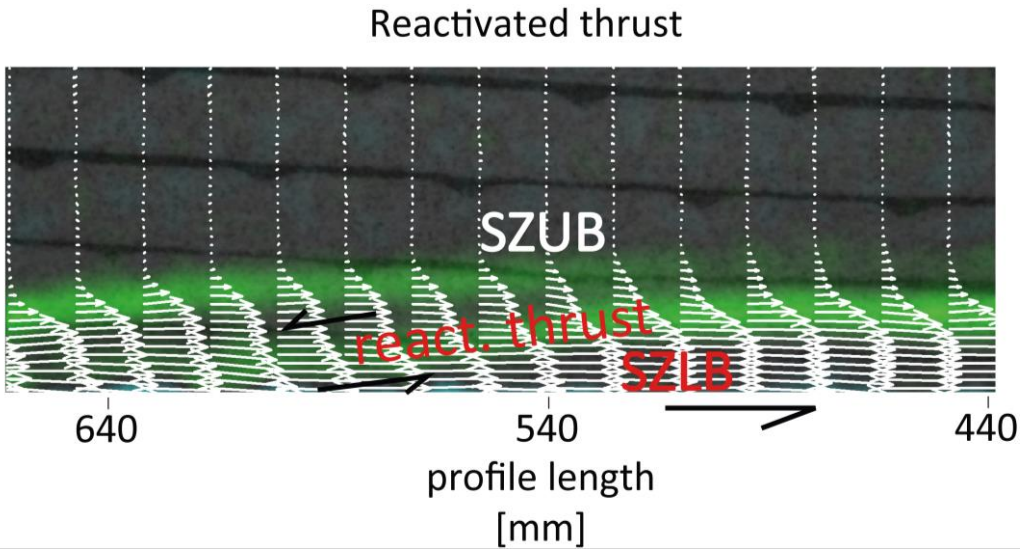

Figure 5.4.8. *Close-up of the SC from a digital image recorded by PIV during thrust reactivation. A segmented flow behavior is observed, decreasing the final amount of transported material inside the SC.*

5.4.5 SC response to different material strengths

A distinctive SC feature was the lengths of the Back segments related to the strength of the wedge. Their widening was similar, but it became longer with a smaller internal friction. The weakest wedge F1 had the finally widest and longest Back segment compared to F2 and F3, and R0 had the thinnest and shortest.

5.4.6 The stability of wedges with different material strengths

By strengthening the material of the wedges, the critical taper value was

slightly reduced, as a stronger wedge is able to accommodate deformation without becoming thicker (Davis et al., 1983; Dahlen et al., 1984; Dahlen, 1984: Fig. 5.4.9). Different compositions of our wedges resulted in different geometries of the frontal slope (Fig. 5.4.4). For compositions other than sand, the frontal slope had a curved slope, and therefore it was not possible to measure their taper. However, we inferred that, as the frontal domain thrusted or faults were reactivated until late stages of convergence (Fig. 5.4.2), this segment was unstable. The higher number of localized shear zones in experiments with higher friction relative to those with pure sand seems to be an expression of the higher angularity of sugar crystals in comparison to the well rounded sugar ones (Klinkmueller and Schreurs, 2010).

The slope of the middle domain in the different wedges subsided similarly to that of the reference experiment R0, but reached lower values of subsidence and basal erosion with decreasing sugar proportion. The widest stability field, such as for the experiment R0, makes its taper less likely to form localized shear slip lines. Subsidence in this series was through diffuse deformation, as observed for the reference model (pictures in Fig. 5.4.4a, b and c and Figs. 5.1.1 and 5.4.1)

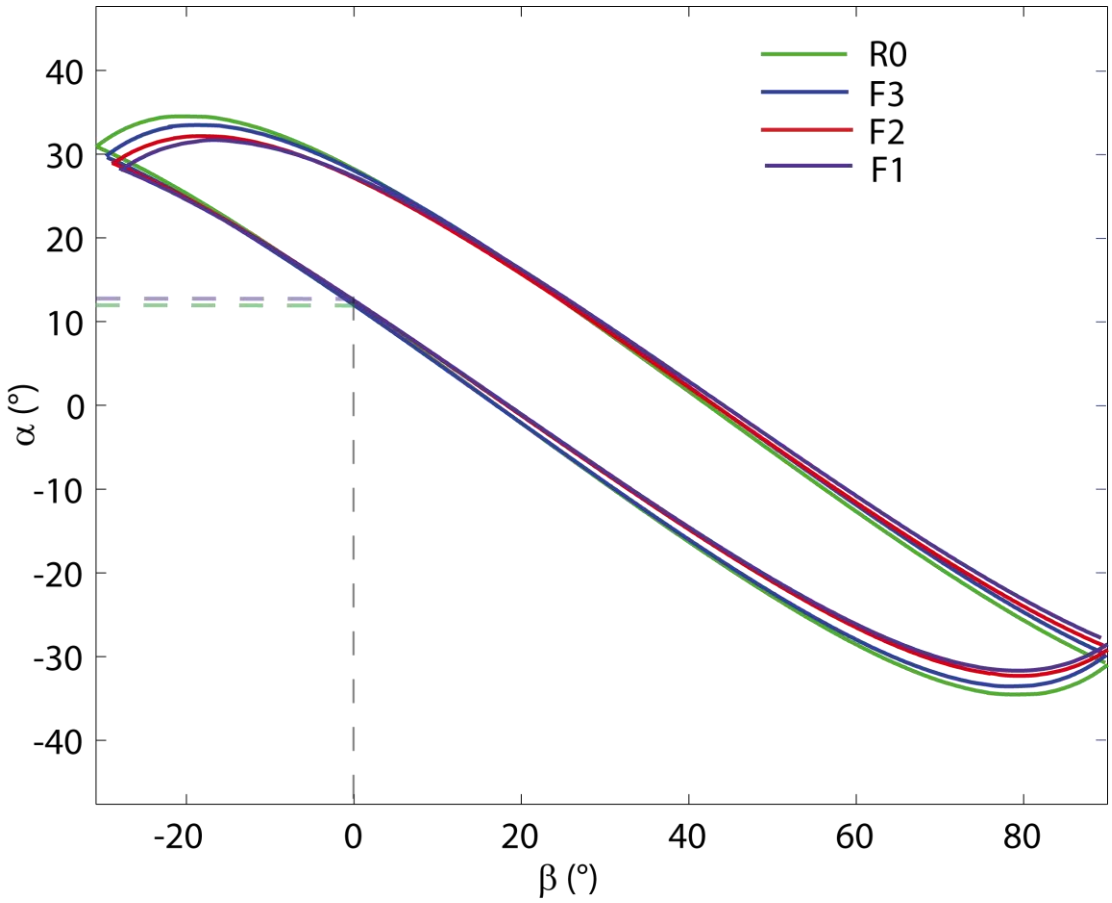

Figure 5.4.9. *Taper stability fields for the third experimental series IF. The constraints used are stable dynamic and stable static internal frictions, where the stable static corresponds to the internal friction of the granular material and the stable dynamic to the basal friction (for further information see Section 4.1.2iii).*

5.4.7 Analysis and discussion of the role of the forearc strength in erosional margins

(i) Analysis of the strength of the experiments and role in basal erosion

The length of the back segments was different for each experiment of this series, especially during the third stage (Fig. 5.4.5). Comparing lengths, flows rates at the RC point and basally eroded material among the different experiments, the back segment in the pure sand wedge was longer and had a slower flux of sediment leaving the system than stronger wedges. The stronger the wedge, the shorter its back segment and faster the movement of the particles exiting the wedge. The two experiments F2 and F3 had similar lengths and similar volumes of eroded material. The sifting technique to build up the wedges was the same, which results in well compacted material. Plots of shear stress vs time show that compaction prior to fracture increases along with internal friction (Fig. 4.1.2).

A shorter back segment of the channel and its faster material flux compared to the reference experiment resulted in a higher capacity for compaction of the sand-sugar mixture. The higher compacted the material, the easier the displacement of small-size particles, leading to a faster transport of the sediment into the SC and to an increase of basal erosion.

We did not find a direct correlation between the μ_{BSD} / μ_{SD} ratio of the different wedges composing this series (which would cause basal erosion) and basal erosion. In theory, the former should be ≥ 1 for basal erosion to occur (Adam et al., 2000). However, we observed smaller basal friction / internal friction ratios for the wedges with sugar (μ_{BSD} / μ_{SD} = 0.9; Table 3) than for the pure sand one (μ_{BSD} / μ_{SD} = 1.02; Table 3). Similar results were obtained in a previous study (Klinkmüller and Schreurs, 2010), where the use of rounded to very rounded sands resulted in a lower internal- but a higher basal- friction than for angular to very angular sands, when using alkor foil in the base. Indeed, the previous observation proves that the basal friction / internal friction ratio does not need to be necessarily "large" in order to lead to larger basal erosion. Consequently, this suggests basal erosion occurs not directly as a result of upper-lower plate contact, but from the SZUB of the SC.

The reactivation of thrusts was significant for experiment F1, the weakest wedge of the series. It is interesting to note that the reactivation of thrust structures, as occurring in our wedges or the ones of Lohrmann et al. (2006), may correspond to the Riedel shear faults described by Collot et al. (2011). As it was observed, apart from facilitating the migration of fluids outside the SC (von Huene et al., 2004), they would accommodate the subsiding rock layer in the new space created by the rotation of the fault. In our experiments, the reactivation of thrusts locally decreased the flux of the SC.

(ii) Comparison with former analogue studies

The inclusion of the PIV method with sandbox experiments has recently substantially improved understanding of processes that in nature are not possible to observe (Adam et al., 2005; Lohrmann et al., 2006). Phases of the SC during the two types of convergent margins can explain transient features displayed on the surface. In Lohrmann et al.'s experiments (2006), basal erosion was constrained to the reactivation of thrusts (similar to that in Fig. 5.1.1iv), subsequently replaced by material from frontal erosion. The only segment that underwent subsidence was the frontal one. In our

experimental wedges, the reactivation of thrusts of the SZUB is also an indicator for basal erosion. Thus, basal erosion is restricted to these seaward dipping faults. Basal erosion within the Middle segment was observed as an uninterrupted process, since it was mostly triggered by the active shear zone SZUB. We attribute this difference to the wider size of the gap and the material used in experiments of the other study cited here. This assumption is supported by the observation that (1) the only time a reactivation took place was with the larger size of the gap in the first series SG and that (2) the higher frequency of reactivation was related to sand, rather than sand-sugar mixtures in series IF (Section 5.4.1).

(iii) Comparison with nature

When the volume of sugar was higher than sand in the mixture (exp. R0), the experimental wedges reached mass transfer volumes that were more similar to those estimated for natural wedges. As sugar has a smaller bulk density than sand, the accretion in the frontal segment of the wedges composed of a mixture of sugar-sand was higher than in the case of wedges composed of only sand. The same reasoning can be attributed to a longer tip segment observed for wedges with a mixed composition. Therefore, the experiments of the series correspond likely to B type margins according to Cloos and Shreve (subduction erosion but some underplating close to the wedge's toe; 1988b).

A crystalline basement may tend to be removed as large and angular pieces or blocks, while an accretionary prism may be eroded by piecemeal. The former shows more similarities with the sugar crystals, the latter with sand grains, hence this erosion style may correspond to the one observed in our experiment series IF.

5.5 High and low topography of the subducting basal plate controlling evolution of forearcs: the fourth series Highs and Lows HL

The aim of the last experiment series was to study the tectonic evolution of convergent margins with bathymetric anomalies in the subducting plate. The series is constituted by two consecutive stages of the same experiment, called HL.1 for the first stage and HL.2 for the second stage (Table 2). The wedge had the same geometric initial conditions and set up as the reference experiment, only varying the sand-sugar proportion in the mixture (125 cm initial length x 30 cm high; rough conveyor belt; gap size = 6 mm; Sand : Sugar = 9:1; Table 2). After the total convergence of 480 cm in HL.1, the surface of the conveyor belt from the toe of the wedge "seaward" was modified by placing several wooden sticks every 10 cm across the conveyor belt, simulating topographic "highs and lows" structures. The sticks of 2 mm height x 25 mm length, represent highs of 200 m height x 25 m length when scaled to nature, separated by a distance of 10 km representing the low (von Huene and Ranero, 2003, von Huene and Lallemand, 1990; Fig. 5.5.1). Hence, the initial setup for experiment HL.2 was, (a) wedge geometry corresponded to the final geometry of the wedge HL.1 (~102 cm length x 30 cm height; Fig. 5.5.2a) and (b) the modified conveyor belt surface (Fig. 5.5.1). The experiment HL.2 ran a total convergence of 600 cm, to ensure that the stable state was achieved. The evolution of both stages HL.1 and HL.2 was compared at the last 150 cm of convergence, after having already reached their steady state.

5.5.1 Kinematic evolution of erosional wedges with different subducting plate topography

Rates of frontal erosion and tip retreat were higher in experiment HL.2 compared with HL.1. During the last 100 cm of convergence, basal erosion rates of experiment HL.1 exceeded those for HL.2 (Fig. 5.5.3a).

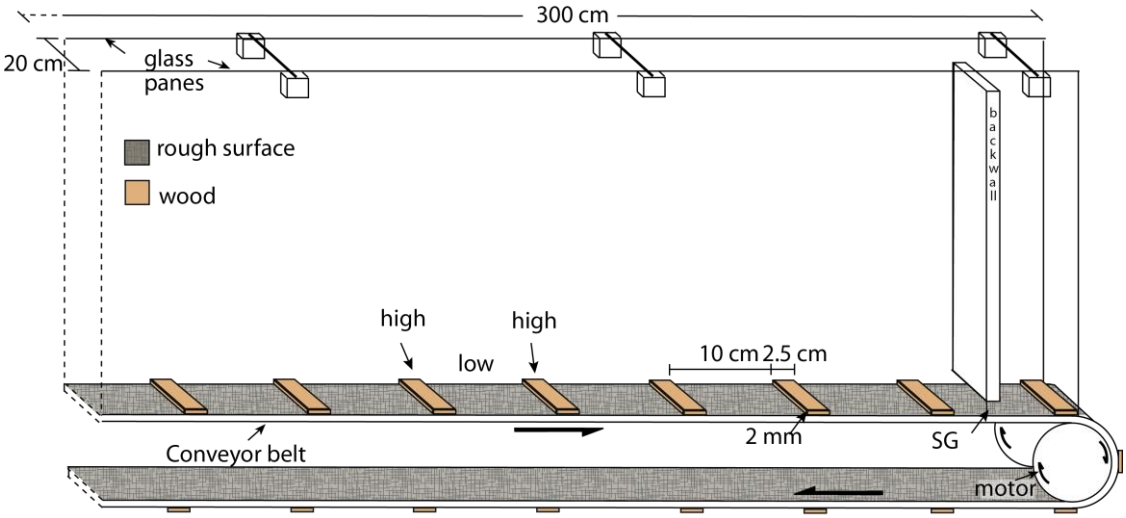

Figure 5.5.1. *Model configuration of set-up for the topographic highs and lows representation*

Material from frontal slides and collapses in the HL.1 is added and placed close to the wedge toe, while basal removal of sediment is located arcwards, closer to the rigid back-wall (Fig. 5.5.2a). HL.1 surface underwent uplift by accretion of sediment, being located at the frontal segment (a 10 cm x 10 cm frontal prism evolved). A forethrust rooted at the base of the backwall emerged at the surface slope as an out-of-sequence thrust and controlled the deformation of the wedge. Subsidence of the middle slope occurred between the frontal prism and the point of emergence of the out-of-sequence thrust. Basal erosion at the rear segment was enhanced close to the active thrust as a consequence of a SG (for further details see Section 5.1.7).

On the contrary, in experiment HL.2 basal erosion and subsidence developed close to the wedge tip and accretion of material was null (Fig. 5.5.2b). Consequently, the contractional frontal prism was completely consumed. The middle slope angle developed a steep curved geometry close to the wedge toe, as a consequence of the strong basal erosion (Fig. 5.5.2b).

The change from the rough surface of the conveyor belt to a high and low topographic surface, modified the place of the "erosive zone" from near the backwall in HL.1 to close to the wedge toe in HL.2.

Geometry of the SC for experiment HL.1 was similar to that described for the reference experiment R0 (cf. Figs. 5.1.2 and 5.5.4a). For experiment HL.2, the geometry varied substantially, where the SZUB consists not of a single thrust, but resembles a chain (5.5.4b; See video on DVD).

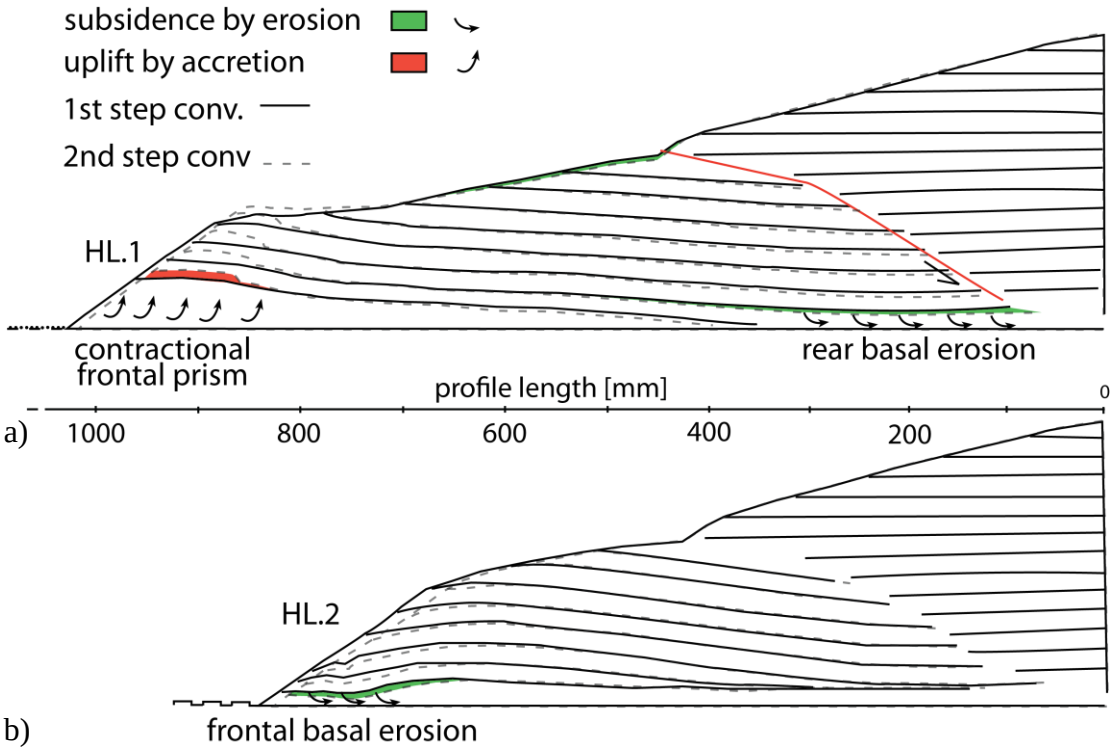

Figure 5.5.2. *Cartoon of the two consecutive steps of convergence during the last stage of experiments HL.2 and HL.1.*

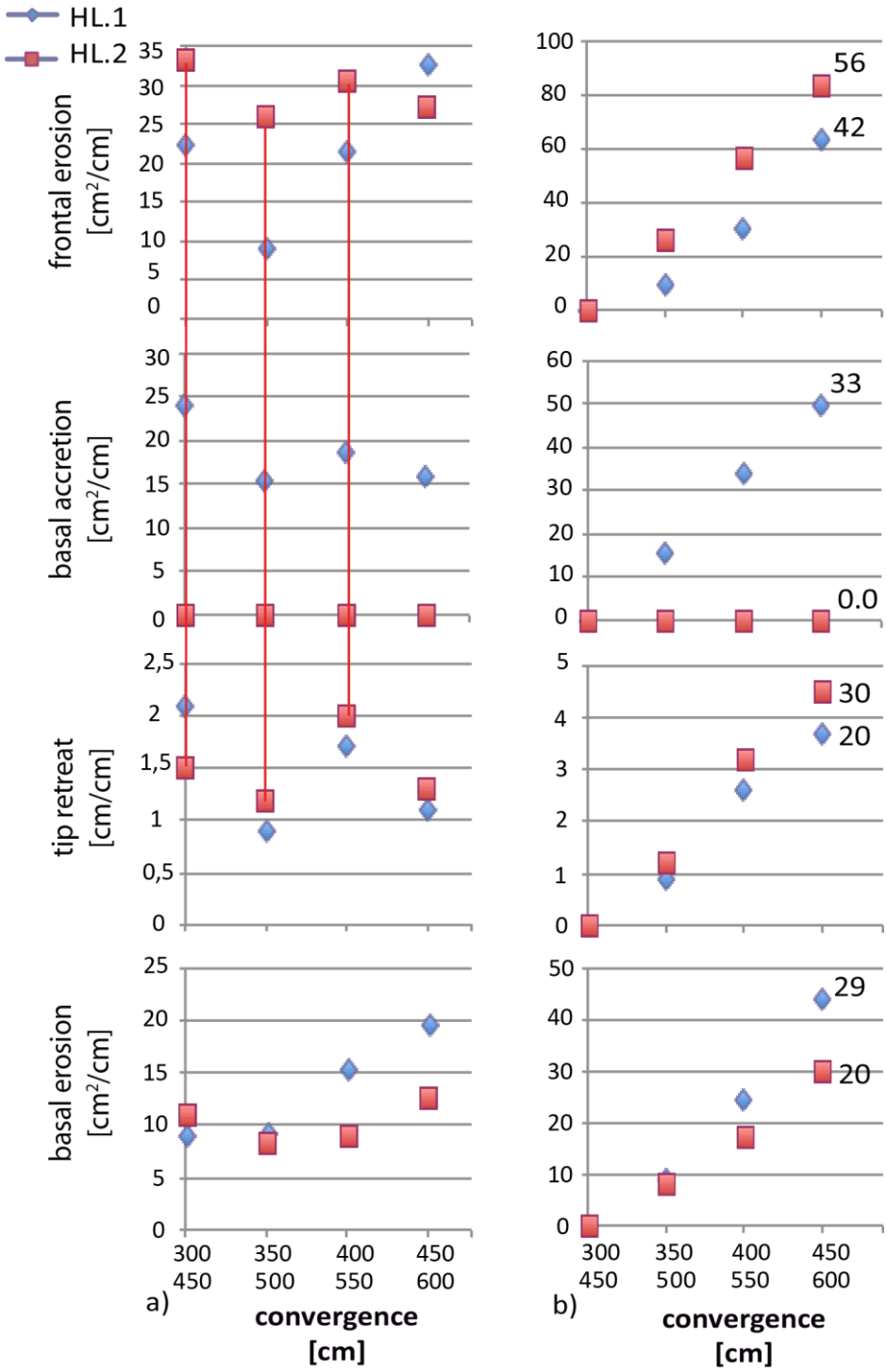

Figure 5.5.3. *a) Comparison of the different mass transfer rates of experiments of the fourth series HL while testing different topography of the conveyor belt during the last 150 cm of convergence (i.e. after 350 cm and 450 cm of convergence for HL.1 and HL.2 respectively). The coeval distribution of rates between frontal erosion and tip retreat is displayed as red vertical lines, whose color identifies the HL.2 experiment. b) Comparison between the different mass transfer volumes of the series. Quantities were normalized for direct comparison of volumes (initial values null at 300 cm and 450 cm of convergence for experiment HL.1 and HL.2, respectively). The numbers represent the bulk material transfer rates as derived from the final values of the bulk areas (or displacement in the case of tip retreat), expressed as equivalent values in nature (km eroded/my).*

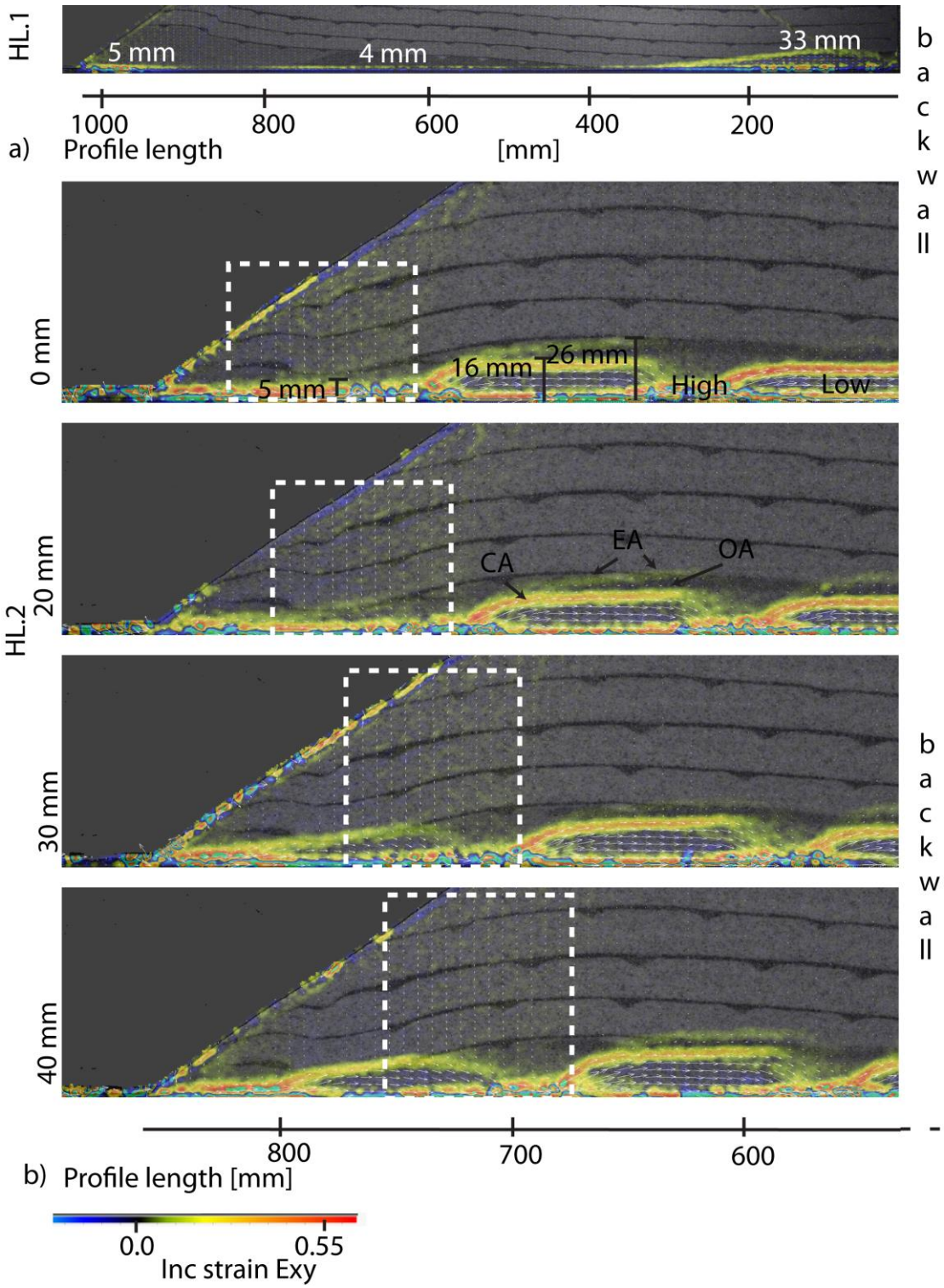

Figure 5.5.4. *a) snapshot of SC at the steady state with a low rough surface conveyor belt. b) Evolution of SC with one of the horsts on the downgoing plate entering at the tip of the wedge in the uppermost picture until 40 mm of convergence later. Dashed frames show subsidence migration together with movement of the conveyor belt, right over the low structure. High particle velocities are indicated by yellow and red colors. SC thickness is indicated.*

The chain's links reached a thickness of 16 to 26 mm (1600-2600 m in nature) over lows and thin out to about 3 mm over highs (300 m in nature; Fig. 5.5.4b). New highs in the system created new chain links ≤8 mm thick (or 800 m in nature) and the thickest lens was visible further 100 mm from the tip (10 km in typical forearcs).

5.5.2 Quantification of the mass transfer modes

The erosional effect of the SG boundary condition was less effective with the highs of experiment HL.2, decreasing the final amount of basal erosion (Fig. 5.5.3b). Instead, the high-relief surface enhanced frontal erosion, increasing both this and the retreat of the tip, compared to the low-relief experiment (Fig. 5.5.3b)

The analysis of the digital images recorded by PIV revealed that the removal of material at the Frontal segment was enhanced due to the passage of highs and lows beneath the wedge (Fig. 5.4.4b). The space between two consecutive highs destabilized the frontal prism, over-steepening it and subsequently leading to mass failure and collapse. The material gathered in the lows was afterwards integrated into the SC. This increased the number of slumps by a factor of almost two compared with the rough conveyor belt (5 for HL.1 vs 9 for HL.2).

5.5.3 Analysis of the horizontal vs the vertical component of the velocity field inside the SC

The SC chain structure consists of several high velocity paths between highs (Fig. 5.5.5b). Each "chain link" structure is demarcated at the top by a continuously active upper curved shear zone (CA; Fig. 5.5.4b).

Erosion was triggered by the high closest to the tip and the subsiding area moved over this until a new high went into the wedge (white dashed frames in Fig. 5.5.4). The new high entering beneath the tip again triggered erosion at the toe, deactivating erosion by the old high. In this process, wedge toe and frontal segment moved up and down cyclically (Fig. 5.5.5b).

Inside the link structures the speed decreases forward but is always faster than in CA. Over the CA, new faults were initiated and reactivated episodically (EA; Fig. 5.5.4b). An occasionally active zone placed between the CA and that EA with velocities of the flow decreasing from the first to the second (OA; Fig. 5.5.4b). Ablation occurs at exactly two places: the wedge tip and at the high closest to the tip's CA rear part that bends to the SC (number 3 in Fig. 5.5.5b, snapshot at 450 cm of convergence and v_x plot). The greatest velocities were at the top of the highs, smaller and regular along the CA and decreasing arcwards, where the minimum value is next to the ablation segment of the lens (number 1, 2 and 3 in Fig. 5.5.5b, respectively).

5.5.4 Analysis and discussion of the role of the topography of the subducting plate in erosional margins

(i) Impact of highs and lows in the experiments and role in basal erosion

Accretion and erosion are evidenced by particles' paths in both experiments (HL.1 and HL.2), but their loci and implications are different. When the simulated horsts reach the tip, the sediment rises and immediately falls into the simulated grabens. Both accretion and erosion occurs in the frontal segment of the wedge. The presence of horsts passing through the SG reduces the influence of this factor,

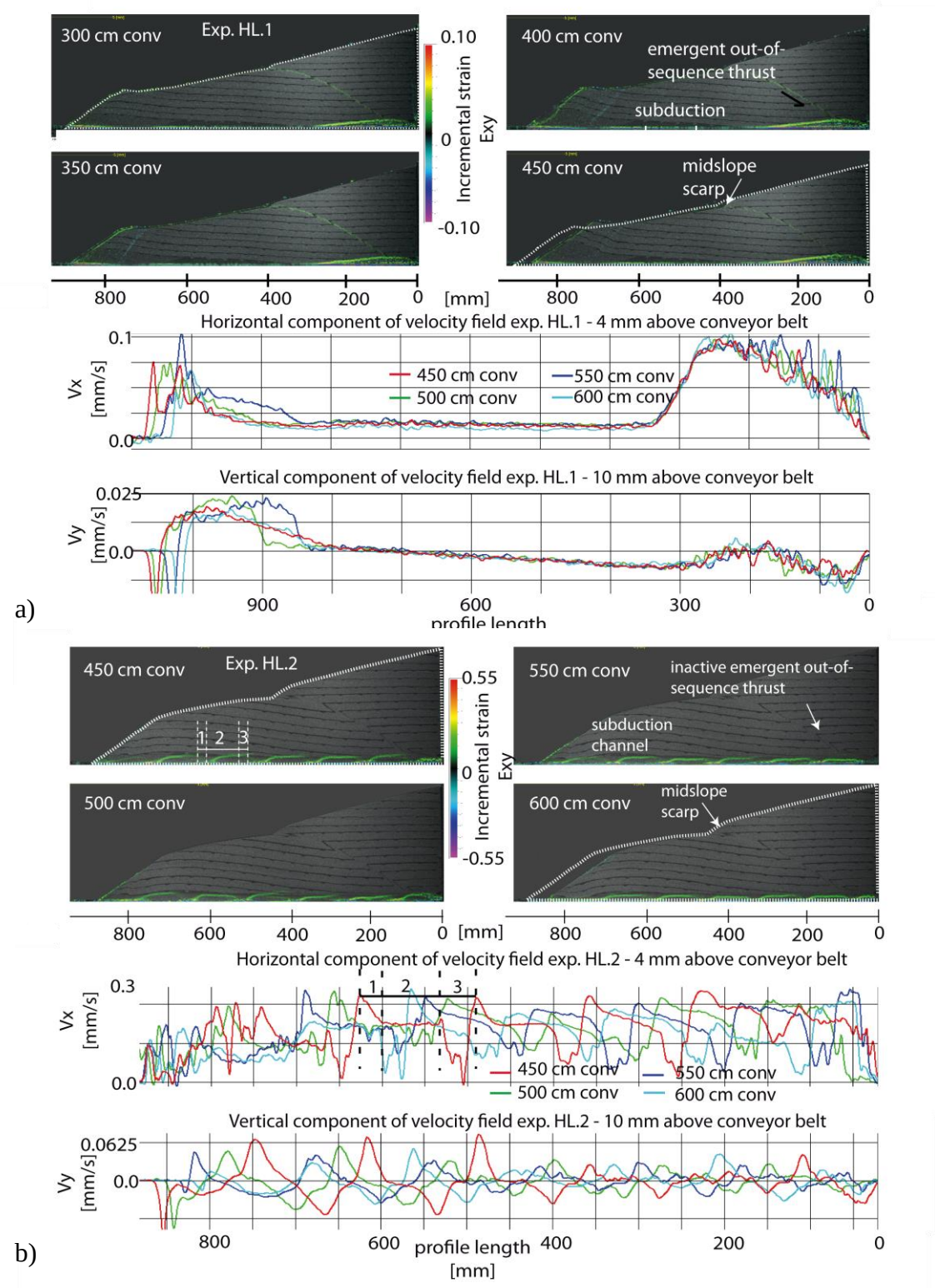

Figure 5.5.5. *Snapshots of experiments every 50 cm of convergence for different subducting plate topography as a) rough conveyor belt and b) highs and lows, respectively. The corresponding horizontal and vertical component of the velocity field (v_x, v_y) of particles are directly compared (4 mm and 10 mm above the conveyor belt, respectively) (lower plots). Different stages every 50 cm of convergence are represented by the sequential color order red, green, blue and cyan. Initial geometry of the wedge is compared with the last state geometry (dashed lines). Numbers 1, 2 and 3 indicate different places along the lens-shaped bodies in the SC, as indicated in upper picture at 450 cm of convergence.*

stopping basal erosion at the segment near to the rigid wall (HL.1), localizing it at the front. Upward and downward vertical displacement plots show that both values are similar. All eroded material is transported into the SC and discharged through the subduction window, with no accretion.

(ii) Comparison with nature:
The presence of irregular bathymetry is obvious in many seismic profiles with scarce sediments on the surface (Section 2.2). They are interpreted as a consequence of the bending of the oceanic plate into the trench (Ranero and Sallares, 2004; von Huene and Ranero, 2003; von Huene et al., 2006). Friction by bathymetric anomalies has been proposed in some studies as erosional mechanism (Jarrard, 1986; Uyeda and Kanamori, 1979; Lallemand et al., 1994; Kukowski et al., 2001).

In particular, a structure consisting of topographic highs and lows (as horst and grabens) is considered as an abrasive system, subjected to high compressional stress (e.g. Clift et al., 2003; Clift and Vannucchi, 2004; Hampel et al., 2004; Bangs et al., 2006). Hypothetically, horsts and grabens easily break and become disaggregated from the frontal part, enhancing frontal erosion and trench retreat (Schweller and Kulm, 1978; Hilde and Sharman, 1978; von Huene and Lallemand, 1990; Kukowski and Oncken, 2006). Grabens collect the sediment collapsed from the slope, leveling and smoothing the rough subducting surface (Aleutian Trench, McCarthy and Scholl, 1985; Tonga margin, Balance et al., 1989; Japan, von Huene and Culotta, 1989; von Huene and Ranero, 2003; Sallares and Ranero, 2005). It was also proposed by Shipley and Moore (1986) that a blanket of sediments on top of the seafloor buffers the impact of horst and graben topography, implying that an abrasive environment is unlikely.

Nature and thickness of the subduction channel greatly differ beneath the margin segments with smooth and rough morphology (Section 2.2). In Japan and Peru, horsts are covered by a blanket thicker than 500 m and the amount of eroded material transported by grabens was twice as much (von Huene and Lallemand, 1980). Our experimental results from a disrupted belt showed a SC with a configuration of “horsts” and “grabens” similar to those found in margins: chain link structures near the tip reached 800 m thickness and 300 m thickness over horsts (values scaled to nature). These values are consistent with those found in forearcs over graben structures (Chile, Ecuador; 2.2). According to Collot et al. (2011), low velocity zones next to the lens-shaped bodies beneath the middle slope (Section 2.2) would correspond to underplated material. However, recent uplift has been documented only in coastal and continental areas. From what we observed from our experimental results, we postulate they might correspond to the upper damage zone (OA in Fig. 5.5.4b), which is located over the chain link structures.

Over a lower surface roughness (experiment HL.1), the SC’s upper boundary is a continuous thrust, thin at the frontal and middle segments, and becoming thicker toward the back (as the reference in Fig. 5.1.2; Fig. 5.5.4a). It must be considered that the conveyor belt in our experiment did not have a sediment cover, which in nature might reduce the influence of the irregularities (von Huene et al., 1999; Kukowski and Oncken, 2006).
A slightly deformed zone or *frontal prism* is formed (Tsuru et al., 2000)

with debris and fragmented rock from the continuous slumps (von Huene et al., 1999). Beneath, grabens double their sizes due to bending under the forearc (Ranero el al., 2006). This frontal prism is present along several erosional margins. They originate from different accretive prism conditions, experimenting active basal erosion (Wang and Hu, 2006). In general, they are small structures (5-15 km wide and ~1-2 km high), such as those reported for Costa Rica (Weinrebe and Ranero, 2003), Peru (Kukowski et al., 2001; Hampel, 2002), North of Chile (Sallares and Ranero, 2005) Northern Japan (Kobayachi et al., 1998), Nicaragua (von Huene at al., 2004) and Ecuador (Sage et al., 2006). The different state of stress domains, together with structural styles, reveals active contraction in the frontal prism and extension in the middle slope (von Huene et al., 1999). Moreover, von Huene et al (2004), based on an analysis of the internal structure of the Northern Chile forearc, determined a lower basal friction than could be predicted there. This place has a very high-relief bathymetry (up to 1500 m of bathymetry difference between horst and grabens) of the Nazca plate in front of the Chilean trench. This suggests that the debris sediments, cumulated in the narrow frontal prism, are then incorporated into the SC filling grabens, smoothing the SC and hence reducing the abrasive capacity and overall friction of the lower plate.

Comparing digital images recorded by PIV of the final stages of the experiments, we observe a contrasting structural evolution. A 10 cm x 10 cm frontal prism evolved with a low relief floor surface HL.1. In contrast, with high relief (experiment HL.2), basal erosion consumed the prism completely, improving frontal erosion (cf. Fig. 5.5.3b, HL.1 and HL.2). The details of digital images reveal that the emulated horsts indent the tip while abrading it and material is carried between them toward the SC.

The prism that is absent in our experiment HL.2 but observed in nature may show the sediment-bared surface of the conveyor belt. The spaces between highs and lows are large enough compared to the sediment supply so that they do not overwhelm, thus an accretionary body can not develop. The SC geometry, resulting from this series, can show an implication above a fault zone, where asperities represent an important role in the stress and strain distribution. However, there is no evidence of forearcs with a frontal segment as in the HL.2 experiment, therefore a horst graben structure without any sediment is unlikely.

The complete evolution of the series from a forearc type initially as HL.1 and later a type HL.2 could represent the Japan case since the Pleistocene, with a fast subsidence of the lower slope and a prominent scarp structure on the lower slope (von Huene and Culotta, 1989). This might be by a progressive decreasing supply at the trench, accelerating the subduction frontal erosion since then.

6. CONCLUSIONS

An experimental data set of 12 analog experiments distributed into 4 series was established in order to investigate deformation processes related to the shallow portion of erosional convergent margins. Each experiment series was designed to investigate systematically a specific parameter. The design of these experiments was based on 70 preliminary test experiments (10 cm width x 50 cm length x different heights; Appendix A2), which had been performed to investigate a wide range of parameters. Several different configurations had been tested to study the influence of parameters that can become crucial for subduction erosion, although these were non-systematic studies. The main reason for that was that, as we lack a thorough understanding of parameters influencing subduction erosion, to perform small test experiments was much faster and simpler compared to perform experiments in a huge apparatus. The results of the test experiments allowed to decide about the final configuration of the experimental series, which then were performed in a considerably bigger experimental apparatus.

The structure of selected, erosional convergent margins, where well constrained from reflection seismic images, was interpreted in the context of experimental observations and predictions were made e.g. for the material transfer governing deformation at those margins. However, analog experiments have limitations due to (a) the physical properties of the granular analogue materials (i.e. material homogeneity vs different rock types), (b) the differences in failure style (i.e. distributed vs localized deformation) and (c) the lack of pore fluids (i.e. dry, subareal wedges vs submarine wedges).

However, still, the analogue experiments allowed us to come up with specific conclusions:

(1) Quantification of material transfer under systematically controlled boundary conditions:
   (i) For different widths of the subduction gap, an erosion ratio > 1 was observed when the capacity of the subduction gap was larger than the capacity of the subduction channel close to the tip of the wedge. Accretionary wedges developed when the subduction gap size was smaller than the capacity of the subduction channel close to the tip of the wedge.
   (ii) For different initial surface slopes, an erosion ratio > 1 occurred in case of wedges which were in the stable or critical state according to critical taper theory. Basal erosion as large as almost three times the frontal erosion was observed when the middle and upper slopes of the wedge maintained a stable state.
   (iii) For different strengths of the experiment material, an erosion ratio slightly > 1 occurred when the wedge material was relatively strong compared to the sand.
   (iv) If the subducting plate, i.e. the conveyor belt in the experiments, exhibited considerable topography, frontal erosion was significant and basal accretion close to zero. In the latter case, basal erosion was restricted to beneath the lower slope.

(2) Tectonic evolution, flow and geometric features of the subduction channel SC was found to be dependent on :

(i) For different widths of the subduction gap, a segmentation of the SC occurred when the capacity of the subduction gap was ≥ than the capacity of the SC close to the tip of the wedge. The segmentation was identified from the distribution of the velocity within the subduction channel. Wedges with a narrow SG developed a SC with uniform velocities along the base of the wedge. A wider SG led to the development of a SC with an inhomogeneous distribution of velocities along the base of the wedge, segmenting the SC and the slope geometry

(ii) For different surface tapers, a regular geometry of the SC occurred when the wedge was stable or critical. Subcritical tapers exhibited thicker SCs and irregular geometry through the higher recurrence of thrust reactivation beneath the lower and middle slopes.

SC thickness varied between very thin to very thick (from meters to kilometers) when the dip of the slope defined critical or stable tapers.

(iii) For different wedge strengths, a higher recurrence of thrust reactivation beneath the middle and upper slopes was observed when the wedge material was relatively weak, i.e. consisted of sand and not of the strong sand-sugar mixture.

A higher frequency of thrust reactivation led to a decrease of the total material transported by the SC.

(iv) The geometry of the SC was strongly modified from a sub-parallel to a "chain" shear zone, when the roughness of the incoming plate was high, simulating topographic highs and lows.

(3) Seismic reflection profiles or bathymetric data can be used for correlating experimental results with structures in forearcs, deformation processes and conditions upon the subduction channel:

(i) Large frontal prisms most likely coincide with a narrow SG (or global capacity) and convergent margins undergoing basal erosion with localized subsidence at the middle-upper slope have a wide SG.

(ii) Segmentation of the continental slope with the slope becoming shallower towards the interior of the orogen is indicative of basal removal of material beneath the middle and upper slope.

(iii) Scarps imply out-of-sequence thrusting and a global subduction capacity larger than the inlet capacity.

(iv) Margins with a pervasively fractured and sediment-bare oceanic plate undergo preferentially frontal erosion and enhanced basal erosion beneath the lower slope. The geometry of the SC is represented by a "chain" shape.

From all parameters tested, SG had the strongest influence on the wedge and the SC deformation, defining an accretionary or erosional margin. The surface taper defined a much larger erosion ratio for stable than for non-

stable wedges. The locus and amount of mass transfers were defined by the topographic structures of the conveyor belt and strong wedges had higher basal erosion than weak wedges.

7. OUTLOOK

1) Further modification of the experimental setup may include the study of a wider range of analogue granular materials, to also test the wide variety of rheologies or rock alteration in nature. Those former studies addressing erosional convergent margins have generally considered homogeneous wedges, while in nature this is an unlikely case.

2) Seismic analysis for the subduction channel could be better integrated with sandbox experiments. With the better resolution of seismic lines and a complementary analysis from analogue experiments a good correlation to natural observations can be achieved. The effect of topography of the incoming plate or a "global control point" should be considered for earthquake studies, as both parameters showed a large impact at the rear part of the wedge, where the seismogenic zone typically begins.

3) Some improvement to analogue experiments could include:
   (i) To model arcward variations in physical properties, integrating a slightly weaker segment beneath the middle-upper slope of the wedge
   (ii) To model variations in physical properties from the base of the wedge upwards, such as planes of weakness
   (iii) To include a thin layer of sediment on the conveyor belt in the "high and low" experimental setup

8. BIBLIOGRAPHY

Abers, G.A. (2005). Seismic low-velocity layer at the top of subducting slabs: observations, predictions, and systematics. Phys. Earth Planet. Inter., 149(1–2): 7–29.

Adam, J. and Reuther, C.D. (2000). Crustal dynamics and active fault mechanics during subduction erosion. Application of frictional wedge analysis on to the North Chilean Forearc. Tectonophysics, 321: 297-325.

Adam, J., Urai, J., Wieneke, B., Oncken, O., Pfeiffer, K., Kukowski, N., Lohrmann, J., Hoth, S., van der Zee, W., Schmatz J. (2005). Shear localisation and strain distribution during tectonic faulting: New insights from granular-flow experiments and high-resolution optical image correlation techniques, J. Struct. Geol., 27(2): 283 – 301, doi:10.1016/j.jsg.2004.08.008.

Armijo, R. and Thiele, R. (1990). Active faulting in northern Chile: ramp stacking and lateral decoupling along a subduction plate boundary?. Earth Planet. Sci. Lett., 98: 40–61.

Aubouin, J., Bourgois, J., and Azema, J. (1984). A new type of active margin: the convergent-extensional margin, as exemplified by the Middle America Trench off Guatemala. Earth Planet. Sci. Lett., 67:211-218.

Bachmann, R., J. Glodny, Oncken, O. and Seifert, W. (2009). Abandonment of the South Penninic-Austroalpine palaeosubduction zone, Central Alps, and shift from subduction erosion to accretion: Constraints from Rb/Sr geochronology, J. Geol. Soc., 16: 217–231, doi:10.1144/0016-76492008-024.

Ballance, P. F., Scholl, D. W., Vallier, T. L., Stevenson, A. J., Ryan, H. and Herzer, R. H. (1989). Subduction of a Late Cretaceous seamount of the Louisville chain at the Tonga Trench: A model of normal and accelerated tectonic erosion. Tectonics, 8: 953–962.

Bangs, N. L. B., Gulick, S. P. S. and Shipley T. H. (2006). Seamount subduction erosion in the Nankai Trough and its potential impact on the seismogenic zone. Geology, 34(8): 701–704, doi:10.1130/G22451.1.

Bangs, N. L., and Cande, S. C. (1997). Episodic development of a convergent margin inferred from structures and processes along the southern Chile margin. Tectonics, 16(3): 489–503, doi:10.1029/97TC00494.

Beaumont C, Ellis S, Pfiffner A. (1999). Dynamics of sediment subduction-accretion at convergent margins: Short-term modes, long-term deformation, and tectonic implications. J. Geophys Res., 104(B8):17573–17602.

Bonini, M. (2007). Deformation patterns and structural vergence in brittle–ductile thrust wedges: An additional analogue modelling perspective. Journal of Structural Geology, 29(1): 141-158.

Bose, S., Mandal, N., Mukhopadhyay, D.K., Mishra, P. (2009). An unstable kinematic state of the Himalayan tectonic wedge: evidence from experimental thrust-spacing pat- terns. Journal of Structural Geology 31 (1): 83–91.

Bourgois, J., Pautot, G., Bandy, W., Boinet, T., Chotin, P., Huchon, P., Mercier de Lepinay, B., Monge, F.,

Monlau, J., Pelletier, B., Sosson, M., von Huene, R. (1988). Sea Beam and seismic reflection imaging of the tectonic regime of the Andean continental margin off Peru (4°S to 10°S). Earth Planet. Sci. Lett., 87: 111 –126.

Brace, W. F. and Byerlee J. D. (1966). Stick-slip as a mechanism for earthquakes. Science, 153: 990–992, doi:10.1126/science.153.3739.990.

Byerlee, J. (1978). Friction of rocks. Pure Appl. geophys.,116(4-5): 615–626.

Byrne, D.S., Wang, W. and Davis, D. (1993). Mechanical role of backstops in the growth of forearcs. Tectonics, 12: 123-144.

Cadet, J.P., Kobayashi, K., Aubouin, J., Boulegue, J., Dubois, J., Von Huene, R., Jolivet, L., Kanazawa, T., Kasahara, J., Koizumi, K., Lallemand, S., Nakamura, Y., Pautot, G., Suyehiro, K., Tani, S., Tokuyama, H. and Yamazaki, T. (1985). De la fosse du Japon a la fosse des Kouriles: Premiers resultats de la campagne oceanographique franco-japonaise Kaiko (Leg III). C.R. Acad. Sci. Paris, 301, Ser. II, 5: 287-296.

Cadet, J.P., Kobayashi, K., Aubouin, J., Boulegue, J., Dubois, J., Von Huene, R., Jolivet, L., Kanazawa, T., Kasahara, J., Koizumi, K., Lallemand, S., Nakamura, Y., Pautot, G., Suyehiro, K., Tani, S., Tokuyama, H. and Yamazaki, T. (1987). The Japan trench and its juncture with the Kuril trench: cruise results of the KAIKO project, Leg 3. Earth Planet. Sci. Lett., 83: 267-284.

Calahorrano, A. (2005). Structure de la Marge du Golfe de Guayaquil (Equateur) et propriétés physiques du chenal de subduction, à partir des donnés de sismique marine, réflexion et refraction. Ph.D document, Univeristé Pierre et Marie Curie-Paris 6, 221pp.

Calahorrano, A., Sallares, V., Collot J.Y., Sage, F. and Ranero, C. (2008). Non linear variations of the physical properties along the southern Ecuador subduction channel: results from depth-migrated seismic data. Earth Planet. Sci. Lett. doi : 10.1016/j.epsl.2007.11.061

Calassou, S., Larroque, C., Malavieille, J. (1993). Transfer zones of deformation in thrust wedges: An experimental study. Tectonophysics, 221(3-4): 325-344.

Chapple, W. (1978). Mechanics of thin-skinned fold- and-thrust belts. Bulletin of the Geological Society of America, 89: 1189–1198.

Christeson, G.L., McIntosh, K.D., Shipley, T.H., Flueh, E.R., Goedde, H. (1999). Structure of the Costa Rica convergent margin, offshore Nicoya Peninsula. J. Geophys. Res. 104:25443–25468

Clift, P.D., and MacLeod, C.J. (1999). Slow rates of tectonic erosion estimated from the subsidence and tilting of the Tonga Forearc Basin. Geology, 27: 411 – 414.

Clift, P.D., Pecher, I., Kukowski, N., Hampel, A. (2003). Tectonic erosion of the Peruvian forearc, Lima Basin, by subduction and Nazca Ridge collision. Tectonics, 22(3), 1023, doi:10.1029/2002TC001386.

Clift, P. and Vannucchi, P. (2004). Controls on tectonic accretion versus erosion in subduction zones: Implications for the origin and

recycling of the continental crust. Rev. Geophys., 42, RG2001, doi:10.1029/2003RG000127.

Clift, P. and Hartley A.J. (2007). Slow rates of subduction erosion and coastal underplating along the Andean margin of Chile and Peru. Geology, 35: 503–506, doi: 10.1130/G23584A.1.

Cloos, M. and Shreve, R.L. (1988a). Subduction-Channel Model of Prism Accretion, Melange Formation, Sediment Subduction, and Subduction Erosion at Convergent Plate Margins: 1. Background and Description. Pure and Applied Geophysics, 128(3-4): 455–500.

Cloos, M. and Shreve, R.L. (1988b). Subduction-Channel Model of Prism Accretion, Melange Formation, Sediment Subduction, and Subduction Erosion at Convergent Plate Margins: 2. Implications and Discussion. Pure and Applied Geophysics 128, (3-4): 501–545.

Cloos, M. (2006). Paper No. 16-6, Session No. 16, Backbone of the Americas—Patagonia to Alaska, (3–7 April 2006), Mendoza, Mendoza Province

Coats, R. R. (1962). Magma type and crustal structure in the Aleutian Arc. In Crust of the Pacific Basin. Geophys. Monogr. Ser., 6: 92-109. Washington, DC: Am. Geophys. Union

Collot, J.Y., Charvis, P., Gutscher, M.A., Operto S. (2002). Exploring the Ecuador-Colombia Active Margin and Interplate Seismogenic Zone. Eos Trans. AGU, 83(17): 185, 189-190, doi:10.1029/2002EO000120.

Collot, J.Y., Ribodetti, A., Agudelo, W., Sage, F. (2011). The South Ecuador subduction channel: Evidence for a dynamic mega-shear zone from 2D fine-scale seismic reflection imaging and implications for material transfer. J. Geophys. Res., 116, B11102, doi:10.1029/2011JB008429.

Contreras-Reyes, E., Flueh, E.R., Grevemeyer, I. (2010). Tectonic control on sediment accretion and subduction off south central Chile: Implications for coseismic rupture processes of the 1960 and 2010 megathrust earthquakes. Tectonics, 29, TC6018, doi: 10.1029/2010TC002734

Contreras-Reyes, E. and Carrizo, D. (2011). Control of high oceanic features and subduction channel on earthquake ruptures along the Chile-Peru subduction zone. Physics of the Earth and Planetary Interiors, 186(1-2): 49-58.

Dahlen, F.A., Suppe, J., Davis, D.M. (1984). Mechanics of fold-and-thrust belts and accretionary wedges: cohesive Coulomb theory. Jour. Geophys. Res. 89: 10087-10101.

Dahlen, F.A. (1984). Noncohesive critical Coulomb wedges: an exact solution. J. Geophys. Res. 89: 10125–10133;

Dahlen, F. A. and Suppe, J. (1988). Mechanics, growth, and erosion of mountain belts. In: Clark, S., Burchfield, B. c. and Suppe, J., editors, Processes in Continental Lithospheric Deformation, 218: 161–178.

Dahlen, F.A. (1990). Critical taper model of fold-and-thrust belt sand accretionary wedges. Annu.Rev. Earth Planet. Sci. 1: 55-99.

Davis, D., Suppe, J., Dahlen, F.A. (1983). Mechanics of fold-and-thrust

belts and accretionary wedges. J. Geophys. Res. 88: 1153–1172.

Delouis, B., Cisternas, A., Dorbath, L., Rivera, L., Kausel, E. (1996). The Andean subduction zone between 22 and 25°S (northern Chile): precise geometry and state of stress. Tectonophysics, 259: 81–100.

DeMets, C. and Dixon, T.H. (1999). New kinematic models for Pacific-North America motion from 3 Ma to present: I. Evidence for steady motion and biases in the NUVEL-1A model. Geophys. Res. Let. 26: 1921–1924.

Du Bernard, X., Eichhubl, P., Aydin, A. (2002). Dilation bands: A new form of localized failure in granular media. Geophysical Research Letters, 29(24), 2176, doi:10.1029/2002GL015966.

Eberhart-Phillips, D., Martin, R. (1999). Plate interface properties in the north-east Hikurangi subduction zone, New Zealand, from converted seismic waves. Geophys. Res. Lett. 26(16): 2565–2568.

Ellis, S., Beaumont, C., Pfiffner, O.A. (1999). Geodynamic models of crustal-scale episodic tectonic accretion and underplating in sub- duction zones. J. Geophys. Res. 104(B7):15169–15190

Fagereng, A. and Sibson, R.H. (2007). Is the Chrystalls Beach Accretionary Mélange a Fossil Subduction Channel Shear Zone? AGU Fall Meeting 2007

Fincham, A.M. and Spedding, G.R. (1997). Low cost high resolution DPIV for measurement of turbulent fluids. Experiments in Fluids 23: 449–462.

Gerbault, M., Mpodozis, J., Farias, C., Pardo M, M. (2009). Continental Margin Deformation along the Andean Subduction zone: Thermomechanical Models. Physics of the Earth and Planetary Interiors, doi:10.1016/j.pepi.2009.09.001

Gilluly, J. (1963). Tectonic evolution of the western United States. Geol. Soc. London Q. J. 119: 133-174

Glodny, J., Lohrmann, J., Echtler, H., Gräfe, K., Seifert, W., Collao, S., Figueroa, O. (2005). Internal dynamics of a paleoaccretionary wedge: insights from combined isotope tectonochronology and sandbox modelling of the South-Central Chilean forearc. Earth Planet. Sci. Lett. 231(1–2): 23–39

Gurnis, M. (1992). Rapid continental subsidence following the initiation and evolution of subduction. Science, 255: 1556-1558.

Gutscher, M.A., Kukowski, N., Malavieille, J., Lallemand, S.E. (1996). Cyclical behavior of thrust wedges: insights from high basal friction sandbox experiments. Geology 24: 135-138.

Gutscher, M.A., Kukowski, N., Malavieille, J., Lallemand, S.E. (1998a). Episodic imbricate thrusting and underthrusting: Analog experiments and mechanical analysis applied to the Alaskan Accretionary Wedge. J. Geophys. Res., 103(B5): 10161-10176.

Gutscher, M.A., Kukowski, N., Malavieille, J., Lallemand, S.E. (1998b). Material transfer in accretionary wedges from analysis of a systematic series of analog experiments. Journal of Structural Geology, 20(4): 407-416.

Hampel, A. (2002). The migration history of the Nazca Ridge along the Peruvian active margin: A re-

evaluation and some geological implications. Earth and Planetary Science Letters, 203: 655–679.

Hampel, A., Adam, J. and Kukowski, N. (2004). Response of the tectonically erosive south Peruvian forearc to subduction of the Nazca Ridge: Analysis of three¿dimensional analogue experiments. Tectonics 23: doi: 10.1029/2003TC001585. issn: 0278-7407.

Hampel, A., Kukowski, N., Bialas, J., Hübscher, C., Heinbockel, R. (2004). Ridge subduction at an erosive margin - the collision zone of the Nazca Ridge and South Peru. Journal of Geophysical Research, 109, B2, B02101, doi: 10.1029/2003JB002593.

Harders, R., Ranero, C. R., Weinrebe, W., Behrmann, J.H. (2011). Submarine slope failures along the convergent continental margin of the Middle America Trench. Geochem. Geophys. Geosyst., 12, Q05S32, doi:10.1029/2010GC003401.

Heki, K. (2004). Space geodetic observation of deep basal subduction erosion in northeastern Japan. Earth and Planetary Science Letters, 219(1-2), 28: 13-20, doi:10.1016/S0012-821X(03)00693-9.

Hilde, T.W.C. (1983). Sediment subduction vs. accretion around the Pacific. Tectonophysics, 99: 381– 397.

Hilde, T. W. C. and Uyeda, S. (1983). Trench depth: Variation and significance. In: Geodynamics of the Western Pacific-Indonesian Region, Geodyn. Ser., vol. 11, edited by T. W. C. Hilde and S. Uyeda, pp. 75–89, AGU, Washington, D. C., doi:10.1029/GD011p0075.

Horsfield, W.T. (1977). An experimental approach to basement-controlled faulting. Geologie en Mijnbouw, 56(4): 363-370.

Hoth, S., Hoffmann-Rothe, A., Kukowski, N. (2007). Frontal accretion: An internal clock for bivergent wedge deformation and surface uplift. J. Geophys. Res., 112, B06408, doi:10.1029/2006JB004357.

Hubbert, M.K. (1937). Theory of scale models as applied to the study of geological structures. Bulletin of the Geological Society of America, 48: 1459–1520.

Hubbert, M.K., and Rubey, W.W. (1959). Role of fluid pressure in mechanics of overthrust faulting, I, Mechanics of fluid-filled solids and its application to overthrust faulting. Geol. Soc. Am. Bull., 70: 115-166.

IODP Preliminary Report 334 (Expedition 334 Scientists (2011)). Costa Rica Seismogenesis Project (CRISP): sampling and quantifying input to the seismogenic zone and fluid output. IODP Prel. Rept., 334. doi:10.2204/iodp.pr.334.2011

Jarrard, R. D. (1986). Terrane motion by strike-slip faulting of forearc slivers. Geology, 14: 780–783.

Krabbenhöft, A., Bialas, J., Kopp, H., Kukowski, N., Hübscher, C. (2004). Crustal structure of the Peruvian Continental Margin from wide- angle seismic studies. Geophys. J. Int. 159: 749–764

Keppie, D.F., Currie, C., Warren, C. (2009). Subduction erosion modes: Comparing finite element numerical models with the geological record. Earth Planet. Sci. Lett., doi:10.1016/j.epsl.2009.08.009

Kirby, S. H., Engdahl, E. R., Denlinger, R. (1996). Intermediate-depth intraslab earthquakes and arc volcanism as physical expressions of crustal and uppermost mantle metamorphism in subducting slabs (overview). In: Subduction Top to Bottom, Geophys. Monogr. Ser., vol. 96, edited by G. E. Bebout, et al., pp. 195 – 214, AGU, Washington, D.C.,

Klinkmüller, M. and Schreurs, G. (2008). The shear zone geometry of different granular analogue modelling materials under compression: insights from experiments monitored by X-ray Computed Tomography and image analysis software. GeoMod 2010.

Kobayashi, K., Nakanishi, M., Tamaki, K., and Ogawa, Y. (1998). Outer slope faulting associated with the western Kuril and Japan trenches. Geophysical Journal International, 134: 356–372.

Kopp, H.; Kukowski, N. (2003). Backstop geometry and accretionary mechanics of the Sunda margin. Tectonics, 22(6), 1072: 1-16, doi: 10.1029/2002TC001420

Kopp, H., Flueh, E.R., Petersen, C.J., Weinrebe, W., Wittwer, A., Meramex Scientists (2006). The Java margin revisited: Evidence for subduction erosion off Java Earth Planet. Sci. Lett., 242(1–2): 130-142.

Koyi, H.A. (1997). Analogue modelling; From a qualitative to a quantitative technique, a historical outline. *Journal of Petroleum Geology*, 20(2): 223-238.

Kukowski, N., von Huene, R., Malavieille, J., Lallemand, S. (1994). Sediment accretion against a buttress beneath the Peruvian continental margin as simulated by sandbox modeling. Geologische Rundschau, 83: 822–831.

Kukowski, N., Hampel, A., Bialas, J., Huebscher, C., Barckhausen, U., Bourgois, J. (2001). Tectonic erosion at the Peruvian margin: Evidence from swath bathymetry data and process identification from 3D sandbox analogue modeling. Eos Trans. AGU, 82(47), Fall Meet. Suppl., Abstract T31A- 0817.

Kukowski, N., Malavieille, J., Gutscher, M.A., Lallemand, S.E., Reston, T.J. (2002). Mechanical decoupling and basal duplex formation observed in sandbox experiments with application to the Western Mediterranean Ridge accretionary complex. Mar. Geol. (187): 29–42.

Kukowski, N. and Onken, O. (2006). Subduction Erosion – the "Normal" Mode of Fore-Arc Material Transfer along the Chilean Margin?; In: Oncken O, Chong G, Franz G, Giese P, Götze H-J, Ramos VA, Strecker MR, Wigger P (eds) The Andes – active subduction orogeny. Frontiers in Earth Science Series, Vol 1. Springer-Verlag, Berlin Heidelberg New York: 216–236

Kukowski, N., Hampel, A., Hoth, S., Bialas, J. (2008). Morphotectonic and morphometric analysis of the Nazca plate and the adjacent offshore Peruvian continental slope - Implications for submarine landscape evolution. Marine Geology, 254(1-2): 107-120.

Lallemand, S.E., Schnurle, P., Manoussis, S. (1992a). Reconstruction of subduction zone palcogeometries and quantification of upper plate material losses caused by tectonic erosion, J. Geophys. Res., 97: 217-239.

Lallemand, S.E., Malavieille, J., Calassou, S. (1992b). Effects of oceanic ridge subduction on accretionary wedges: Experimental modeling and marine observations. Tectonics, 11: 1301-1313.

Lallemand, S.E., Schnurle, P., Malavieille, J. (1994). Coulomb theory applied to accretionary and non-accretionary wedges: Possible causes for tectonic erosion and/or frontal accretion. Journal of Geophysical Research, 99: 12033–12055

Lallemand, S. E. (1998). Possible interaction between mantle dynamics and high rates of arc consumption by subduction processes in circum-Pacific area, in Mantle Dynamics and Plate Interactions in East Asia, Geodyn. Ser., vol. 27, edited by M. F. J. Flower et al., pp. 1–9, AGU, Washington, D. C., doi:10.1029/GD027p0001.

Langseth, M.G., von Huene, R., Nasu, N., Okada, H. (1980). Subsidence of the Japan Trench forearc region of northern Honshu. Oceanol. Acta, Proceedings 26th International Geological Congress, Geology of Continental Margins Symposium, Paris, July 7-17.

Laursen, J., Scholl, D.W., von Huene, R. (2002). Neotectonic deformation of the central Chile margin: Deepwater forearc basin formation in response to hot spot ridge and seamount subduction. Tectonics, 21(5), 1038, doi:10.1029/2001TC901023.

Lehner, F. K. (1986). Comments on "Noncohesive critical Coulomb wedges: An exact solution" by F. A. Dahlen, J. Geophys. Res., 91(B1): 793–796, doi:10.1029/JB091iB01p00793.

Lickorish, W.H., Ford, M., Bürgisser, J., Cobbold, P.R. (2002). Arcuate thrust systems in sandbox experiments: a comparison to the external arcs of the Western Alps. Geo- logical Society of America Bulletin 114 (9): 1089–1107.

Lohrmann, J., Kukowski, N., Adam, J., Oncken, O. (2003). The impact of analogue material parameters on the geometry, kinematics, and dynamics of convergent sand wedges. Journal of Structural Geology, 25(10): 1691–1711.

Lohrmann, J., Kukowski, N., Krawczyk, C.M., Oncken, O., Sick, C., Sobiesiak, M., Rietbrock, A. (2006). Subduction channel evolution in brittle forearc wedges – a combined study with scaled sandbox experiments,seismological and reflection seismic data and geological field evidence. In: Oncken, O., Chong, G., Franz, G., Giese, P., Götze, H.J., Ramos, V.A., Strecker, M.R., Wigger, P. (eds) The Andes – active subduction orogeny. Frontiers in Earth Science Series, Vol 1. Springer-Verlag, Berlin Heidelberg New York: 237–262

McCarthy, J. and Scholl, D. (1985). Mechanisms of subduction accretion along the central Aleutian Trench. Geological Society of America Bulletin, 96(6): 691-701

McClay, K.R. (1996). Recent advances in analogue modelling: uses in section interpretation and validation. In: Buchanan, P.G., Nieuwland, D.A. (Eds.), Modern Developments in Structural Interpretation, Validation and Modelling Geological Society Special Publication, 99: 201–225.

Mercier de Lepinay, B., Michaud, F., Calmus, T., Bourgois, J., Poupeau, G., Saint Marc, P., The NAUTIMATE team. (1997). Large Neogene

subsidence event along the Middle America Trench off Mexico (18°–19°N): Evidence from submersible observations. Geology, 25: 387–390.

Miller, H. (1970a). Das Problem des hypothetischen Pazifischen Kontinentes gesehen von derchilenischen Pazifikkueste. Geol. Rundsch. 59: 927–938.

Miller, H. (1970b). Vergleichende Studies an pramesozoischen Gesteinen Chiles unter besondererBerucksichtigung ihrer Kleintektonik. Geotek. Forsch. 36: 1–64

Murauchi, S. and Ludwig, W.J. (1980). Crustal structure of the Japan Trench: the effect of subduction of ocean crust. In: Scientific Party, Init. Repts. DSDP, 56, 57, Pt. 1: Washington (U.S. Govt. Printing Office): 463-469.

Nilforoushan, F., Koyi, H., Swantesson, J.O.H., Talbot, C. (2008). Effect of basal friction on surface and volumetric strain in models of convergent settings measured by laser scanner. Journal of Structural Geology, 30(3): 366–379.

Oncken, O., Sobolev, S., Sitller, M. (2003). Seismic imaging of a convergent continental margin and plateau in the central Andes (Andean Continental Research Project 1996 (ANCORP' 96)). J. Geophys. Res. 108 (B7) Art. No. 2328.

Oncken, O., Hindle, D., Kley, J., Elger, K., Victor, P., Schemmann, K. (2006). Deformation of the Central Andean Upper Plate System - Facts, Fiction, and Constraints for Plateau Models - In:
Oncken, O., Chong, G., Franz, G., Giese, P., Götze, H.J., Ramos, V., Strecker, M., Wigger, P. (Eds.), The Andes - Active Subduction Orogeny, Springer, 3-27.

Paterson, M.S. (1978). Experimental Rock Deformation - The Brittle Field, 254 pp., Springer, New York.

Panien, M., Schreurs, G., Pfiffner, A. (2006). Mechanical behaviour of granular materials used in analogue modeling: insights from grain characterization, ring-shear tests and analogue experiments. Journal Structural Geology 28: 1710-1724.

Patzig, R. (2000). Lokalbeben-Tomographie der Umgebung von Antofagasta (Nordchile) sowie Betrachtungen der Magnituden-Häufigkeits-Parameter in dieser Region. PhD thesis, Freie Universität Berlin

Platt, J.P. (1986). Dynamics of orogenic wedges and the uplift of high-pressure metamorphic rocks. Geol. Soc. Am. Bull., 97: 1037 – 1053.

Ramberg, H. (1981). Gravity, deformation and the earth‘s crust. Academic Press, New York.

Ranero, C.R., von Huene, R., Flueh, E., Duarte, M., Baca, D., McIntosh, K. (2000). A cross section of the convergent Pacific margin of Nicaragua. Tectonics, 19(2): 335–357, doi:10.1029/1999TC900045.

Ranero, C.R. and von Huene, R. (2000). Subduction erosion along the Middle America convergent margin. Nature 404(6779): 748-752.

Ranero, C.R. and Sallares, V. (2004). Geophysical evidence for hydration of the crust and mantle of the Nazca plate

during bending at the north Chile trench. Geology, 32(7): 549–552.

Ranero, C.R., von Huene, R., Weinrebe, W., Reichert, C. (2006). Tectonic processes along the Chile convergent margin. In: Oncken, O., Chong, G., Franz, G., Giese, P., Götze, H.J., Ramos, V.A., Strecker, M.R., Wigger, P. (eds) The Andes – active subduction orogeny. Frontiers in Earth Science Series, Vol 1. Springer-Verlag, Berlin Heidelberg New York: 91–119.

Ranero, C.R., Grevemeyer, I., Sahling, H., Barckhausen, U., Hensen, C., Wallmann, K., Weinrebe, W., Vannucchi, P., von Huene, R., McIntosh, K. (2008). The hydrogeological system of erosional convergent margins and its influence on tectonics and interplate seismogenesis: Geochemistry Geophysics Geosystems, 9(3), Q03S04, doi: 10.1029/2007GC001679.

Rutland, R.W.R. (1971). Andean orogeny and ocean floor spreading. Nature 233: 252–255

Sage, F., Collot, J.Y., Ranero, C. (2006). Interplate patchiness and subduction-erosion mechanisms: Evidence from Depth Migrated Seismic Images at the Central Ecuador convergent margin. Geology, 34(12): 997–1000.

Sallarès, V. and Ranero, C. (2005). Structure and Tectonics of the erosional convergent margin off Antofagasta, North Chile (23°30'S). Journal of Geophysical Research - Solid Earth and Planets, 110. B06101. ISSN 0148-0227, doi:10.1029/2004JB003418.

Scarano, F. and Riethmuller, M.L. (2000). Advances in iterative multigrid PIV image processing. Experiments in Fluids (Suppl.) 29: 51–60.

Schellart, W.P. (2000). Shear test results for cohesion and friction coefficients for different granular materials: scaling implications for their usage in analogue modeling. Tectonophysics, 324: 1-16.

Scheuber, E. and Reutter, K. J. (1992). Magmatic arc tectonics in the Central Andes between 21º and 25ºS. Tectonophysics, 205: 127 – 140.

Scheuber, E. (1994). Tektonische Entwicklung des nordchilenischen aktiven Kontinentalrandes: Der Einflu·von Plattenkonvergenz und Rheologie. Geotektonische Forschungen. 81: 1-131.

Scholl, D.W., Christensen, M., von Huene, R., Marlow, M. (1970). Peru-Chile Trench Sediments and Sea-Floor Spreading. Geological Society of America Bulletin, 81: 1339-1360.

Scholl, D.W., von Huene, R., Vallier, T.L., Howell, D.G. (1980). Sedimentary masses and conceptsabout tectonic processes at underthrust ocean margins. Geology, 8: 564–568.

Scholl, D. W., von Huene, R., Ryan, H. F. (2002). Basal subduction erosion and the formation of the Aleutian Terrace and underlying forearc basin. In: Program and Abstracts, 3rd Biennial Workshop on Subduction Processes Emphasizing the Kurile-Kamchatka-Aleutian Arc: 61– 62, Geophys. Inst., Univ. of Alaska, Fairbanks.

Schulze, D. (1994). Entwicklung und Anwendung eines neuartigen Ringschergerätes.
Aufbereitungstechnik, 35(10): 524–535.

Shipley, T.H. and Moore, G.F. (1986). Sediment accretion, subduction and dewatering at the base of the trench slope off Costa Rica: A seismic reflection view of the decollement, J. Geophys. Res., 91: 2019-2028.

Schweller, W.J. and Kulm, L.D. (1978). Extensional rupture of oceanic crust in the Chile Trench. Mar. Geol., 28: 271-291.

Scholl, D. (2002). Basal Subduction Erosion and the Formation of the Aleutian Terrace and Underlying Forearc Basin. Proceeding of the 3rd International Biennial Workshop on Subduction Processes, University of Alaska, Fairbanks, June 10-14.

Scholl D. and von Huene R. (2009). Implications of estimated magmatic additions and recycling losses at the subduction zones of accretionary (non-collisional) and collisional (suturing) orogens. Geological Society, London, Special Publications 2009, 318: 105-125, doi:10.1144/SP318.4

Sick, C., Yoon, M.K., Rauch, K., Buske, S., Lüth, S., Araneda, M., Bataille, K., Chong, G., Giese, P., Krawczyk, C., Mechie, J., Meyer, H., Oncken, O., Reichert, C., Schmitz, M., Shapiro, S., Stiller, M., Wigger, P. (2006). Seismic images of accretive and erosive subduction zones from the Chilean margin. In: Oncken O, Chong G, Franz G, Giese P, Götze H-J, Ramos VA, Strecker MR, Wigger P (eds) The Andes –active subduction orogeny. Frontiers in Earth Science Series, Vol 1. Springer-Verlag, Berlin Heidelberg New York: 147–170.

Silver, E.A. (1969). Late Cenozoic underthrusting of the continental margin off northernmost California. Science 166(3910): 1265-66

Sobiesiak, M.M., Meyer, U., Schmidt, S., Götze, H.J., Krawczyk, C. (2007). Asperity generating upper crustal sources revealed by b-value and isostatic residual anomaly grids in the area of Antofagasta. Journal of Geophysical Research, 112, B12308, doi: 10.1029/2006JB004796.

Stem, C. R. (1991). Role of subduction erosion in the generation of Andean magmas. Geology, 19: 78-81.

Terzaghi, K. (1943). Theoretical Soil Mechanics. John Wiley, New York.

Tilling, R.I., Heliker, C., Wright, T.L. (1987). Eruptions of Hawaiian Volcanoes: Past, Present, and Future: U.S. Geological Survey General Interest Publication, 54 pp.

Toth, J. and Gurnis, M. (1998). Dynamics of subduction initiation at preexisting fault zones. J. Geophys. Res., 103: 18053-18067.

Tsuru, T., Park, J.O., Takahashi, N., Kodaira, S., Kido, Y., Kaneda, Y., Kono, T. (2000). Tectonic features of the Japan Trench convergent margin and fracture zones beneath northeastern Japan revealed by multi-channel seismic reflection data. J. Geophys. Res., 105: 16403-16413.

Tsuru, T., Park, J., Miura, S., Kodaira, S., Kido, Y. and Hayashi, T. (2002). Along-arc structural variation of the plate boundary at the Japan Trench margin: Implication of interplate coupling. Journal of Geophysical Research 107(B12): doi: 10.1029/2001JB001664. issn: 0148-0227.

Uyeda, S. and Kanamori, H. (1979). Back-arc opening and the mode of

subduction. J. Geophys. Res., 84(3): 1049–1061

Vanneste, L. and Larter, R. (2002). Sediment subduction, subduction erosion, and strain regime in the northern South Sandwich forearc. J. Geophys. Res., 107(B7), 2149, doi:10.1029/2001JB000396.

Vannucchi, P., Scholl, D.W., Meschede, M., McDougall-Reid, K. (2001). Tectonic erosion and consequent collapse of the Pacific margin of Costa Rica: Combined implications from ODP Leg 170, seismic offshore data, and regional geology of the Nicoya Peninsula. Tectonics, 20: 649–668.

Vannucchi, P., Ranero, C.R., Galeotti, S., Straub, S., Scholl, D.W., McDougall-Ried, K. (2003). *Fast rates of subduction erosion along the Costa Rica Pacific margin: implications for non-steady rates of crustal recycling at subduction zones.* Journal of Geophysical Research-Solid Earth, 108 (B11). ISSN 0148-0227.

Vannucchi, P., Galeotti, S., Clift, P., von Huene, C. (2004). Long-term subduction-erosion along Guatemala margin of the Middle America trench. Geology, 32(7): 617-620, doi: 10.1130/G20422.1

Vannucchi, P., Remitti, F., Bettelli, G. (2008). Geologic record of fluid flow and seismogenesis along an erosive subducting plate boundary. Nature, 451: 699-703, doi:10.1038/nature06486.

Vannucchi, P., Sage, F., Phipps Morgan, J., Remitti F., Collot, J.Y. (2012). Toward a dynamic concept of the subduction channel at erosive convergent margins with implications for interplate material transfer. Geochemistry Geophysics Geosystems, 13(1): 1-24, doi: 10.1029/2011GC003846.

von Huene, R., Aubouin, J. et al. (1985). Summary: Leg 84, Middle America Trench transect off Guatemala and Costa Rica. In: von Huene, R., Aubouin, J., et al. Initial reports of the Deep Sea Drilling Project, Volume 84: Washington, D.C., Government Printing Office: 939–957.

von Huene, R. and Culotta, R. (1989). Tectonic erosion at the front of the Japan Trench convergent margin. Tectonophysics, 160: 75–90,

von Huene, R. and Lallemand, S. (1990). Tectonic erosion along the Japan and Peru convergent margins. Geol. Soc. Am. Bull., 102: 704-720.

von Huene, R. and Scholl, D. (1991). Observations at convergent margins concerning sediment subduction, subduction erosion, and the growth of continental crust, Rev. Geophys., 29(3): 279– 316.

von Huene, R., Klaeschen, D., Cropp, B., Miller, J. (1994). Tectonic structure across the accretionary and erosional parts of the Japan Trench margin. J. Geophys. Res., 99(B11): 22349-22361

von Huene, R. and Ranero, C.R. (1998). Analogous segmentation, ocean crust, continental margin, and volcanoes in Costa Rica. Eos Trans. AGU 79 (45), Fall Meet. Suppl.F, 395.

von Huene, R., Weinrebe, W., Heeren, F. (1999). Subduction erosion along the North Chile margin. J. Geo- dyn., 27: 345–358.

von Huene, R., Ranero, C.R., Weinrebe, W., Hinz, K. (2000). Quaternary convergent margin

tectonics of Costa Rica, segmentation of the Cocos Plate, and Central American volcanism. Tectonics, 19(2): 314–334, doi:10.1029/1999TC001143.

von Huene, R. and Ranero, C.R. (2003). Subduction erosion and basal friction along the sediment-starved convergent margin off Antofagasta, Chile. J. Geophys. Res., 108(B2), 2079, doi:10.1029/2001JB001569.

von Huene, R., Ranero, C.R., Vannucchi, P. (2004). Generic model of subduction erosion. Geology, 32(10): 913–916, doi: 10.1130/G20563.1

von Huene, R., Ranero, C.R., Scholl, D. (2009). Convergent Margin Structure in High-Quality Geophysical Images and Current Kinematic and Dynamic ModelsS. In: Lallemand and F. Funiciello (eds.), Subduction Zone Geodynamics, 137. doi:10.1007/978-3-540-87974-9, © Springer-Verlag Berlin Heidelberg 2009

Wang, K. and Hu, Y. (2006). Accretionary prisms in subduction earthquake cycles: The theory of dynamic Coulomb wedge. Journal of Geophysical Research, 111, B06410, doi: 10.1029/2005JB004094

Wang, K., Hu, Y., von Huene R., Kukowski, N. (2010). Interplate earthquakes as a driver of shallow subduction erosion. Geology, 38: 431-434, doi: 10.1130/G30597.1

Weinrebe, W. and Ranero, C.R. (2003). RV SONNE Cruise Report SO173/2 ‘‘Subduction’’: Kiel, GEOMAR Report 116, 142 pp.

Wessel, J., Fryer, P., Wessel, P. and Taylor, B. (1994). Extension in the northern Mariana forearc. J. Geophys. Res., 99(B8): 15181-15203.

White, D.J., Take, W.A., Bolton, M.D. (2001). Measuring soil deformation in geotechnical models using digital images and PIV analysis. 10th International Conference on Computer Methods and Advances in Geomechanics. Tucson, Arizona. pp 997-1002 pub. Balkema, Rotterdam.

Wieneke, B. (2001). PIV adaptive multi-pass correlation with deformed interrogation windows. PIV Challenge 2001: 1–6.

Willett, S., Beaumont, C. and Fullsack, P. (1993). Mechanical model for the tectonics of doubly vergent compressional orogens. Geology, 21(4), 371–374.

Zhu, J. (2010). Crustal structure and subduction erosion in the central Costa Rica subduction zone. Dissertation zur Erlangung des Doktorgrades der Mathematischen-Naturwissenschaftlichen Fakultat der Christian-Albrechts-Universitat zu Kiel. 129 pp.

10. Zusammenfassung

Die hohen tektonischen Aktivitätsraten und das Vorkommen großer Erzablagerungen haben konvergente Plattenränder zum Fokus intensiver Forschung werden lassen. Von den zwei prinzipiellen Typen konvergenter Plattenränder (akkretiv und erosiv) machen die tektonisch erosiven Ränder mindestens 60% der Gesamtheit der Konvergenzzonen aus. Ihre Erforschung gestaltet sich schwieriger als bei akkretiven Rändern, weil durch die an ihnen ablaufende tektonische Verschluckung keine geologischen Hinweisstücke, aus denen Rückschlüsse auf aktive Prozesse zu ziehen wären, aufzufinden sind. Das ist der wahrscheinliche Grund, warum sich ein Großteil der Forschung auf akkretive Systeme konzentriert. Die vorliegende Studie jedoch zielt auf die Erforschung der weniger gut verstandenen erosiven Plattenränder ab.

Wir versuchen hierbei, Parameter, die möglicherweise die auftretenden Typen von Massenbewegungen kontrollieren oder beeinflussen, zu identifizieren. Dieses Vorhaben wird umgesetzt durch die Simulation mittels vier verschiedener Serien von analogen Sandkasten-Experimenten, in denen körniges Material verwendet wird, welches das gleiche Deformationsverhalten wie spröder Fels besitzt. Jede dieser Serien zielt auf die Erforschung des Einflusses eines Parameters, der möglicherweise Subduktionserosion auslöst, ab: die Menge an Sediment, die durch den Subduktionskanal (SK) entlang des Slabs nach unten transportiert werden kann, die durch den Keilwinkel bestimmte Auflast, die auf Material im Akkretionskeil wirkt, die internen Eigenschaften des Keils (mechanische Stärke) und die Topographie der basalen Grenzfläche, die mit dem Keil interagiert. Zusätzlich zur Analyse der skalierten physikalischen Experimente konnten wir mittels PIV, einer Methode zur Visualisierung von Materialfluss, bestimmte Muster von Massenbewegungen identifizieren.

Wir analysierten unsere Experimente hinsichtlich der Entwicklung interner und basaler Massenbewegungstypen (vertikale und horizontale Komponenten des Geschwindigkeitsfelds der Partikel), Muster dieser Massenbewegungstypen, Keilgeometrie, Entwicklung des SK und der Reibungseigenschaften des verwendeten körnigen Materials. Für jede der Experimentserien wurden diese Charakteristika diskutiert und auf Eigenschaften verschiedener real existierender erosiver Plattenränder weltweit bezogen, wobei ihre Relevanz im Bezug auf den Erosionsprozess bewertet wurde.

Einige gemeinsame Eigenschaften erosiver Plattenränder wurden in den ersten konzeptuellen Modellen abgeleitet, die auf eine Erklärung der Verschluckung des Forearcs abzielten. Im Vergleich zu akkretiven Forearcs besitzen erosive Plattenränder größere Keilwinkel, und ihre Neigungsfläche wird typischerweise in ein oberes, mittleres und unteres Segment aufgeteilt. Die Neigungsfläche zeigt Merkmale von Extension, wie Abschiebungen, landwärts geneigte Blöcke und seewärts geneigte Forearcs, aktive Massenbewegungen und damit einhergehende irregulär geformte Oberflächen. Die bei erosiven Rändern rauere ozeanische Platte zeigt höhere Konvergenzgeschwindigkeiten und ist mit einer dünneren Sedimentschicht bedeckt. Die Mächtigkeit des SK beträgt gewöhnlich weniger als 2 km, das frontale Prisma ist kleiner. Subsidenz mit gleichzeitiger Neigung und Abschiebungen deformieren entweder das mittlere oder obere Segment der Neigungsfläche, oder beide. Manche erosiven Plattenränder zeigen steile Abbruchkanten im mittleren Segment. Verstärkte Subsidenz, die von basaler Erosion verursacht wird, wird gewöhnlich im Bereich des mittleren bis oberen Segments beobachtet.

Das Deformationsverhalten von Mohr-Coulomb Materialien (wie Fels oder körniges Material, welches hier verwendet wurde) ist gekennzeichnet von zeitlich variablen Werten der Reibungsfestigkeit

(maximale, stabil-statische oder stabil-dynamische Reibungsfestigkeit). Dies hat zur Folge, dass für die Analyse des kritischen Keilwinkels die auftretenden örtlichen und zeitlichen Änderungen der Reibungsfestigkeit bei der Interpretation berücksichtigt werden müssen.

Zuerst wurde ein Idealbild eines erosiven Forearcs als Referenzexperiment kreiert, um das bestgeeignete Szenario zur Erzeugung von basaler Erosion zu erzeugen. Um das zu erreichen, bauten wir einen initial kritischen Keil, ohne die Akkretion einer mit der ozeanischen Platte hereinkommenden Sandschicht, mit einer basalen Entkopplungszone mit hoher Reibung, Materialausfluss an der Rückseite und mechanisch starker Zusammensetzung des verwendeten körnigen Materials. Die ersten Beobachtungen zeigten eine starke wechselseitige Beeinflussung zwischen der Segmentierung des SK und der Deformation des Keils.

Die räumliche Verteilung der Reibungsfestigkeit im Keil bestimmt hauptsächlich die örtliche Lage und das Volumen der verschiedenen Massenbewegungsprozesse. Die maximale Festigkeit beeinflusst vor allem den frontalen Teil des Keils. Unterhalb des mittleren und oberen Segments der Neigungsfläche wurde die Deformation von der zwischen stabil, statisch und maximal variierenden Reibungsfestigkeit bestimmt und definierte das hintere Segment des SK (dessen obere Grenzfläche eine Scherzone ist). Das Verhalten von Letzterem legte das mechanische Verhalten des Keils fest und definierte sein mittleres und hinteres Segment. Basale Erosion trat hauptsächlich unterhalb des mittleren und oberen Teils der Neigungsfläche auf. Verschiedene Phasen der Entwicklung der einzelnen Komponenten des Geschwindigkeitsfelds konnten beobachtet werden, was darauf hindeuten mag, dass Subduktionserosion ein irregulär verlaufender Prozess ist.

Das veränderliche Verhalten der Reibungsfestigkeit bestimmt auch den Materialfluss im SK. Die erste Serie von Experimenten, in der der Ausfluss von Material auf der Rückseite des Keils variiert wurde, bestätigte den starken Einfluss des SK auf dessen Entwicklung. Keile mit wenig Materialverlust auf der Rückseite entwickelten einen SK mit gleichmäßig verteilter Materialflussgeschwindigkeit entlang der Unterseite des Keils. Größere Ausflussmengen führten zu SK mit einer Segmentierung in Bereiche verschiedener Geschwindigkeiten, was auch eine veränderte Geometrie der Neigungsfläche zur Folge hatte. Letztere zeigte sich vergleichbar mit der Aufteilung in oberes, mittleres und unteres Segment der Neigungsfläche, welche in realen Forearcs beobachtet wird.

Die zweite Serie von Experimenten war der Analyse des Einflusses des Keilwinkels gewidmet. Sie zeigte, dass die zeitliche Abfolge der verschiedenen Werte für die Reibungsfestigkeit die Geometrie des SK, und damit auch die Stabilität des Keils, kontrolliert. Stabile Keile (definiert durch einen großen Keilwinkel) zeigten höhere Erosionsverhältnisse (Verhältnis von basaler zu frontaler Erosion) als kritische Keile (mit kleineren Keilwinkeln), wobei die Werte für Erstere den in der Natur beobachteten Größenordnungen entsprachen. Keile mit Keilwinkel oberhalb des kritischen Winkels zeigten eine starke Tendenz (~40%), massive SK-Strukturen (~18 km) zu bilden, was vergleichbar zu Beobachtungen für Nordchile oder Japan ist.

Die dritte Serie, die zur Evaluierung des Einflusses der internen Reibungseigenschaften des verwendeten körnigen Materials der Keile durchgeführt wurde, zeigte, dass basale Erosion in stärkerem Maße bei mechanisch starken Keilen auftritt, was auf kristallines Basement bezogen werden könnte (gewöhnlich der Fall bei erosiven Plattenrändern).

Im Rahmen der vierten Serie wurde der Einfluss von Topographie auf der subduzierenden Platte getestet. Diese

bathymetrischen Anomalien führten zu erhöhter frontaler und basaler Erosion im vorderen Segment des Keils und verhinderten basale Erosion in dessen hinterem Teil.

Diese Studie ist die Erste, die systematisch mögliche kinematische Rahmenbedingungen zur Erzeugung von Subduktionserosion untersucht. Wir stellen fest, dass von den getesteten Parametern die Öffnung auf der Rückseite des Keils, die den Materialausfluss aus dem System regelt, den größten Einfluss auf den Prozess der Subduktionserosion hat. War die Menge des ausfließenden Materials größer als die Menge Material, die am Fuße des Keils subduziert wurde, entwickelte sich der Rand erosiv. Der zweite wichtige Parameter ist der Winkel der Neigungsfläche, der in starkem Maße die Menge an basal erodiertem Material bestimmt.

A1. APPENDIX 1: Geological setting of erosional margins

The Northern **Chilean** segment is largely affected by the subduction of ridges. For instance, segment ~22-23ºS has high roughness from the interaction with the Iquique Ridge (Fig. 1.1.1), promoting the activity of extension and mass wasting. A little northward (~21ºS), the effect of the ridge seems to be minor (Calahorrano et al., 2008). The lower plate dip is 8°, but at 60 km from the trench axis it increases abruptly to 18° into the seismogenic zone (Delouis et al., 1996).

A small <5 km wide frontal prism (Figs. 2.2.1a and A1.1; Sallarès and Ranero, 2005) is formed with material from mass wasting. The lower and middle slope dip moves from ~7º, decreasing landward to ~3.5º at the upper slope. Seismic images from the basement at the lower slope show a series of 5 km thick base-parallel structures (Fig. 2.2.1b). Transport of the subducted oceanic sediment layer occurs together with basal erosion and underthrusting below the lower (Adam and Reuter, 2000; Clift and Hartley, 2007) and middle slopes (von Huene and Ranero, 2003).
The Central Chile segment (Laursen et al., 2002), affected by the Juan Fernandez Ridge, presents a midslope basin of ~3 km depth. The basin genesis is the subsidence of the middle slope due to the subduction of the ridge since ca. 10 Ma, but with episodes of compressional deformation, which increases seaward. Tilting of the upper slope is contemporaneous to the basin formation. Normal faults within the sediments in Valparaiso Basin are scarce and they do not reach the basement. At the lower slope they reflect gravitational collapse. Subduction of the ridge has accelerated subsidence at the middle slope. To the north of the ridge, lower and middle slopes are cut by seaward dipping normal faults, implying material has been removed basally. The subsidence is more important in its inner edge, close to the upper slope (at 62 km from the deformation front), becoming slower near the lower to middle slope break (~0.5 vs ~0.3 km/Ma respectively). The earthquake focal mechanism indicates thrust faulting (Delouis et al., 1996).

In **Peru** (Fig. 1.1.2) the Nazca plate dips between 5.5 and 9° and is almost depleted of a sedimentary cover, and has a prominent roughness which decreases to the south (Hampel et al., 2004; Kukowski et al., 2008). To the North of the Nazca Ridge, the Yaquina area has several ridge-shaped bodies oblique to the margin. The area to the south of the Nazca Ridge (Southern Peru-Northern Chile) shows an important roughness of the oceanic plate. The Mendaña Fracture zone collides perpendicular to the trench.
The Peruvian trench is fed with sediment from slumping (Hampel et al., 2004) and thrust faults are imaged in the small frontal prism (von Huene and Suess, 1988). The slope dip decreases from ~9.5° in the lower slope to 4.4° at the middle slope and the upper section of the outer forearc decreases to 2.4° (Hampel et al., 2004). The lower slope shows in general a high local and regional scale roughness and is at the verge of failure everywhere, by over steepening caused by subduction erosion (Kukowski et al., 2008; Section 2.1). A low velocity frontal prism is smaller than 20 km width and the basement is probably Paleozoic (Kukowski et al., 2008). The lower slope surface in the Mendaña

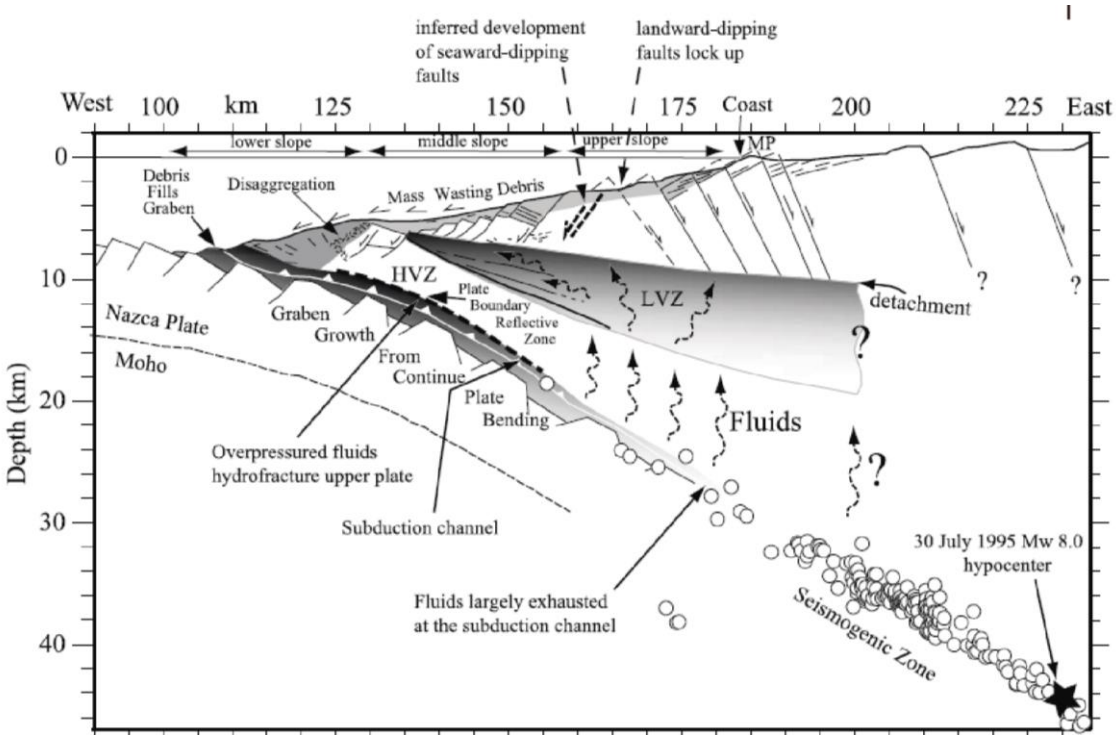

Figure A1.1. *Tectonic interpretation from seismic line from Northern Chile (CINCA SO104-13by Sallares and Ranero, 2005*

Fracture zone does not seem to be affected by the collision (Kukowski et al., 2008).

However, in the area to the south affected by passage of the Nazca Ridge (since Middle Miocene), the lower slope is basally eroded, subsiding and over steepening it, triggering gravitational collapses and slumps (Li, 1995). The lower slope is cover by sediment from wasting of large collapses and slumps. Also uplift of the forearc is observed in this part of the margin (Hampel et al., 2004; Saillard et al., 2011). Landward dipping reflectors delineate imbricated sedimentary rocks offscraped from the lower plate (von Huene and Suess, 1988; von Huene et al., 1996; Clift et al., 2003).

The midslope surface which undergoes long-term subsidence, deformed with canyons and high-angle normal faults (Moberly et al., 1982; von Huene and Lallemand, 1990), possesses an irregular topography and hosts some small to medium size extensional basins in its upper portion. The largely faulted Neogene sediments at the middle and upper slope at the central part of Peru mostly dip seaward and some cut the seafloor and separate rotated blocks (Moore and Taylor, 1988). They are associated with downslope gravity forces by over steepening of the margin (Kemp and Lindsley-Griffing, 1989; von Huene et al., 1988).

The geometry of the upper slope is mainly stable (Kukowski et al., 2008). Transition from the upper slope to the outer shelf is indicated by gullies, showing erosional processes involved (Hampel et al., 2004). The southern Peru area exhibits a slow and modest

uplift of the coast since 2 Ma (Clift and Hartley, 2007). The shelf extensional structures are related to dewatering, subsidence and local extension, and also to the release and accommodation of short term coseismic compression events (Saillard et al., 2011).

In the **Ecuadorian** margin (Fig. 1.1.3) the thickness of the sediment blanket (500-1500 m) transported on the Nazca plate varies associated to the Carnegie Ridge, the erosion of the Andean Western Cordillera and the Grijalva Fracture Zone (GFZ); Calahorrano et al., 2008). The smooth part of the Farallon plate is to the south of the GFZ (Fig. A1.2a), while a rough surface characterizes the Nazca plate to the north (Fig. A1.2b; Calahorrano et al., 2008).
The frontal sediment prism is 3-10 km wide and the lower slope angle is about 7°, decreasing upslope at the midslope to 3.5°.
The frontal segment of the forearc shows a compressional regime. In the south, the basin of the Gulf of Guayaquil is subsiding quickly, trapping sediments coming from the Andes reaching ~7 km depth at the upper slope (Collot et al. 2002; Fig. A1.2c). Several normal faults cross the thick sediment apron at the middle slope. Further north of the GFZ, in the southern flank of the Carnegie Ridge, the surface of the slope of the margin is irregular (Sage et al., 2006), with large embayments at the middle and upper slope, indicating basally removed material by tunneling (e.g., Ranero and von Huene, 2000; von Huene et al., 2000). From ~1°35'S to the north, the surface slope is recognized as smooth and linear (Fig. A1.2e; Sage et al., 2006). The segment 2°5'S-1°N facing the Carnegie Ridge has an steep inner trench slope steep and the coastal areas have been uplifted (Quaternary terraces >300 m), blocking sediments going to the trench. The front is locally indented by the impact of the several meters high and ~15 km wide seamounts (Fig. A1.2d).

The oceanic plate in **Costa Rica** (Fig.1.1.4) has an average dip angle of ~9° (i.e. average taper ~12.5°; Zhu, 2010). Three segments with different degrees of roughness are recognized in the lower plate: the Cocos Ridge in the south, a seamount segment in the center and a smooth surface segment to the NW (Ranero and von Huene, 2000).

From the 4 km width frontal prism (Kimura et al., 1997; von Huene and Scholl, 1991; Ranero and von Huene, 2000; Maltman and Vannucchi, 2004), the dip of the slope changes from 8º to an average of 3.5º upslope (Zhu, 2010). The irregular morphology of the slope with slumps and gravitational collapses at the front, becomes more stable and smoother toward the upper slope, with some canyons.
The impact of the seamounts with an unusual height (likely as an heritage of the Galapagos hot spot) is affecting retreat of the toe and groves on the surface slope (Fig. A1.2a; von Huene

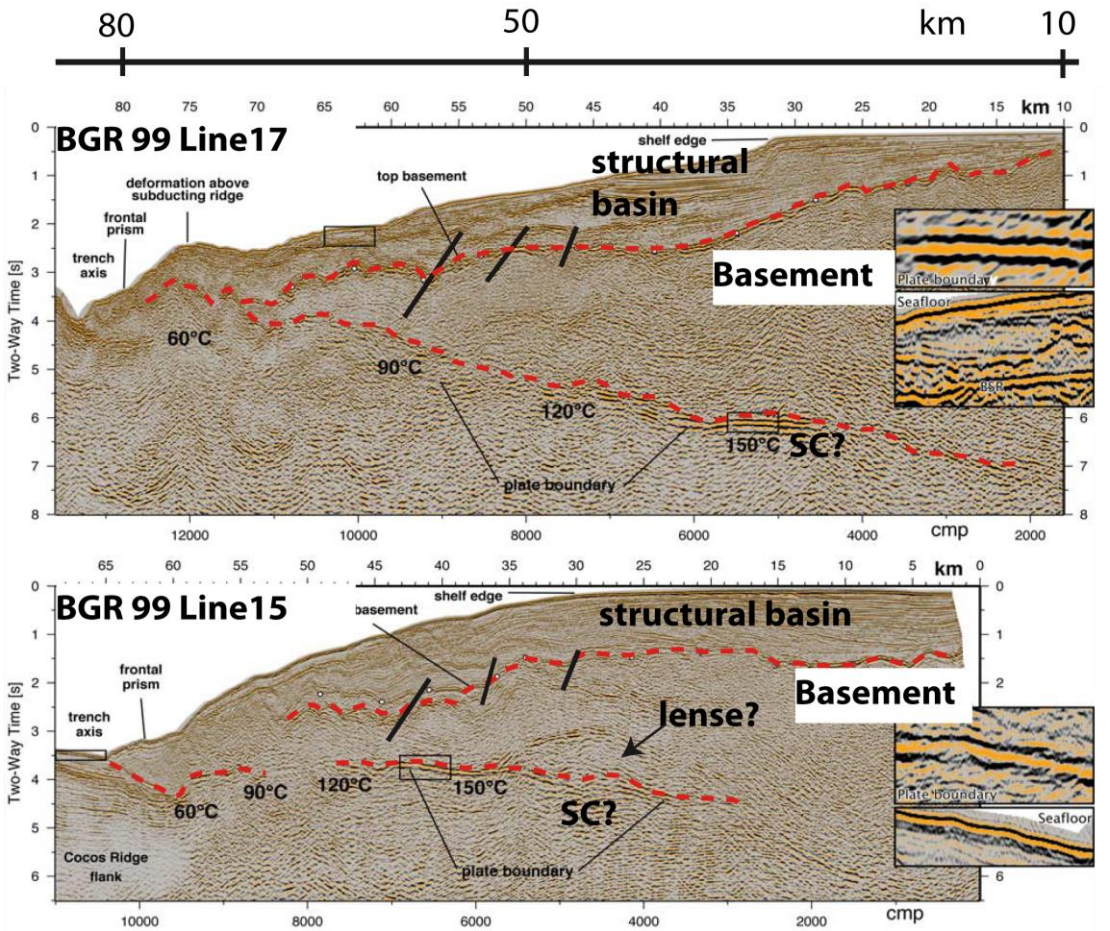

Figure A1.2. *Multichannel seismic profiles across Costa Rica (After Ranero et al., 2008). The upper red-dashed line shows the bottom of the sediment covering the slope, lower dashed red line indicates the top of the subduction channel. The bold black lines highlight some of the normal faults cutting the slope apron and/or basement. a) Multichannel seismic reflection where a seamount is subducting. b) Multichannel seismic reflection where the flank of Cocos Ridge subducts*

and Scholl, 1991). Thrusts identify the lower slope and landward dipping normal faults are seen at the middle and upper slope, changing their dip to more horizontal towards the latter (Fig. 2.2.2; von Huene and Ranero, 1998; Vannucchi et al., 2001). Only slight normal faulting cuts the sediment apron at the middle and lower slopes, also reaching the basement (Fig. A1.2a; Weinrebe and Ranero, 2003). The underthrusting of the Cocos Ridge has increased the subsidence rate after the Miocene and may be accelerating basal erosion ca. 5-6.5 Ma (Fig. A1.2b; Vannucchi et al., 2003; Weinrebe and Ranero, 2003). The Expedition 334 (2011) in the northwestern flank of the Cocos Ridge identified compressional structures at the middle slope (some of the thrust faults have been reactivated as normal faults) and extensional faults at the upper slope. Where the oceanic plate is little faulted, the continental plate shows the most stable morphologhy, with gentle dips and canyons in the mid-upper slopes (Fig. 9a). Here, evidence for basal tectonic erosion has been captured in seismic profiles as megalenses at the base of the forearc (Fig. 2.2.2; von Huene et al., 2000) and tunneling (von Huene et al., 2000; Exp. 334; Vannucchi et al., 2001).

The thin (~5 km) oceanic plate off **Nicaragua** (Fig. 1.1.4) is pervasively faulted and contains some smaller seamounts. It would potentially control the continental slope taper and morphology, which is less stable than off the smooth Nicoya segment (Ranero and von Huene, 2000; Harders et al., 2011; Also see discussion of Section 3.2.1c). Variations of the dip of the oceanic plate are also call to explain basal erosion below the middle forearc (Ranero et al., 2000; See also Section 3.2a.iv). A small prism (<10 km, Ranero et al., 2000) with accreted sediment forms the front of the continental wedge. The initial dip ~6°of the lower slope increases to 17º toward the middle slope and at the upper portion drops to 2.5°. Echelon ridges, slumps and canyons interrupt the surface of the lower slope, and massive normal faults cut the middle slope, because of the abrupt steepening from lower to middle slope (Fig. 2.2.3). The middle-upper slope basin is ~3 km, deepening towards the continent (12 km depth and 40 km width; Ranero et al., 2000). The disrupted surface results from the entrance of the pervasively fractured oceanic plate beneath it (Fig. A1.3; von Huene et al., 2004; Ranero et al., 2008). The steep taper, the scars and landslides on the surface of the slope are showing that basal erosion is likely active (Ranero et al., 2000). A long term regional subsidence began between Oligocene and Miocene. During the early Miocene the current upper continental slope subsided ~2 km and 3-4 km along the mid- to upper slope transition (Weinrebe and Ranero, 2003). The faster subsidence ~5-6.5 Ma occurred in Costa Rica is not documented here.

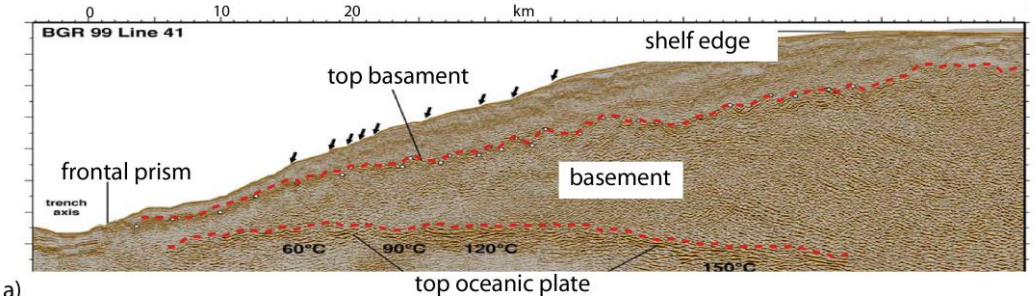

Figure A1.3. *Seismic profile across Nicaragua, after Ranero et al., 2008. Multichannel seismic reflection of the structures at its southernmost edge, next to Costa Rica margin. A "normal" rough oceanic crust subducts. No ridges or seamounts are present in the area.*

Horst and graben structures below a thin sediment layer can be observed in seismic records of the lower plate in **Guatemala** (Fig. 1.1.4). No large seamounts are present in the area (Weinrebe and Ranero, 2003; Harders et al., 2011). When entering the trench, the plate is bent, continuing to greater depth with a steeper dip.

The lower slope angle forearc is ~6°, decreases to 3° in the middle and is almost horizontal at the upper slope (von Huene, Aubouin et al, 1985). The associated taper is ~16° (Vannucchi et al., 2004). Its frontal prism consists of upper plate basement (Aubouin and von Huene, 1985). Failure and several scarps from the seaward dipping normal faults are present in the lower slope, close to the frontal prism (Fig. A1.4a; Aubouin et al., 1984; Aubouin and von Huene, 1985). Updip, in the middle and upper slope of the massive wedge, the landward dipping normal faults are less common (Fig. A1.4b; Auboin et al., 1984). From the middle

slope, up across the shelf edge and also in the upper slope basin, some few contractional structures are seen in Cretaceous rocks (von Huene, Aubouin et al, 1985). During the late Paleocene, the middle and upper slope area was uplifted (the present edge of the shelf) and the ~1-2 km deep basin at the middle and upper slope is present since Eocene (von Huene, Aubouin et al, 1985; Aubouin and von Huene, 1985). In the shoreline area, the basin achieves as much as ~10 km depth (Seely et al., 1974; Seely, 1979; Ladd and Schroder, 1985; von Huene, 1989). Subsidence in the middle slope increases since the Miocene (Vannucchi et al., 2004).

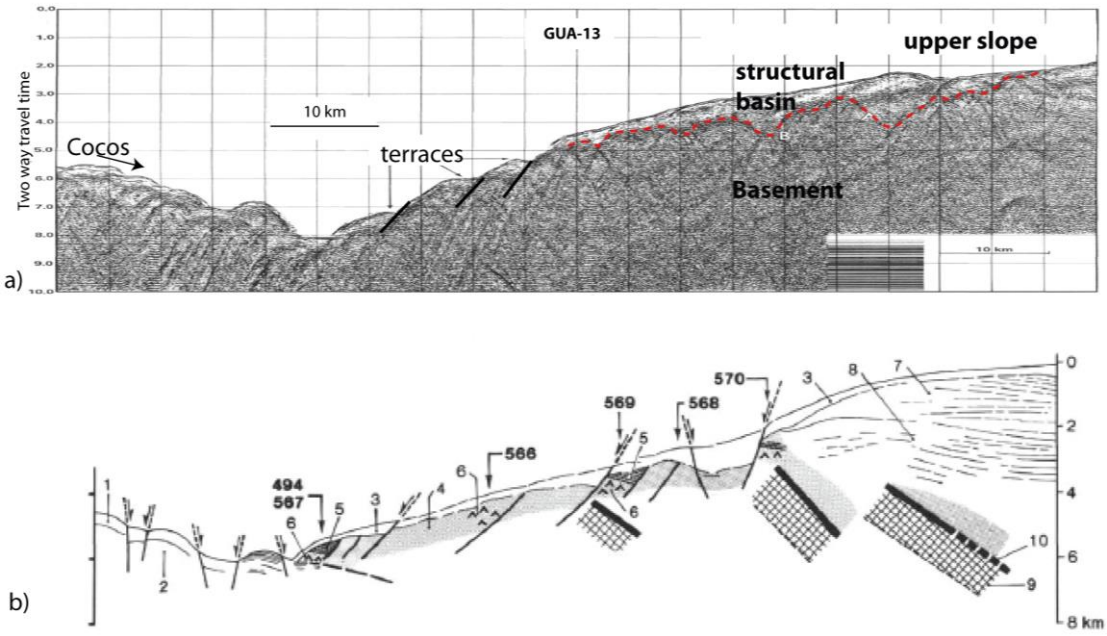

Figure A1.4. *a) seismic reflection section GUA 15 (~91°W) after Ladd et al., 1982, in Guatemala. Seismic velocities of 6.5 to 6.8 km/s. b) Interpretation of structures of the Guatemalan margin. Major landward dipping reflections are interpreted as thrust faults (von Huene, Aubouin et al., 1985).*

A nearly flat slab (Scholl et al., 2002) subducts beneath the middle slope of the **Aleutian** trench slope (Fig. 1.1.A1). A 2-3 km deep forearc basin is bounded at its seaward side by a high angle reverse fault, but a landward extensional regime is depicted (Davis and von Huene, 1987; Scholl et al., 2002). The basin is a consequence of dominant subcrustal erosion, which subsidence should have started well before the late Cenozoic. The basin formation indicates an enhanced material loss during the last 5-6 Ma, mainly thinning the mid slope area. Here, the opposite situation of what is observed in the Northern Chile-Southern Peru segment forms the forearc, with uplift dominating the frontal segment and basal erosion below the basin (Wells et al., 2003).

In NW **Japan** (Fig. 1.1.5), sharp normal faults identify the subducted lower plate (Fig. 12a; von Huene et al., 1994; von Huene and Lallemand, 1990). The horsts structures,which are cut by faults seems to be very deformed and begin to disintegrate landward, smoothing the surface of the lower plate in the vicinity of the stick-slip zone (Tsuru et al., 2000; Figs. 1.2 and A1.5).

The lower part of the small frontal accretionary body is filled with sediment from the middle slope slumps, as indicated by canyons and re-entrants. The lower slope is mostly steep and rugged. In a seismic line ~40°N is observed that the lower slope is divided by a steep ca. ~20º scarp, localized ~5-10 km from the deformation front (von Huene et al., 1994; von Huene and Culotta, 1989; Figs. 2.2.4). Whereas the upper part of the lower slope dips ~9°, the dip slope becomes gentler seaward. Basal transport of sediment is imaged beneath the former until the middle slope, and regional subsidence is confirmed with core drillings. Since the Pleistocene, the first ~17 km of the front of the margin are no longer exposed to deposition but to erosion, which is likely responsible for the rapid subsidence of the lower slope (von Huene and Culotta, 1989).

Frequent small normal faults and fractures increase in number toward the middle slope (von Huene and Culotta, 1989). Steep normal faults along strike interrupt the surface of the middle slope-terrace (Cadet et al., 1985; von Huene et al., 1994). As they dip seaward, they may be generated by a slope failure driven by gravitational collapse (von Huene and Culotta, 1989; von Huene and Lallemand, 1990). The upper slope topography is approximately smooth (Cadet et al., 1987), with some canyons (von Huene and Culotta, 1989; von Huene et al., 1994).

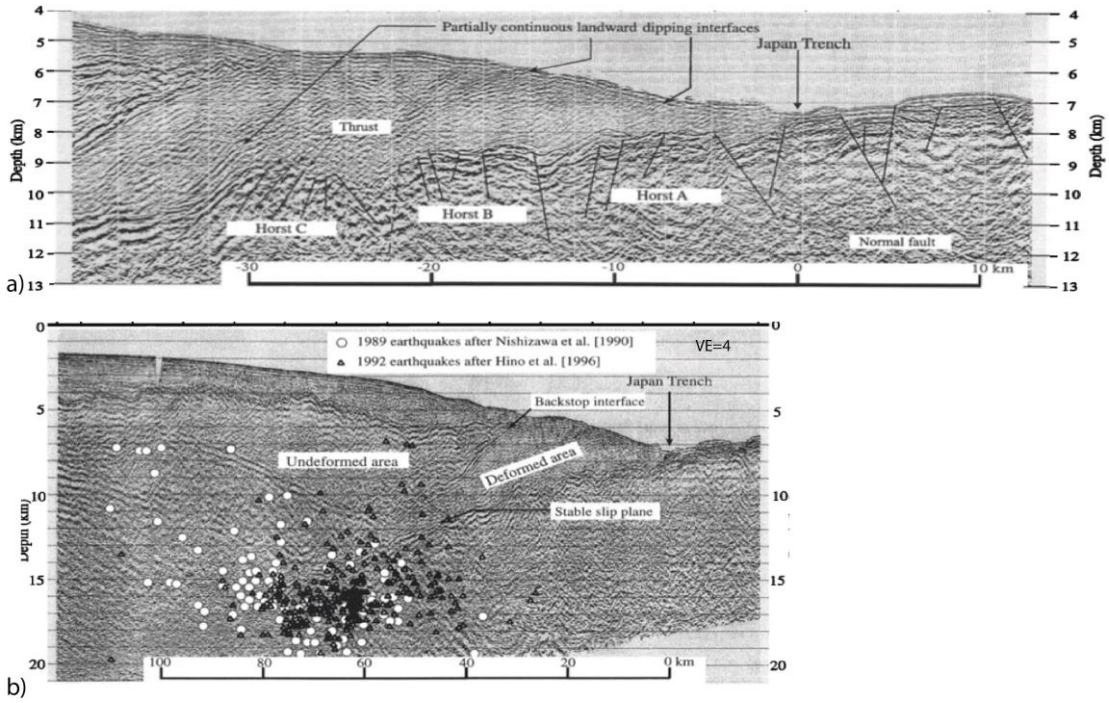

Figure A1.5*. Japan Margin (from Tsuru et al., 2000) a) seismic profile showing the deformation of horst structures, cut by several normal faults. b) Seismicity rapidly increases landward whereas oceanic crust is more deformed, thus the updip limit of the seismogenic zone coincides with the area of deformed sediments and destruction of horst structures*

The trench zone of **Tonga** (Fig. 1.1.A2) is largely affected by the Louisville Ridge. The oceanic plate shows pervasive fractures, faulting normally as it flexes the trench (likely hydrated) and large horst and graben

structures (Contreras-Reyes et al., 2011). The convergence is very fast, the plate covers with a little sedimentary blanket shows thermal maturity (Clift and MacLeod, 1999).

This sediment starved trench reaches depths of ~11 km, making it one of the deepest in the world, and possesses steep angles (10°) in some parts of the inner walls (Ballance et al., 1989). The lower slope is significantly fractured, fluid-satured and the midslope forearc was trenchward tilted, as a consequence of the frontal and basal erosion. Deep gullies show the highly eroded upper slope and the basin is fed through the canyon (Fig. A1.6; Clift and MacLeod, 1999; Contreras-Reyes et al., 2011). Extensional features of the forearc are trenchward-dipping normal faults and the several hundred km long-2 km offset scarp, indicating gravitational collapse (Contreras-Reyes et al., 2011).

Events of seaward tilting, significant shortening of the forearc (80 km), mostly by a major steepening of the trench slope and an accelerated subsidence and erosion are related to current and past collisions of the Louisville Ridge (Clift and MacLeod, 1999; Contreras-Reyes, 2011). The identified arcward tilting (32-16 Ma) and uplift of the forearc would suggest the gauge of initial collision of seamounts with the trench (Contreras-Reyes, 2011).

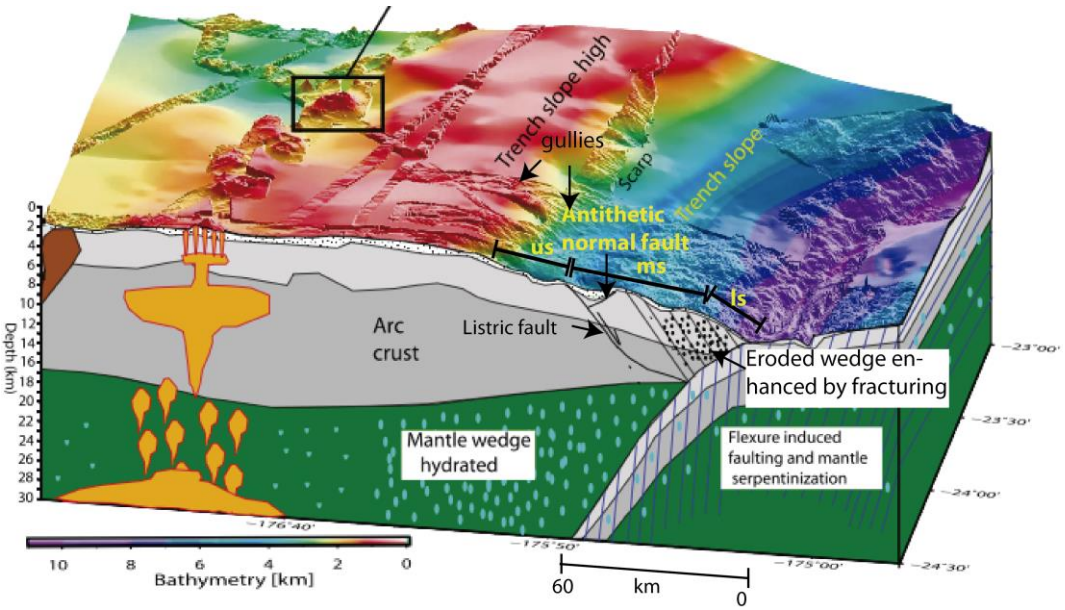

Figure A1.6. *Sketch from Tonga Arc (after Contreras-Reyes et al., 2011). The large scarp is interpreted to be a consequence of extension. us, ms and ls are the upper, middle and lower slopes, respectively.*

The **South Sandwich** islands (Fig. 1.1.A3) a difference of others foreacs with an upper, middle and lower slopes, consist of a small frontal prism (<6 km wide), a lower slope and a bench in the upper part. The bench is > 2°, its width increases from 40 km in the north to 80 km in width southward, with no indicators of extensional strain. The lower forearc slope angles are typically 7° - 9°, locally reaching up to 12°. The transition from the upper to the lower forearc segments is abrupt in the north, but more gradual in the south. The northern lower forearc slope includes two almost flat-lying terraces, whereas the southern lower forearc slope has no terraces and is narrower. Typically, block faulting, listric faulting, mass wasting, and

channels formed by turbidity currents are present in seismic profiles. The lower slope shows signs of gravitational collapses, due to subduction making the frontal segment unstable.

A2. APPENDIX 2: Preliminary tests and experiments not considered in this study in the 2D small box

During the first year, around 70 tests experiments were performed in a 1 m long and 10 cm wide box (Table en A2.1.1). The base of the box is covered with a conveyor belt with a rough surface simulating the oceanic crust. A body wedge-shaped rests on the belt emulating an outer forearc. The initial wedge geometry is 50 cm x 12 cm x (different heights) cm and its back leans against a rigid wall. The material composing the wedge is sifted in different layers separated by thin black sand layers in order to be able distinguish the internal wedge deformation.

The reason for these preliminary tests was that the experiments performed in this small box were fast and simple, allowing to investigate a wide range of parameters. The results of the test experiments allowed a decision about the final configuration of the experimental series, which would be performed in the bigger experimental apparatus, which is basically more than 2 times in volume. For this reason, several different configurations were tested to study the influence of parameters that can become crucial for subduction erosion, although those were non-systematic studies. The models were organized into groups depending on the parameter to be analyzed: i) Initial surface slope, ii) Position, composition and size of bodies embedded in the wedge, iii) Basal dip, iv) Height of the opening at the lower edge of the back wall (referred as well as subduction gap), v) Basal topographic/material properties and vi) strength of the wedge. Bodies embedded in the wedge act as heterogeneities: glass beads represent a weak material, or corn flour represents a strong material

The decision about the final configurations in the big experimental apparatus was made based on the results from the small device (e.g. Fig. A2.1). Finally, by considering the major observed features (slope angle, slope configuration, type and position of structures, tracking of material transfer; Fig. 5b), the key experiments were chosen. A part of the quantitative results are shown in Figure 5a. In it, different initial slope angles, basal angles, conveyor belts with different surfaces, shapes of the wedges and different heterogeneities embedded in the wedges were tested. Graphical analysis of tip retreat and lower slope angles manifested that weak and strong zones (heterogeneities) embedded in the wedge affected notoriously both, decreasing lower slope for wedge with a weak zone (Fig. A2.1a-Sand wedge-Glass beads lens vs Sand wedge-Corn Flour lens) and decreasing retreat of the tip with weak and strong zones (Fig. A2.1a-Sand wedge-Glass beads lens and Sand wedge-Corn Flour lens vs Sand wedge-Mix material lens). On the one hand, the presence of weak against strong heterogeneities contributes a broader distribution of localized shear zones. Particles' displacements show longer and more complex movements of the sediment inside the wedge, with some uplift zones and other subducting (Fig. A2.1b). On the other hand, "Sand models" plots manifest stronger tip retracting during the first 20 cm of convergence and afterwards, eventually it became slower. This change in the velocity of the tip retreat after the 20 cm convergence coincides with the time with a change of the lower slope angle, which became smaller in mostly of the experiments. Results from "Sand models" group

vary only on the tip retreat although they do not on lower angle. First appreciations link a disrupted surface of the conveyor belt (Fig. A2.1a-Pure.Sand.Chain.Test and Pure.Sand.Chain) and lower basal friction to a faster tip retreat (Fig. A2.1a-conveyor.Belt.Sand_Glass.Beads and Conveyor. Belt.1Sand_2 No. Sand).

The final conclusions of all the experiment performed during the first year of work indicate that the tip of the wedge retreated faster if the wedge included heterogeneities or the initial surface slope was lower.

The structural style of the wedge was strongly influenced by the presence, position and composition of the heterogeneities. When the heterogeneity (lens in Fig. A2.1b) was composed of glass beads and was directly placed on the conveyor belt, a reverse fault developed in the middle and rear part of the wedge (Fig. A2.1b) and basal accretion occurred mainly between the sandpaper and the heterogeneity. The mechanically weak material accumulates most of the deformation and transmits the strain towards the rear part. In cases with an initially low surface slope, reverse faulting was favored in the lower slope. A lower initial slope angle implies a smaller normal force, permitting an easier accumulation of accreted material, which translates into a faster tip retreat. In contrast, when the heterogeneity was composed of a mixture of flour and sand, deformation was concentrated close to the toe of the wedge during initial stages of convergence and was evenly distributed over the entire wedge afterwards. The stronger material initially acted as a backstop concentrating the strain in the front. Subsequently, only uplift was observed.

See pictures of experiments on DVD, in A2.2

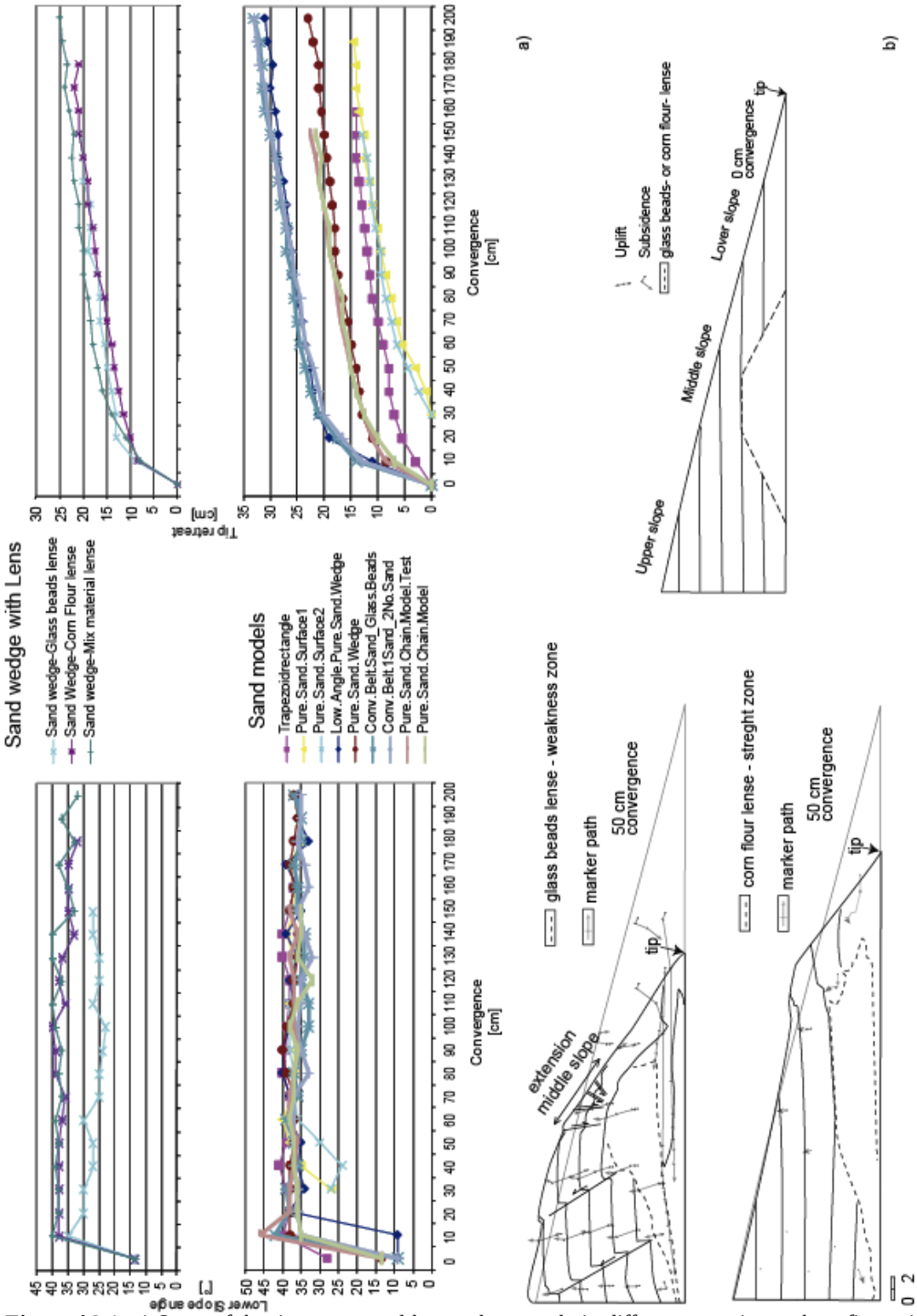

Figure A2.1. *a) Some of the tip retreat and lower slope angle in different experimental configurations tested in the small apparatus. Included are experiments that are not directly mentioned in this progress report, though they were part of the tested models. b) Cartoon comparing two stages of heterogeneous sand wedges. Upper sketch corresponds to the initial stage. Left and right bottom sketches compare after 50 cm of convergence. A weak lens aids to develop extensional structures on the middle slope and a compressional zone below the slope of the wedge (bottom left). A stronger lens centers thrust structures at the frontal part of the wedge, reducing deformation of the wedge (bottom right). Path of the triangular markers during 150 cm of convergence are indicated on their respective model.*

A2.1. List of experiments performed in the small 2D box

Table is divided in two parts, where the second part each experiment is referred by its Exp.#.

CB: Conveyor Belt

CF: Corn Flour

Gap: Height at the foot of the backwall

Name	Exp. #	Nomenclature	Short description	initial geometric shape
test.Lenses.Basal.Detachment	3	TLBD	Weakness zone is formed by colored sand lenses surrounded by thin glass bead layers, embedded in the lower zone of a wedge shaped sand body.	Wedge
Lenses	4	LCS	Weakness zone is formed by colored sand lenses surrounded by thin glass bead layers, embedded in the lower zone of a wedge shaped sand body.	Wedge
Pure.Sand.Wedge	5	PSW	wedge shaped body of pure sand	Wedge
Pure.Sand.Surface 1	6	PSS1	2 initially horizontal-sand layers on the conveyor belt will form the wedge as the conveyor belt moves. Initial thickness of each layer is 2 cm. Steady state is considered as initial state.	Horizontal layers
Pure.Sand.Surface 2	7	PSS2	same as PSS1 but with 3 layers of 1 cm thickness each	Horizontal layers
Trapezoidrectangle	8	TR	trapezoid-rectangular body of pure sand	Trapezoid-rectangle
Lenses.2cm.Over.Sandpaper	9	L2OS	same as L2O but the weakness zone is shorter and located 2cm over the sand paper	Wedge
Lenses.10cm.Length	10	L10cmL	same as L2O but the weakness zone is in the frontal part of the wedge	Wedge
Test.Backstop.Pure.Sand.Surface	11	TBPSS	Initial horizontal layers of sand on the conveyor belt will form the wedge due to movement of the conveyor belt. Steady state is considered as initial state. Backstop is to avoid border conditions of the backwall.	Horizontal layers
Backstop.Pure.Sand.Surface	12	BPSS	Repetition of TBPSS	Horizontal layers
Lenses.2nd.Middle.Level	13	L2ndML	same as L10cmL but the weakness zone is distributed along the length of the wedge (2 cm-over the sand paper)	Wedge
Isolate.Lenses	14	IL	The weakness zone consists of several isolate lenses which are distributed in the whole wedge	Wedge
Glass.Beads.Lens	15	GBL	The weakness zone is a single glass bead lens embedded in a wedge shaped sand body and located 2 cm over the conveyor belt	Wedge
Big.Glass.Beads.Lens	16	BGBL	same as GBL but lens is 1cm over the conveyor belt.	Wedge
Glass.Beads.Lower.Part	17	GBLP	The weakness zone is a single glass bead lens located directly on the CB. The lens is embedded in a wedge shaped sand body.	Wedge
Big.Glass.Beads.Lower.Part	18	BGBLP	same as GBLP but the lens is bigger	Wedge

Big.Mortar.Lower. Part	19	BMoLP	same as GBLP but the lens is composed of CF	Wedge
Low.Angle.Lenses	20	LAL	Colored sand lenses surrounded by thin glass bead layers, embedded in the lower zone of a wedge shaped sand body	Wedge
Low.Angle.Glass. Beads.Lens	21	LAGBL	The weakness zone is a single glass bead lens embedded in a wedge shaped sand body and placed directly on the CB	Wedge
Low.Angle. Pure.Sand.Wedge	22	LAPSW	wedge shaped body of pure sand	Wedge
Lenses.Mix1	23	LM1	same as LCS but lenses are composed by sand and CF.	Wedge
Lenses.2nd.Middle. Level.Mix	24	L2ndMLM	same as L2ndML but the lenses are composed of sand and CF.	Wedge
Low.Angle.Lenses. Mix	25	LALM	same as LAL but lenses are composed of sand and CF	Wedge
Isolate.Lenses.Mix	26	ILM	same as IL but lenses are composed of sand and CF.	Wedge
Bix.Mix.Lower.Part	27	BMiLP	same as BGBLP but lenses are composed of sand and CF.	Wedge
Lenses.Mix	28	LM	same as LCS but lenses are composed of sand and CF.	Wedge
Lenses.10cm.Lengt h.Mix1	29	L10cmLM1		Wedge
Lenses.10cm.Lengt h.Mix	30	L10cmLM	same as L10cmL but lenses are composed sand and CF	Wedge
Lenses.5	31	LCS5	same as LCS but β is 5°.	Wedge
Pure.Sand.Wedge. 5	32	PSW5	same as PSW but β is 5°.	Wedge
Big.Glass.Beads.Lo wer.Part.5	33	BGBLP5	same as BGBLP but β is 5°.	Wedge
Lenses.10cm.Lengt h.5	34	L10cmL5	same as L10cmL but β is 5°.	Wedge
Lenses.2nd.Middle. Level.5	35	L2ndML5	same as L2ndML but β is 5°.	Wedge
Low.Angle.Glass. Beads.Lens.5	36	LAGBL5	same as LAGBL but β is 5°.	Wedge
Glass.Beads.Lower. Part.5	37	GBLP5	same as GBLP but β is 5°.	Wedge
Low.Angle.Glass.Be ads.Lens.Low.Veloc ity	38	LAGBLLV		Wedge
Low.Angle.Mix.Len s	39	LAML	same as LAML but the lens is composed of sand and CF.	Wedge
R1.Low.Angle.Glass .Beads.Lens	40	R1LAGBL	repetition of LAGBL	Wedge
R2.Low.Angle.Glass .Beads.Lens	41	R2LAGBL	repetition of LAGBL	Wedge
Isolate.Glass.Beads .Lenses	42	IGBL	Same as LCS but lenses are of glass beads.	Wedge
Conv.Belt.Sand_ Glass.Beads	43	CBS_GB	same as LAPSW but detachment (CB) alternates sand and glass every 10 cm	Wedge

1cm.Wall.Low.Angle.Glass Beads. Lense	44	1cmWLAGBL	same as LAGBL but the gap at the foot of the backwall is 1 cm.	Wedge
Sand.Surface.Thin. Glass.Beads.Layer	45	SSTGB	same as PSS1 but there is a layer of glass beads between the sand layers and the gap at the foot of the back wall is 3 mm	Horizontal layers
Sand.Surface.Alternating.Glass.Beads.Layers	46	SSAGBL	same as PSS1 but there are layers between the sand layers and the gap at the foot of the back wall is 3 mm	Horizontal layers
R1.Glass.Beads.Lower.Part	47	R1GBLP	Repetition 1 of GBLP	Wedge
R2.Glass.Beads.Lower.Part	48	R2GBLP	Repetition 2 of GBLP	Wedge
Conv.Belt.1Sand_2No.Sand	49	CB1S_2NS	same as LAPSW but detachment (CB) alternates sand and CB surface every 10 and 20 cm respectively	Wedge
R3.Glass.Beads.Lower.Part	50	R3GBLP	Repetition 3 of GBLP	Wedge
Pure.Sand.Chain.Model.Test	51	PSCHMT	same as PSW but detachment (CB) is represented by a "teethed surface"	Wedge
Big.Glass.Beads.Lower.Part.3°	52	BGBLP3°	similar as BGBLP, but α and β are different	Wedge
Pure.Sand.Wedge.3°	53	PSW3°	wedge shaped body of pure sand	Wedge
Glass.Beads.Lower.Part.Front	54	GBLPF	same as GBLP but lens is in frontal part of the wedge	Wedge
Smaller.Lenses.Test	55	SLT	Same as GBL but lens is composed of several colored sand semi circumferences.	Wedge
Pure.Sand.Chain.Model	56	PSCHM	same as PSW but detachment (CB) is represented by a "teethed surface"	Wedge
Smaller.Semicircumferences	57	SS	Same as GBL but lens is composed of several colored sand lenses.	Wedge
Glass.Beads.Lower.Part.Big.Box	58	GBLPBB	Same as GBL but wedge width is 20 cm	Wedge
R1Glass.Beads.Lower.Part.Big.Box	59	R1GBLPBB	repetition of GBLPBB	Wedge
Glass.Beads.Lens.Lower.Part	60	GBLLP	Same as GBL but the lens isdirectly on the conveyor belt.	Wedge
Glass.Beads.Lower.Part.Overburden	61	GBLPO	Same as GBL but the lens is covered with 6 cm more of sand.	Wedge
Lenses.2cm.Over	62	L2O	Same as LCS but weackness zone is 2cm over the CB	Wedge
Mix.Wedge.20%	63	MW20%-0.6	The weakness zone is a single glass bead lens located directly on the CB. The lens is embedded in a wedge shaped 20%CF and 80%sand body.	Wedge
Mix.Wedge.10%	64	MW10%-0.6	Same as MW20%-0.6 but wedge is composed of 10%CF and 90%sand body.	Wedge
R1Mix.Wedge.10%	65	R1MW10%-0.6	Repetition of MW10%-0.6	Wedge
Glass.Beads.Lower.Part	66	MW0%	Same as GBLP but gap is 0	Wedge
Mix.Wedge.20%.0cm.Gap	67	MW20%-0	Same as MW0% but wedge is composed of 20%CF and 80%sand	Wedge
Mix.Wedge.10%.0cm.Gap	68	MW10%-0	Same as MW20% but wedge is composed of 10%CF and 80%sand	Wedge

Mix.Wedge.10%.1cm.Gap	69	MW10%-1	Same as MW20% but wedge is composed of 10%CF and 90%sand and gap is 1 cm	Wedge
R1Mix.Wedge.20%.0cm.Gap	70	R1MW20%-0	Repetition of MW20%-0	Wedge
Glass.Beads.Lower.Part.1cm.Gap	71	MW0%	Same as GBLP but gap is 1 cm	Wedge
Mix.Wedge.20%.1cm.Gap	72	MW20%-0	Same as MW20% but gap is 1 cm	Wedge

	angles				Length (L)/ Height (H) (cm)	Length (l1, l2) /Height (h) (mm)		weakness zone	
Exp. #	(α+β) inicial (°)	β (°)	gap back wall (mm)	Box width (cm)	Wedge size	Weakness zone	Composition weakness zone	On /over conv. belt	Obs.
3	13,5°	0°	6	10	L:50 H:12	l:34 h:4	Sand/sand and glass beads layers	on	Detach-ment zone with glass beads
4	13,5°	0°	6	10	L:50 H:12	l1:15; l2:34; h:4	Sand/sand and glass beads layers	on	
5	13,5°	0°	6	10	L:50 H:12	-	-	-	
6	13°	0°	7,5	10	L:52 H: 13,6	-	-	-	
7	12°	0°	6	10	L: 44,5 H: 12	-	-	-	
8	8°	0°	6	10	L: 50 H: 10	-	-	-	
9	13,5°	0°	6	10	L:50 H:12	l1:1; l2:20; h:4	Sand/sand and glass beads layers	over	
10	13,5°	0°	7	10	L:50 H:12	l1: 1; l2:30; h:4	Sand/sand and glass beads layers	over	
11		0°		10	L: H:	-	-		technical problems
12		0°	7	10	L: 43 H: 12	-	-	-	
13	13,5°	0°	7	10	L:50 H:12	l1: 38, l2:41; h:3,5 distributed several isolate lenses	Sand/sand and glass beads layers	over	
14	13,5°	0°	7	10	L:50 H:12		Sand/sand and glass beads layers	over	
15	13,5°	0°	8	10	L:50 H:12	l1:3; l2:14; h:2	Sand/glass beads	on	
16	13,5°	0°		10	L:50 H:12	l1:4; l2:22; h:4	Sand/glass beads	on	weakness zone at 1 cm over CB

17	13,5°	0°	7	10	L:50 H:12	l1:6; l2:22; h:4	Sand/glass beads	on	
18	13,5°	0°	7	10	L:50 H:12	l1:10; l2:32; h:4	Sand/glass beads	on	
19	13,5°	0°	7,5	10	L:50 H:12	l1:10; l2:32; h:4	Sand/mortar	on	
20	11°	0°	6	10	L:50 H:10	l1:10; l2:30; h:4	Sand/sand and glass beads layers	on	
21	9°	0°	7	10	L: 50 H:8	l1:16; l2:30; h:2	Sand/glass beads	on	
22	9°	0°	6,5	10	L: 50 H:8	-	-	-	
23	13,5°	0°		10	L:50 H:12	l: h:	Sand/sand-CF mixture and glass beads layers	on	technical problems
24	13,5°	0°	7,5	10	L:50 H:12	l1: 38, l2:41; h:4	Sand/sand-CF mixture and glass beads layers	over	
25	9°	0°	7	10	L: 50 H:8	l1:10; l2:30; h:4	Sand/sand-CF mixture and glass beads layers	over	
26	13,5°	0°	8	10	L:50 H:12	distributed several islate lenses	Sand/sand-CF mixture and glass beads layers	over	
27	13,5°	0°	7	10	L:50 H:12	l1:10; l2:32; h:4	Sand/sand-CF mixture	on	
28	13,5°	0°	8	10	L:50 H:12	l1:15; l2:34; h:4	Sand/sand-CF mixture and glass beads layers	on	
29	13,5°	0°		10	L:50 H:12	l1: 1; l2:30; h:4	Sand/sand-CF mixture and glass beads layers	over	technical problems
30	13,5°	0°	8	10	L:50 H:12	l1: 1; l2:30; h:4	Sand/sand-CF mixture and glass beads layers	over	
31	13,5°	5°	7	10	L:50 H:12	l1:15; l2:34; h:4	Sand/sand and glass beads layers	on	
32	13,5°	5°	7	10	L:50 H:12	-	-	-	
33	13,5°	5°	7	10	L:50 H:12	l1:9; l2:30; h:4	Sand/glass beads	on	
34	13,5°	5°	6,5	10	L:50 H:12	l1: 1; l2:30; h:4	Sand/sand and glass beads layers		
35	13,5°	5°	7	10	L:50 H:12	l1: 38, l:41; h:4	Sand/sand and glass beads layers		
36	9°	5°	8	10	L: 50 H:8	l1:15; l2:30; h:2	Sand/glass beads	on	

37	13,5°	5°	7	10	L:50 H:12	l1:5; 2l:19; h:4	Sand/glass beads	on	
38	9°	0°		10	L: 50 H:8	l1:15; l2:30; h:2	Sand/glass beads	on	
39	9°	0°	7	10	L: 50 H:8	l1:16; l2:30; h:2	Sand/sand-CF mixture and glass beads layers	on	
40	9°	0°		10	L: 50 H:8	l1:16; l2:28; h:2	Sand/glass beads	on	without normal faulting
41	9°	0°		10	L: 50 H:8	l1:16; l2:28; h:3	Sand/glass beads	on	without normal faulting
42	13,5°	0°	8	10	L:50 H:12	distributed several islate lenses	Sand/glass beads		
43	9°	0°	7	10	L: 50 H:8	-	-	-	
44	9°	0°	10	10	L: 50 H:8	l1:16; l2:28; h:2	Sand/glass beads		
45	19°	0°	3	10	L: 38 H: 11,7	-	-	-	
46	14°	0°	8	10	L: 54 H: 12	-	-	-	
47	13,5°	0°	7,5	10	L:50 H:12	l1:6; l2:23; h:4	Sand/glass beads	on	
48	13,5°	0°	7	10	L:50 H:12	l1:6; l2:22; h:4	Sand/glass beads	on	
49	9°	0°	7	10	L: 50 H:8	-	-	-	
50	13,5°	0°	8	10	L: 50 H:8	l1:6; l2:22; h:4	Sand/glass beads	on	
51	13,5°	0°		10	L:50 H:12	-	-	-	technical problems
52	10,5°	3°		10	L:50 H:12	l1:12; l:30; h:4	Sand/glass beads	on	2 parameters changed
53	10,5°	3°		10	L:50 H:12	-	-	-	2 parameters changed
54	13,5°	0°	8	10	L:50 H:12	l1:5; l2:22; h:4	Sand/glass beads	on	
55	13,5°	0°	8	10	L:50 H:12	l1:6; l2:24; h:4	Sand/sand and glass beads layers	on	
56	13,5°	0°	8	10	L:50 H:12	-	-	-	
57	13,5°	0°	6	10	L:50 H:12	l1:6; l2:24; h:4	Sand/sand and glass beads layers	on	
58	13,5°	0°	6	20	L:50 H:12	l1:6; l2:22; h:4	Sand/glass beads	on	floor not horizontal
59	13,5°	0°	6	20	L:50 H:12	l1:6; l2:22; h:4	Sand/glass beads	on	

60	13,5°	0°	6	10	L:50 H:12	l1:3; l2:14; h:2	Sand/glass beads	on
61	13,5°	0°	6	10	L:63 H:16	l1:5; l2:20; h:4	Sand/glass beads	on
62	13,5°	0°	6	10	L:50 H:12	l1:15; l2:34; h:4	Sand/sand and glass beads layers	over
63	13,5°	0°	6	10	L:50 H:12	l1:6; l2:2; h:4	20%CF-80%sand/glass beads	on
64	13,5°	0°	6	10	L:50 H:12	l1:6; l2:2; h:4	10%CF-90%sand/glass beads	on
65	13,5°	0°	6	10	L:50 H:12	l1:6; l2:22; h:4	20%CF-80%sand/glass beads	on
66	13,5°	0°	0	10	L:50 H:12	l1:6; l2:22; h:4	0%CF-100%sand/glass beads	on
67	13,5°	0°	0	10	L:50 H:12	l1:6; l2:22; h:4	20%CF-80%sand/glass beads	on
68	13,5°	0°	0	10	L:50 H:12	l1:6; l2:22; h:4	10%CF-90%sand/glass beads	on
69	13,5°	0°	1	10	L:50 H:12	l1:6; l2:22; h:4	10%CF-90%sand/glass beads	on
70	13,5°	0°	0	10	L:50 H:12	l1:6; l2:22; h:4	20%CF-80%sand/glass beads	on
71	13,5°	0°	1	10	L:50 H:12	l1:6; l2:22; h:4	0%CF-100%sand/glass beads	on
72	13,5°	0°	1	10	L:50 H:12	l1:6; l2:22; h:4	20%CF-80%sand/glass beads	on

A3. APPENDIX 3: Experiments performed in the 2D big box

See also movies and pictures on DVD, in A3.3

A3.1 Tectonic interpretation of principal experiments

Reference experiment R0

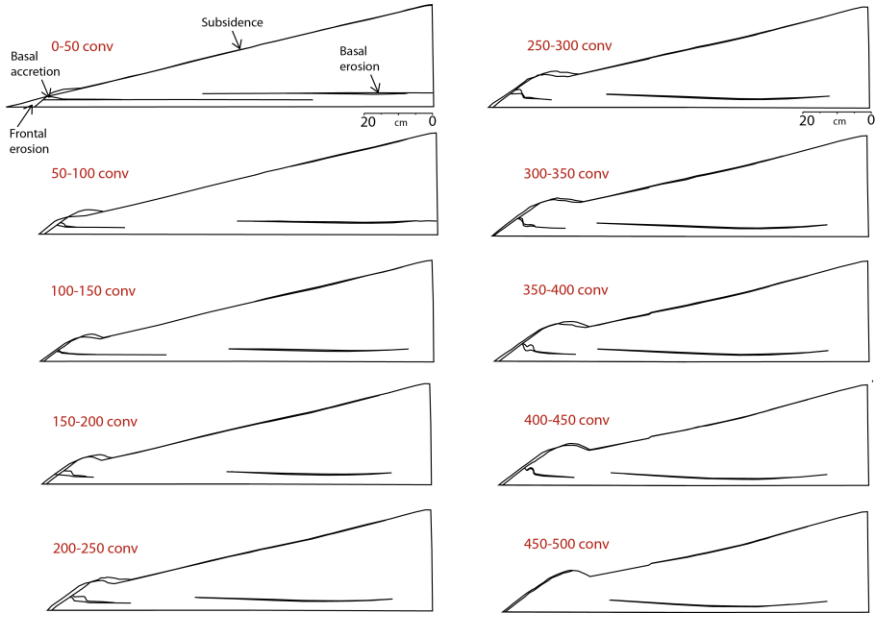

Series Subduction Gap SG

Experiment G1

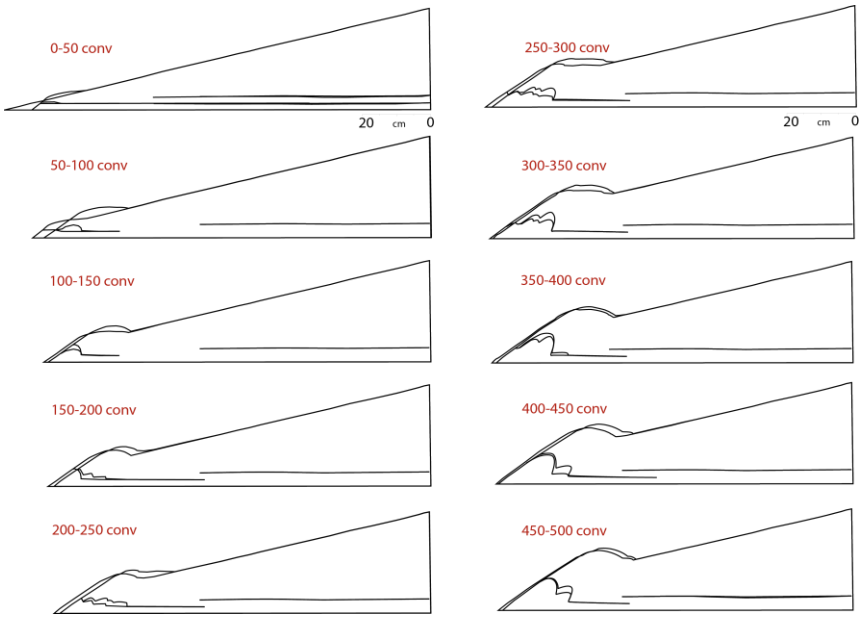

Experiment G2

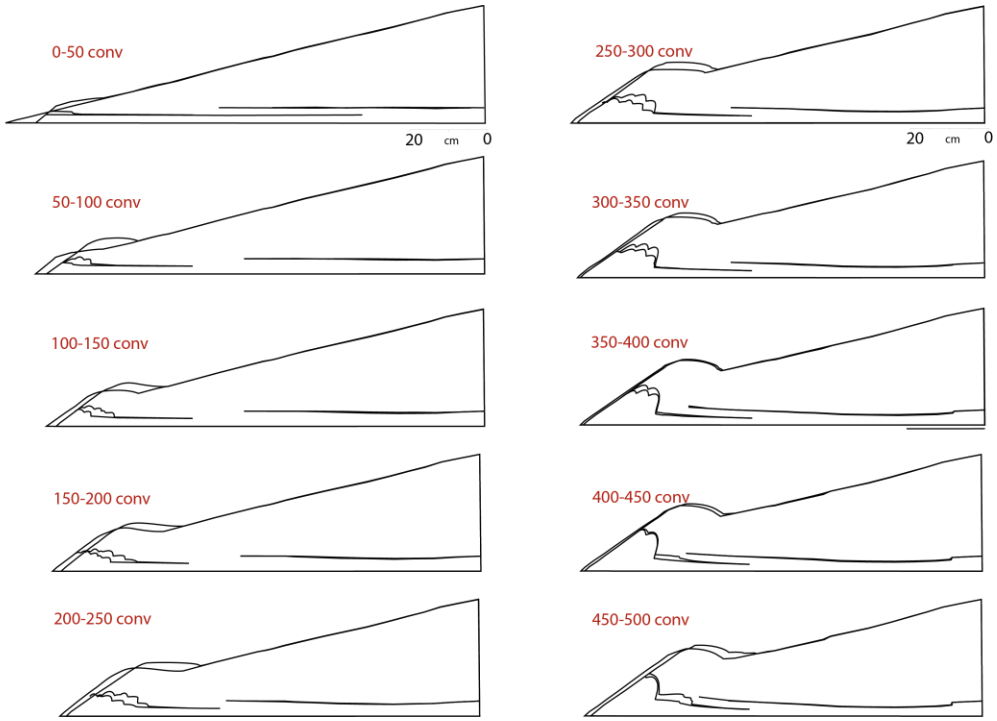

Series Surface Taper ST

Experiment T1

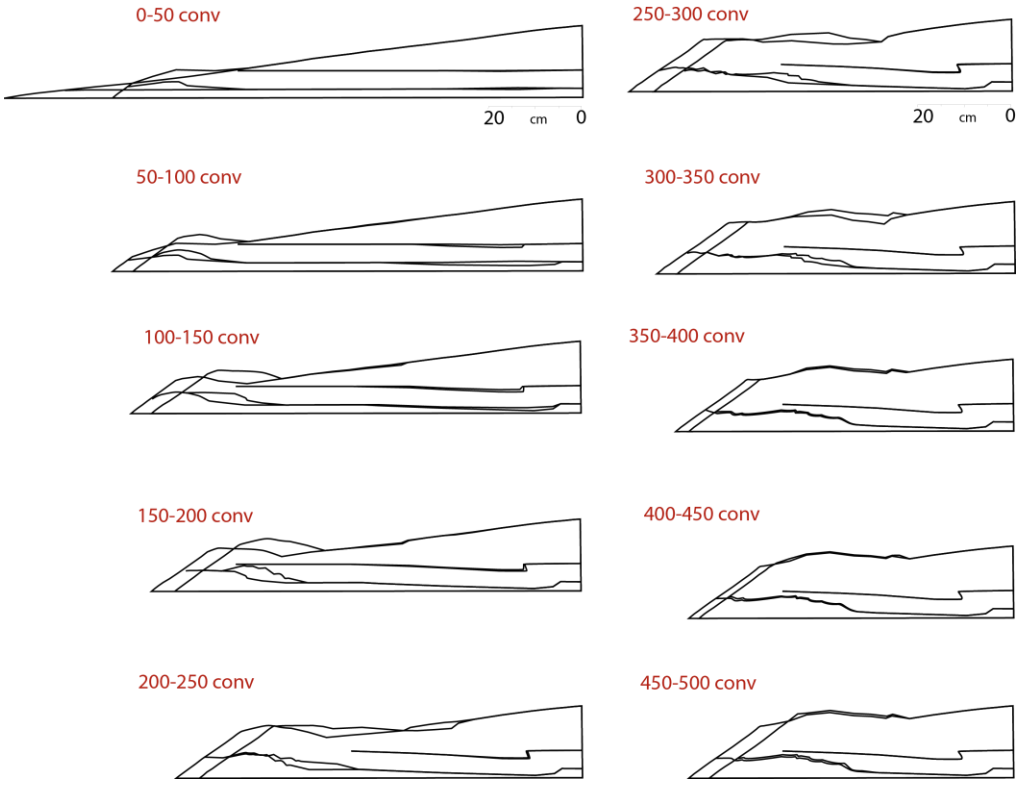

Experiment T2

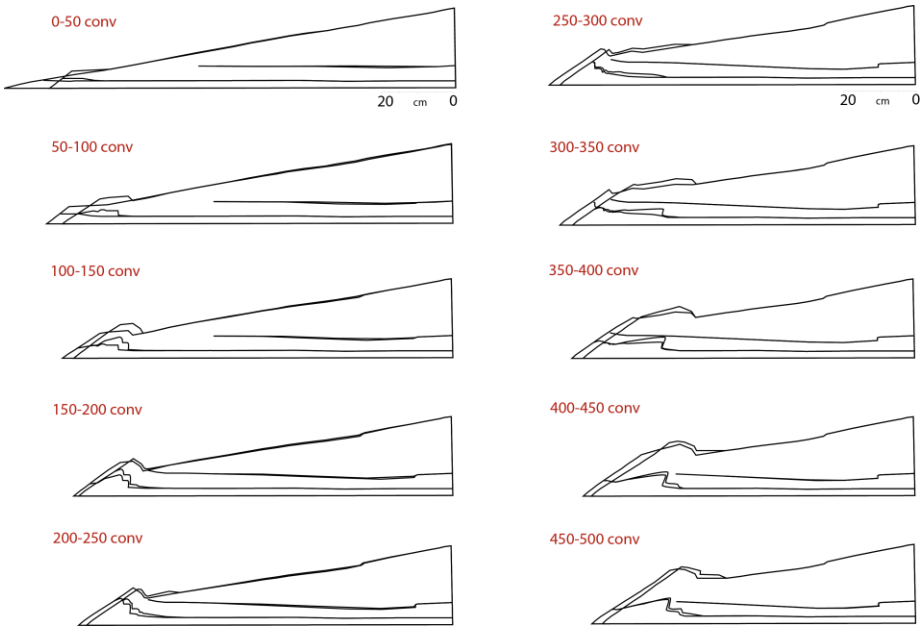

Experiment T4

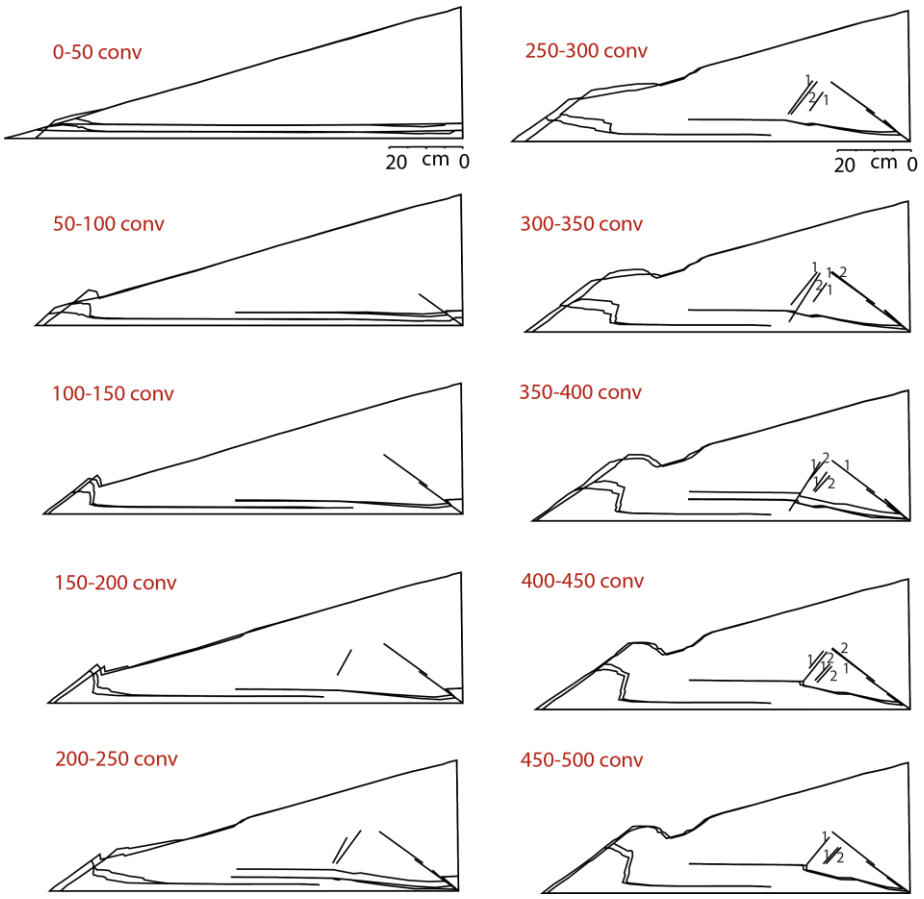

Experiment T5

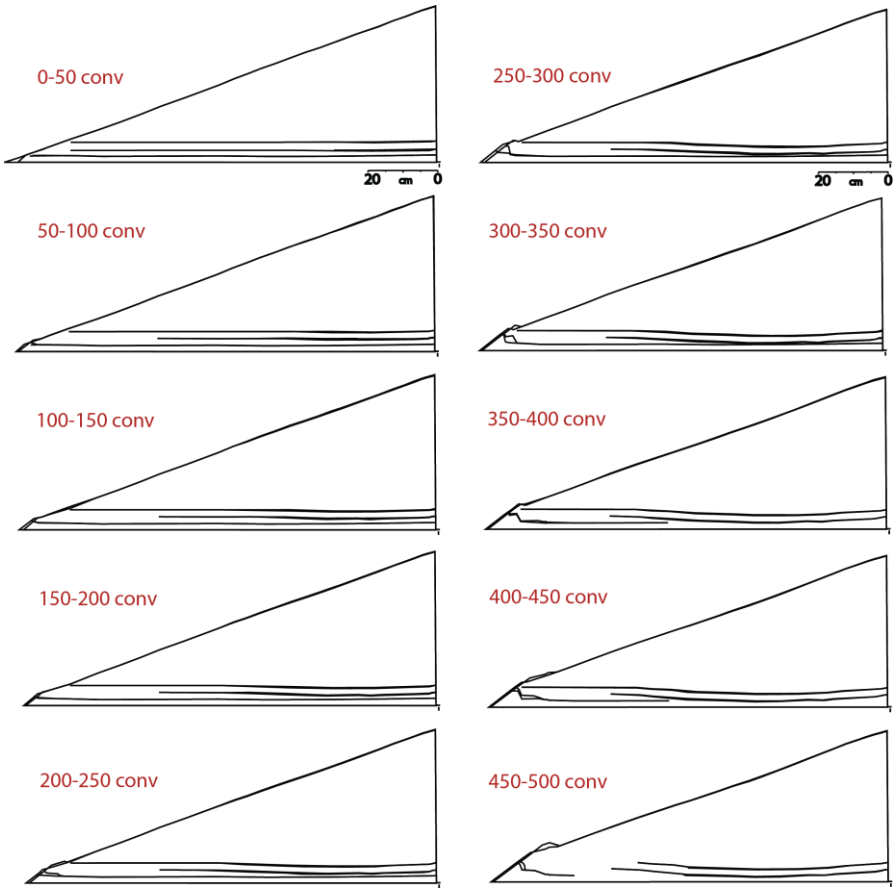

Series internal Friction IF

Experiment F1

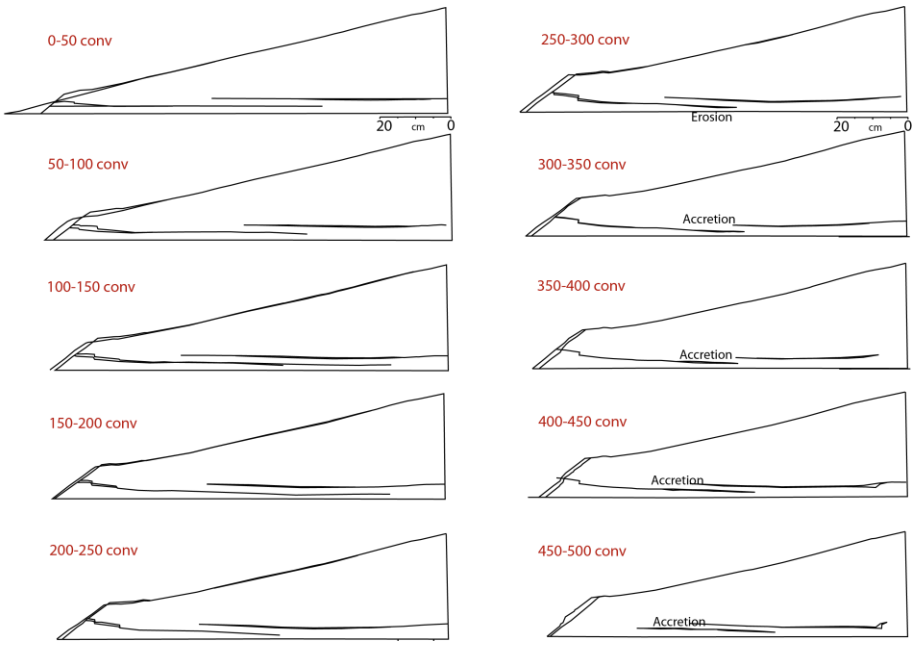

Experiment F2

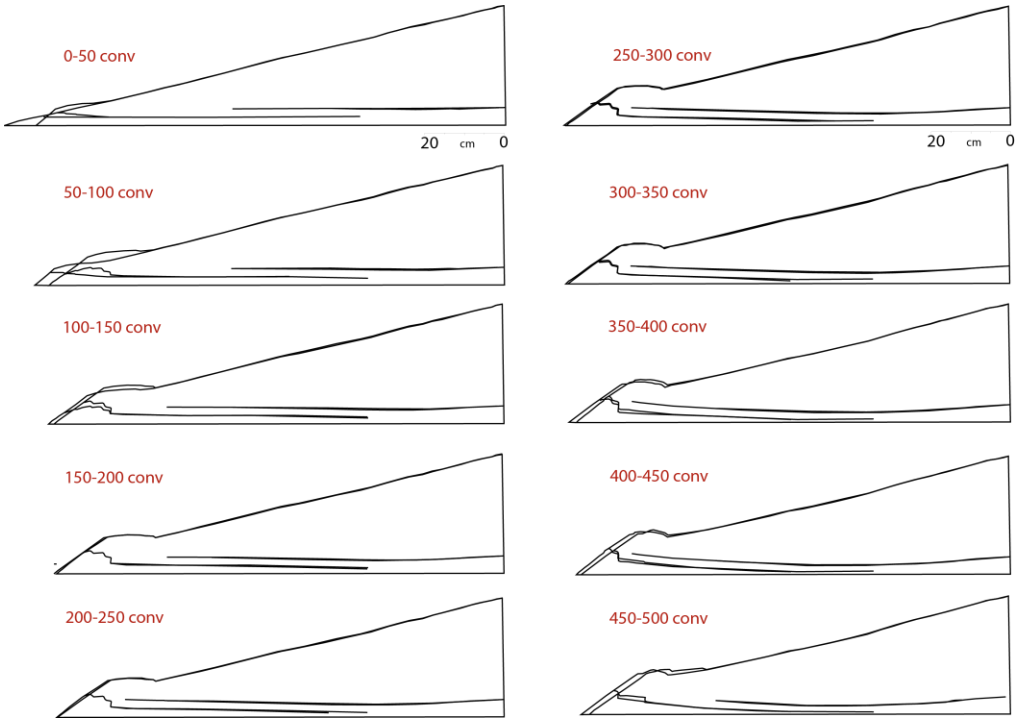

Experiment F3

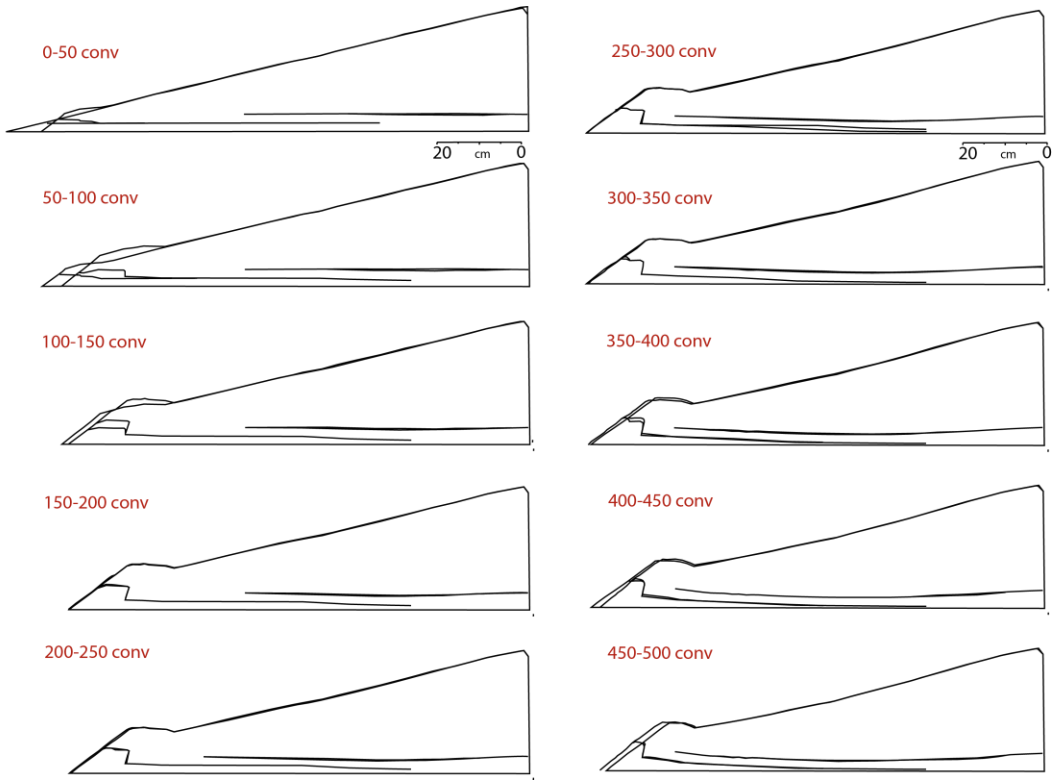

Series Highs and Lows HL
Experiment HL.1 and HL.2

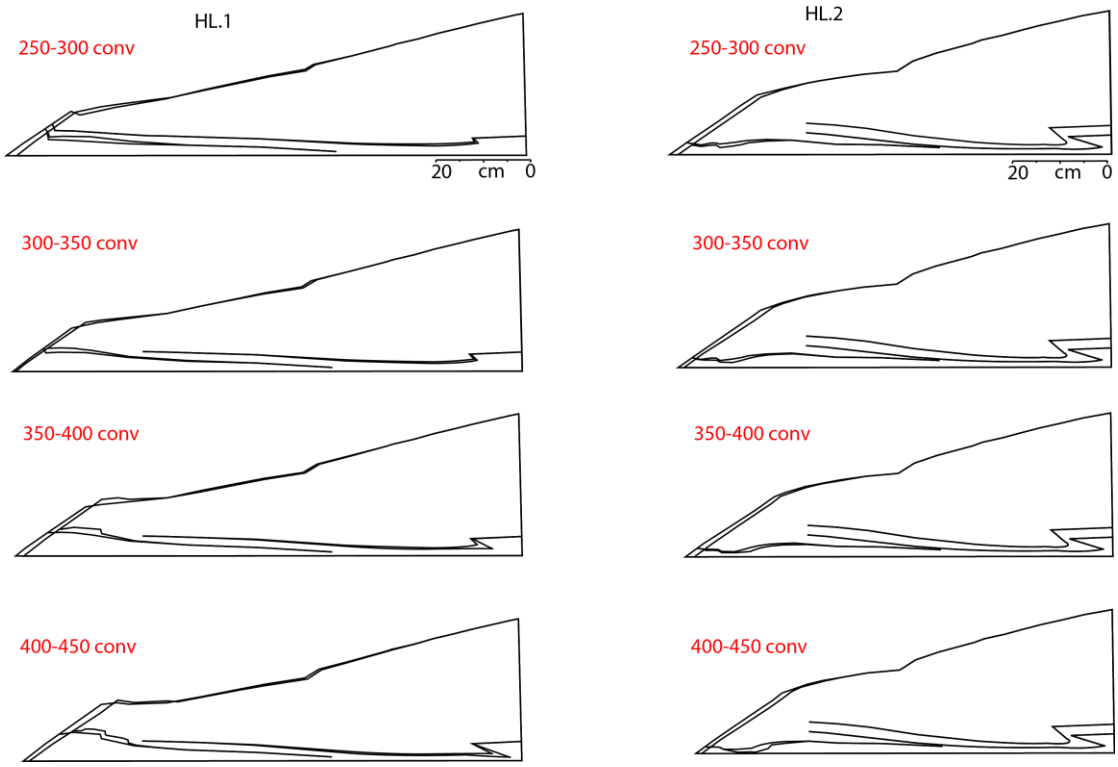

A3.2. List of all experiments in the big 2D box

Number of repetitions of a specific experiment corresponds to the recurrence of a forethrust at the base of the back wall

Exp. #	Nomenclature	%sugar-sand	Weakness bodies	initial slope angle α	gap back wall	Comments	Tested parameter	Times repetitions
1	PSW	100% sugar	No	α = 13,5°	6 mm	frontal accretion, basal erosion upper and middle slope.	Initial slope/internal friction	3 (because out of sequence thrust)
4	10°PSW	100% sand	No	α = 10°	6 mm	strong frontal accretion/forethrust	Initial slope	1
5	7°PSW	100% sand	No	α = 7°	6 mm	strong frontal accretion/forethrust.	Initial slope	1
6	4Sa6Su	40% sand-60% sugar	No	α = 13,5°	6 mm	frontal accretion, basal erosion upper and middle slope	Initial slope/internal friction	1
7	10°4Sa6Su	40% sand-60% sugar	No	α = 10°	6 mm	strong frontal accretion/forethrust	Initial slope	1
8	7°4Sa6Su	40% sand-60% sugar	No	α = 7°	6 mm	strong frontal accretion/forethrust	Initial slope	1
10	9Sa1Su	90% sand-10% sugar	No	α = 13,5°	6 mm	Out of sequence thrust	internal friction	2 (because out of sequence thrust)
12	8Sa2Su	80% sand-20% sugar	No	α = 13,5°	6 mm	frontal accretion, basal erosion upper and middle slope	internal friction	2 (because out of sequence thrust)
13	6Sa4Su	60% sand-40% sugar	No	α = 13,5°	6 mm	frontal accretion, basal erosion upper and middle slope	internal friction	1
15	2Sa8Su	20% sand-80% sugar		α = 13,5°	6 mm	Out of sequence thrust	internal friction	2 (because out of sequence thrust)
16	16°PSW	100% sugar	No	α = 16°	6 mm	Out of sequence thrust	initial slope	1
17	16°4Sa6Su	40% sand-60% sugar	No	α = 16°	6 mm	Out of sequence thrust	initial slope	1
18	20°4Sa6Su	40% sand-60% sugar	No	α = 20°	6 mm	small frontal accretion, strong basal erosion upper and middle slope	initial slope	1
19	10°PSW_chain	100% sand	No	α = 10°	6 mm	strong frontal erosion/stable slope	chain	1
20	9Sa1Su_chain	90% sand-10% sugar	No	α = 13,5°	6 mm	strong frontal erosion/stable slope	chain	1
21	6Sa4Su_chain	60% sand-40% sugar	No	α = 13,5°	6 mm	Out of sequence thrust	chain	1
22	Chain_6Sa4Su	40% sand-60% sugar	No	α = 13,5°	6 mm	140 cm convergence	chain	1
23	10°4Sa6Su_3mm	40% sand-60% sugar	3z	α = 10°	3 mm	frontal accretion, basal erosion upper and middle slope	Subduction window size	1
24	4Sa6Su_2mm	40% sand-60% sugar	No	α = 13,5°	2 mm	strong frontal accretion	Subduction window size	1
25	4Sa6Su_4mm	40% sand-60% sugar	No	α = 13,5°	4 mm	strong frontal accretion, basal erosion upper and middle slope	Subduction window size	1
26	4Sa6Su_4mm2_3	40% sand-60% sugar	no	α = 13,5°	3 mm	Technical problems	Subduction window	1

27	PSW_10	100% sugar	No	α = 13,5°	10 mm	Out of sequence thrust	size Subduction window size	1
28	PSW.GBL	100% sugar	Yes	α = 13,5°	6 mm	frontal accretion, middle and upper slopes critical	low friction lense	1

Erklärung

Hiermit versichere ich, dass die vorliegende Dissertation ohne unzulässige Hilfe Dritter und ohne Benutzung anderer als der angegebenen Literatur angefertigt wurde. Die Stellen der Arbeit, die anderen Werken wörtlich oder inhaltlich entnommen sind, wurden durch entsprechende Angaben der Quellen kenntlich gemacht. Diese Arbeit hat in gleicher oder ähnlicher Form noch keiner Prüfungsbehörde vorgelegen.

Berlin, Dezember 2012